Boundary layer processes impacting the surface energy balance in the Arctic

Julia Maillard

To cite this version:

Julia Maillard. Boundary layer processes impacting the surface energy balance in the Arctic. Atmospheric and Oceanic Physics [physics.ao-ph]. Sorbonne Université, 2022. English. NNT : 2022SORUS515 . tel-04638981

HAL Id: tel-04638981
https://theses.hal.science/tel-04638981

Submitted on 8 Jul 2024

SORBONNE UNIVERSITÉ - PARIS
ÉCOLE DOCTORALE 129
SCIENCES DE L'ENVIRONNEMENT

THÈSE

pour obtenir le titre de

Docteur en Sciences

de Sorbonne Université
Mention : Physique de l'Atmosphère

Présentée et soutenue par
Julia Maillard

Boundary layer processes impacting the surface energy balance in the Arctic

Thèse dirigée par François Ravetta & Jean-Christophe Raut

préparée au Laboratoire ATMosphères, Observations Spatiales (LATMOS)

soutenue le 7 juillet 2022

Jury :

Rapporteurs :	Julia Schmale	- EPFL
	Timo Vihma	- Finnish Meterological Institute
Directeurs :	François Ravetta	- LATMOS (Sorbonne Université)
	Jean-Christophe Raut	- LATMOS (Sorbonne Université)
Présidente :	Solène Turquety	- LATMOS (Sorbonne Université)
Examinateurs :	Javier Fochesatto	- University of Alaska Fairbanks
	Elsa Dieudonné	- Université du Littoral Côte d'Opale
	Étienne Vignon	- LMD (Sorbonne Université)

Contents

List of Acronyms

SEB	surface energy balance	26
SLP	sea-level pressure	15
BL	boundary layer	17
MOST	Monin–Obukhov stability theory	96
MWST	minimum wind speed for sustainable turbulence	9]
ALPACA	Alaskan Layered Pollution And Chemical Analysis	36
R_b	bulk Richardson number	32
R_f	flux Richardson number	
L	Monin-Obukhov length	23
ζ	dimensionless Monin-Obukhov height	24
κ	van Kármán constant	
AO	Arctic Oscillation	14
PNA	Pacific North American	14
SBI	surface based temperature inversions	22
COD	cloud optical depth	22
LWP	liquid water path	22
$\mathbf{CF_{LW}}$	cloud longwave radiative forcing	29
$\mathbf{CF_{SW}}$	cloud shortwave radiative forcing	29
$\mathbf{LW_{net}}$	net longwave flux	28
$\mathbf{SW_{net}}$	net shortwave flux	28
$\mathbf{SW_{d}}$	downwards shortwave flux	28
α	surface albedo	28
LAI	leaf area index	107
SZ	solar zenith angle	28
H	turbulent sensible heat flux	25

Résumé long

Contents

1 Introduction

1.1 L'Arctique : description et enjeux

L'Arctique est la région du globe située à son extrême nord. Ses limites exactes varient selon les définitions : parfois, il s'agit de toutes les latitudes auxquelles le soleil reste en dessous de l'horizon toute la journée au moment du solstice d'hiver ; parfois, de la zone de l'hémisphère Nord où la température moyenne du mois de Juillet est en-dessous de 10°C. Au centre de l'Arctique se trouve un océan, dont une grande partie est couverte de glace même en été. Deux masses continentales entourent cet océan. Très faiblement peuplé, l'Arctique continental est majoritairement couvert de toundra, ainsi que de taïga (ou forêt boréale) dans sa partie sud.

L'Arctique est une zone d'étude cruciale pour la communauté scientifique car c'est une région clé du réchauffement climatique. En effet, l'Arctique se réchauffe environ deux fois plus vite que le reste du globe [Serreze & Barry 2011] ; ce phénomène est nommé "amplification arctique". L'étendue minimale annuelle de la banquise (en septembre) diminue et la glace de mer pluriannuelle est remplacée par une glace de mer qui fond et re-gèle chaque année [Overland *et al.* 2018].

Plusieurs mécanismes de rétroaction ont été avancés pour expliquer l'amplification arctique. Le premier d'entre eux est la rétroaction glace-albédo : lorsque la glace de mer fond, l'eau qui se trouve en-dessous est révélée et l'albédo de l'océan diminue. La part de rayonnement solaire absorbée par la surface augmente donc, ce qui favorise la fonte de la glace. Théorisé pour la première fois à la fin du 19ème

siècle [Arrhenius 1896], ce mécanisme s'est avéré plus récemment être un élément important de l'amplification arctique, mais pas le facteur dominant [Winton 2006]. Deuxièmement, l'atmosphère de l'Arctique est fréquemment très stable. Cela signifie qu'une augmentation de température à la surface y est confiné au lieu d'être propagée vers des altitudes plus élevées par des mouvements de convection, comme cela serait le cas près de l'équateur. Le rayonnement infrarouge supplémentaire généré par cette augmentation de la température près de la surface est alors dirigé vers le bas au lieu de sortir de l'atmosphère, et la surface se réchauffe donc encore plus [Bintanja *et al.* 2011]. Ce mécanisme est un facteur prépondérant de l'amplification arctique [Pithan & Mauritsen 2014].
Enfin, il existe une rétroaction liée au nuage mais le signe et l'ampleur de cette rétroaction ne sont pas clairs [Pithan & Mauritsen 2014]. Les nuages peuvent également interagir avec l'amplification arctique d'autres manières. Au début de l'automne, par exemple, la formation de nuages est accrue au-dessus des zones libres de glace, ce qui augmente le flux infrarouge descendant et favorise le réchauffement [Kay & Gettelman 2009]. D'autre part, les nuages peuvent réguler la rétroaction glace-albédo en été en absorbant le rayonnement solaire descendant [Choi *et al.* 2020].

Les mécanismes décrits ci-dessus agissent dans la plus basse de l'atmosphère, appelée couche limite. Une meilleure compréhension des processus ayant lieu dans la couche limite arctique est donc très importante pour l'étude de l'amplification arctique.

1.2 Processus clés de la couche limite Arctique

La couche limite atmosphérique est "la partie de la troposphère qui est directement sous l'influence de la surface terrestre" [Stull 1988]. Elle est caractérisée par la présence de turbulence, qui peut-être générée soit par flottabilité, soit par cisaillement du vent. Dans une atmosphère stable, la flottabilité est négative et tend donc à s'opposer aux déplacements des masses d'air : la seule source de turbulence est donc le cisaillement.

La couche limite arctique se distingue de celle des moyennes latitudes car l'ensoleillement y varie suivant un rythme saisonnier et non journalier : la variabilité diurne y est donc moins marquée. En hiver, le rayonnement solaire est presque totalement absent et les nuages jouent donc un rôle prépondérant en tant qu'émetteur radiatif. En absence de nuages et de rayonnement solaire, la surface se refroidit fortement et une inversion de température peut s'installer sur plusieurs jours. Ci-dessous, les deux éléments clés de la couche limite arctique que sont les nuages et la stabilité seront détaillés.

Nuages bas Plusieurs méthodes permettant de détecter et mesurer les caractéristiques des nuages existent. Historiquement, l'observation humaine était utilisée pour établir des statistiques de fréquence nuageuse, mais cette méthode est peu précise en absence de luminosité extérieure [Hahn *et al.* 1995]. Les instruments de télédétection active au sol tels que les radars et les lidars sont plus précis, mais à cause de contraintes logistiques à très hautes latitudes, le réseau de tels instruments est peu dense. En particulier, les mesures au-dessus de la banquise ont uniquement lieu au cours de campagnes ponctuelles telles que SHEBA (Surface HEat Budget of the Arctic Ocean), en 1999–2000 ou N-ICE (Norwegian young sea ICE) en 2015, qui ont par nature une couverture spatiale et temporelle réduite. Les mesures satellites sont donc souvent utilisées pour établir des statistiques nuageuse en Arctique, à cause de leur large couverture spatiale et temporelle. Cependant, ces mesures spatiales peuvent fortement varier d'un instrument à une autre, et diffèrent également de mesures au sol [Chan & Comiso 2013, Blanchard *et al.* 2014, Zygmuntowska *et al.* 2012]. Les instruments de télédétection active à bord des satellites (par exemple, le lidar CALIOP à bord de CALIPSO ou le radar CPR à bord de CloudSat) ont également une "zone aveugle" au-delà de 82°N, ce qui limite leur utilité au-dessus de l'océan Arctique.

Quelque soit la technique de mesure employée cependant, trois caractéristiques générales de la couverture nuageuse en Arctique se dégagent des statistiques. Premièrement, les nuages sont très fréquents : environ 70 % en moyenne sur l'année. Deuxièmement, leur variabilité saisonnière est prononcée avec un maximum en été et en automne, et un minimum en hiver. Troisièmement, ils sont très bas, les nuages avec une base en dessous de 400 m étant particulièrement fréquents [Dong *et al.* 2010, Intrieri *et al.* 002b, Wang & Key 2004]. Une autre caractéristique importante des nuages est leur épaisseur optique, qui dépend principalement de leur phase : plus le nuage contient d'eau liquide, plus il absorbera de rayonnement. Les nuages arctiques sont principalement composés d'eau en été, de glace en hiver, et sont souvent de phase-mixte en automne [de Boer *et al.* 2009, Mioche *et al.* 2015]. Ils sont donc en moyenne plus épais optiquement en été qu'en hiver [Wang & Key 2004].

Stabilité et inversions de température Une inversion de température est définie comme une couche d'atmosphère où la température augmente au lieu de diminuer sur la verticale. Par la suite, on s'intéressera plus particulièrement aux inversions de températures au niveau de la surface, qui sont fréquentes en Arctique avec une variabilité saisonnière marquée. Différentes études, à partir de données de radiosondages, ont donné des fréquences d'occurrence de plus de 80% en hiver ; en été, cette valeur est beaucoup plus basse [Bradley *et al.* 1992, Serreze *et al.* 1992, Zhang *et al.* 2011]. En présence d'inversions de température à la surface, la couche limite est statiquement stable, c'est-à-dire que la flottabilité est négative. En revanche, le cisaillement de vent peut continuer à produire de la turbulence mécaniquement. Le niveau de turbulence mécanique est quantifié par des indicateurs de stabilité dynamique tels que le nombre de Richardson ou la longueur réduite d'Obukhov. En général, on différencie deux régimes de stabilité. Le premier, nommé régime de stabilité faible, est marqué par une turbulence continue et soutenue [Mahrt 1998] : la couche limite est bien décrite par la théorie de Monin–Obukhov [Grachev *et al.* 2005]. Le régime de stabilité fort, quant à lui, présente un très faible niveau de turbulence, qui peut être intermittente. Il se produit généralement dans des conditions de ciel clair et de nuit, lorsque le refroidissement radiatif de la surface est très fort. Ce régime est parfois aussi appelé régime "découplé", car l'absence de mélange vertical déconnecte la surface de l'atmosphère. La théorie de la similitude peut ne pas être applicable pour décrire la turbulence dans de telles conditions, et la théorie du profil log-linéaire du vent "s'effondre" [Malhi 1995, Mahrt 1998]. La limite entre ces deux régimes dépend des études. Par exemple, selon [Mahrt 1998], la couche limite est peu stable lorsque la longueur réduite d'Obukhov ζ est entre 0 et 0.06 et très stable lorsque ζ est supérieur à 1. D'autres études, telles que [Grachev *et al.* 2013], ont montré que le régime de stabilité forte était caractérisé par des valeurs du nombre de Richardson supérieures à 0,25.

1.3 Bilan d'énergie de surface

Le bilan d'énergie de surface correspond à la somme des flux de chaleur à l'interface sol–atmosphère (ou neige–atmosphère). Ce bilan d'énergie doit être égal à 0 : c'est la condition à la limite basse de l'atmosphère. Dans la suite, les trois flux de chaleurs qui seront étudié dans cette thèse sont présentés.

Flux radiatifs Dans l'atmosphère, les flux radiatifs se font principalement dans deux bandes de longueur d'onde. Entre 4 et 30 μm, on parle de flux infrarouge : la terre et l'atmosphère émettent dans cette bande. Entre 0.2 et 3 μm, en revanche, le soleil est le seul émetteur. Le rayonnement dans cette bande est alors qualifié de "solaire".

La principale source de variabilité du flux radiatif reçu en surface, mis à part le mouvement de la terre autour du soleil, sont les nuages. Ceux-ci ont un impact opposé sur le rayonnement solaire et infrarouge. D'une part, les nuages diffusent le rayonnement solaire et diminuent donc le flux radiatif solaire reçu en surface. C'est ce qu'on appelle "l'effet albédo des nuages". D'autre part, les nuages émettent comme des corps gris dans le spectre infrarouge et augmentent donc le flux infrarouge reçu par la surface. Au total, les nuages peuvent donc réchauffer ou refroidir la surface : leur effet dépend de l'angle zénithal, de l'albédo de surface, et des caractéristiques des nuages (principalement, de leur épaisseur optique).

Dans l'Océan Arctique, le forçage radiatif des nuages est en général positif (c'est-à-dire qu'ils réchauffent la surface) la majorité de l'année, sauf une courte période de fin juin à juillet, lorsque le rayonnement solaire est important et l'albédo de la surface est encore élevé [Intrieri *et al.* 002a]. En hiver, la distribution du flux infrarouge net reçu en surface est bimodale [Stramler *et al.* 2011, Graham *et al.* 2017]. Le premier mode, autour de -40 W m^{-2}, est associé à l'absence de nuage, ou à la présence de nuages de glace, fins et peu émetteurs. Le deuxième mode, autour de 0 W m^{-2}, est associé à la présence de nuages optiquement épais. Le forçage radiatif exercé par les nuages est donc d'environ 40 W m^{-2}. Le rayonnement solaire étant absent, ces deux modes du flux radiatif net définissent deux états distincts de la couche limite.

Flux turbulent de chaleur sensible Le flux turbulent de chaleur sensible est causé par le mélange turbulent de parcelles d'air de températures différentes. Par exemple, en présence d'une inversion de température, les mouvements turbulents feront descendre les parcelles d'air plus chaudes et remonter les parcelles d'air plus froides malgré la flottabilité. Le flux turbulent de chaleur sensible sera alors positif, ce qui correspond à un réchauffement à la surface. En revanche, le flux turbulent de chaleur sensible sera négatif en conditions instables.
Le flux turbulent de chaleur sensible (H) entre une altitude donnée et la surface est souvent calculé de la façon suivante :

$$H \propto C_h U \Delta T \tag{1}$$

avec U la vitesse du vent à l'altitude de calcul et ΔT la différence de température avec la surface. C_h est le coefficient d'échange turbulent. Dans des conditions stables, il est proportionnel à une fonction de stabilité qui dépend d'un paramètre de stabilité (longueur réduite d'Obukhov ou nombre de Richardson). Quand le paramètre de stabilité est grand, c'est-à-dire quand l'atmosphère est dynamiquement stable, les mouvements turbulents se développement plus difficilement. La fonction de stabilité et donc C_h tendent alors vers 0.

1.4 Objectifs et méthodologie de la thèse

L'objectif de cette thèse était d'améliorer notre compréhension de la couche limite arctique de l'Arctique et des différents processus qui l'affectent. Deux processus semblent être particulièrement importants. Premièrement, les nuages sont un facteur crucial de variabilité dans la couche limite de l'Arctique et ont un impact sur le bilan d'énergie de surface en exerçant un forçage radiatif. Deuxièmement, la vitesse du vent contrôle la turbulence ; dans des conditions de ciel clair, des vitesses de vent élevées peuvent maintenir un flux turbulent de chaleur sensible élevé, empêchant le développement d'inversions fortes. De plus, les mesures atmosphériques sont relativement rares à hautes latitudes à cause de contraintes logistiques. Cette thèse a donc mis l'accent sur les expériences de terrain et l'analyse des données issues de nouvelles campagnes. La compréhension de la relation entre les observations et la théorie est facilitée par la modélisation. Le modèle méso-échelle WRF ainsi que de petits modèles conceptuels ont été utilisés à cette fin.

2 Résultats

2.1 Variabilité saisonnière et impact radiatif des nuages au-dessus de la glace de mer

Plusieurs bouées instrumentées ont été déployées dans l'Océan Arctique dans le cadre de la campagne de mesure IAOOS (2014 - 2019). Prises dans la banquise, ces bouées ont ensuite dérivé pendant plusieurs mois. A l'issue de la campagne, les lidars installés sur les bouées IAOOS ont livré 1777 profils exploitables, majoritairement à des latitudes supérieures à 82°N, c'est-à-dire dans la zone aveugle des satellites polaires.

Lors de cette thèse, l'ensemble des données lidar IAOOS ont été traitées et analysées. Il a notamment fallu corriger l'atténuation causée par le gel qui s'accumulait sur la fenêtre du lidar, selon la procédure détaillée dans [Mariage 2015]. Le signal a également dû être déconvolué pour réduire les effets de la saturation du récepteur lorsque la luminosité était intense. Ensuite, un algorithme a été mis en œuvre pour détecter les couches de nuages et calculer leur épaisseur optique. Les mesures de flux radiatif en surface obtenues lors de la campagne N-ICE 2015, au cours de laquelle quatre bouées IAOOS ont été déployées ont également été exploitées. Les résultats majeurs découlant de cette analyse sont présentés ci-dessous.

Bien que le faible nombre de profils pour certains mois (notamment décembre et avril, lorsque les lidars étaient fréquement givrés) soit source d'incertitude, il y a des différences statistiquement significatives entre l'été d'une part, et les mois d'avril, novembre et décembre de l'autre, en ce qui concerne la couverture nuageuse et les propriétés optiques et géométriques des nuages. Tout d'abord, la fréquence mensuelle d'occurrence de nuages bas (c'est-à-dire, dont la base est inférieure à 2 km) est minimale en avril et en novembre/décembre et supérieure à 85% de mai à octobre, avec deux maxima en juin et octobre. La fréquence d'occurrence annuelle moyenne est autour de 76%. Ensuite, la couche de nuage la plus basses est géométriquement plus épaisse en octobre, et plus mince en été. Ceci est probablement lié aux intrusions d'humidité en provenance de l'Atlantique au début de l'automne. Enfin, on constate que les bases des nuages de première couche sont extrêmement basses en toutes saisons : moins de 120 m dans une grande majorité des cas.

Les lidars IAOOS détectent des couches nuageuses multiples à des taux beaucoup plus faibles que dans d'autres études, car la première couche nuageuse amortit généralement complètement le signal. Les épaisseurs optiques et géométriques totales des nuages provenant des campagnes précédentes et des données satellitaires sont beaucoup plus importantes que celles mesurées durant IAOOS, en particulier en été lorsque les nuages multicouches les plus fréquents. L'épaisseur optique des couches individuelles de nuages mesurée durant IAOOS est maximale en octobre.

L'impact sur la surface des nuages arctiques est également variable selon les saisons. En octobre et novembre, les nuages réchauffent la surface : les températures à 2 m associées aux profils sans nuage sont inférieures d'environ 8 K comparées à celles associées aux profils contenant au moins un nuage bas. En été par contre, il n'y a pas de différence statistiquement significative en ce qui concerne les températures de surface entre les profils sans nuages et les profils avec nuages.

Les données des lidars IAOOS déployés pendant la campagne N-ICE ont également permis d'identifier deux modes dans la distribution du flux infrarouge net mesuré pendant N-ICE en avril–juin. Le premier mode, centré autour de -72 W m^{-2}, est associé aux profils lidar IAOOS sans nuages, tandis que le deuxième est centré autour de -11 W m^{-2} et correspond aux profils lidar nuageux. Ces modes sont analogues aux modes radiatifs hivernaux bien connus, sauf que le mode "opaque" est beaucoup plus répandu (plus de 80 %) et que les deux modes sont espacés de 60

W m^{-2}, contre 40 W m^{-2} en hiver. Les nuages exercent donc un réchauffement infrarouge plus important en été qu'en hiver, ce qui est probablement lié à la plus grande proportion d'eau liquide dans les nuages en été. Au printemps et en été, les nuages ont également un effet de refroidissement solaire. Cet effet dépend non seulement de l'angle zénithal solaire et de l'albédo, mais aussi fortement de l'épaisseur optique des nuages.

Au total, pendant la période d'avril à juin de la campagne N-ICE2015, les nuages ont exercé un forçage radiatif positif sur la surface. En effet, l'effet albédo des nuages compense leur effet de réchauffement infrarouge uniquement pour de très grandes épaisseurs optiques et pour des angles zénithaux supérieurs à 60°. Sur l'ensemble des mois d'été au centre de l'océan Arctique, les nuages optiquement épais provoquent un forçage radiatif négatif de 80 W m^{-2} alors que les nuages optiquement minces continuent à réchauffer la surface. Il est donc important d'avoir une bonne estimation de l'épaisseur optique de la colonne entière d'atmosphère pour pouvoir calculer l'effet radiatif des nuages sur la surface. La compensation de l'effet de réchauffement infrarouge des nuages par leur effet d'albédo explique qu'il n'y ait pas de différence nette de température près de la surface entre les profils IAOOS avec et sans nuages pendant les mois d'été.

Les résultats exposés ci-dessus ont fait l'objet d'un article publié dans le journal Atmospheric Chemistry and Physics [Maillard *et al.* 2021].

2.2 Impact d'un flux local sur les inversions de température en Alaska

La campagne hivernale pré-ALPACA 2019 s'est déroulée du 23 novembre au 12 décembre 2019 à Fairbanks, en Alaska. Menée par des chercheurs de six laboratoires français et de l'Université d'Alaska Fairbanks (UAF), elle a servi de campagne préliminaire à la campagne principale ALPACA, prévue pour janvier-février 2022 dans le cadre de l'initiative PACES (Pollution atmosphérique en Arctique : climat, environnement et sociétés) de l'International Global Atmospheric Chemistry (IGAC) et de l'International Arctic Science Committee (IASC). Dans ce cadre, un anémomètre sonique, un radiomètre et un thermomètre ont été installés dans un champs enneigé appartenant à l'UAF. Un lidar a également été installé dans le centre de Fairbanks, permettant d'analyser les mesures de flux en regard de la couverture nuageuse. Ces mesures ont pu être exploitées pour investiguer l'impact d'une circulation locale sur le bilan d'énergie de surface et le développement d'une inversion de température en surface.

Tout d'abord, une étude de cas mettant en évidence le phénomène étudié est présentée. Dans les jours précédant le 5 décembre 2019, des conditions synoptiques anti-cycloniques ont provoqué un mouvement subsident au-dessus de Fairbanks, entraînant la disparition des nuages par compression adiabatique et des flux radiatifs nets largement négatifs (moins de -50 W m^{-2}). Une forte inversion de température en surface s'est alors développée au niveau de l'aéroport de Fairbanks, tandis que les vitesses du vent proche de la surface restaient faibles (moins de 2 m s^{-1}). Au site de mesure du champs, en revanche, la vitesse du vent a augmenté le 5 décembre pour atteindre des valeurs supérieures à 5 m s^{-1}. Le flux de chaleur sensible turbulent a augmenté en parallèle, tandis que le gradient de température proche de la surface ($\Delta T = T_{2m} - T_S$) diminuait. Le 6 décembre, le gradient de température a atteint son maximum à l'aéroport et son minimum au champs, ce qui suggère que des processus différents étaient à l'oeuvre aux deux sites de mesure.

L'ensemble des données de la campagne a ensuite été analysé. Il a été démontré qu'un régime de vent particulier, appelé circulation locale ('Local Flow', LF), avait cours au champs. Le LF était caractérisé par une direction constante du vent (nord-ouest), correspondant à la sortie de la vallée de Goldstream. Il était fortement accentué dans des conditions de ciel clair : les vitesses du vent au site du champs étaient significativement plus élevées en l'absence de nuages qu'en leur présence.

L'association de la présence de ciel clair et d'une vitesse de vent accrue lors de la campagne pré-ALPACA est intéressante car la vitesse du vent est un facteur important pour déterminer le régime de stabilité. En effet, lorsque la vitesse du vent est inférieure à 2 m s^{-1}, une diminution du flux radiatif net est associée à une augmentation forte du ΔT de surface. Cela correspond à un régime très stable stable et contrôlé radiativement. En revanche, lorsque la vitesse du vent est supérieure à 3 m s^{-1}, la turbulence est maintenue même pour des flux radiatifs nets très fortement négatifs (régime faiblement stable). Le mélange mécanique qui en résulte fait que le gradient de température à proximité de la surface reste proche de zéro. En raison du LF, c'est le scénario le plus fréquent par temps clair au site du champs.

Le bilan énergétique de surface sur le site du champs présente deux modes préférentiels. Le premier mode est associé à des vents faibles et à la présence de nuages. Le flux radiatif net est d'environ -5 W m^{-2} tandis que le flux de chaleur sensible turbulent est d'environ 0 W m^{-2}, et le résidu du SEB est faible. Le second mode est caractérisé par des vitesses de vent élevées et un ciel clair. Le flux radiatif net est d'environ -45 W m^{-2} et le flux de chaleur sensible turbulent d'environ 13 W m^{-2}. Dans ce deuxième mode, le résidu du SEB est positif au-delà des erreurs de mesure aléatoires, ce qui indique un flux de chaleur positif manquant à la surface. Pour l'épisode du 5 au 7 décembre, nous estimons qu'un gradient horizontal de température de 1,5 à 3 K km^{-1}, menant à une advection horizontale de chaleur par le LF, expliquerait ce résidu.

En résumé, l'analyse de la campagne pré-ALPACA a montré que des écoulements à petite échelle peuvent pénétrer dans des bassins d'air froid et stable en Arctique, comme la vallée de la Tanana, et causer une modification locale du bilan d'énergie et du régime de stabilité. Ceci est potentiellement important pour les études de la pollution atmosphérique locale aux hautes latitudes puisque les épisodes de pollution se produisent pendant les conditions froides et stables. Ces résultats ont fait l'objet d'un article qui est accepté dans le journal Boundary-Layer Meteorology.

2.3 Modélisation des inversions de température au-dessus des forêts

L'analyse des mesures pré-ALPACA a montré que des écoulements locaux peuvent générer des niveaux de turbulence suffisants pour empêcher le développement de conditions fortement stables, même en cas de fort refroidissement radiatif. Les résultats semblaient conformes aux prédictions du minimum wind speed for sustainable turbulence (MWST). Nos premières tentatives de modélisation de l'épisode du 4 au 8 décembre 2019 avec WRF ont montré que le modèle ne capturait pas l'écoulement local spécifique qui avait été observé. En revanche, il reproduisait bien une certaine variabilité de la vitesse du vent liée à la topographie. Cela a alors soulevé la question de l'impact que cette variabilité aurait sur l'inversion de température de la couche de surface.

Comme le centre de l'Alaska est majoritairement couvert de forêts, il a été nécessaire de prendre en compte les effets du couvert végétal sur le bilan d'énergie de surface. Un modèle analytique simple comprenant une couche sous la canopée, et une au-dessus, a donc été développé et comparé au modèle à une couche de [van de Wiel *et al.* 2017]. Ce modèle à deux couches prédit une diminution plus graduelle du gradient de température en fonction de la vitesse du vent que le modèle à une couche. De plus, la courbe du gradient de température de la couche supérieure en fonction de la vitesse du vent a une forme de 'S', c'est-à-dire qu'elle exhibe une transition abrupte d'une valeur élevée à une valeur plus basse entre 3 et 4 m s^{-1}. Cette forme est caractéristique des modèles à une couche. La couche inférieure, en revanche, présente un gradient de température maximal entre 3 et 4 m s^{-1}. Cependant, les résultats dépendent fortement de la valeur choisie pour l'émissivité de la canopée. En comparaison de ces modèles analytiques à une et deux couches, deux modules de couche de surface du modèle méso-échelle WRF ont ensuite été étudiés : Noah-MP (2 couches) et Noah-LSM–MYJ (1 couche). Il est apparu que ces modèles ont tendance à fixer des limites très restrictives sur les coefficients de diffusion turbulente et les paramètres de stabilité, de sorte qu'un niveau excessif de turbulence est maintenu et qu'ils peinent à reproduire de très fort gradients de température.

Une approche combinée a ensuite été utilisée pour étudier plus en détail les performances des différents modèles de couche de surface.

Tout d'abord, un vaste ensemble de mesures effectuées au 'Poker Flats Research Range' (PRR), site appartenant au réseau Ameriflux et situé au nord de Fairbanks, a été analysé. Le site PRR est situé dans une zone de forêt basse, la hauteur moyenne des arbres étant d'environ 2,5 m. En conditions nocturnes et en absence de nuages, le gradient de température dépend fortement du flux infrarouge descendant et de la vitesse du vent. Lorsque la vitesse du vent à 16 m était inférieure à 2 m s^{-1}, le profil de température est inversé jusqu'à la surface et le nombre de Richardson est supérieur à 0,25. Néanmoins, le flux de chaleur sensible turbulent n'est pas nul. D'autre part, lorsque la vitesse du vent est supérieure à 4 m s^{-1}, le profil de température est à peu près constant jusqu'à 1,5 m (donc, dans la canopée). En-dessous, en revanche, un fort gradient de température subsiste. Le nombre de

Richardson est alors inférieur à 0,25, ce qui correspond traditionnellement à un régime "faiblement stable". En outre, la relation entre l'inversion de température de chaque couche et la vitesse du vent est qualitativement similaire au modèle théorique à deux couches.

Ensuite, quatre modèles de couche de surface ont été implémentés en Python : Noah-LSM–MYJ, Noah-MP, et des versions modifiées de chaque. Les modèles codés en Python prennent comme variable d'entrée la vitesse du vent, le flux infrarouge descendant, et la température du sol ainsi que plusieurs paramètres et calculent la température de surface. La capacité de ces modèles à reproduire les observations du site PRR a donc pu être évaluée. Les modèles à deux couches donnent tous deux de meilleurs résultats que les modèles à une couche, qui ont tendance à produire des gradients de température trop faibles lorsque la vitesse du vent en entrée est élevée. D'autre part, le modèle Noah-MP original prédit des gradients de température trop faibles lorsque la vitesse du vent est faible. Dans l'ensemble, le modèle Noah-MP modifié a livré les meilleurs résultats.

Trois de ces quatre modèles différents (Noah-LSM–MYJ original et modifié, et Noah-MP) ont ensuite été implémentés dans le code source de WRF et leur impact a pu être évalué sur une étude de cas. Les modèles Noah-LSM ont tendance à prévoir une très grande variabilité spatiale du gradient de température découlant de la variabilité spatiale de la vitesse du vent. Le modèle Noah-MP produit des inversions de température plus faibles, mais plus étalées dans l'espace.

3 Perspectives

L'impact des nuages et des circulations locales sur le bilan d'énergie de surface de surface a été mis en évidence dans cette thèse. Les caractéristiques de la surface, telles que la présence d'une canopée forestière et la couverture neigeuse, influencent également le bilan d'énergie de surface et les inversions de température. Ceci pose plusieurs questions et ouvre des perspectives pour des travaux futurs.

D'une part, le jeu de données lidar obtenu lors de la campagne IAOOS a été exploité pour mieux comprendre les caractéristiques macro-physiques des nuages arctiques. En parallèle, des travaux ont été menés pour obtenir les flux radiatifs descendants à partir du rayonnement de fond de ciel mesuré par le lidar. Jusqu'ici, cette méthode a été validée en utilisant les données lidar des bouées IAOOS qui ont dérivé a proximité du camps de base N-ICE 2015. L'application de cette méthode au reste de la base de données IAOOS résultera en un large jeu de données sur les flux radiatifs à très hautes latitudes et ouvrira des perspectives pour étendre l'analyse de la section 2.1.

D'autre part, cette thèse a soulevé des questions concernant les écoulements locaux, et en particulier celui observé au site du champslors de la campagne pré-ALPACA. Les seules données disponibles pour décrire cet écoulement pendant la campagne pré-ALPACA provenaient d'un anémomètre sonique. Cela signifie que l'étendue spatiale de ce flux reste incertaine. Son étendue verticale, sa structure turbulente et son interaction avec le profil de température sont inconnues : les données de profileurs de température et lidars vent, déployés pendant la campagne ALPACA de 2022, devraient apporter un éclairage sur cette question. De plus, l'origine du flux et ses dimensions horizontales une fois qu'il entre dans la vallée de Tanana ne sont pas non plus connues. Des mesures en amont sont nécessaires pour vérifier qu'il prend bien sa source dans la Goldstream Valley. Celles-ci étaient disponibles lors de la campagne ALPACA 2022 et leur analyse pourrait constituer une étude complémentaire.

D'autres perspectives découlent de la modélisation des inversions de température et de la turbulence en présence d'un couvert forestier. Le modèle analytique à deux couches qui a été développé indique un fort impact de l'émissivité de la canopée sur le gradient de température sous la canopée. Pour des canopées très émissives, on prévoit que la couche située sous la canopée reste instable même si la couche d'air au-dessus est très stable. Le site PRR d'Ameriflux était caractérisé par une faible émissivité de la canopée : il serait donc intéressant de comparer le comportement du modèle à des mesures effectuées dans une forêt dense avec des arbres plus hauts.

L'impact des nuages, du vent et de la canopée sur le bilan énergétique de surface dans l'Arctique sera étudié plus en détail par le projet IMPECCABLE (IMPact on the Energy budget of mixed-phase Clouds and Canopy in the Arctic Boundary-LayEr), financé par Sorbonne Université - Émergence. Dans le cadre de ce projet, une campagne de mesures aura lieu dans une zone de forêt à Sodankylä, en Finlande, d'octobre 2022 à mai 2023. Les caractéristiques macro et microphysiques des nuages seront déterminées à l'aide d'une synergie radar-lidar, et seront comparées aux mesures radiométriques des flux radiatifs afin de déterminer des paramétrisations plus précises de ces flux pour les modèles à méso-échelle. Un mât de mesure équipé de radiomètres et d'anémomètres soniques permettra d'étudier le bilan énergétique de la canopée. Ceci fournira un jeu de données très complet caractérisant le bilan énergétique de la couche limite et de la surface en hiver, et constituera une extension importante du travail commencé dans cette thèse.

CHAPTER 1

Introduction

Contents

1.1 The Arctic Region: presentation and climate

The Arctic is the region of the Earth which is situated at its extreme northerly latitudes. It can be defined in several ways. In a narrow sense, it is as the area north of the Arctic Circle (approximately 66.5 °N): beyond this line, the sun does not rise above the horizon on the winter solstice and does not set on the summer solstice. More widely, it is sometimes defined as the zone of the northern hemisphere where the average July 2 m temperature does not exceed 10°C. The area to the immediate south of the Arctic is known as the sub-Arctic and shares many similarities with it. Characteristics of the Arctic and sub-arctic, for example, include wide variations in daytime duration between summer and winter and very cold temperatures. In the central part of the Arctic lies an ocean, part of which melts and re-freezes during the year cycle while the rest is permanent (or multiyear) sea-ice. The sea-ice extent is maximum in March at around 15 million km^2 (1981-2010 climatology). In this month, the sea-ice stretches from the northern coast of North America to the northern coast of Eurasia (Fig. 1.1). It then melts during spring and summer, reaching its minimum extent in September at around 6 million km^2. The continental part of the Arctic is marked by the presence of permafrost; the ground cover is tundra at high latitudes and boreal forest (or taiga) in the subarctic zone. Because of the harsh conditions, the difficulty in building infrastructure, and the scarcity of food, the Arctic is very sparsely populated. The largest city is Murmansk, a port on the Barents Sea which had around 287 847 inhabitants in 2020.

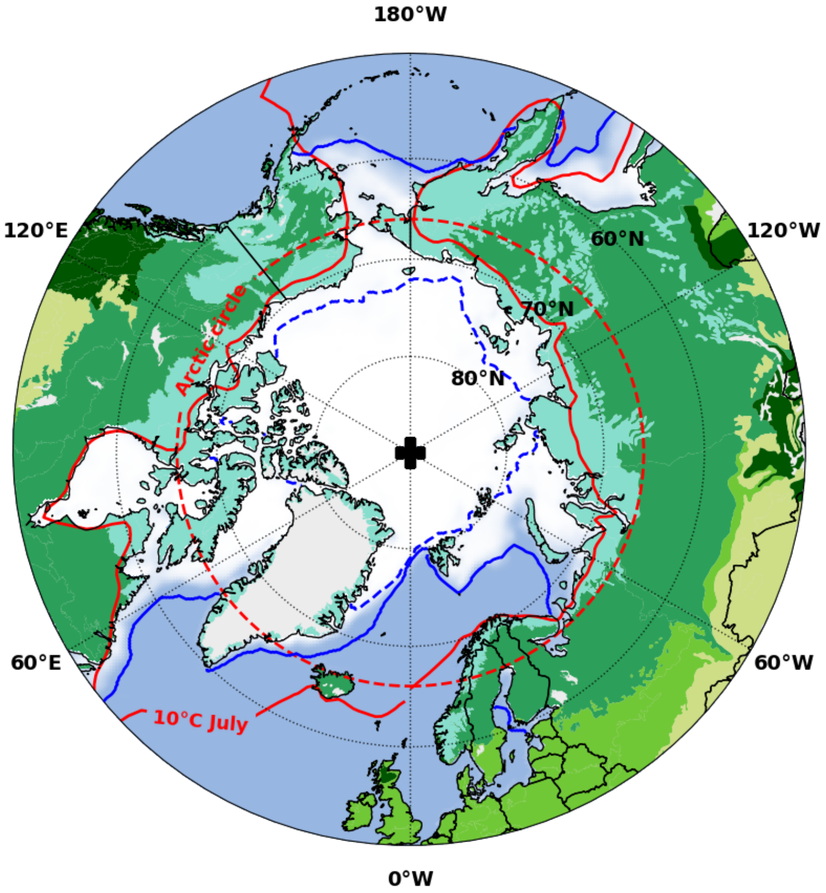

Figure 1.1: Map of the Arctic region. The dashed red line indicates the Arctic Circle, and the continuous red line corresponds to the (smoothed) 10°C July isotherm from the ERA5 1981–2010 2 m temperature climatology. The dashed and continuous blue line indicate the median sea-ice extent in September and March respectively (data taken from the National Snow and Ice Data Center, available online at `https://masie_web.apps.nsidc.org/pub/DATASETS/NOAA/G02135/`). The colour corresponds to the biome, taken from the World Wildlife Fund (`https://www.worldwildlife.org/publications/terrestrial-ecoregions-of-the-world`). Teal areas are tundra and medium green areas are taiga.

The evolution of the Arctic climate is currently marked by both interannual variability which follows favoured modes (so-called climate patterns) and a longer-term change caused by global warming.

Historically, two main climate patterns were known. The first is an extension of the Pacific North American (PNA) pattern [Overland & Wang 2005]. The other, the Arctic Oscillation (AO), is very correlated to the well-known North Atlantic Oscillation [Thompson & Wallace 1998]. These two patterns account for nearly half of the variance of the sea-level pressure (SLP) on timescales greater than 1 yr in the Arctic [Quadrelli & Wallace 2004]. The Arctic Oscillation pattern is perhaps the best known and is mostly dominant in the winter. A positive AO is defined by a circular pattern of negative SLP (cyclonic) anomalies centred around the North Pole. In this configuration, the middle latitude jet stream is enhanced, keeping cold air locked in the Arctic. Furthermore, a positive winter AO index has been linked to pronounced sea-ice extent minima the following September, possibly by favouring export of sea-ice through the Fram Strait [Rigor *et al.* 2002, Kwok *et al.* 2013]. Meanwhile, a negative AO index is associated to higher pressures over the Arctic and a weakened, more meandering jet stream. This tends to bring cold Arctic air down to the midlatitudes. However, in recent years, a pattern has emerged which does not map onto either the PNA or AO patterns. Unlike the AO, its structure is dipolar, with high pressures over Siberia and low pressures over the Canadian Arctic [Overland & Wang 2005]. This structure tends to funnel warm air from the south into the Arctic along its isobars, favouring moisture intrusions into the Arctic [Woods *et al.* 2013]. Accordingly, it is also linked to higher surface air temperatures and cloud cover in the Arctic [Overland *et al.* 2012, Kay & Gettelman 2009] and has been shown to have greater influence on September sea-ice anomalies than the winter AO [Wu *et al.* 2006, Hegyi & Taylor 2017].

The Arctic is a crucial zone of study for the scientific community because it is a key region of global warming. Indeed, the Arctic is warming at approximately two to three times the rate of the rest of the globe [Serreze & Barry 2011], a phenomenon known as "Arctic Amplification". The sea-ice extent minimum (in September) is decreasing and thick, multiyear sea-ice is being replaced by year-growth sea-ice [Overland *et al.* 2018]. In the early 21st century, Arctic warming was interpreted as the consequence of strongly positive AO indexes in the 90s affecting the patterns of polewards transport into the Arctic [Moritz *et al.* 2002]. In this framework, Arctic warming was thought to be normal inter-decadal variability. However, it has continued and accelerated in recent years even though the AO index has been alternating between positive and negative values [Graversen *et al.* 2008]: other factors must therefore be at work.

A number of feedback mechanisms have been proposed to explain Arctic Amplification. The first of these is the ice-albedo feedback: as the sea-ice melts, the sea water beneath is exposed and the albedo of the Arctic Ocean decreases. This in turn favours more melting as more shortwave radiation is absorbed. First theorised at the end of the 19th century [Arrhenius 1896], this mechanism was more recently shown to be an important part of Arctic Amplification, but not the dominant factor [Winton 2006]. Comparing results between a model with locked albedo and one with variable albedo, [Graversen & Wang 2009] found that the sea-ice albedo feedback contributed $\approx 15\%$ to Arctic amplification. Nevertheless, it plays an overall large part in the Arctic surface warming: surface temperatures were around 33% higher in the model with variable albedo [Graversen & Wang 2009].

Secondly, stable atmospheric conditions with an inverted temperature profile are frequent in the Arctic (Sect. 1.2.2). This means that surface warming is confined

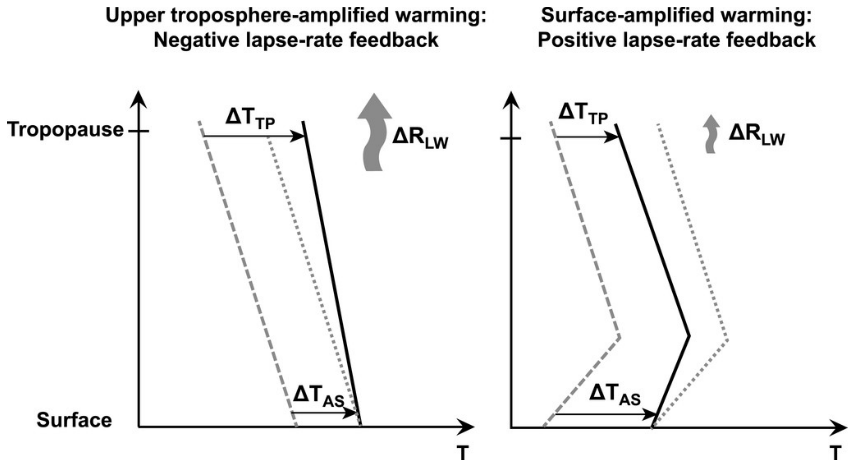

Figure 1.2: Conceptual illustration of the lapse-rate feedback in the Tropics (left) and the Arctic (right), taken from [Pithan & Mauritsen 2013]. The Arctic is characterised by inverted temperature profiles. Under these conditions, a surface temperature increase ΔT_{AS} is not efficiently transported upwards so that ΔT_{TP} (the top-of-troposphere warming) is small. The longwave radiation increases in response to the temperature increase. However, only a small part of this increased longwave goes out to space (ΔR_{LW}); instead, most of it is directed downwards, leading to further warming. This is known as a positive lapse-rate feedback. On the other hand, the tropics are characterised by strong vertical convection: surface warmings are rapidly propagated to the top of the troposphere, where they are efficiently radiated out to space and do not contribute to further warming the surface. This is a negative lapse-rate feedback.

there instead of being transported to higher altitudes by convection, as would be the case near the Equator. The additional longwave radiation generated by this near-surface temperature increase does not go out to space but is instead directed downwards, further increasing warming [Bintanja *et al.* 2011] (Fig. 1.2). This mechanism, termed "lapse-rate feedback", has been shown to be the main contributor to Arctic amplification [Pithan & Mauritsen 2014].
A cloud feedback on surface warming is also expected. [Vavrus 2004] showed that forcing a global climate model with increased CO2 led to higher vertically integrated cloud fraction in the Arctic compared to lower latitudes. However, the sign and magnitude of this feedback are unclear [Pithan & Mauritsen 2014]. Clouds may also interact with Arctic amplification in other ways, for example by responding to sea-ice loss. In the early autumn, cloud formation is increased over ice-free areas, which in turn increases the downwelling radiative flux and favours warming [Kay & Gettelman 2009]. On the other hand, clouds may regulate the sea-ice albedo feedback in the summer by absorbing downwelling shortwave radiation [Choi *et al.* 2020].

The mechanisms outlined above all concern the lowest part of the atmosphere,

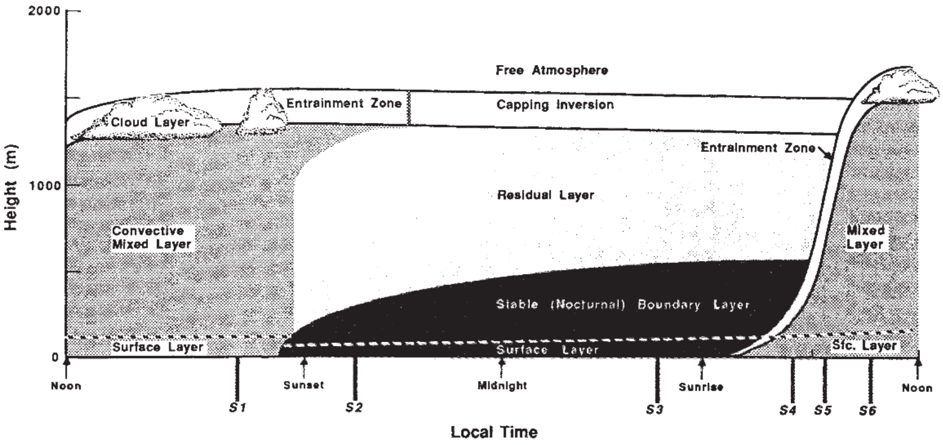

Figure 1.3: Schematic evolution of the boundary-layer over a diurnal cycle in the midlatitudes. Taken from [Stull 1988].

known as the boundary-layer, which is also where the warming in the Arctic is confined. This highlights the importance of the Arctic boundary–layer from a climate perspective.

1.2 The Arctic Atmospheric boundary-layer

The atmospheric boundary layer (BL) is "the part of the troposphere that is directly influenced by the presence of the Earth's surface, and responds to surface forcings with a timescale of about an hour or less" [Stull 1988]. It is characterised by the presence of turbulence, which can either be generated by buoyancy or mechanically, i.e. through wind shear due to the presence of the ground. The limit between boundary-layer and the overlying free atmosphere can be defined as the altitude where there is a sharp decrease of turbulence. Unstable boundary layers are marked by decreasing potential temperature profiles, leading to convection: buoyancy is the main generator of turbulence. Stable boundary layers, on the other hand, have negative buoyancy, meaning that the potential temperature profile increases near the surface; in that environment a displaced mass of air tends to return to its position. Turbulence is mechanically driven, and is often strongly dampened by the negative buoyancy.

In the midlatitudes, the BL exhibits a marked diurnal cycle because the surface responds to changes in shortwave radiation. Daytime is marked by large amounts of incoming shortwave radiation which heats the ground, leading to a decreasing temperature profile and convective movement. This is known as a convective mixed layer, and it may be separated from the free atmosphere by clouds and a capping inversion. The top of the boundary layer reaches 1–2 km in the afternoon. Stable boundary layers occur predominantly during the nighttime when the surface is

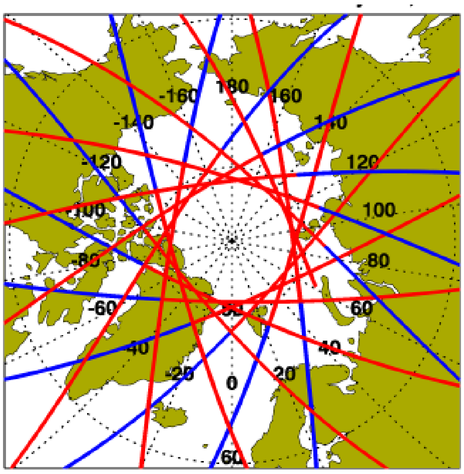

Figure 1.4: Example of CALIPSO (Cloud-Aerosol Lidar and Infrared Pathfinder Satellite Observation) satellite tracks over the Arctic on 21 March 2019. The satellite blind zone corresponds to the circle at latitudes $> 82°$N in which no tracks are present. Red tracks occurred during the daytime, and blue tracks during the nighttime. Image taken from `https://www-calipso.larc.nasa.gov/products/lidar/browse_images/std_v4_showdate.php?browse_date=2019-03-21`

at a radiative deficit and are therefore often termed "nocturnal boundary layers". A temperature inversion typically develops near the ground after sunset while a residual neutral layer often remains aloft (Fig. 1.3).

The Arctic BL operates quite differently. Shortwave radiation varies mainly on a seasonal, not daily, timescale, so that the daytime/nighttime dichotomy of the midlatitudes is less marked. In the summer, the boundary-layer may be well mixed but it remains relatively shallow compared to the midlatitudes. [Tjernström 2005], for example, observed that the BL was around 100 m high and topped by clouds and [Cheng-Ying *et al.* 2011] measured BL heights 240–430 m for April–June. During the winter longwave radiation becomes dominant, and clouds, as a longwave emitter, become particularly important. If conditions remain anticyclonic for several days, long-lasting stable stratification may develop. In this case, the residual layer may be completely eroded, leaving the stable layer in direct contact with the free atmosphere. The BL height is difficult to measure in these circumstances, but has been estimated at 10–150 m in Antarctica by [Pietroni *et al.* 2011].

Some main characteristics of the Arctic boundary-layer are detailed below.

1.2.1 Arctic low clouds

Data on clouds in the Arctic was historically sourced from weather reports (i.e. visual observation), either in weather stations or from ships. This method has several limitations. Firstly, the lack of light during the winter months is a source of bias, so that it has been suggested that only moonlit observations should be kept

[Hahn *et al.* 1995]. Secondly, low-level ice crystal clouds are often misreported due to ambiguous classification in the weather code [Curry *et al.* 1996]. Lastly, cloud altitude and other characteristics cannot be determined from eye observation alone. Nevertheless, several early statistics of Arctic cloud frequencies were derived from weather reports and showed broad agreement, with consistent seasonal variability in cloud cover - i.e. a maximum in summer (often greater than 90 %) and a minimum in winter (40 - 68%) [Hahn *et al.* 1995, Curry *et al.* 1996].

More complete and reliable datasets can be obtained using ground-based instrument synergies. For example, ceilometers are often used to determine the cloud base while radars detect the cloud top and microwave radiometers serve to measure the liquid/ice water path. Such a dataset was obtained at the Utqiagvik ARM site on the North Slope of Alaska. Using 5 months of data (May–September 2000), [Dong & Mace 2003] determined a total cloud fraction of 0.87 with a maximum of 0.96 in September. More than half of this cloud fraction was from low-level clouds, i.e. with a top underneath 3 km altitude: indeed, the mean cloud base was about 0.4 km, corresponding roughly to the BL top in the Arctic. These results were then extended to form a 10-year (1998–2008) statistic of cloud fraction [Dong *et al.* 2010]: cloud fractions were shown to increase from March (0.57) to May (0.84), remain high from May through October (0.8–0.9), then decrease again from November to March. Such ground-based instrumental synergies are of course harder to implement over the sea-ice due to logistical constraints. Studies of clouds over the Arctic Ocean have mostly taken place during field campaigns, during which instruments are set up on ice-locked research vessels or ice floes in their close vicinity. One of the most extensive of these campaigns was SHEBA (Surface Heat Budget of the Arctic Ocean), which took place from October 1997 – October 1998 in the Beaufort Sea. [Intrieri *et al.* 002b] reported monthly average cloud fractions greater than 60 % during SHEBA. Cloud fraction was highest (more than 80 %) and relatively constant from March to September, and lowest from October to February. Clouds were often multilayered, but distributions of lowest cloud base showed very defined peaks in the lowest kilometer in all months, confirming the importance of boundary-layer clouds. More recently, the Arctic Summer Cloud-Ocean Study (ASCOS) took place onboard the icebreaker Oden from 2 August – 9 September 2008 [Tjernström *et al.* 2012]. During this period, the average cloud fraction was 90% including 80% of boundary-layer clouds, although this proportion may be overestimated because of the exclusive use of a ceilometer, which has limited vertical range, for cloud detection. The MOSAiC (Multidisciplinary Drifting Observatory for the Study of Arctic Climate) expedition (September 2019 – September 2020), similar in scope to SHEBA but with a drift in the Atlantic sector of the Arctic, has yielded some first observations on the interactions of clouds and aerosols, with year-long statistics to follow [Engelmann *et al.* 2021].

In light of the temporal and spatial limitations of ground-based observations at very high latitudes and over the Arctic Ocean, satellite data is also used. Examples of satellite instruments often used to study clouds include MODIS (or Moderate Resolution Imaging Spectroradiometer) onboard Aqua and Terra and AVHRR (Advanced Very High Resolution Radiometer) onboard NOAA 19. These are passive remote sensors, which cannot obtain information on the vertical distribution of chemical species or clouds but have the advantage of observing large swathes of the Earth atmosphere around their track so that no blind zone remains. Active remote sensors such as the Cloud-Aerosol Lidar with Orthogonal Polarization (CALIOP), onboard CALIPSO, or the radar aboard CloudSat, yield much more detailed data on the vertical but have limited data in the polar orbit "blind zone". For satellites in the A-Train (like CALIPSO and CloudSat), this corresponds to latitudes above 82°N (Fig. 1.4). Some examples of cloud fraction climatologies obtained from satellite data are shown in Fig. 1.5. There is broad agreement, similarly to ground-based observations, of a maximum cloud fraction of more than 80 % in late summer, and a winter minimum, but timing and exact values differ. [Liu *et al.* 2012] also measured the prevalence of low-level clouds (defined in this article as those with a base under 2000 m) at 70% of all clouds in all months.

Several studies have pointed out that cloud satellite data may differ significantly both between instruments, and from ground-based measurements and reanalyses [Chan & Comiso 2013, Blanchard *et al.* 2014, Zygmuntowska *et al.* 2012]. In general, satellite-born passive instruments such as radiometers may have difficulty in distinguishing clouds from the bright sea-ice or snow below, especially in low-light winter conditions [Chan & Comiso 2013], while active instruments struggle to identify low-altitude clouds [Zygmuntowska *et al.* 2012]. Furthermore, spatial and time averaging differences between satellites and ground-based (or airborne) instruments make comparing the two complex [Mioche & Jourdan 2018]. Regardless of the dataset used, however, most studies of Arctic clouds point to 1) their prevalence ($\approx 70\%$ on average during the year); 2) pronounced seasonal variability with a maximum in summer and autumn, and a minimum in winter; and 3) their low base altitude, with boundary-layer clouds being especially frequent. The mechanisms behind the seasonal variation in cloud amount and characteristics are still an open question. One possible explanation is the influence of the sea-ice: because surface evaporation increases over open water compared to the ice, cloudiness and sea-ice amounts should follow the same annual cycle [Beesley & Moritz 1999]. However, clouds have been shown to respond to sea-ice loss in the autumn, but to be largely insensitive to it in the summer [Kay & Gettelman 2009, Morrison *et al.* 2018]. [Taylor *et al.* 2015] further showed that cloud properties were largely dependent on atmospheric stability, with stable conditions being associated to decreased cloud fraction and cloud water. Because stable conditions are more frequent in the winter (Sect. 1.2.2), this is coherent with the minimum cloud frequency being reached in this season. Lastly, synoptic conditions and long range transport may also play a role [Beesley & Moritz 1999]. For example, water-containing clouds in the Arctic winter are often associated to so-called moisture intrusions caused by cyclones originating in the lower latitudes [Woods *et al.* 2013].

Another important characteristic is that these low-level often contain at least some liquid water even at very low temperatures, making them mixed-phase. [Shupe *et al.* 2006], for example, found that during SHEBA clouds were mixed-

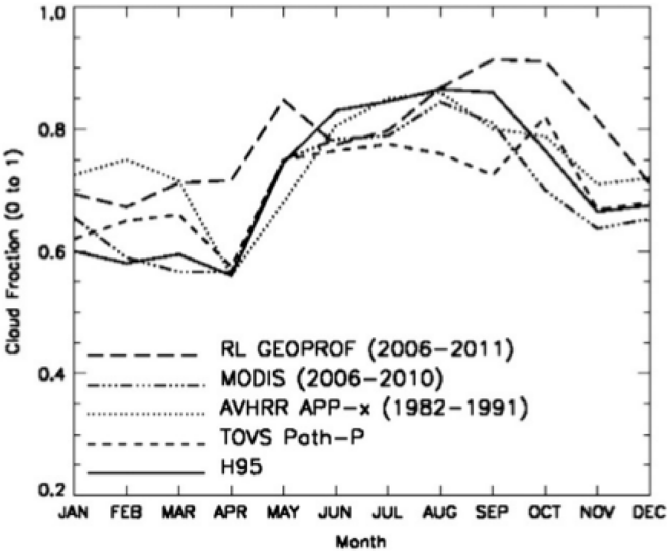

Figure 1.5: Figure from [Liu *et al.* 2012] comparing cloud fraction monthly climatologies over the entire Arctic from three different studies. The continuous line (labelled "H95") corresponds to results from [Hahn *et al.* 1995]. The thin dashed and fine dotted lines correspond to results from [Wang & Key 2004]. The Extended AVHRR APP (AVHRR APP-x, fine dots) and TIROS-N Operational Vertical Sounder Polar Pathfinder (TOVS Path-P, thin dashes) are datasets which are derived from the measurements taken by the AVHRR and TOVS instruments aboard the NOAA polar orbiting satellites respectively. Lastly, the thick dashed and dash-dotted lines correspond to results from [Liu *et al.* 2012]. The Radar–Lidar Geometrical Profile Product (RL-GEOPROF, thick dashes) is derived from measurements made by the CloudSat satellite, which is part of the A-Train. The MODIS (dash-dots) results are derived from measurements by the instruments of the same name aboard the Aqua and Terra satellites.

phase 59% of the time, corresponding to an overall frequency of 41 %. This frequency varied from 10% in December to 70% in September. Using data from the Mixed-Phase Arctic Cloud Experiment (MPACE) in Utqiagvik, Alaska and the Study of Environmental Arctic Change (SEARCH) in Eureka, Nunavut, Canada, [de Boer *et al.* 2009] similarly showed that mixed-phase clouds were especially prevalent in autumn, with summer clouds tending to be solely composed of liquid and winter clouds of ice. This has been confirmed by satellite studies over the whole Arctic region [Mioche *et al.* 2015]. The cloud phase is an important characteristic because it determines the cloud optical depth (COD), which in turn impacts its radiative forcing on the surface (Sect. 1.3.1). Indeed, the cloud optical depth is approximately proportional to the liquid water path (LWP) [Sengupta *et al.* 2003, Shupe & Intrieri 2003], with ice being a much smaller contributor due to the lower density of ice crystals. Because liquid water path is much easier to measure directly (for example with a microwave radiometer), COD is most often derived from it using an empirical formula and independent climatologies of COD in the Arctic are rare and patchy. [Curry *et al.* 1996] cited values of 2–24 for low-level cloud optical depth in the summer and 5.1–6.7 in the winter, both from direct ground-based measurements. From lidar measurements, [de Boer *et al.* 2009] obtained average values of 2–3 for the winter and > 3 in the summer for mixed–phase clouds while [Turner 2005] showed that 63 % of clouds were single–layer and had an optical depth < 6 during SHEBA. Of these single-layer clouds, nearly half were mixed-phase and ice-only clouds had very low optical depths. However, lidar measurements of COD tend to be biased low because the lidar signal is often attenuated before reaching the cloud top. [Wang & Key 2004] contained one of the most extensive climatologies of COD in the Arctic, based on satellite data. Monthly mean COD values in the Arctic were found to be between 4–6, with very slight maxima in February and October.

1.2.2 Boundary layer stability

Surface based temperature inversions (SBI), defined as temperature increasing with the vertical from the surface, are a characteristic feature of the Arctic atmosphere. Studies of temperature inversions most commonly make use of radiosonde data, from which statistics of inversion frequency, height (sometimes called depth or thickness, i.e. the difference between the inversion base and top altitudes) and strength (sometimes called intensity, the difference between base and top temperature) can then be derived. A drawback of this method is the relative rarity of radiosonde data over the sea-ice, which makes it difficult to precisely determine spatial variability of SBIs; however, unlike satellite data, radiosonde has a high vertical resolution even near the surface and the SBI layer can therefore be identified precisely.

Using radiosonde data, SBIs have been shown to exhibit consistent spatial and seasonal variability. From Soviet drifting and land station data in Eurasia, [Serreze *et al.* 1992] showed that low-level inversions of all types (either surface based or with a base beneath 700 mbar) occurred nearly 100 % of the time from autumn to spring, and 89% of the time in summer. The median inversion depth was maximum in winter at around 1200 m and minimum in summer, as was the median inversion strength. Inversion frequency, height and strength were all larger in East Siberia than in western Eurasia near the Norwegian Sea. [Bradley *et al.* 1992], looking at near-coastal station data from the North American Arctic, also found a marked seasonal cycle with SBI frequency of more than 80% in winter and less than 20% in the summer at Alert, Canada for example. The maximum monthly inversion height (400–850 m depending on the station) and strength (8–15 K) were also reached in winter. [Zhang *et al.* 2011] is a more recent study, based on radiosonde data from the 1990–2009 period. It confirmed that Arctic SBIs are "more frequent, deeper, and stronger in winter and, to a lesser extent, in autumn, than in spring and summer". Furthermore, it exhibited the same east–west gradient in inversion characteristics in Eurasia than [Serreze *et al.* 1992], making it clear that this is a robust feature of the spatial variability of temperature inversions. A possible explanation for this is the more maritime climate in western Eurasia [Zhang *et al.* 2011].

The presence of SBIs is often linked to negative net radiation at the surface [Bradley *et al.* 1992], which partly explains their greater frequency in winter and their observed link to clear-sky conditions [Kahl 1990]. Using high-resolution radiosonde data collected over several case studies in Fairbanks, Alaska, [Malingowski *et al.* 2014] showed that the formation of an SBI was triggered by strong cooling at the surface due to radiative imbalance which then propagated upwards. Often called "radiative inversions", SBIs caused by radiative imbalance during anticyclonic conditions have been found to occur in up to 85 % of soundings from January to April in the Arctic [Busch *et al.* 1982]. However, even in favourable anticyclonic conditions, the development of SBIs may be disrupted by local flows. It has been observed that by increasing turbulent mixing, the presence of drainage flows may interrupt the cooling cycle compared to stagnant “cold pool” conditions [Martínez *et al.* 2010]. Other measurements over the Arctic sea-ice showed that, in summer, SBIs are often caused by the advection of warm air aloft [Palo *et al.* 2017].

Temperature inversions are a significant feature of the Arctic boundary layer because they cause static stability, i.e. the buoyancy is negative and will tend to return displaced air masses to their initial position, inhibiting convection. However, even in the presence of static stability there may be dynamic instability, for example turbulence created due to the mechanical effects of wind shear. This can be quantified through the Richardson gradient (R_i) or bulk (R_b) numbers, or through the Monin-Obukhov length (L) for example. These are defined in the following way:

$$\begin{aligned} R_i &= \frac{g}{T}\frac{\partial \theta}{\partial z} / \left|\frac{\partial V}{\partial z}\right|^2 \\ R_b &= \frac{g \cdot z}{T_0}\frac{\theta(z) - \theta_s}{V(z)^2} \qquad (1.1) \\ L &= \frac{-u_*^3 T_0}{\kappa g \overline{w'\theta'_s}} \end{aligned}$$

with z the altitude, g the gravity constant, θ the potential temperature (and θ_s the surface potential temperature) and T_0 the ambient air temperature; V is the horizontal wind speed, w the vertical wind speed and u_* is the friction velocity. $< \cdot >'$ symbolises the deviation from the mean and $\overline{< \cdot >}$ the average. R_i and R_b are positive if the boundary layer is statically stable, and negative otherwise; large positive values of these numbers mathematically correspond to largely positive temperature gradient and weak shear, indicating a more dynamically stable boundary layer. The dimensionless Monin-Obukhov height (ζ) parameter, defined as z/L with z the measurement altitude, is similarly positive in statically stable conditions. Indeed, in a statically stable atmosphere, an upwards displacement of an air parcel ($w' > 0$) will be accompanied by a negative temperature fluctuation ($\theta' < 0$). Conversely, a downwards displacement of the same air parcel will be accompanied by a positive temperature fluctuation. Therefore, $\overline{w'\theta'}$ is negative and L is positive. Large values of ζ denote strong dynamic stability.

The turbulence in the (statically) stable boundary layer is often subdivided into two separate regimes, termed "weakly" or "strongly" stable, corresponding to different levels of dynamic stability. Sometimes a "transition" regime is also added [Mahrt 1998, Grachev *et al.* 2005]. The precise definition of these regimes varies between studies, but some often stated defining characteristics are as follows. The "weakly stable" regime is marked by continuous and sustained turbulence and corresponds to lower surface cooling and higher wind speeds [Mahrt 1998]. The boundary layer is well described by Monin–Obukhov theory [Grachev *et al.* 2005]. This regime corresponds to what is commonly termed "nocturnal boundary layer" in the mid-latitudes, topped by a residual layer and a capping inversion [Van Ulden & Wieringa 1996]. The very stable regime, on the other hand, has a very low level of turbulence that might manifest as bursts (hence this regime is sometimes called "intermittent turbulence"). It usually occurs in clear-sky, night-time conditions when radiative surface cooling is very strong. This is sometimes also called "decoupled" regime, as the lack of vertical mixing disconnects the surface from the atmosphere. Similarity theory may not be applicable to describe the turbulence in such conditions, and the log-linear wind profile theory "breaks down" [Malhi 1995, Mahrt 1998]. If this strongly stable regime sets in for a few days, as is frequent in the Arctic, there may be no residual layer left such that the boundary layer height is either very shallow or not well defined. On the other hand, non-turbulent motions such as gravity waves may become important [Grachev *et al.* 2005].

Several criteria have been introduced for separating the two regimes. [Mahrt 1998], based on measurements at 10 m altitude, found that the boundary layer is weakly stable for $0 < \zeta < 0.06$ and strongly stable for $\zeta \gg 1$. Often, some threshold on the Richardson number is used: a frequently given critical value of R_i beyond which turbulence is suppressed is 0.25. This is based on experimental and theoretical arguments. [Webb 1970] and [Businger *et al.* 1971] showed that when ζ, tends to infinity (corresponding to very strong dynamic stability), R_i will tend to a constant value of about 0.2 under standard Monin–Obukhov theory. [Rohr *et al.* 1988], meanwhile, showed experimentally that there was no growth of

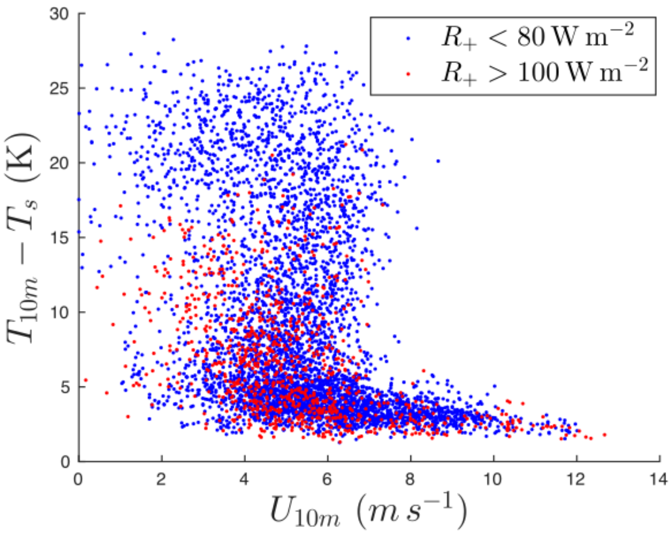

Figure 1.6: Measured surface temperature inversion $\Delta T = T_{10m} - T_s$ as a function of the wind speed at 10 m in Dome C, Antarctica. Data shown corresponds to stable conditions during the 2014/2015 period. Blue dots correspond to received radiation (defined as incoming longwave plus net shortwave) less than 80 W m^{-2}. Red dots correspond to incoming radiation more than 100 W m^{-2}. This figure is taken from [van de Wiel *et al.* 2017]

turbulence in a stably stratified shear flow for values of R_i greater than 0.25. In the Arctic context, [Grachev *et al.* 2013] found that the critical Richardson number was between 0.2 and 0.25 using data collected during the SHEBA experiment. It should be noted that it has repeatedly been shown that there is no value of the Richardson number beyond which the turbulence is entirely suppressed and the flow becomes laminar [Galperin *et al.* 2007]. Instead, some turbulence is always maintained but it becomes weak and intermittent.

One issue in using parameters such as R_i or ζ to qualify the state of the entire boundary layer is that they are inherently local parameters. For one value of L, ζ takes on very different values depending on the measurement altitude. Furthermore, they cannot be used to relate the stability of the boundary layer to external synoptic forcing such as the longwave radiative flux or the geostrophic wind speed, which would make it possible to predict whether a given period is likely to be weakly or very stable [van de Wiel *et al.* 2012]. Recently, several studies have developed the idea of MWST to overcome these difficulties. In this framework, a constant wind speed (U) is considered as an external forcing to the system (this wind speed can variably be the crossing point wind speed as in [van de Wiel *et al.* 2012], or the wind speed at the beginning of the night as in [van Hooijdonk *et al.* 2015]). Because the turbulent sensible heat flux (H) increases with wind shear, there exists a value of the wind shear (U_{min}) below which the H is unable to compensate the energy demand at the surface due to radiative cooling and ground conduction effects (Sect. 1.3). The surface is then at an energy deficit, and begins to cool. This increases the stability, which in turn suppresses the mixing and therefore the turbulent sensible heat flux: the BL transitions to a strongly stable regime. The shear capacity is defined as $SC = U/U_{min}$. This parameter has been shown to separate the two different regimes at all altitudes, so that one value of SC, instead of a range, can be used to differentiate the weakly from the strongly stable boundary layer [van Hooijdonk *et al.* 2015].

Dynamic stability regimes have been studied in both the polar regions. Using data from the SHEBA field experiment, [Grachev *et al.* 2005] determined four distinct stability regimes, with the first corresponding to the weakly stable regime and the last to the supercritical, very stable regime (the other two were transitional regimes). This very stable regime was marked by values of the Richardson flux and gradient numbers above 0.2 and vanishing heat fluxes. However, the collapse of turbulence (very stable regime) was defined for individual measurement altitudes, and therefore did not characterise the BL as a whole. More recently, [Vignon *et al.* 2017] analyzed measurements at Dome C, Antarctica and found two regimes (weakly and very stable) separated by a threshold wind speed which agreed with the predictions of the MWST theory. This characteristic resulting 'S' shape of $\Delta T = T_{10m} - T_s$ as a function of V is shown in Fig. 1.6: the very stable regime corresponds to the higher branch ($\Delta T > 20$ K) and the weakly stable regime corresponds to the lower branch ($\Delta T < 5$ K).

1.3 Surface energy balance

The surface energy balance (SEB) refers to the sum of the heat (energy) fluxes at the ground–atmosphere interface (otherwise known as the surface). This equilibrium is crucial because it is the boundary condition at the bottom of the BL - more precisely, it determines the surface temperature. Since the surface is theoretically an infinitely narrow layer, it has a heat capacity of zero and the surface energy balance equation can be written as:

$$0 = \mathrm{R_n}(z = 0) + \mathrm{G} + \mathrm{H}(z = 0) + \mathrm{L}(z = 0) \tag{1.2}$$

with $\mathrm{R_n}$ the net radiative flux, G the ground heat flux, H the turbulent sensible heat flux and L the turbulent latent heat flux. All fluxes in this equation (and in the rest of this thesis) are defined to be positive if they transfer heat to the surface, and negative otherwise. "$z = 0$" indicates that these are the fluxes at an altitude z of 0 m, i.e. at the surface. By definition, ground heat flux (G) is the conductive heat flux at the surface. In practice however, these fluxes are most often measured at some height h above the ground, as represented in Fig. 1.7 (most often, $h \approx 2$ m). The heat budget of the air layer of height h can be calculated by vertically integrating the equation for the conservation of heat (see for example [Stull 1988]). This yields:

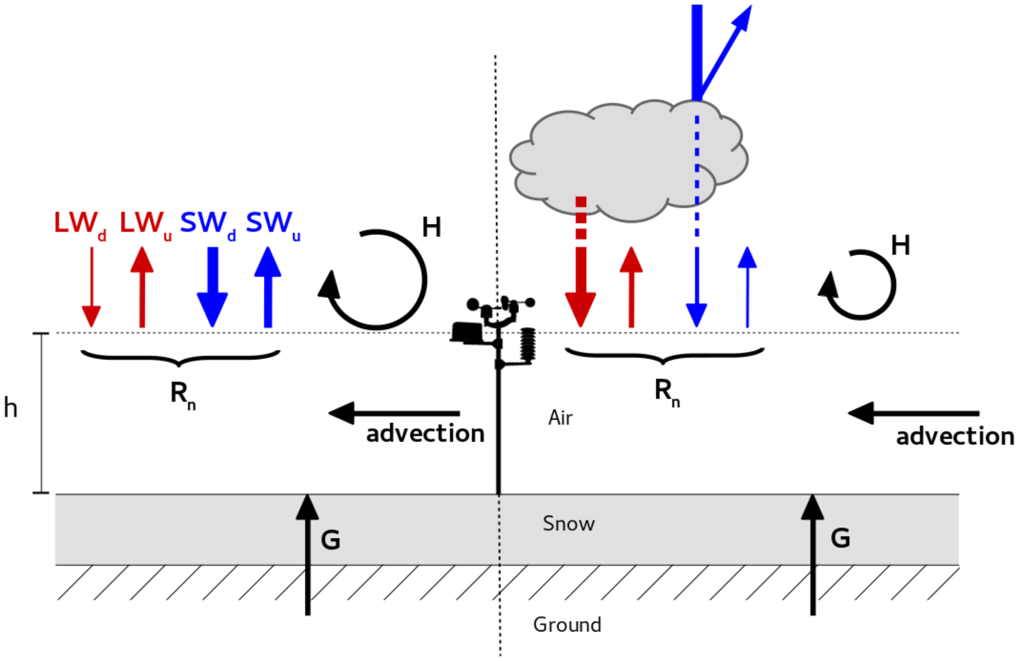

Figure 1.7: Schematic of the Arctic energy fluxes in clear (left) and cloudy (right) conditions, measure at a certain height h. The longwave fluxe are represented in red, and the shortwave fluxes in blue. A measurement mast is represented in the centre. The different arrow sizes represents, in a schematic manner, the varying magnitudes of the different fluxes: clouds increase the downward longwave flux but decrease the downward shortwave (Sect. 1.3.1). Note that in the winter, the shortwave fluxes are often negligible in both cases.

$$\begin{aligned}\overbrace{\rho C_p h \frac{\partial T}{\partial t}}^{\text{storage}} + \overbrace{\rho C_p h \left(u\frac{\partial T}{\partial x} + v\frac{\partial T}{\partial y}\right)}^{\text{advection}} &= \mathrm{R_n}(z=0) + \mathrm{H}(z=0) + \mathrm{L}(z=0) \\ &\quad - (\mathrm{R_n}(z=h) + \mathrm{H}(z=h) + \mathrm{L}(z=h))\end{aligned} \tag{1.3}$$

with C_p the air specific heat capacity, ρ the air density, u the x-component of the wind speed, v the y-component of the wind speed, and T the vertical average of the air temperature over the air layer. The heat storage term corresponds to the energy that is taken up by modifying the air temperature. The (horizontal) advection term corresponds to the transport of heat by the mean flow. Note that some third-order additional terms have been neglected here: for example, horizontal turbulent divergence or vertical heat advection. The measured heat energy budget can then be found by combining Eqs. 1.2 and 1.3.

$$\rho C_p h \frac{\partial T}{\partial t} + \rho C_p h \left(u\frac{\partial T}{\partial x} + v\frac{\partial T}{\partial y}\right) = \mathrm{R_n}(z=h) + \mathrm{G} + \mathrm{H}(z=h) + \mathrm{L}(z=h) \tag{1.4}$$

Because the heat capacity of air is very small, the heat storage and advection terms in this formulation of the SEB are often considered to be negligible. Nevertheless, measurements of the fluxes on the right hand side of Eq. 1.4 often do not end up balancing out to zero [Leuning *et al.* 2012, Mauder *et al.* 2020]. In the rest of this section, the main energy fluxes in the Arctic context are introduced in more detail.

1.3.1 Radiation and cloud forcing

Radiation in the Earth's atmosphere is often divided into two broad wavelength bands, termed longwave and shortwave. Longwave radiation covers wavelengths of 4–30 μm; typically, the major emitters in the longwave band are the Earth and its atmosphere. Shortwave radiation, on the other hand, covers wavelengths of 0.2–3 μm, which includes the visible spectrum (400–800 nm). The only body hot enough to emit at these wavelengths in the solar system is the Sun. Shortwave radiation is therefore sometimes also called "solar radiation". In the midlatitudes, shortwave radiation is the major contributor to the surface energy balance. It is absorbed by the ground during the day, heating it. This creates an unstable temperature profile with a warmer surface underlying a cooler atmosphere. In the polar regions however, solar radiation is absent during the winter and remains quite weak even in the summer due to the large solar zenith angle (SZ). Longwave radiation then becomes a crucial, and even dominant, process of the SEB.

The net radiation affecting the surface can therefore be decomposed into a net longwave flux ($\mathrm{LW_{net}}$) and net shortwave flux ($\mathrm{SW_{net}}$). Both of these are the difference between the upward (emitted or reflected by the surface) and downward radiation:

$$\begin{aligned} \mathrm{R_n} &= \mathrm{LW_{net}} + \mathrm{SW_{net}} \\ \mathrm{LW_{net}} &= \mathrm{LW_d} - \mathrm{LW_u} \\ \mathrm{SW_{net}} &= \mathrm{SW_d} - \mathrm{SW_u} \end{aligned} \tag{1.5}$$

The upward fluxes ($\mathrm{SW_u}$ and $\mathrm{LW_u}$) are relatively simple to calculate. First, the ratio of the downwards shortwave flux ($\mathrm{SW_d}$) to $\mathrm{SW_u}$ is a surface characteristic called the surface albedo (α). Snow and sea-ice both have very high α and therefore reflect a large part of the incoming shortwave radiation, while water and melted ice have lower albedo. During SHEBA, for example, the albedo was shown to range from 0.8–0.9 in April and to decrease steadily until it reached 0.4 in late July. This July value is an average: indeed as the snow melted, ponds formed with an albedo of 0.1 amidst zones of bare (non snow covered) ice with an albedo of 0.65 [Perovich 2002]. The N-ICE drift took place in a thinner ice zone compared to SHEBA but similar values were observed: 0.85 in the winter, decreasing to 0.72 by late June [Walden *et al.* 2017]. Second, the surface emits as a grey body in the longwave. The emissivity also depends on the nature of the surface: snow, for example, has a very high thermal emissivity of about 0.99 [Warren 1982], meaning it practically radiates as a blackbody.

The downward radiative fluxes are more complex to determine without a radiative transfer model. Indeed, they depend on the temperature profile, humidity

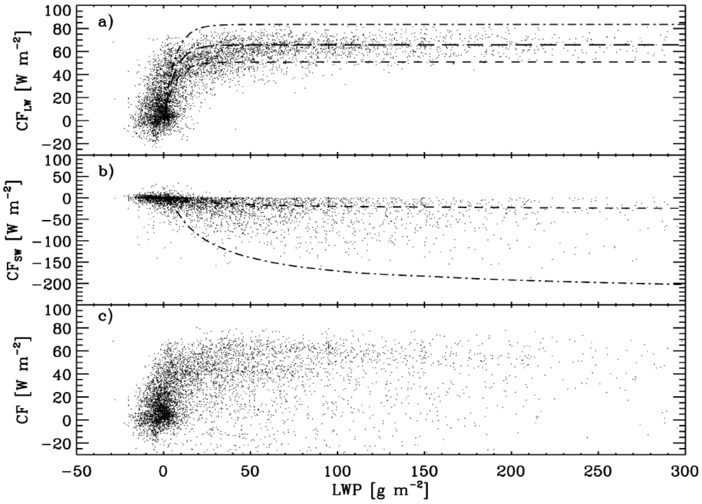

Figure 1.8: Plot of longwave (top), shortwave (middle) and total (bottom) cloud forcing as a function of LWP from SHEBA measurements. Dashed lines correspond in the top two plots to theoretical curves for different values of the optical depth. Figure taken from [Shupe & Intrieri 2003].

and the concentration of different gaseous species. $\mathrm{SW_d}$ additionally depends on the SZ. However, one of the main factors affecting the downward radiative fluxes are clouds. The effect of clouds on the radiative fluxes is called the cloud radiative forcing. The cloud longwave radiative forcing ($\mathrm{CF_{LW}}$) and cloud shortwave radiative forcing ($\mathrm{CF_{SW}}$) are defined as:

$$\begin{aligned} \mathrm{CF_{LW}} &= \mathrm{LW_{net,cloud}} - \mathrm{LW_{net,clear}} \\ \mathrm{CF_{SW}} &= \mathrm{SW_{net,cloud}} - \mathrm{SW_{net,clear}} \end{aligned} \tag{1.6}$$

where $\mathrm{LW_{net,cloud}}$ is the net longwave flux received at the surface in the presence of clouds, and $\mathrm{LW_{net,clear}}$ is the longwave flux received in the exact same atmospheric conditions, but without clouds (same for the shortwave). Negative values of the forcing therefore correspond to a cooling effect (i.e., less radiation received at the surface, which all else equal would lead to a decrease in surface temperature) and positive values to a warming effect. $\mathrm{CF_{SW}}$ is negative because clouds scatter shortwave radiation away from the surface. This is called the "cloud-albedo effect". On the other hand, $\mathrm{CF_{LW}}$ is positive because longwave clouds emit as grey bodies in the longwave spectrum (Fig. 1.7). These two phenomena therefore have a competing effect from a surface perspective. $\mathrm{CF_{LW}}$ and $\mathrm{CF_{SW}}$ must therefore be estimated in more detail to determine the sign of the total cloud radiative forcing.

Some theoretical aspects of cloud longwave radiative forcing are first introduced. Clouds emit as a grey body, following the formula:

$$F_c = \varepsilon_c \sigma T_c^4 \tag{1.7}$$

where σ is the Stefan-Boltzmann constant, T_c the cloud base temperature and ε_c the

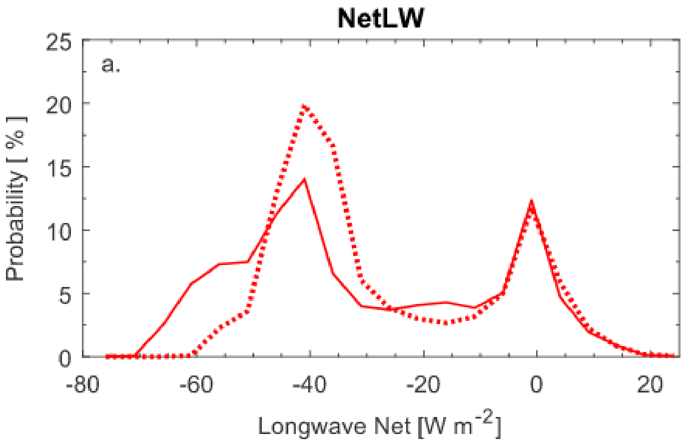

Figure 1.9: Comparison of the $\mathrm{LW_{net}}$ distributions observed during SHEBA (dashed line) and N-ICE (continuous line) during the winter. Figure taken from [Graham *et al.* 2017].

cloud emissivity, which is directly linked to the cloud optical depth τ: $\varepsilon_c = 1 - e^{-\tau}$ [Platt 1973]. Cloud longwave radiative forcing is directly related to F_c, and will therefore increase with cloud temperature (creating an indirect dependence on cloud altitude) and with cloud optical depth (and thus cloud microphysics as seen in Sect. 1.2.1). Measurements from the SHEBA campaign were found to be coherent with these relations [Shupe & Intrieri 2003]. $\mathrm{CF_{LW}}$ ranged from 0 to more than 60 W m^{-2}, with the lowest values corresponding to $T_c <$ -30 °C and the highest part of the range recorded for $T_c >$ -15 °C. Annual mean cloud longwave radiative forcing was 52 and 16 W m^{-2} for liquid-containing and ice-only clouds respectively. The dependence of $\mathrm{CF_{LW}}$ on LWP is visible in Fig. 1.8. In total, $\mathrm{CF_{LW}}$ tends to be larger in the summer when clouds are warmer and contain more liquid water [Dong *et al.* 2010, Wang & Key 2004].

The impact of clouds on the surface longwave radiation in the Arctic is such that the winter $\mathrm{LW_{net}}$ distribution is bimodal. The first mode, termed "radiatively clear" is usually around -40 W m^{-2} and corresponds to the absence of emissive, liquid-containing clouds (some clouds may be present but are at higher altitudes or ice-only). The other, called "opaquely cloudy", is centered around 0 W m^{-2} and corresponds to the presence of very emissive clouds. These modes were first defined during the SHEBA campaign [Stramler *et al.* 2011]. They were shown to correspond to two "states" of the BL: the average temperature profile for radiatively clear instants had low surface temperature and a strong SBI, while the average temperature profile for opaquely cloudy instants had markedly higher surface temperatures and decreased close to the ground [Stramler *et al.* 2011]. These two Arctic winter states were further observed during the N-ICE 2015 campaign [Graham *et al.* 2017] (Fig. 1.9) and in the Admundsen Gulf [Raddatz *et al.* 2015], so that they appear to be an Arctic wide characteristic.

$\mathrm{CF_{SW}}$ is more complex to establish because no simple formula exists linking the shortwave transmittance of clouds to their optical depth. This is because the effect of clouds on the diffuse part of the shortwave radiation is difficult to estimate: it can either be calculated using a radiative transfer model [Loyer *et al.* 2021], or be empirically parametrized, for example in [Fitzpatrick *et al.* 2003]. Furthermore, like $\mathrm{SW_{net}}$, $\mathrm{CF_{SW}}$ depends both on α and SZ. [Shupe & Intrieri 2003] showed that during SHEBA, $\mathrm{CF_{SW}}$ increased with LWP, but the increase was much more gradual than for $\mathrm{CF_{LW}}$ (Fig. 1.8). Furthermore, the strongest cooling for both ice-only and liquid-containing clouds were correlated with the lowest SZ values and ranged from -15 to -55 W $\mathrm{m^{-2}}$. Because the solar zenith angle is completely dependent on the date, time and latitude, this meant that this strongest cooling occurred in a limited time window in the summer. [Dong *et al.* 2010] also observed a maximum in $\mathrm{CF_{SW}}$ in the summer, linked not only to the SZ but also to the decreased albedo due to snowmelt.

Putting these elements together, it has been shown that the longwave warming effect is larger than the shortwave cooling effect (and therefore, clouds have a net warming effect on the surface) in all months except for a short window in late July, when the snow is melted and the solar zenith angle still small [Shupe & Intrieri 2003, Dong *et al.* 2010, Wang & Key 2004]. However, the exact dependence of the total cloud radiative forcing on cloud macrophysical characteristics such as optical depth or LWP remains unclear (Fig. 1.8).

1.3.2 Turbulent sensible heat flux

H corresponds to the heat flux caused by turbulent mixing of air parcels with different temperatures. For example, if the temperature profile increases with the vertical (as is the case during a SBI), turbulent mixing will bring warmer air parcels down and colder air parcel up in spite of buoyancy. This will lead to a surface warming: hence, H will be positive. On the other hand, H will be negative if the temperature profile decreases with the vertical, i.e. in unstable conditions. From a theoretical point of view:

$$H = -\rho C_p \overline{w'\theta'} \tag{1.8}$$

with ρ and C_p the density and specific heat capacity of air respectively, w the vertical wind speed and θ the potential temperature. $\overline{w'\theta'}$ cannot be directly derived from the Reynolds decomposition of the equations of motion for zero- or first degree closures and must be parametrised. In a bulk formulation, H at a certain level z typically depends both on U, the wind speed at that level, and ΔT, the temperature difference between z and the surface:

$$H = \rho C_p C_h U \Delta T \tag{1.9}$$

C_h is the turbulent exchange coefficient for heat and its exact formulation may vary between parametrisations. In stable conditions, it always includes a "stability function" which corrects H so that it does not continue growing linearly with ΔT.

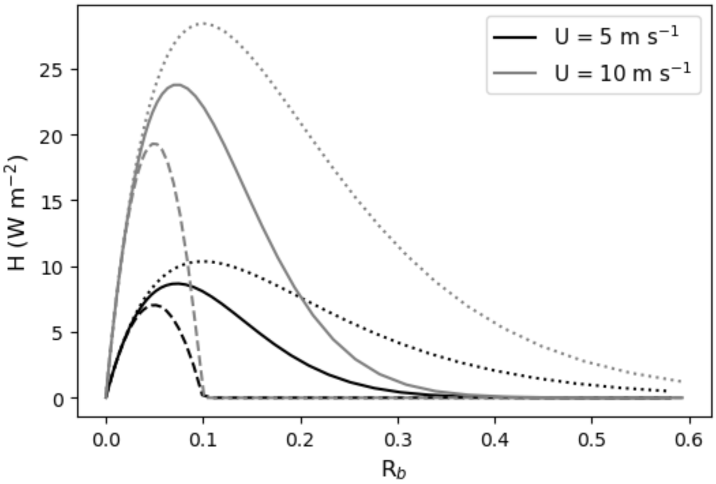

Figure 1.10: Example of the turbulent sensible heat flux as a function of stability (here, the Richardson number) for two different wind speeds (black: 5 m s^{-1} and grey: 10 m s^{-1}) according to Eq. 1.9. Line styles indicate the different stability functions, which are described in [van de Wiel *et al.* 2017]: cutoff (dashed), short-tail (continuous) and long-tail (dashed).

Indeed, this behaviour would be non-physical as it is known that in very stable conditions turbulence collapses and H tends to zero (Sect. 1.2.2).

Here an example is given of a bulk Richardson number (R_b) formulation for C_h. This was first introduced by [Louis 1979] as a bulk (vertically averaged) version of the classical Monin-Obukhov formulation, which uses ζ as a stability parameter instead. In recent years this formulation has often been used for its analytical simplicity [van de Wiel *et al.* 2012, van Hooijdonk *et al.* 2015, van de Wiel *et al.* 2017]. In this formulation:

$$C_h = \frac{\kappa^2}{\ln(z/z_0)^2} f(R_b) \tag{1.10}$$

with κ the van Kármán constant, z_0 the roughness length and f the stability function. The roughness length depends on the surface type: snow and ice have very low roughness lengths ranging from 0.7 mm to 1 cm, an order of magnitude lower than most snow-free vegetated surfaces [Pomeroy & Brun 2001]. The resulting values of H are shown in Fig. 1.10 for two values of U and three different stability functions. This simple representation shows the characteristic "bell-shape" of H, which first increases with R_b due to the linear dependence on ΔT and then decreases once the stability function becomes very small, corresponding to the collapse of turbulence under very stable conditions. This was for example observed during SHEBA: for values of $R_b > 0.2$, H tended to 0 [Grachev *et al.* 2005]. It also illustrates the dependence of H on the shear (wind speed) at all values of R_b. Note that the short-tailed stability function (continuous line) gives identical results to the usual Monin-Obukhov ζ formulation with the log-linear [Businger *et al.* 1971, Dyer 1974] similarity functions [England & McNider 1995].

The stability functions are derived empirically from field measurements of H, U and T; for example, the 1968 Kansas field experiment [Businger *et al.* 1971]. The turbulent sensible heat flux is most often measured using a sonic anemometer, which measures all three wind speed components as well as the temperature at high frequency (often, 10 or 20 Hz). $\overline{w'\theta'}$ can then be calculated as the covariance of w and θ over a given time window, often 10 or 30 minutes. This method is known as eddy covariance and its implementation can be tricky, with implications on the accuracy of measurements in complex terrains. Here it might be noted, for example, that the choice of the time window is an important parameter. The theoretical average and deviations to the average correspond to statistics over an ensemble of realisations at a given point and time. Since these ensemble of realisations cannot be observed in reality, time-statistics are used instead. However, using a too short time window may lead to lower frequency movements (large eddies) being cut out, even though they may contributed significantly to H [Malhi *et al.* 2005].

Measurements of H in the Arctic tend to exhibit seasonal variability with positive values in the winter (when SBIs are frequent) and negative values in the summer [Westermann *et al.* 2009, Walden *et al.* 2017]. The magnitude of the flux tends to be small compared R_n, and even sometimes compared to the ground heat flux (Sect. 1.3.3), especially in the winter. Comparing measurements from ASCOS, AOE-2001 and SHEBA, [Tjernström *et al.* 2012] found that values were in the [-15;15] W m^{-2} range with some skew towards negative values in late August. [Walden *et al.* 2017] found typical values of [20;30] W m^{-2} in the winter and [-20;0] W m^{-2} in the spring/summer during N-ICE. At a tundra site in Siberia, [Langer *et al.* 2011] measured slightly larger absolute average turbulent sensible heat flux of -22 W m^{-2} in the summer, but in the winter this values was 9 W m^{-2}, much smaller than the average ground heat flux. It is clear, however, that local variation in surface characteristics may have a large impact on H. [Batchvarova *et al.* 2001] showed, for example, that the estimated regional heat flux in Finish Lapland was only 30–50 % of the measured flux in a coniferous forest.

1.3.3 Ground heat flux

G is a conductive heat flux from the ground to the surface due to the temperature difference between the two. Sometimes, latent heat releases due to phase changes (permafrost thaw or refreeze) are included in the ground heat flux, but this will not be explored further in this thesis. When a snowpack is present, G is the conductive heat flux through the snow layer and can be simply estimated as:

$$G = -\frac{\lambda_s}{d_s}(T_S - T_g) \tag{1.11}$$

where λ_s and d_s are the snow conductivity and snow depth respectively, T_S is the snow surface temperature and T_g the temperature of the ground underneath. Snow thermal conductivity varies with density but is usually close to 0.2 W m^{-1} K^{-1}, which is 6 times less than soil [Pomeroy & Brun 2001]: the snow layer has an insulating effect. Because of this, the ground beneath the snowpack can therefore remain much warmer than the overlying atmosphere. [Helgason & Pomeroy 2012], for example, measured a difference of around 30 °C across a 42.5 cm layer of snow in the Canadian Arctic. G is therefore usually positive in the winter.

Experimental studies have shown the importance of G, which can represent up to 30 % of the net longwave in winter over the continent (around 17 W m^{-2}, twice the observed turbulent sensible heat flux) [Langer *et al.* 2011]. However, much lower values can also be found in the literature. On Svalbard, for example, the measured average winter G ranged from -3 to 6 W m^{-2} depending on the measurement method and period. This was around three times smaller than the turbulent sensible heat flux [Westermann *et al.* 2009]. The relative magnitude of H and G therefore seems to be variable: it might be that under strongly stable condition, H is collapsed and G becomes dominant because the surface is very cold, while in weakly stable conditions H remains important and G is smaller.

1.4 Thesis objectives & research methodology

The aim of this thesis is to improve our understanding of the Arctic SEB variability, and the different BL processes affecting it. This is a broad question, but from the bibliography outlined above two processes stand out, leading to the two main research questions which are outlined below. First, clouds are a major driver of variability in the Arctic boundary-layer and impact the surface energy balance by exerting radiative forcing. Second, wind speed controls the turbulence; under clear-sky conditions, elevated win speeds can maintain a high turbulent sensible heat flux which impacts the development of strong SBIs. Another key result from the bibliography was the relative dearth of surface-based measurements at high latitude. This thesis has therefore placed emphasis on field experiments and data analysis from novel campaigns. Understanding the relation between observations and theory is aided by modelling. The meso-scale model Weather Research and Forecasting (WRF) as well as small conceptual models were used for this purpose.

1. **How do the macrophysical properties of clouds vary on a seasonal basis and how does this impact the surface radiative fluxes at very high latitudes over the Arctic Ocean?**

Clouds are ubiquitous in the Arctic and have an important impact on the surface radiative fluxes, which are the dominant term in the Arctic SEB. Clouds emit longwave radiation and scatter shortwave radiation. In the winter, solar radiation is negligible; the presence and absence of low-level clouds therefore define two modes in the LW_{net} distribution, corresponding to two distinct states in the Arctic winter boundary layer. Their effect in the summer is more uncertain because of the competing impact on the shortwave radiative flux, which appears to be more gradually dependent on characteristics such as the cloud optical depth. The seasonal variation

Figure 1.11: Left: photo of a IAOOS buoy locked into the ice in the Arctic Ocean. The lidar is the white tube and temperature sensors are located on the mast. Photo taken by V. Mariage [Mariage 2015]. Right: photo of the measurement mast during the pre-ALPACA campaign in Fairbanks, Alaska. The CNR4 radiometer is visible; the sonic anemometer hadn't yet been installed. Photo taken by J. Maillard.

in cloud characteristics and radiative forcing is an important question, because it is expected to control the ice-melt [Kay & Gettelman 2009, Choi *et al.* 2020]. Despite wide acknowledgement of the importance of clouds in the Arctic atmosphere, however, there is a lack of long-term ground-based measurements due to logistical constraints, especially over the sea-ice, while satellite measurements have limited coverage at very high latitudes [Kay *et al.* 2016].

In order to answer question 1, novel data from the Ice, Atmosphere, Arctic Ocean Observing System (IAOOS) field campaign was therefore used. The IAOOS campaign was a multi-year experiment with lidar-equipped buoys which were locked into the sea-ice and drifted with it [Koenig *et al.* 2016]. Part of the resulting lidar dataset had already been exploited to study the vertical distribution of aerosols [Di Biagio *et al.* 2018] and to compare cloud statistics to reanalyses and satellite observations [Di Biagio *et al.* 2021]. However, a large majority of the available profiles remained to be analyzed. These profiles spanned several years and covered latitudes above 82 °N in the satellite blind zone. A IAOOS buoy had also drifted in the vicinity of the N-ICE 2015 [Walden *et al.* 2016] ice floes, creating opportunities for cross-comparison with radiometric data obtained during this campaign.

Chapter 2 describes the development of a three-season statistic of cloud cover and macrophysical characteristics from the lidar dataset. The importance of COD in determining the net cloud radiative forcing is evidenced and it is shown that cloud characteristics and impact on the surface are fundamentally different between summer and autumn.

2. **How do the SEB and stability regimes vary in the cloudless, continental BL? How is this variability represented in meso-scale models?**

Although clouds are one of the main drivers of variability in the BL, there is evidence that the cloudless Arctic BL also exhibits marked variability between a weakly stable and a strongly stable state, with the turbulent sensible heat flux collapsing to zero in the latter case. Recent theoretical advances such as MWST [van de Wiel *et al.* 2012, van Hooijdonk *et al.* 2015] and field measurements in the Antarctic show that wind speed controls the switch between the two regimes. It is also known that local factors such as local flows or terrain type impact the turbulence and therefore the turbulent sensible heat flux even under cloudless conditions, especially over the continent where there are greater topographic variations.

In order to prepare for a wider scale Alaskan Layered Pollution And Chemical Analysis (ALPACA) campaign initially set to take place in January 2021 (and later moved to January 2022 because of the COVID-19 pandemic), the pre-ALPACA campaign took place in Fairbanks, Alaska in November-December 2020. The main aim of this campaign was to form a better understanding of air pollution in the Arctic by looking at cold-condition and low-light aerosol chemistry. However, an additional goal was to study the formation of strongly stable surface conditions, as they impact the dispersion of surface emissions. This provided an opportunity to gather data on the SEB in continental, cloudless conditions and study the interplay between stability and the surface fluxes. Furthermore, previous studies had shown that Fairbanks experienced both very strong winter SBIs [Malingowski *et al.* 2014] as well as local flows affecting the BL stability in cloudless conditions [Fochesatto *et al.* 2013], making it an interesting location for the proposed question. I was able to participate in installing and monitoring the instruments over the course of this campaign.

Chapter 3 presents the pre-ALPACA results. In coherence with the information obtained during the first part of this thesis, clouds had a major impact on the SEB and defined two modes in the $\mathrm{LW_{net}}$. A local circulation was observed to develop preferentially in clear-sky conditions from a nearby valley system. This flow meant that even under clear-sky conditions with very strong radiative cooling at the surface, a significant turbulent sensible heat flux was maintained and the weakly stable regime persisted.

Analysing these results then raised the question of the representation of the impact of wind speed on the surface layer inversion in meso-scale models such as WRF. These models often have difficulty in reproducing observed state of the boundary-layer in low wind speed, stable cases [Tastula & Vihma 2011, Holtslag *et al.* 2013]; this is especially true for operational models (i.e., numerical weather prediction) where excessive levels of turbulence are often forced [Sandu *et al.* 2013, Baas *et al.* 2019]. [Sterk *et al.* 2015] found that temperature inversions were underestimated by WRF in clear-sky conditions at three sites with varying surface characteristics: Cabauw (Netherlands), Sodankylä (Finland) and Halley (Antarctica). This study also underscored the importance of the land surface characteristics, and especially vegetation fraction. From experimental studies, tree canopies are known to impact the turbulence and temperature profiles in stable conditions [Batchvarova *et al.* 2001]. This is an important aspect to take into account as a large part of the continental Arctic and sub-Arctic is covered in forests.

Previous modelling studies have tended to evaluate models by comparing their output (either in 3D or single column mode) to measurements [Holtslag *et al.* 2013, Sterk *et al.* 2015]. Another approach, in order to assess how wind speed would impact the surface temperature gradient, is to isolate the surface-layer scheme from the larger model framework. This makes it possible to run the WRF surface layer schemes "offline" for a wide variety of input variables and land surface parameters. The surface layer scheme outputs can then more directly be compared both to measurements at a given site and to simple analytical models such as [van de Wiel *et al.* 2017]. Improvements can also be tested in a versatile fashion before being re-coded within the main WRF model.

In Chapter 4, this method is applied to two WRF surface layer schemes. One of these schemes is a 1-layer model similar in principle to [van de Wiel *et al.* 2017], while the other is a more complex 2-layer model which takes the canopy effects more explicitly into account. Modified versions of each schemes are developed and the performance of the four schemes (original and modified 1 and 2-layers) are then compared to long-term measurements at the Ameriflux Poker Flats Research Range site near Fairbanks, Alaska, which is in a forest. The modifications are then implemented in the WRF codes and evaluated.

Lastly, conclusions and perspectives from the present thesis are presented in Chapter 5.

CHAPTER 2

Characterisation and surface radiative impact of Arctic low clouds

---

Contents

2.1 Introduction

One of the main Arctic boundary-layer processes studied in this thesis is low-level clouds. As outlined in Chapter 1, these clouds are a very important part of the Arctic Ocean climate system, as there is evidence that the radiative forcing that they exert limits warming in the summer and accelerates it in the autumn. However, measurements of clouds over the sea-ice is often limited to ship-based campaigns such as SHEBA (1999), ASCOS (2001), N-ICE (2015) or most recently MOSAiC (2019). These range in duration from a few months to a year, making it impossible to establish multi-year statistics. Satellite data has better spatial and temporal coverage, but satellite-borne instruments often experience difficulty in capturing low level clouds. In this context, the IAOOS campaign was developed jointly by the LATMOS and LOCEAN laboratories of Sorbonne University. Autonomous instrumented buoys were locked into the sea-ice and drifted with it for periods of a few months to more than a year, regularly transmitting the acquired data and GPS coordinates back to the French polar institute (IPEV) office in Brest, France, from 2014 to 2019. On the ocean-facing side of the buoy, instruments included salinity and water temperature sensors, and an Ice Mass Balance measurement system

[Koenig *et al.* 2016]. Atmospheric instruments included a micro lidar for detecting aerosols and clouds, and temperature and pressure sensors. The lidar data obtained by one of the buoys has already been exploited by [Di Biagio *et al.* 2018] and [Di Biagio *et al.* 2021]. However, the full dataset contained 5 years of data on low cloud characteristics over the sea-ice and remained to be treated and analysed. The results were published as an article in Atmospheric Chemistry and Physics in 2021 [Maillard *et al.* 2021], which is reproduced below.

2.2 Article

2.2.1 Introduction

The Arctic is a key region of climate change: it is warming about twice as fast as the middle latitudes. This phenomenon, called "Arctic amplification", is most commonly attributed to the ice-albedo feedback, which is due to areas of open ocean exposed by melting sea ice absorbing more solar radiation. However some models with fixed albedos also appear to show amplified warming in the Arctic, pointing to other mechanisms at work [Winton 2006, Pithan & Mauritsen 2014]. Clouds are one of the main contributors to uncertainty in global climate models because cloud feedbacks and cloud-aerosol interactions are still poorly understood; however, clouds appear to be of particular importance in the Arctic [Tjernström *et al.* 2008], where they play a very important role in the climate system. Indeed, Arctic clouds are observed to influence the melting of sea ice [Kay & Gettelman 2009] and may exert control on the ice-albedo feedback this way. However, these effects and processes are seasonally variable and not well represented by annual means [Kay & Gettelman 2009].

Firstly, the cloud cover in the Arctic has a large seasonal variability: it is especially extensive in the summer and reaches a minimum in the winter [Curry *et al.* 1988, Curry *et al.* 1996]. This result is well attested in the literature although values and trends tend to differ between studies and instruments. For example, during the Surface Heat Balance of the Arctic (SHEBA) campaign, winter cloud occurrence measured from a combined radar/lidar was 70%. It increased to over 80% in the summer months and reached a 95% peak in September [Shupe *et al.* 2006]. Using data from CALIPSO (Cloud-Aerosol Lidar and Infrared Pathfinder Satellite Observations), [Zygmuntowska *et al.* 2012] find two peaks of 85% and 90% in May and October respectively, and a minimum in January-March around 70%, in good agreement with [Shupe *et al.* 2006]. However, in the same study, cloud fractions retrieved from the space-borne Advanced Very-High-Resolution Radiometer (AVHRR) instrument were < 60% for the whole October-April period, and never rose above 80%.

Cloud microphysical characteristics and radiative impact are also seasonally-dependant. Winter clouds contain mostly ice and are therefore less emissive than summer liquid-containing clouds, although mixed-phased clouds maintain themselves throughout the year [Morrison *et al.* 2011]. However, seasonal statistics of cloud optical depth (COD) over the Arctic ocean are scarce and uncertain: based on the AVHRR radiometer data for example, [Wang & Key 2004] found a slight seasonal variation in the cloud optical depth over the Arctic ocean, with a peak in May and October (> 6) and lower values (≈ 5) in the winter. It has been shown that cloud radiative forcing is positive (i.e., clouds warm the surface) for much of the year, except for a short period in late June to early July when the cloud shortwave forcing is larger than the longwave forcing [Intrieri *et al.* 002a]. Indeed, in contrast to winter, clouds impact the surface radiative budget in two competing ways in the summer. As in winter, they provide longwave warming; but they also have a shortwave cooling effect, by preventing solar radiation from reaching the surface.

Large uncertainties remain about the characteristics of Arctic clouds and their surface impact, in part because more data and observations are needed [Kay *et al.* 2016]. Ground-based measurements are sparse in the Arctic because of the harsh conditions and the lack of permanent settlements. The ground-based measurement stations of the International Arctic Systems for Observing the Atmosphere (IASOA) network [Uttal *et al.* 2016], for example Eureka (Nunavut, Canada) or Barrow (Alaska) are necessarily coastal. Nevertheless, ground-based stations have continuous data coverage with a record covering several years, and have therefore given precious information on Arctic clouds and their properties [Shupe *et al.* 2011, Nomokonova *et al.* 2019]. Measurements on the sea-ice take the form of ship-based or airborne campaigns, covering only a narrow spatial and temporal window. The first such campaign was SHEBA, which covered a full year from October 1997 to October 1998. Although it yielded significant results [Stramler *et al.* 2011, Shupe *et al.* 2006], it is now more than 20 years old and not representative of the modern Arctic. Subsequent campaigns aimed at studying the Arctic's changing conditions such as the Arctic Summer Cloud Ocean Study (ASCOS) [Tjernström *et al.* 2014], the ACLOUD/PASCAL campaign [Wendisch *et al.* 2019], the Arctic Clouds in Summer Experiment (ASCE) [Sotiropoulou *et al.* 2016] or the Norwegian Young Sea Ice Experiment (N-ICE) [Walden *et al.* 2016] covered one to six months, disproportionately in the summer. Most recently, the Multidisciplinary drifting Observatory for the Study of Arctic Climate (MOSAiC) campaign is a one year-long study of the Arctic climate, with clouds as one of many research axes. The drift is due to end in September 2020.

In this context, many established statistics - e.g., [Wang & Key 2004] - make use of satellite measurements, which have large coverage but are flawed at high latitudes. Indeed, spectroradiometers (such as MODIS, or the AVHRR) may have difficulties in distinguishing clouds from the underlying sea-ice. Their performance also differs between the dark winter months and the summer [Zygmuntowska *et al.* 2012]. All in all, there are large differences in measured values between instruments [Chan & Comiso 2013]. Satellite-based lidars such as the instrument aboard CALIPSO give more reliable measurements but are limited to 82°N because of the satellite flight path [Winker *et al.* 2009]. Their record is also more limited in time than that of ground-based stations (from 2006 for CALIPSO).

This paper presents results of the Ice, Atmosphere, Arctic Ocean Observing

System (IAOOS) field experiment lidar measurements. This novel database offers a ground-based view of lower tropospheric clouds at very high latitudes (over 80°N) over a significant period of time - from 2014 to 2019 [Mariage 2015]. A small part of this dataset has already been analysed in [Di Biagio *et al.* 2018] and [Mariage *et al.* 2017]. Here it is treated as a whole to extract a multi year statistic of the April to December cloud cover along the track of the drifting buoys. First, the IAOOS field campaign and other relevant datasets are presented (Sect. 2). Then the treatment of the IAOOS lidar data and the derivation of cloud characteristics are explained (Sect. 3). The obtained statistics of cloud frequency, and geometrical and optical properties are presented in Sect. 4. Finally the impact of clouds on surface temperatures and radiative balance is explored (Sect. 5).

2.2.2 Data used

2.2.2.1 The IAOOS field campaign: a 5 year study of the Arctic troposphere

Deployed instruments The IAOOS field experiment was led by Sorbonne University - through the LATMOS and LOCEAN laboratories - with the support of several structures, among which the French polar institute IPEV (Institut polaire français Paul-Emile Victor) and the technical division of the Institute for Earth Sciences and Astronomy (CNRS-INSU) from 2014 to 2019. The main campaign objective was to "collect real time observations of the ocean, ice, snow and atmosphere of the Arctic", offering a complementary viewpoint to that of satellites [L2]. In order to do this, several instruments were installed on an autonomous floating platform (or buoy). These buoys were then locked into the pack ice and left to drift with it for a duration of several months to a year. During that time period, the buoys were tracked by GPS and communicated the acquired data to the IPEV office in Brest (48°23'24" N, 4°29'24" W) every day.

The main instrument on the "atmosphere" side of the buoys was a micro lidar, which was was designed to study lower troposphere and has a clear-sky range of around 4.4 km in the daytime, and 13.7 km at night, with a vertical resolution of 15 m [Mariage 2015, Mariage *et al.* 2017]. The wavelength was chosen in the near infrared (808 nm) in order to avoid disturbing the local fauna while maintaining a distinct molecular signal. This is similar to many commercial ceilometers [Mariage 2015]. However, it had to be custom made to resist the tough Arctic conditions. Indeed, several key components of a lidar are sensitive to ambient temperature variations, and the buoys' operating conditions in the pack ice could be up to 40°C colder than the lab where it was calibrated. The lidar therefore had to be modified and isolated in order to keep it at a near constant temperature [Mariage 2015]. Furthermore, the tube containing the lidar emitter and receiver was topped with a window that, in operating conditions, was often covered by frost. This layer of frost attenuates the signal, and, in extreme cases, totally blinds the lidar. In order to overcome this problem a window heating system was put in place. The actual

Buoy	**Start date**	**End date**	**Nb of exploitable profiles**
B02	13/04/2013	02/12/2014	462
B12	26/04/2015	05/06/2015	73
B24	06/04/2017	20/11/2017	322
B25	15/08/2017	28/10/2018	429
B27	19/04/2018	17/03/2019	491

Table 2.1: Start and end date of the buoy lidar data acquisition and number of exploitable profiles. Note that buoy B07 also yielded some profiles [Di Biagio *et al.* 2018] which are not treated here.

heating was limited to the 10-minute interval before the two- to four-time daily profile acquisition in order to avoid draining the battery too fast. Theoretically, this ensured that the lidar window was clear during measurement. However, in practice, the frost prevented lidar measurements from mid-December to early March. The frost problem will be further detailed in Sect. 2.2.3.1.

The buoys were also equipped with temperature and pressure sensors for measuring outside conditions; and internal temperature and humidity sensors for monitoring the lidar system. On the underwater portion of the buoys, a float measured ocean temperature and salinity while an Ice Mass Balance system acquired temperature profiles of the snow, ice and liquid water layers - see [Koenig *et al.* 2016].

Buoys and tracks The first IAOOS platform was deployed in 2013. Since then, more than 20 buoys have drifted in the Arctic pack ice, and the last one was deployed in August 2019. However, not all buoys were equipped with lidars and not all deployed lidars operated successfully. In particular, the data transmission system of the 2016 buoys functioned poorly, and there are no exploitable lidar profiles from July 2015 to March 2017 (see Table 2.1). All in all, five buoys yielded usable lidar data, amounting to 1777 profiles covering the April to December months. A vast majority of the drift took place north of 82°N (red circle, Fig. 2.1). Furthermore, apart from one buoy, all trajectories were confined to the Atlantic sector of the Arctic, reflecting the transpolar drift stream. Indeed, most buoys studied here were locked into the ice close to the North Pole.

2.2.2.2 Other data

N-ICE The Norwegian Young Sea Ice Experiment (N-ICE) campaign took place from January to June 2015. During that time, the research vessel Lance drifted with four different ice floes [Walden *et al.* 2016, Cohen *et al.* 2017, Walden *et al.* 2017]. The first two drifts took place during the winter (January - March 2015) while the last two drifts occurred in the late spring to early summer period (April to June 2015). On each floe, a "Supersite" ice camp was installed about 300 m away from the research vessel. Atmospheric measurements were mostly performed at this Supersite.

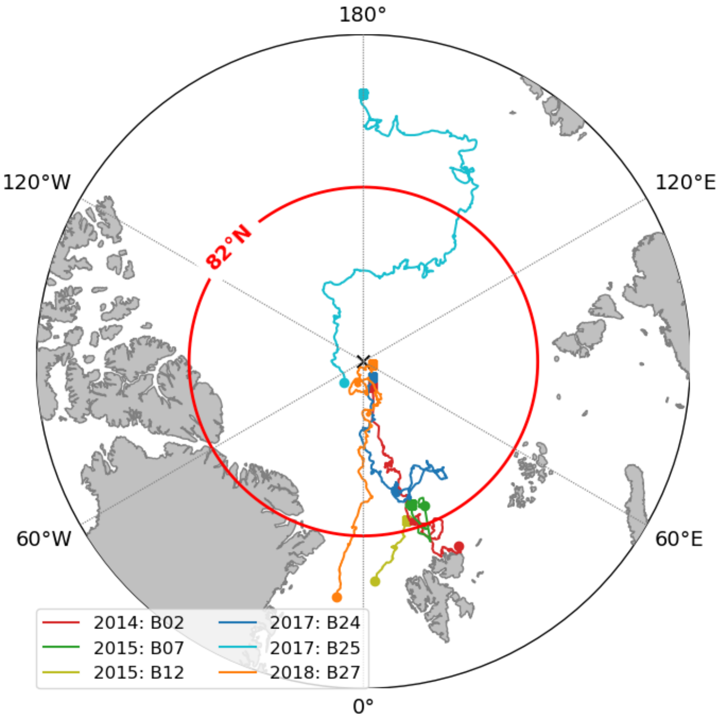

Figure 2.1: Map of the IAOOS buoy tracks, 2014-2019 (this map only includes buoys which delivered the lidar data exploited in this article). The different colours correspond to the different buoys, with the year of launch indicated. The red circle corresponds to the 82°N latitude: north of this circle, no satellite lidar data is available.

Surface longwave fluxes (up and down) were measured with a Kipp & Zonen CGR4 pyrgeometer, which has a 4.5 to 42 μm bandwith. The shortwave fluxes (up and down) were measured with a Kipp & Zonen CMP22 pyranometer (200 to 3600 nm bandwidth). Both these instruments were heated and ventilated using a Kipp & Zonen CVF4 unit. Their accuracy is 3% (or 5 W m^{-2}) for the shortwave, and 2% (or 3 W m^{-2}) for the longwave [Walden *et al.* 2017, Hudson *et al.* 2016]. The temperature at two meters was measured with a ventilated and shielded Vaisala HMP-155A sensor which has an accuracy of 2.4% (or 0.3°C) [Graham *et al.* 2017, Cohen *et al.* 2017]. In addition, radiosondes were launched twice-daily from the research vessel, yielding profiles of relative humidity, temperature and wind speed [Walden *et al.* 2017].

Four IAOOS buoys were deployed during this campaign and drifted in the ice floe close to the research vessel. In particular, the B12 buoy was locked into the third ice floe 200m away from the Supersite from end of April to the beginning of June 2015 (Fig. 2.1). Because of the proximity of the buoy to the Supersite over this period, the N-ICE surface radiative flux and temperature measurements can be used as a complement to the IAOOS data. This allowed us to evaluate the radiative impact of clouds on the surface in late spring to early summer (Sect. 2.2.5.2 and 2.2.5.3).

ERA5 ERA5 is the new reanalysis from the European Center for Medium-Range Weather Forecast, replacing ERA-Interim [Hersbach *et al.* 2020]. ERA5 provides hourly or four times daily estimates of many weather variables on a 0.25°x0.25° grid and with 137 vertical levels. It is made available online with a three month delay [Copernicus Climate Change Service (C3S)]. Here we interpolated the ERA5 values on the IAOOS positions using bilinear interpolation in space (and linear interpolation in time) during the N-ICE drift period. This allowed us to compare the radiative flux values measured during N-ICE with the ERA5 reanalyses (see Sect. 2.2.5.2).

2.2.3 Methodology of the IAOOS lidar data treatment

2.2.3.1 Overcoming Arctic-specific challenges

Lidar window frost Several problems are associated with the autonomous drift of a lidar in harsh Arctic conditions, as outlined in Sect. 2.2.2.1. In particular, the cold conditions cause frost to form on the lidar window, because the installed window heating system could not operate the whole time in order to preserve batteries. This caused the signal to be attenuated and therefore the system constant C - which is the ratio of the raw signal in photon numbers to the actual signal - to diminish.

Because it is crucial to know the system constant value in order to extract geophysical information from the raw lidar signal, this effect had to be corrected. The correction method was put in place by [Mariage 2015]. First a "frost index", γ is defined:

$$\gamma = \frac{P_0}{P}$$

where P is the lidar window reflection peak, and P_0 the minimal value taken by P over the course of a drift. P_0 is therefore assumed to be the value of the reflection peak when the window is entirely frost-free. γ then ranges from approximately 1 when the window is frost free to very low values ($< 5 \cdot 10^{-2}$) when the window is totally opaque. In fact, this frost index becomes a proxy for the window transmittance.

Under the assumption that aerosol load is very low in the high Arctic, C can be calculated from cloud-free profiles. Its values are then compared to the frost index. As could be expected, $\frac{1}{C}$ diminishes with γ: that is, the signal is dampened when the window is covered with frost. An empirical fit of $\frac{1}{C}$ as a function of γ can then be established [Mariage 2015]. This allows us to deduce the value of C for each profile from the value of γ. The fitting coefficients were determined independently for each buoy when possible, since the frost index depends on P_0, which is buoy specific.

It should be noted however that when the frost is too thick ($\gamma \leq 0.05$), no usable signal is recoverable. This means that there were no exploitable lidar profiles in late December to early March. Furthermore, this frost correction method naturally causes uncertainty on the obtained value of C. Around 11% of profiles have values of γ between 0.1 and 0.3. In this case, [Mariage 2015] estimates that the window frost correction leads to a 30% error on C. A further 3% of profiles have $0.05 \leq \gamma < 0.1$, in which case the error on C can be up to 60%. For $\gamma \geq 0.3$, the C error tends towards the frost-free system constant determination error, which is around 10% [Mariage 2015]. The system constant is used in the calculation of the attenuated scattering ratio, from which all cloud quantities are derived (Sect. 2.2.3.2). However, it is difficult to quantify the impact of its error on cloud detection, in part because it depends on the sign of the error. An overestimated C would lead to under-detection of cloud layers, and vice versa. In practice, visual inspection of the profiles indicates that the cloud detection algorithm outlined below is robust to the errors that may be incurred through the window frost correction.

Receiver saturation due to reflective low clouds The detectors used in the IAOOS lidar are avalanche photodiodes, and can reach saturation. This means that if they are exposed to a signal which is too intense, the photon count goes down. If the saturation is very intense, the photon count can even reach zero [Exc 2018]. Following saturation, the photon number count then slowly increases back up to its normal background value. Saturation is not usually an issue in most lidar operation situations; however during the Arctic summer, background noise levels are high due to shortwave radiation and the reflective sea ice and the signal reflected by the very low cloud cover is often enough to saturate the detector. This problem was observed from the very first deployment of the IAOOS buoys [Mariage 2015]. It translates visually into a lidar signal which dips below background noise levels at a certain altitude, and then slowly increases back to the background. Over the whole IAOOS period, approximately 30% of profiles were concerned by this phenomenon.

A saturated profile may contain some geophysical data above the saturation altitude; therefore, it was important to correct this effect. We hypothesised that the saturated signal S_{sat} resulted from the convolution of the "true" signal S with a saturation impulse response function (IRF):

$$S_{sat}(z) = S(z) * IRF(z)$$

The goal was therefore to deduce S from the measured profile, i.e. S_{sat}. A deconvolution algorithm was therefore put into place [Richardson 1972, Refaat *et al.* 2008]. The deconvolution process recovered useful signal from the saturated profiles in about a third of cases. In the remaining two-thirds, the "true" signal was only background noise. This represented an appreciable gain in data for the IAOOS campaign.

2.2.3.2 Derivation of cloud characteristics from raw lidar data

The lidar profile treatment program is a simplified version of the CALIPSO treatment algorithm described by [Winker *et al.* 2009].

Attenuated scattering ratio calculation The first step involves calculating the attenuated scattering ratio:

$$SR_{att} = \frac{(S-B)\cdot z^2}{C\cdot O(z)\cdot \beta_m(z)T_m(z)^2} = (1+\frac{\beta_p(z)}{\beta_m(z)})\cdot T_p(z)^2 \tag{2.1}$$

where

- S is the raw signal;
- B the background noise (calculated as the mean of the raw signal above 20 km, where there is no geophysical signal due to attenuation);
- z the altitude above the lidar, which is at sea level;
- C is the system constant, which varies with the lidar window frost as described above;
- $O(z)$ is the overlap factor between the lidar source and receiver: this factor is determined for each buoy as the average ratio of the raw signal to the calculated Rayleigh signal for very clear, cloudless days. The overlap creates a minimum height underneath which the signal cannot be resolved: a sort of lidar "blind zone";
- $\beta_p(z)$ and $\beta_m(z)$ are the particulate and molecular backscatter ratios at altitude z, respectively;
- T_p and T_m are the particulate and molecular transmission at altitude z, respectively.

The Rayleigh (molecular) backscatter and transmission are calculated according to [Bucholtz 1995], using vertical temperature and pressure profiles from ERA5 reanalyses.

Cloud detection Clouds are then detected by applying a threshold to SR_{att}, since in the absence of particulate attenuation the attenuated scattering ratio will be equal to 1 ($\beta_p = 0$, $T_p^2 = 1$). The initial threshold, S_t, is set to 1.1 at $z = 0$ and increases with altitude in order to take into account that noise increases on the vertical [Winker & Vaughan 1994].

The base of a feature is detected when seven consecutive points are above the threshold. The top is detected either when SR_{att} has fallen beneath the threshold and has stopped decreasing (a condition inspired by [Winker & Vaughan 1994]) or when the signal is below the noise level. The noise level is defined as $2\sigma z^2$, where σ

is the standard deviation of the raw signal above 20 km. Assuming gaussian noise, 95% of pure noise fluctuations are therefore beneath this level.

Above the features, SR_{att} will again be constant but equal to $T_f^2(z_{top})$, where z_{top} is the top altitude of the features and T_f its transmission, because of the particle attenuation. This means that new features above this feature will be missed unless the threshold is modified to take the feature attenuation into account. Therefore, above a feature, the threshold is updated to $T_f^2 \cdot S_t$.

Once detected, a feature is determined to be a cloud if its spread, defined as the ratio of maximum feature SR_{att} to average below-feature SR_{att}, is greater than 100 (or 20 for higher-altitude layers for which average below-feature SR_{att} is strongly impacted by noise).

Calculation of optical depth and lidar ratio When the lidar beam goes through the cloud layer and reaches the particle-free air on the other side, the cloud transmission can be directly calculated as the ratio of the mean SR_{att} above and below the cloud layer over a minimum of 20 points (or 300 m).

However, this was rarely the case during IAOOS, especially in the summer when the noise level is high. Over the whole IAOOS campaign, only 14% of all features were transparent to the lidar. In all other cases, the cloud transmission T_c^2 was calculated from the integrated attenuated backscatter (IAB), assuming a constant lidar - or backscatter-to-extinction - ratio S_c within the cloud layer:

$$IAB = \int_{z_0}^{z_1} \beta_p(z) \cdot e^{-2\int_{z_0}^{z} \eta\alpha_p(z')dz'} dz = \frac{1}{2\eta S_c}(1 - T_c^2) \tag{2.2}$$

with z_0 and z_1 the bottom and top of the cloud, α_p the particle extinction coefficient and η the multiple scattering coefficient [Platt 1973]. The IAB can then be calculated from the attenuated scattering ratio and molecular backscatter [Winker *et al.* 2009] :

$$\begin{aligned} IAB \approx & \int_{z_0}^{z_1} SR_{att}(z) \cdot \beta_m(z)dz \\ & - \frac{1}{2}(z_1 - z_0) \cdot (\beta_m(z_0)SR_{att}(z_0) + \beta_m(z_1)SR_{att}(z_1)) \end{aligned} \tag{2.3}$$

The (relatively few) cases where the cloud layer transmission could be independently calculated were used to derive values of the multiple-scattering lidar ratio $S^* = \eta S_c$ by inverting Eq. (2.2).

For both Rayleigh- and IAB-derived T_c, the cloud optical depth τ_c can then be deduced:

$$T_c = e^{-\eta \cdot \tau_c} \tag{2.4}$$

The multiple-scattering coefficient η was assumed constant and equal to 0.8, based on previous analyses of the IAOOS data [Mariage *et al.* 2017, Di Biagio *et al.* 2018].

Uncertainty and limits of the method Equation (2.2) implies that as $T_c^2 \to 0$, $IAB \to \frac{1}{2\eta S_c}$. This means that for optically thick clouds, a small error on the value of IAB or S_c risks propagating to a large error on COD. The error is also asymmetrical: an overestimation of IAB or S_c yields a much worse result on COD than an underestimation of these same quantities. In practice, if the lidar ratio of a cloud of true optical depth 1.5 is underestimated by 10%, the measured optical depth will be ≈ 1.1. On the other hand, if it is overestimated by the same amount, the measured optical depth will be ≈ 2.2. In some cases, overestimation of lidar ratio or IAB can even lead to negative T_c^2 values, which is non-physical and doesn't allow for the calculation of optical depth. In practice, therefore, this method is appropriate mainly for optically thinner cloud layers. We will refer to "low-IAB" cloud layers, for which the method does not lead to non-physical results (i.e., the cloud layer is thin enough that this method works well). This accounts for 42% of all features. We will call "high-IAB" cloud layers those for which calculated T_c^2 is negative. These mathematically correspond to clouds with higher IAB, and therefore higher COD, than low-IAB cases. The inclusion of these high-IAB COD values in the statistic will be discussed in Sect. 2.2.4.3.

Although uncertain in other respects, this COD calculation method has the advantage of being only faintly impacted by background noise levels. On the other hand, noise levels can have a strong impact on the cloud top determination. Tests with simulated lidar signals indicate that cloud top determination error reaches up to 150 m for typical summer noise levels and optically thicker clouds ($\tau_c \approx 2.5$). This error is much lower for low noise levels, such as are found in the high Arctic during the polar night (October - March). This difference must be kept in mind when interpreting seasonal variation of cloud geometrical thickness (Sect. 2.2.4.2).

2.2.4 Seasonal variability of Arctic low cloud properties during IAOOS

2.2.4.1 Frequency of cloud presence

IAOOS data confirms that low clouds (i.e., with a base under 2 km) are very frequent in the Arctic, especially in the summer. Average monthly cloud frequency from March to December, defined as the average of monthly ratios of profiles containing at least one cloud with base lower than 2 km to all profiles, is 75%. This value is coherent with previous statistics of cloud fraction above 80°N derived from satellites, for example [Wang & Key 2004] and [Curry *et al.* 1996], which usually give a global annual cloud cover of around $60-70\%$, with a maximum in summer and a minimum in November - April.

Observed seasonal variation of cloud fraction can differ strongly between satellites [Wang & Key 2004, Zygmuntowska *et al.* 2012]. [Chan & Comiso 2013] found large disagreements between MODIS and CALIOP in the Arctic, for example, especially over sea-ice and during the polar night. This is because MODIS finds it difficult to differentiate between the surface and the clouds when relying only

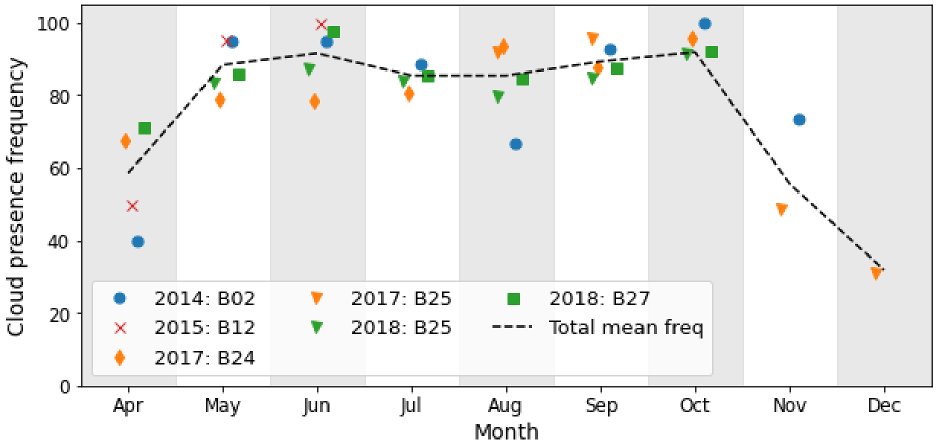

Figure 2.2: Monthly variation of low cloud frequency, defined as the number of profiles that contain at least one cloud layer with base lower than 2 km divided by the total number of profiles for the month, for five IAOOS buoys. The dashed line represents the total monthly cloud frequency over all IAOOS profiles. It is only calculated for months with more than 30 profiles in total.

on IR channels. On the other hand, [Blanchard *et al.* 2014] shows that there is good general agreement and similar trends in cloud fraction over Eureka (Nunavut, Canada) between CALIOP, MODIS, CloudSat and the IIR instrument aboard CALIPSO, with a global maximum in September - November and a minimum in March - May. However, discrepancies between passive and active instruments remain [Blanchard *et al.* 2014]. Ground-based measurements play a key part in quantifying seasonal cloud cover variability in the Arctic, although they are often sensitive primarily to lower-level clouds. Averaging visual observations from ships and ice-camps above 80°N, [Hahn *et al.* 1995] found that cloud cover was globally stable around 60% in winter, increasing to 80% from April to June, and decreasing again from September to November. A maximum of 85% was reached in August/September. The combined lidar-radar measurements at SHEBA give slightly higher values of 70% in winter and 90% in summer, with an earlier transition (February to April) and a peak in September [Intrieri *et al.* 002b].

The results of IAOOS dataset are shown in Table 2.3 and Fig. 2.2. Note here that the number of profiles available for each month is variable, both because of the more favorable operation conditions in the summer and the timing of the buoy deployment (usually in May). As such, there are more than 200 profiles from May to September, around 100 in April and October, and less than 54 in November and December (months with less than 30 profiles, i.e. January, February, and March, are not treated in this article). Care must therefore be taken in analysing the results of late autumn and winter. A 90% confidence interval for the cloud occurrence frequency can be estimated from a Bayesian calculation, assuming that the number of cloudy profiles follows a binomial distribution and supposing an appropriate a priori distribution for the cloud frequency from the literature (Appendix 2.2.7.1).

The IAOOS data shows a similar trend as the literature, with generally higher cloud cover values. From May to October, clouds are present over 85% of the time (Fig. 2.2). In contrast to the previous ground-based climatologies outlined above, there are two peaks at more than 0.9 in the monthly cloud frequency, although they differ little from the summer baseline. The first is in June, which has a mean cloud frequency of 0.92 and a confidence interval of $(0.88 - 0.94)$. The second peak is in October, also with a mean cloud frequency of 0.92 but with a slightly wider confidence interval $(0.85 - 0.95)$ because of the lower number of profiles. This is reminiscent of the results of [Zygmuntowska *et al.* 2012], from CALIPSO data, which show a peak in cloud occurrence above 0.9 in October. July and August have slightly lower cloud frequency values (0.85 $(0.82 - 0.88)$ and 0.85 $(0.8 - 0.89)$ respectively). However, since there is non negligible overlap between the confidence intervals of June/October and the other summer months, it is difficult to draw solid conclusions as to May - October variability.

In the IAOOS dataset, April and November appear to mark a sharp transition in cloud occurrence frequency from the summer values. April has a cloud frequency of 0.59 $(0.52 - 0.67)$ while the cloud frequency in November is 0.56 $(0.48 - 0.68)$. While the confidence intervals are quite wide here due to the lower number of profiles, there is no overlap with the summer confidence intervals. This suggests that the lower cloud frequencies observed during the months of April and November is meaningfully different from that of the months of May through October. December cloud frequency is lower still, at 0.32 $(0.29 - 0.51)$. Note however the width of the confidence interval and the fact that the December data corresponds to a single year of measurement (2017).

It is not possible to robustly quantify interannual variability in Arctic cloud cover from the IAOOS dataset since there are at most four years of data for each month. Qualitatively, however, the April - May transition in cloud frequency observed by the buoys is quite variable. In 2014, the B02 buoy observed a very sharp spring transition in cloud frequency: from 0.4 $(0.35 - 0.6)$ in April 2014 to more than 0.9 $(0.89 - 0.97)$ in May and June 2014 (blue circles, Fig. 2.2). On the other hand, this transition was much more gradual in 2017 (buoy B24, orange diamonds). The June 2017 cloud frequency is less than 0.8 $(0.69 - 0.85)$, overlapping significantly with the May 2017 cloud frequency confidence interval of $(0.56 - 0.78)$. This is not an effect of spatial variability as both B02 and B24 were drifting in the Atlantic sector of the Arctic (Fig. 2.1).

It has been observed from satellite data that the Atlantic sector is the cloudiest part of the Arctic Ocean [Liu *et al.* 2012, Wang & Key 2004]. This is linked to the low pressure systems and the storm tracks arriving from the northern Atlantic Ocean. Since most of the IAOOS buoys drifted in this sector, the IAOOS dataset must be regarded as most representative of these specific conditions, and not of the ocean-wide cloud characteristics.

Furthermore, the results above pertain to the low cloud cover, i.e. clouds with a base underneath 2 km. Clouds with a base between $2 - 5$ km are much rarer in

Month	N_p (#)	$\frac{N_{ml}}{N_{profiles}}$ (%)	First cloud base (%)			
			$<$ 120m	120 − 500m	500m −2km	2 − 5km
Apr	94	4	96	0	2	2
May	359	4	95	2	1	1
Jun	330	8	87	8	3	1
Jul	342	14	93	1	3	3
Aug	205	12	91	2	5	2
Sep	251	10	90	5	4	1
Oct	98	13	98	2	0	0
Nov	54	2	93	3	3	0
Dec	44	0	93	7	0	0

Table 2.2: Cloud multiple layer and base characteristics for all profiles from April to December. N_p is the total number of lidar profiles for each month (for all years and buoys), and N_{ml} is the number of profiles containing multilayered clouds. The last four columns represent the % of first layer cloud bases in each altitude range. The 120 m cutoff corresponds to the minimum altitude at which the lidar overlap factor can be corrected for all buoys. Cloud bases above 5 km, which correspond to "high-level" clouds in many reanalyses such as ERA5, are not included because the lidar range in perfectly clear daytime conditions is only 4.4 km (Sect. 2.2.2.1).

the IAOOS dataset, occurring only 3% of the time from March to December, with a peak at 8% in July. However, as the lidar signal is often dampened by the first cloud layers, IAOOS statistics of cloud cover above 2 km are expected to be biased low.

2.2.4.2 Cloud geometrical properties

Multi-layer clouds were detected 7% of the time by the IAOOS lidar over the course of the campaign. This value is small compared to previous observations: for example, [Liu *et al.* 2012] find that multi-layer clouds are present 20% of the time year-round, with very low seasonal variation. These results are drawn from satellite observations and [Liu *et al.* 2012] note that they are also underestimated. Ground-based measurements generally attest to frequent multilayering in the summertime, with layers separated by several hundred meters [Curry *et al.* 1988, Curry *et al.* 1996]. SHEBA measurements even show that multi-layer clouds exceeded single-layer clouds in June and July 1998, and occurred on average 45% of the time over the whole experiment period [Intrieri *et al.* 002b]. IAOOS measurements also attest to a higher frequency of multiple layered clouds in summer: they occur more than 10% of the time July - October, and only 4% of the time in April and May (Table 2.2). Only one IAOOS profile contains multilayered clouds in November, and none in December. Despite the low number of total profiles in these months, these values are different from the

July multilayered cloud frequency at a statistically significant level: for November, Fisher's exact test yields a p-value of 0.007 [Fisher 1922]. IAOOS measurements strongly underestimate frequency of multilayered clouds due to the fact that the lowest cloud layer entirely attenuates the lidar signal in most profiles. Furthermore, cloud layers separated by less than 300 m were counted as one in the IAOOS data treatment in order to have a better estimation of cloud transmission (Sect. 2.2.3.2). However, the robust measurement of the geometry of the first cloud layer derived from IAOOS measurements base is a useful statistic. Indeed, the base of the lowest cloud layer is expected to have the strongest impact on surface radiative fluxes as compared to higher cloud layers. Hereafter, all cloud statistics refer to single cloud layers; in most cases, the lowest.

Clouds in the IAOOS dataset are extremely low, with little seasonal variability. From April to December, at least 85% of first layer clouds have a base below 120 m, which is the minimum altitude at which the lidar overlap factor can be corrected for all buoys (Table 2.2). The median base altitude is therefore at 120 m in nearly every month. During ASCOS, which took place in August 2008, the lowest cloud base distribution peaked beneath 100 m [Tjernström *et al.* 2012]. Median first cloud base from SHEBA measurements [Shupe *et al.* 2007] was also less than 120 m for all months except March (179 m) and April (209 m). Nevertheless, higher-altitude first cloud layers were more frequent than during IAOOS, especially in spring to early summer [Intrieri *et al.* 002b].

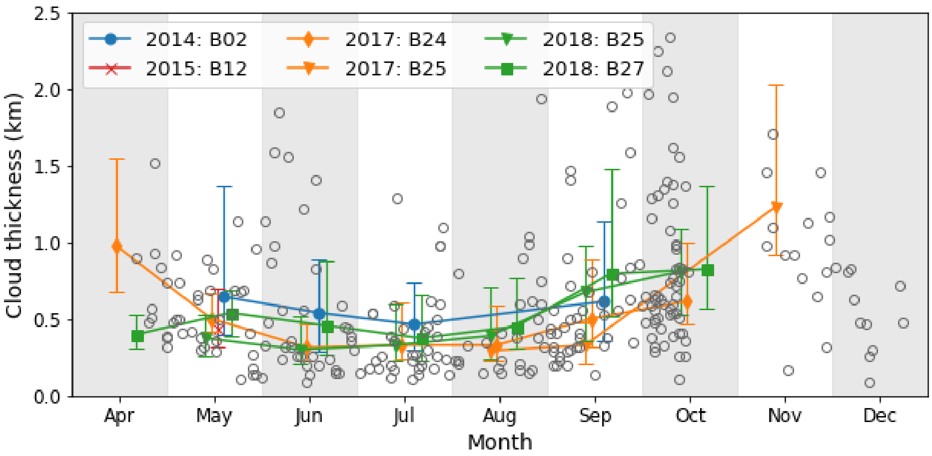

Figure 2.3: Monthly evolution of first layer cloud geometrical thickness (in km), for five IAOOS buoys. The markers represent the median value, and the whiskers indicate the 25th and 75th percentiles. The open circles represent individual cloud thickness values where the lidar signal sees through the cloud layer, i.e. the cloud top is clearly detected. The median, 25th and 75th percentiles are only calculated when more than 15 data points are available.

On the other hand, Fig. 2.3 highlights a significant difference in measurements of single-layer cloud geometrical thickness between summer (May to September) and the months of April, October and November. The median cloud thickness from June to August ranges between 360 and 390 m, whereas it is nearly 750 m in October and March, and more than 1 km in November. This difference appears significant at a statistical level. The Mann-Whitney U for the July and October cloud thickness distributions was 9834.5 (with sample sizes $n_1 = 355$ and $n_2 = 104$), yielding a p-value < 0.001 [Mann & Whitney 1947a]. The same is true for July and April ($U = 5940.5$, $n_1 = 355$ and $n_2 = 60$, p-value < 0.001).

As explained in Sect. 2.2.3.2, it is expected that summer cloud thickness would be underestimated by up to 150 m due to higher noise levels in this period. However, this is too small an error to explain the different median values observed between summer and spring/autumn. Furthermore, these values and trends are coherent with previous studies of single-layer clouds at Barrow and Eureka. For example, the average thickness of single-layer clouds at Barrow from June to August 2000 was 320 m while the September average was 550 m [Dong & Mace 2003]. Over the 2005 to 2008 period the average single-layer mixed-phase cloud thickness at Eureka varied from 200 m to 700 m with maxima in autumn and minima in spring [de Boer *et al.* 2009]. Total thickness of all clouds, single-layered or not, may however be much larger. During SHEBA, median total cloud thickness from radar data was above 1 km in every month, with peaks at around 3 km in April and October [Shupe *et al.* 2007]. These values are from 3 (March/April) to 7 (July/August) times larger than the IAOOS monthly median values.

2.2.4.3 Cloud optical properties

As noted in Sect. 2.2.3.2, cloud layers for which both IAB and T_c^2 are determined independently can be used to calculate the multiple-scattering lidar ratio S^*. In total, there were 207 such cloud layers during the IAOOS period, covering the March to December period. They are shown in Fig. 2.4a, along with the median and the 25th and 75th percentiles for each month. The global median is 17.5 sr, with 90% of values falling in the $7-38$ sr range. Although the spread is quite large, these results are consistent with cloud lidar ratio values found in the literature. For example [O'Connor *et al.* 2004] found that S^* values ranged between 14.5 and 16.5 sr for low water clouds; for ice or mixed-phase clouds, the range was $5-40$ sr, very similar to IAOOS results.

The seasonal variation of S^* is statistically significant: the median S^* for the summer months (JJA) was 23 sr versus 15.5 sr in the autumn (SON). The Mann-Whitney U is 4953.5, with $n_1 = 67$, $n_2 = 98$, yielding a p-value of < 0.001 [Mann & Whitney 1947a]. There are two possible causes for the observed variability in $S^* = \eta S_c$: changes in the multiple scattering coefficient η or S_c. η decreases with cloud temperature [Garnier *et al.* 2015] while S_c depends on cloud microphysical properties, among which cloud droplet effective radius and phase. In the absence of additional measurements, it is difficult to determine which one has the largest impact here, as well as the ultimate physical cause of variation. The monthly median values were then used to calculate COD (Sect. 2.2.3.2).

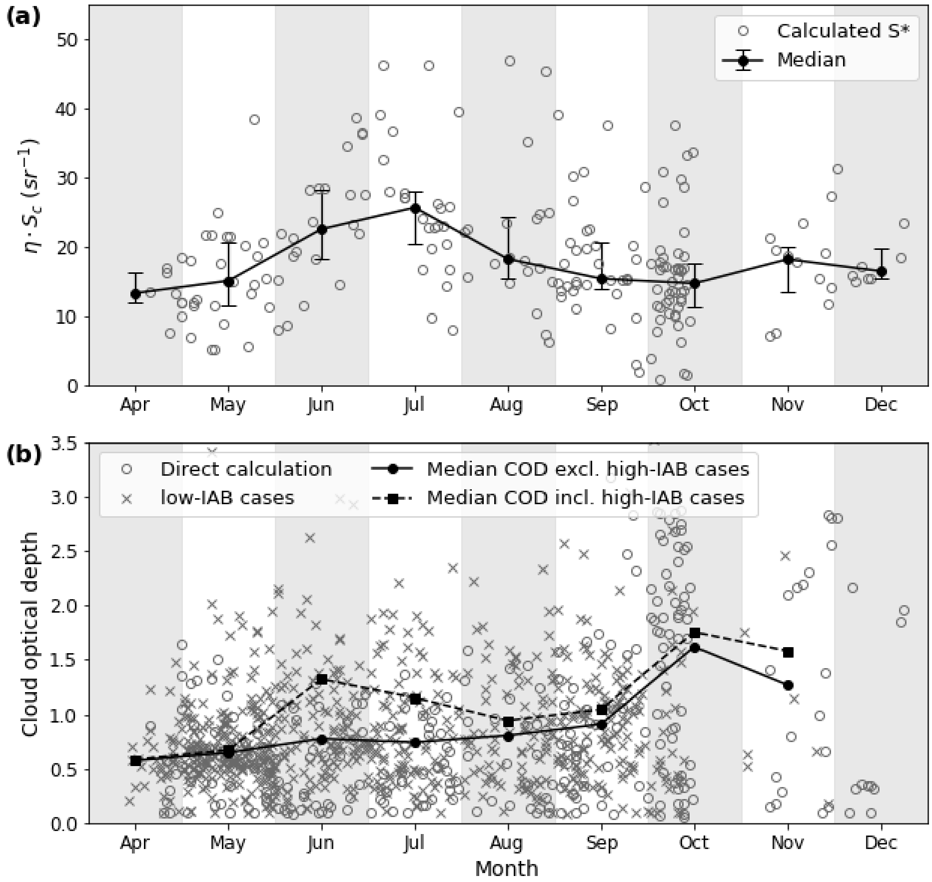

Figure 2.4: Panel a: monthly variations of lidar ratio values over the IAOOS campaigns. The open circles represent the measurements. The filled markers represent the monthly medians, with the whiskers indicating the 25th and 75th percentiles. Panel b: monthly evolution of single-layer COD, for five IAOOS buoys. Open circles represent the Rayleigh-derived cloud optical depths. Crosses correspond to the low-IAB COD values (Sect. 2.2.3.2) Filled markers represent the monthly medians, when high-IAB cases are excluded (circles) or included (squares). These medians are calculated when more than 15 data points are available.

The average single-layer COD during IAOOS excluding high-IAB cases was 0.9, with values ranging from 0.3 to 2.1. These values are small when compared to previous satellite and ground based studies in the Arctic. But as noted in Sect. 2.2.3.2, the retrieval method used for calculating COD from the IAOOS lidar data when the signal is fully attenuated is not suited to optically thick clouds: the rough upper bound of COD which can be measured through this method is 2. As almost 20% of cloud layers observed during the campaign were high-IAB, this likely has a non-negligible impact on results. Furthermore, contrarily to satellite data, IAOOS values are single-layer, not whole column, COD. The contribution of the first layer to total column COD is discussed in Sect. 2.2.5.3. It is therefore understandable that previous studies gave larger COD values. For example, [Curry *et al.* 1996] cites a range of $2 - 24$ with an average of 8 in summer. [Wang & Key 2004] also finds that monthly mean COD (from 1982 - 1999) varied from 4 to 6 in the AVHRR data over the Arctic Ocean. From ground-based lidar measurements at SHEBA, [Turner 2005] shows that 63% of clouds were single-layer with an optical depth < 6, and that optically thin clouds tended to be predominantly composed of ice.

Single-layer COD appears to vary seasonally (Fig. 2.4b). Excluding high-IAB cases, the monthly median COD appears to be almost constant from April to September, and largest in October - November (filled circles). However, this is in part because of the low noise levels in these months as compared to the summer. In October - December, i.e. the months with no sunlight, more than 50% of cloud layers were transparent to the lidar. This proportion is less than 10% in May to July. The COD can therefore be directly calculated for optically thick clouds from late September - December but not in other months. This is visible in Fig. 2.4b: in late September/October, there is a sudden apparition of directly-calculated COD values (open circles) greater than 2. The IAB method, which is an alternative to the direct method of calculating COD when the signal is fully attenuated by the cloud, is mainly suited to optically thin clouds (Fig. 2.4, grey crosses). This creates bias between summer months, for which the COD calculation is limited by noise levels to optically thin clouds, and October - December, during which higher COD values can be calculated.

To overcome this problem, the COD of high-IAB cloud layers was set to 2. This value was chosen as it is the 95th percentile of CODs calculated for low-IAB layers, and high-IAB cloud layers are as a group expected to have higher COD than low-IAB layers. The monthly median COD was then calculated including these high-IAB cases (Fig. 2.4, filled squares). This correction is not quantitatively robust as the value of 2 is arbitrarily chosen, not calculated. However, it accounts for the fact that high-IAB cloud layers exist, and are expected to have higher COD than low-IAB cloud layers, in the calculation of the median. This is helpful for examining the seasonal trend, which otherwise is biased by the presence of noise.

It creates a significant difference in June and July, the months in which the percentage of high-IAB cloud layers is the highest. With this correction, the median monthly COD exhibits two peaks (June and October) and a minima in April. The October peak is however still the annual maximum, and does not appear to be strongly impacted by the inclusion of high-IAB cloud layers. Previous satellite measurements have exhibited a pattern of higher COD in spring and autumn, for instance May and October for the AVHRR data [Wang & Key 2004] over the Arctic Ocean. The IAOOS dataset exhibits this October peak in single-layer COD. Another peak in June appears possible, although the IAOOS measurements are very uncertain in this month.

2.2.5 Cloud impact on surface temperatures and radiative balance

2.2.5.1 Impact of clouds on surface temperatures during IAOOS

Month	Number of profiles	Cloud fraction (%)	Median temperature (°C)		
			Cloudy	Cloudless	Δ
Apr	94	59	-17.7	-21.2	3.5
May	359	88	-9.9	-13.6	3.7
Jun	330	92	-1.5	-1.5	0
Jul	342	85	-0.1	-0.5	0.4
Aug	205	85	-0.9	-1.1	0.2
Sep	251	89	- 3.7	-6	2.3
Oct	98	92	-6.6	-14.6	8.
Nov	54	56	-16.7	-25	8.4
Dec	44	32	-27.9	-28.5	0.6

Table 2.3: Monthly median temperature for cloudy and cloudless profiles from April to December over the whole IAOOS period. Cloudy profiles contain at least one cloud with a base underneath 2 km. Cloudless profiles contain no clouds, or (very rarely) higher level clouds. Δ is the difference between cloudy and cloudless profile median temperatures.

IAOOS lidar profiles can be split into two groups: "cloudy" profiles containing at least one low cloud with a base < 2 km and "cloudless" profiles which contain either no cloud, or higher level clouds. Note that less than 2% of all clouds had a base higher than 2 km (Sect. 2.2.4.2). The temperatures measured by the buoy meteorological station during each lidar profile acquisition can be compared to estimate the effect of the presence of low clouds on surface temperatures.

The 2 m temperature distributions of cloudy and cloudless profiles differ significantly in October-November and April (Table 2.3). The Mann-Whitney test p-value is less than 0.05 (< 0.001 for November) and the common language effect size is more than 70% ($> 80\%$ for October and November). For all of these these months, the 2 m temperature is much lower for cloudless than for cloudy profiles. Indeed, the difference between the medians is of 8°C for the autumn months and around $4-7$°C in the spring (Table 2.3). This difference is probably not due solely to radiative processes, as cloudy situations in the Arctic winter are also associated with the passage of storms, which bring warm, moist air with them. However, as seen in Sect. 2.2.4.3, IAOOS-measured CODs are larger in October/November than April. Since emissivity increases with optical depth, this supports a larger surface warming in autumn than in spring. The months with the lowest median temperature difference between cloudy and cloudless profiles are June, July and August. In fact, the temperature distributions are statistically indistinguishable in these months from the relatively few measurements we have access to here. In particular, there is no month in which cloudless profiles are warmer than cloudy profiles, even though clouds are known to exert negative radiative forcing from late June to early July.

As noted before, clouds are naturally not the only factor impacting surface temperatures or even the downwards longwave radiative flux. Large-scale circulation is also important: for example, high geopotential at 200 hPa is linked to a warming of the troposphere through subsidence, which increases the longwave radiative flux received at the surface [Ding *et al.* 2017]. It is therefore important to check that cloudy and cloudless lidar profiles do not sample different surface pressures. The IAOOS buoys were equipped with barometers as well as temperature sensors. It appears that surface pressures for cloudy and cloudless profiles are not different at a statistically significant level, with the exception of August and November. In both of these months, the lidar profiles that contain clouds appear to coincide with markedly higher surface pressures than those that don't contain clouds (+12 hPa, Mann-Whitney test p-values < 0.005). As surface temperatures in the two groups differ strongly in November but not in August, however, surface pressure does not appear to be a confounding factor for surface temperature and cloud occurrence.

In the following sections, we look at the summer surface radiative balance in order to gain a better understanding of the mechanisms behind this seasonal variation in temperature difference between cloudy and cloudless profiles. First, the link between the net surface longwave flux and the presence of clouds is investigated (Sect. 2.2.5.2) from compared N-ICE and IAOOS measurements. Then, the influence of other factors such as solar zenith angle, temperature and COD on downwards shortwave and longwave fluxes during the N-ICE2015 April to June period is explored (Sect. 2.2.5.3). Lastly, the discussion of the net cloud radiative forcing at the surface is extended to the months of July and August using a simple parametrisation (Sect. 2.2.5.4).

2.2.5.2 Influence of the presence of clouds on the surface net longwave radiative flux

Identification of two summer longwave radiative modes from IAOOS and N-ICE data The 2 m temperature difference between cloudy and cloudless autumn/winter profiles exposed in Sect. 2.2.5.1 is consistent with previous studies. Indeed, it is now well attested that the Arctic climate exhibits two distinct states during the winter, which are distinguished through the surface net longwave flux (netLW) values. The bimodality of netLW was first observed during the SHEBA measurement campaign over the January-February 1998 period [Stramler *et al.* 2011] and has since been confirmed Arctic-wide by satellite observations [Cesana *et al.* 2012]. The "radiatively clear" mode (netLW < -30 W m^{-2}) is associated with strong radiative cooling, high pressures and low temperatures. Clouds may be present but are optically thin and mainly composed of ice. The "opaquely cloudy" mode is characterised by low pressures and relatively higher temperatures, and often associated with so-called "moisture and temperature intrusions" from the midlatitudes [Woods *et al.* 2013]. Clouds are then liquid or mixed-

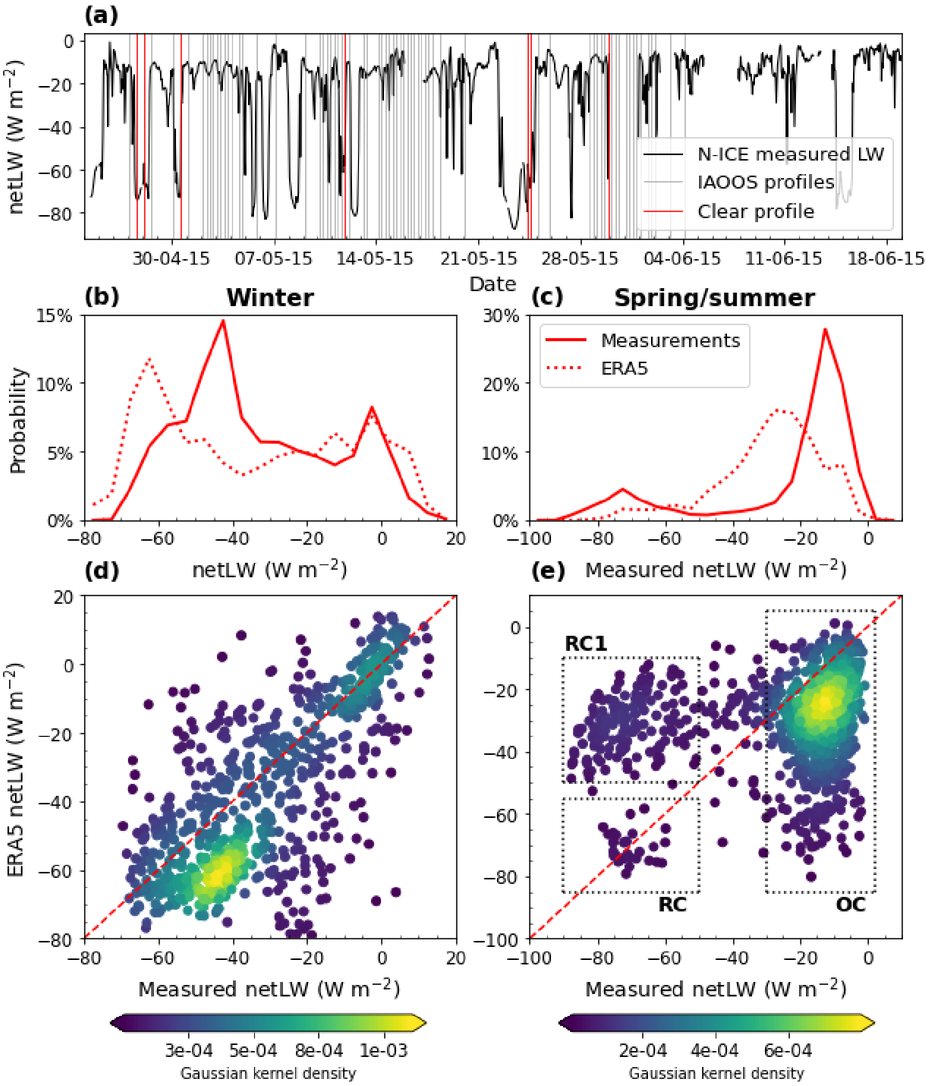

Figure 2.5: Panel a: time series of surface net longwave measurements during the N-ICE field experiment (second period, April-June 2015). The vertical lines indicate the time of IAOOS lidar profiles, with red lines corresponding to cloudless profiles. Panels b and c: histogram of the measured (filled line) and ERA5 (dashed line) net longwave flux during the N-ICE winter (b) and spring/summer (c) campaign periods. Panels d and e: hourly ERA5 vs measured net longwave in during the N-ICE winter (d) and spring/summer (e) campaign periods, with red dashed line indicating the 1:1 line. The colour corresponds to point density as calculated by a Gaussian kernel. For panel (e), three zones have been outlined. Zone "OC" contains points belonging to the opaquely cloudy mode of the measured netLW distribution. Zones "RC1" and "RC2" contain points belonging the radiatively clear mode of the distribution in April and May (RC1) and June (RC2).

phase, and optically thick. These intrusions are one of the main drivers of interannual variability of netLW, with a contribution of about 40% [Woods *et al.* 2013].

Here, we used radiative flux data from the N-ICE field campaign (second period, April - June 2015) to complement the IAOOS lidar observations [Hudson *et al.* 2016]. Measurements from the first period (January to March 2015) of N-ICE have already been shown to confirm the wintertime bimodality of the netLW distribution [Graham *et al.* 2017]. This result is replicated in Fig. 2.5b. A more striking point is that the netLW distribution is also bimodal in spring to early summer (Fig. 2.5c). During this period, netLW values range from -90 to 0 W m^{-2}. The most predominant netLW mode, containing around 80% of data points, is centered around -11 W m^{-2}, while the other is centered around -72 W m^{-2}. As a IAOOS buoy drifted near the main ice camp during April-June 2015, the IAOOS profiles were used to determine whether the sky was cloudless or cloudy at a given moment. The comparison with netLW measurements is represented in Fig. 2.5a. Low netLW values (< -60 W m^{-2}) are associated with IAOOS profiles that are cloudless at least up to ≈ 5 km, which is the maximum range of the lidar. Meanwhile, profiles containing at least one low level cloud (grey lines) corresponded to netLW values larger than -20 W m^{-2}.

This shows that the observed low netLW mode corresponds to a cloudless state and the high netLW mode to a cloudy state. By analogy with the previously established winter radiative states, we name the spring/summer low-netLW mode "radiatively clear" and the high-netLW mode "opaquely cloudy". However, these two modes differ from their winter analogues in several ways. Firstly, the netLW mode values are lower than in the winter. Indeed, both the downwards and upwards components of the longwave flux (LWd and LWu) increase from winter to summer. However, LWu increases more than LWd in both modes, causing a shift to lower netLW values. Secondly, the opaquely cloudy mode is much more frequent in spring/summer than in the winter, representing a large majority of cases. This is coherent with the fact that cloud frequency is much higher in spring/summer than in winter, with a transition in April (Sect. 2.2.4.1). Thirdly, the difference between the two states is ≈ 60 W m^{-2}, much larger than in the winter. This implies that clouds have a larger longwave warming effect in the spring/summer than in the winter, probably linked to larger liquid contents and higher cloud temperatures in this season.

Representation of the two modes in the ERA5 reanalyses The two atmospheric winter states (radiatively clear and opaquely cloudy) are not well reproduced by models [Cesana *et al.* 2012, Pithan & Mauritsen 2014, Graham *et al.* 2017]. In fact, it has been suggested that representing the bimodality of the netLW, pressure and temperature distributions in the wintertime is a key quality criterion for models. ERA-Interim and its successor, ERA5, are among those that partially achieve this [Graham *et al.* 2017]. This is visible in Fig. 2.5d. The opaquely cloudy state lies on the 1:1 line and is therefore well represented. However, the radiatively clear netLW values are underestimated by about 15 W m^{-2}. This is mainly due to an error in the upwards component of the longwave flux. Indeed, ERA5 overestimates the clear mode 2 m temperature by about 5 K; its measured value is $T_{meas} = -32°C$ [Graham *et al.* 2017], while the ERA5 clear mode temperature is $T_{ERA5} = -27°C$. This leads to an error on the longwave upwards flux at the surface (LWu) of:

$$\begin{aligned}\Delta(\text{LWu}) &= 4\varepsilon\sigma \cdot (T_{ERA5} - T_{meas}) \cdot (T_{meas} + 273.15)^3 \\ &\approx 15.6 \text{ W m}^{-2}\end{aligned} \tag{2.5}$$

with ε the surface emissivity, which is assumed to be 0.99 [Walden *et al.* 2017]. The result of Eq. (2.5) is in line with the observed netLW error. It should be noted that this overestimation of near-surface temperatures in clear, stable winter conditions, leading to an underestimation of netLW, is a feature shared by the six reanalyses evaluated by [Graham *et al.* 2019] using the N-ICE campaign data.

In the spring/summer period, [Graham *et al.* 2019] further notes that ERA5 is the least biased of the six evaluated reanalyses with regards to netLW, but has the worst correlation coefficient ($R = 0.15$). Indeed, we find that ERA5 fails to represent the two spring/summer netLW modes. The ERA5 netLW distribution is not bimodal (Fig. 2.5c) and does not align with the measurements (Fig. 2.5e). Three zones have been outlined on figure 2.5e to aid with the following discussion of ERA5 spring/summer netLW error. Zone OC corresponds to measured opaquely cloudy values over all spring/summer. The opaquely cloudy mode is somewhat reproduced by ERA5 (yellow dots denoting a peak in the calculated gaussian kernel density), although its values are underestimated by 11 W m^{-2} on average. The two other boxes correspond to measured radiatively clear values from April/May (RC1) and June (RC2) respectively. June values are well reproduced by ERA5. However, ERA5 vastly overestimates radiatively clear netLW in April and May: there is a 40 W m^{-2} difference with measurements in these month (Fig. 2.5e, RC1).

The difference in ERA5 netLW values between radiatively clear April/May (RC1) and June (RC2) points is due to the downwards component of the longwave flux (LWd). ERA5 LWd is fairly close to measured values in RC2, but is overestimated by ≈ 53 W m^{-2} in RC1. This is partly compensated by a 14 W m^{-2} error on LWu in April/May, similar to what is observed during the winter. Ultimately, the overestimation of LWd in RC1 is due to a faulty representation of cloud fraction in April/May. The ERA5 mean low cloud cover in RC1 is 0.96, even though measurements indicate a radiatively clear, and therefore cloudless, situation. On the other hand, mean low cloud cover in RC2 is 0.06: ERA5 has correctly identified that the sky was cloudless.

In conclusion ERA5 overestimated low cloud cover in April and May, but not June, leading to the observed errors in netLW. More investigation is required as to the ultimate source of this error.

2.2.5.3 Variability of cloud impacts on the downwards radiative fluxes during N-ICE2015

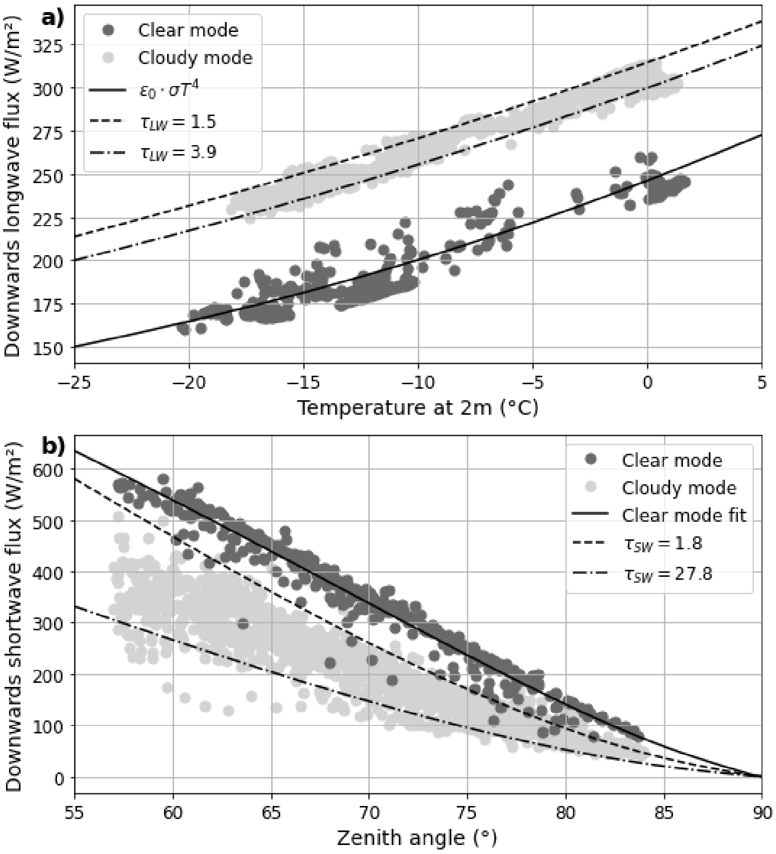

Figure 2.6: Panel a: longwave downwards radiative flux with near-surface (2 m) temperature as measured during the spring/summer period of the N-ICE field campaign. Dark grey points correspond to values for which netLW < -50 W m^{-2} ("radiatively clear" mode) while for light grey points netLW > -20 W m^{-2} ("opaquely cloudy" mode). The filled line correspond to the results of a simple parametrisation of LWd (Eq. (2.6)) in the absence of clouds, while the dashed lines represent the results of the parametrisation for $\tau_{LW} = 1.5$ and $\tau_{LW} = 4.1$. Panel b: same, for shortwave downwards radiative flux vs solar zenith angle. The dashed lines are the results of Eq. (2.7) for $\tau_{SW} = 1.7$ and $\tau_{SW} = 28.2$. For both panels, points are 30-minute averages of measurements.

In the Arctic summer, clouds impact the surface radiative budget in two competing ways: they have a longwave warming effect and a shortwave cooling effect. In Sect. 2.2.5.2, the N-ICE2015 April-June netLW distribution was shown to be bimodal, with the first mode corresponding to the presence of clouds in the IAOOS profiles and the second to their absence. However, other factors than the absence or presence of clouds may impact the surface radiative fluxes, both shortwave and longwave. In this section, the influence of variables such as the solar zenith angle, COD and surface temperature on the downwards fluxes (both longwave and shortwave) from the N-ICE2015 April-June period is explored and parametrisations of these fluxes are introduced.

The longwave effect depends on cloud temperature and phase. Warm, liquid-containing clouds are optically thicker and have much more radiative impact than cold, ice-containing clouds [Shupe & Intrieri 2003]. This is most likely the reason behind the greater difference between netLW modes observed in the spring/summer ($\approx$ 60 W m^{-2}) N-ICE measurement period as compared to the winter ($\approx$ 40 W m^{-2}). The shortwave radiative forcing depends on cloud characteristics as optically thick clouds have higher albedos. It also depends on the solar zenith angle θ and, to a lesser extent, the surface albedo α, due to reflections between the bright surface and the clouds [Shupe & Intrieri 2003].

As shown in Sect. 2.2.5.2, netLW values can be used to discriminate between "radiatively clear" and "opaquely cloudy" instants. The downwards longwave (LWd) and shortwave (SWd) flux components in these two modes are then compared in order to evaluate the impact of clouds on the surface. We will use the following simple estimates of LWd and SWd as a complement to the N-ICE flux measurements [Hudson *et al.* 2016].

- Schematically, the atmosphere can be seen as a cloud layer with emissivity ε_c overlying a cloudless atmospheric layer with emissivity ε_0. If both layers are emitting at temperature T_{2m}, this yields the following expression for LWd:

  $$\text{LWd} = [\varepsilon_0 + \varepsilon_c(1 - \varepsilon_0)] \cdot \sigma \cdot T_{2m}^4 \tag{2.6}$$

  The cloud emissivity can simply be expressed as $\varepsilon_c = 1 - e^{-\tau_{LW}}$ with τ_{LW} the longwave COD. Several simple parametrisations exist for ε_0; here, we choose $\varepsilon_0 = 0.83 - 0.18 \cdot 10^{-0.067 e_0}$, with e_0 the near surface water vapour pressure, which was fitted from summer data at Sodankylä, Finland [Niemelä *et al.* 2001a]. This shows good correspondence to the N-ICE clear mode data (Fig. 2.6a). In fact, equation (2.6) corresponds to a model introduced by [Schmetz *et al.* 1986] under two simplifying assumptions. First, that the cloud cover is equal to 1, which is reasonable in the cloudy mode. Second, that the cloud base and two-meter temperatures are approximately equal. This is justified by cross-comparison of the N-ICE (second period) radiosonde data with the IAOOS lidar profiles: the overwhelming majority of lowest layer clouds have a base beneath 120 m and the median difference between surface and 100 m temperature in the radiosonde profiles is only 1.3°C (with 90% of values falling in the range 0.6 – 2°C).

- SWd can be calculated from the downwards shortwave flux in the absence of clouds F_0 and the cloud correction or cloud broadband transmittance factor T_c:

$$\mathrm{SWd} = \mathrm{F}_0(\theta) \cdot T_c(\theta, \tau_{SW}, \alpha) \tag{2.7}$$

> F_0 depends on atmospheric gas and aerosol content and is usually parametrised to fit to local data [Reno *et al.* 2012, Kambezidis *et al.* 2017]. Here, the fit to N-ICE clear mode data is shown on Fig. 2.6b (filled black line). T_c has been modeled in numerous ways, the simplest depending solely on cloud cover [Niemelä *et al.* 2001b], while more complicated expressions have been derived from the output of radiative transfer models. Here we used the parametrisation of Fitzpatrick [Fitzpatrick *et al.* 2003], which assumes a cloud cover of 1 and depends on the solar zenith angle θ, the surface albedo α and the shortwave COD τ_{SW}. We chose to use a fixed value of $\alpha = 0.8$, as the measured albedo over the N-ICE second period varied from $0.75 - 0.84$ and the model performs poorly for albedos above 0.83 [Fitzpatrick *et al.* 2003].

Downwards longwave radiative flux increased with near-surface temperature T_{2m} and downwards shortwave flux decreased with θ in both radiatively clear and opaquely cloudy modes during the N-ICE April-June measurement period (Fig. 2.6). This evolution is well reproduced by Eqs. 2.6 and 2.7. Furthermore, there is a marked difference in downwards flux between points identified as radiatively clear and opaquely cloudy for both the longwave and shortwave components. In accordance with a cloud longwave warming effect, radiatively clear LWd values are uniformly lower than the opaquely cloudy values for each T_{2m} (Fig. 2.6a). As netLW is the quantity used to discriminate between clear and cloudy points, this is expected. On the other hand, radiatively clear SWd values are higher than opaquely cloudy SWd values for each θ (Fig. 2.6b). This corresponds to the shortwave albedo effect, i.e. clouds reflect solar radiation back to space. The magnitude of this shortwave cloud albedo effect is variable, even for a fixed solar zenith angle. As a first order approximation, this variation is due to the cloud optical properties as the albedo varied little over the measurement period. Equation (2.7) reproduces the spread of observed values for τ_{SW} between 1.7 to 28.2, a range which is coherent with total column COD values from previous studies (Sect. 2.2.4.3). In contrast, the longwave warming effect (i.e., the difference between the dashed/dotted and solid lines in Fig. 2.6a) varies little either as a factor of T_{2m} or τ_{LW}, and remains close to 60 W m^{-2}.

COD variations therefore have a non-negligible impact on the surface radiative balance. For $\theta = 60$, for example, there is an approximately 200 W m^{-2} difference in SWd between the optically thinnest and thickest clouds. This translates into a total shortwave cloud forcing that ranges between -20 to -60 W m^{-2}, assuming an albedo of 0.8 (typical of the N-ICE campaign April-June period). This range is significant when it is contrasted to the typical longwave forcing of ≈ 60 W m^{-2}: even for $\theta = 60$, only the optically thickest clouds could contribute to cool the surface during the April-June N-ICE2015 campaign period. Most clouds continued to warm the surface. This is explored in more depth in Sect. 2.2.5.4.

2.2.5.4 Beyond N-ICE2015: estimating the summer cloud net radiative forcing at the surface

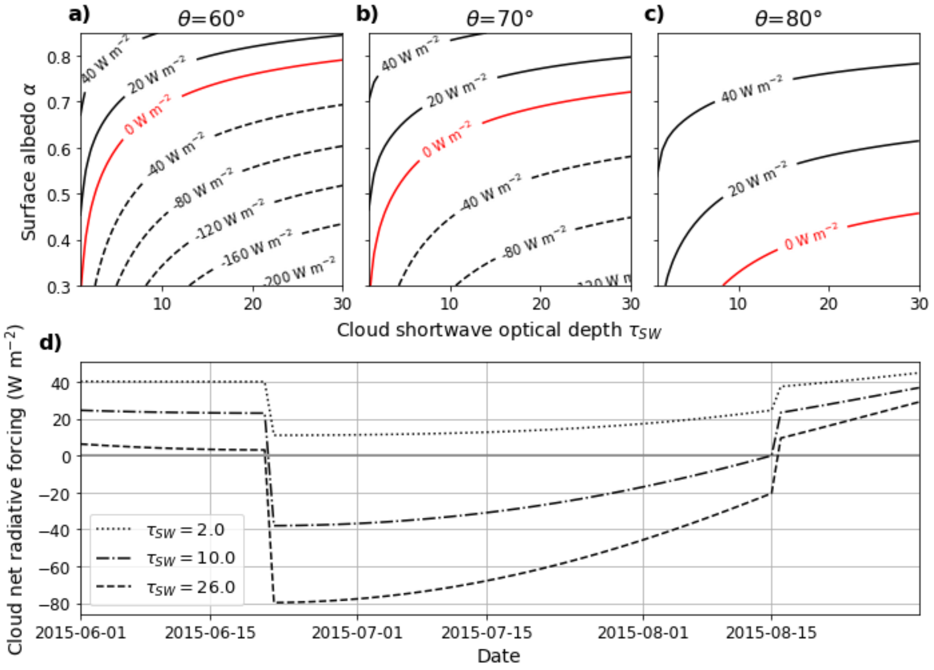

Figure 2.7: Panels a-c: iso-contours of net surface radiative forcing as a function of albedo and cloud shortwave optical depth for three different solar zenith angles (Eq. 2.8). Dashed black lines correspond to negative iso-contours, solid black lines to positive iso-contours, and red lines to the 0 W m^{-2} iso-contour. Panel d: Calculated evolution of the net surface cloud radiative forcing, for three different CODs (dotted line: $\tau_{SW} = 2$; dash-dotted line: $\tau_{SW} = 10$; dashed line: $\tau_{SW} = 26$), over the 2015 summer period. The summer variation of the albedo is constructed based on values from the NCAR Climate System Model [Weatherly *et al.* 1998], and the solar zenith angle values are daily averages at 82°N, 14°W (approximate position of the N-ICE ice camp).

The parametrisations introduced in Sect. 2.2.5.3 appear to work well when confronted with N-ICE radiative flux data: for CODs between 1.8 and 27.8, Eq. 2.7 reproduces the observed spread of downwards shortwave flux values at each zenith angle (Fig. 2.6). They can therefore be used to study the cloud net radiative forcing at the surface (netCF) and its dependence on solar zenith angle, albedo, and cloud optical depth. netCF is calculated according to the following equations:

$$\begin{aligned} \mathrm{CF}_{SW} &= (1-\alpha)\cdot \mathrm{F}_0(\theta)\cdot (T_c(\theta,\tau_{SW},\alpha)-1) \\ \mathrm{CF}_{LW} &\simeq 60\ \mathrm{W\ m^{-2}} \\ \mathrm{netCF} &= \mathrm{CF}_{SW}+\mathrm{CF}_{LW} \end{aligned} \tag{2.8}$$

with CF$_{SW}$ the cloud shortwave radiative forcing and CF$_{LW}$ the cloud longwave radiative forcing. These are counted as positive if they contribute to warm the surface, and negative if they contribute to cool it. In practice, CF$_{LW}$ is positive and CF$_{SW}$ is negative. Because CF$_{LW}$ appears to depend little on surface temperature (Sect. 2.2.5.3), it will be considered constant. T_c and F_0 are the cloud broadband shortwave transmission and the clear-sky downwards shortwave radiative flux respectively, which are calculated as in Sect. 2.2.5.3.

The output of Eq. 2.8 is shown in Fig. 2.7a-c for varying values of the surface albedo α and the cloud shortwave optical depth τ_{SW} for zenith angle values $\theta = 60°$, 70° and 80°. For each angle, the evolution is the same: netCF increases with α and decreases with τ_{SW}. Since CF$_{LW}$ is considered to be constant, this is a shortwave effect. Optically thick clouds reflect more shortwave radiation than optically thin clouds, and the magnitude of this shortwave radiative cooling is larger over low-albedo surfaces. Indeed, since high-albedo sea ice reflects most of the incoming radiation, clouds have a lower absolute impact on the radiative balance over these surfaces. The solar zenith angle affects netCF in a similar fashion. For given values of α and τ_{SW}, netCF increases with θ. The red line in Fig. 2.7a-c represents the 0 W m^{-2} iso-contour, and therefore delimits the regions of the (τ_{SW},α) plane in which clouds have a total net radiative cooling or warming effect. The higher the solar zenith angle, the smaller the region of net radiative cooling.

Equation 2.8 can also be used to estimate a summer cycle of netCF beyond the end of the N-ICE campaign period. In order to do that, values of θ and α must be chosen. While θ is easily calculated for a given date and location (here 82°N, 14°W, which is the approximate position of the N-ICE ice camp), α must be parametrised. We chose the four-level parametrisation for multiyear sea-ice used in the NCAR Climate System Model [Weatherly *et al.* 1998], which has been shown to agree well with SHEBA data [Perovich 2002]. In this model, cold snow is considered to have an albedo of 0.82, melting snow of 0.75, melting ice 0.5 and cold ice of 0.65. The transition between different surface types is naturally dependent on the specific location and year, but an approximate cycle can be constructed. Here the surface is set to be melting snow up to 21 June, melting ice from 21 June to 15 August, and cold ice from 15 August onwards. Indeed, the measured albedo was 0.74 (corresponding to melting snow) at the end of the N-ICE2015 campaign, i.e. on the 19 June 2015.

The results of this calculation are shown in Fig. 2.7d. Up to the 21 June 2015, only the optically thickest clouds ($\tau_{SW} = 26$) have a netCF which approaches zero, while optically thin clouds still contribute to warm the surface. This is in accordance to the N-ICE2015 measurements (Sect. 2.2.5.3). As the surface transitions from melting snow to melting ice on the 21 June, the netCF increases abruptly. This shows the important impact of α on the net cloud radiative forcing. However, τ_{SW} is almost as large a source of variability. The netCF for optically thin clouds ($\tau_{SW} = 2$) remains positive, i.e. they continue to warm the surface, while optically thick clouds ($\tau_{LW} = 26$) have a strong net surface cooling effect of -80 W m^{-2}. The netCF increases with the θ, and netCF values become positive for all τ_{SW} values with the surface transition to cold ice on the 15 August.

This approximate calculation of summer netCF exhibits negative values from the end of June to early August. This is coherent with the previous studies in the central Arctic Ocean, which showed that clouds exerted a cooling effect (i.e. negative radiative forcing) on the surface from the end of June to July [Shupe *et al.* 2006]. It is also coherent with the observation that during IAOOS, surface temperatures were lower in the absence of clouds for spring and autumn months, but not during the summer. However, netCF in these months also appears to depend strongly both on the surface and cloud type. Optically thin clouds may continue to warm the surface throughout the summer while thick, liquid water clouds will have a strong surface cooling effect. In considering the effect of clouds on the surface radiative balance during the summer, it is therefore important to have an accurate estimation of COD and surface albedo. This strong variability in summer netCF may also contribute to explain that the 2 m temperature of cloudless profiles during IAOOS was not different at statistically significant level from that of cloudy profiles in June, July and August (Sect 2.2.5.1). Indeed, if summer netCF over the central Arctic Ocean were uniformly negative, for all clouds, the surface should be observed to be colder in the presence than in the absence of clouds.

2.2.6 Conclusions

The IAOOS field campaign (2014 - 2019) consisted in the deployment of instrumented buoys in the Arctic sea ice. In this study, the whole IAOOS lidar dataset was treated and analysed. This included correcting for window frost as outlined in [Mariage 2015] and deconvoluting the signal to reduce the effects of receiver saturation in bright conditions. An algorithm was implemented to detect cloud layers and calculate their optical depth, either directly when applicable or through the IAB by assuming a constant lidar ratio. Surface radiative flux data from the N-ICE campaign, during which four IAOOS buoys were deployed, and from ERA5 reanalyses, was also exploited.

The low number of profiles in some months causes some uncertainty on specific monthly cloud properties. However, the results show statistically significant differences in cloud cover and optical and geometrical properties of clouds between the summer and April, November and December. Low cloud cover (i.e., with a base beneath 2 km) is found to be 76% averaged over all months of the campaign. Monthly cloud frequency is minimum in April and November/December and over 85% from May - October, with two small maxima in June and October. First-layer clouds are geometrically thickest in October, and thinnest in the summer. This is likely linked to moisture intrusions from the Atlantic in early autumn. Lastly, first-layer cloud bases are found to be extremely low in all seasons: under 120 m in a vast majority of cases.

The IAOOS lidar detects multiple cloud layers at much lower rates than other instruments, because the first cloud layer usually dampens the signal completely. Total cloud optical and geometrical thicknesses from previous campaigns and satellite data are much larger than those measured by IAOOS, especially in the summer when multilayered clouds are known to be most common. The single-layer COD as measured by IAOOS is highest in October.

The surface impact of Arctic clouds is also seasonally variable. In October and November, clouds warm the surface: 2 m temperatures associated with cloudless profiles are up to 8 K colder than those associated with profiles containing at least one low cloud. However, there is no statistically significant difference in surface temperatures between cloudless and cloudy profiles in the summer.

Data from the IAOOS lidar deployed during the N-ICE campaign allowed us to identify two modes in the N-ICE measured netLW distribution in late spring/summer. The "radiatively clear" netLW mode, centered around -72 W m^{-2}, is associated with cloudless IAOOS lidar profiles, while the "opaquely cloudy" mode is centered around -11 W m^{-2} and is linked to cloudy lidar profiles. These are analogous to the well-known winter radiative modes, except that the opaquely cloudy mode is much more prevalent (over 80%) and that the two modes have a 60 W m^{-2} difference, compared to 40 W m^{-2} in the winter. Clouds exert a larger longwave warming in the summer than in the winter, probably linked to the higher proportion of liquid water in clouds. Clouds in the spring/summer also have a shortwave cooling effect. This is shown to depend not only on solar zenith angle and albedo, but also strongly on COD.

During the N-ICE2015 April to June period clouds were observed exert a positive radiative forcing on the surface, with the cloud shortwave albedo effect cancelling out its longwave warming effect only for very large optical depths at zenith angles $> 60°$. Over the full central Arctic Ocean summer cycle, it is estimated that optically thick clouds cause a negative radiative forcing of -80 W m^{-2} but that optically thin clouds continue to have a warming effect. It is therefore important to have a good estimation of whole-column COD in order to calculate the radiative effect of clouds on the surface. The compensation of the cloud longwave warming effect by the shortwave cooling effect explains that there is no clear difference in near-surface temperature between IAOOS cloudless and cloudy profiles during the summer months.

The measured surface radiative fluxes were compared to the output of the ERA5 reanalyses. ERA5 does not accurately reproduce the observed bimodality of the spring/summer netLW distribution. Indeed, it does not correctly identify cloudless periods during April and May (but not June). This issue should be investigated.

Over the period 2014-2019, the IAOOS buoys have delivered 1777 lidar profiles. Despite technical difficulties with both the lidar and the data analysis, this campaign has offered a medium-term 3-season picture of the Arctic lower troposphere above 82°N from ground-based measurement, which is an important complement to satellite data. These results help to broaden our understanding of the Arctic low cloud cover and its impacts on the surface. However, more measurements would be needed to further characterise Arctic clouds. In particular, combined radiometer-radar-lidar measurements would be crucial to allow the study of radiative impacts to be generalised to late summer and especially autumn, when clouds are optically thick and frequent.

2.2.7 Appendix

2.2.7.1 Determination of a 90% confidence interval for cloud occurrence frequency

Let us suppose that the event "presence of a cloud with base $<$ 2 km in a given IAOOS lidar profile" follows a Bernoulli distribution of parameter p, with p the cloud frequency. This seems plausible given that the profiles are at least 6 hours apart, and the events can therefore be considered to be independent. We aim to determine a confidence interval for p based on:

1. Previous studies of clouds in the Arctic, which have shown that p is generally around 0.7;
2. The IAOOS measurements: for each month m, there are n_m profiles of which k_m contain at least one cloud with base $<$ 2 km.

From 1), an "a priori" probability distribution for p can be conceived: for example $\mathcal{N}(0.7, 0.15)$, normalised over the $[0, 1]$ interval. Using the Bayes formula, the IAOOS measurements can then be taken into account to calculate an updated $\Pr(p|\text{meas})$ for each month m:

$$\Pr(p|\text{meas}) = \frac{\Pr(\text{meas}|p) \cdot \Pr(p)}{\Pr(\text{meas})} \tag{2.9}$$

with

$$\begin{aligned} \Pr(\text{meas}|p) &= \mathcal{B}(k_m; n_m, p) \\ \Pr(\text{meas}) &= \sum_{p_i} \Pr(\text{meas}|p_i) \cdot \Pr(p_i) \\ &= \sum_{p_i} \mathcal{B}(k_m; n_m, p_i) \cdot \Pr(p_i) \end{aligned} \tag{2.10}$$

where p_i are the possible values of the parameter p, and $\mathcal{B}(k; n, p) = \binom{n}{k} p^k (1 - p)^{n-k}$ is the binomial probability mass function with parameters n and p. The results of this calculation are shown in Fig. 2.8, which synthesises the results of Sect. 2.2.4.1: the probability distributions for the months of May - October show significant overlap. However, they do not overlap at all with the November, December, March and April distributions, although these are much wider because of the lower number of measurements.

The 5th and 95th percentiles of the distribution of p determined through Eq. 2.9 can then be calculated to yield a 90% confidence interval.

2.2.7.2 Contribution of the lowest cloud layer to the total column COD

Cloud optical depths measured by the IAOOS lidar correspond only to the lowest cloud layer, and not to the total column (Sect. 2.2.4.3). Here we attempt to evaluate the contribution of this lowest layer to the total column COD. This would allow

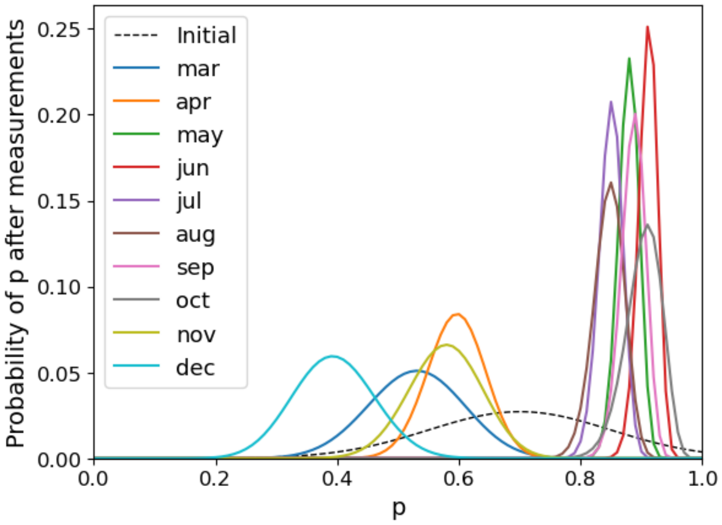

Figure 2.8: Pr(p|meas) as a function of the cloud occurrence frequency p. The dashed black line corresponds to the a priori distribution. The updated distributions for each month (Eq. 2.9) are shown in colour.

Optical depth	5th percentile	Median	95th percentile
τ_{LW}	1.4	2	2.5
τ_{SW}	1.2	7.8	20.2
τ_{808}	0.5	0.9	1.9

Table 2.4: Statistical range (5th, 50th and 95th percentiles) of three different estimations of optical depth: τ_{LW} (from the downwards longwave flux), τ_{SW} (from the downwards shortwave flux) and τ_{808} (calculated from the IAOOS lidar profiles). For a robust comparison, τ_{LW} and τ_{SW} values considered here are interpolated on the IAOOS profile times. The percentiles are therefore established over 54 data points which correspond to the 54 IAOOS profiles. Individual errors carried over from measurement errors on LWd, SWd and T_{2m} are in the range $8-19\%$ (mean 11%) for τ_{SW}, and $8-23\%$ (mean 13%) for τ_{LW}.

better comparison of IAOOS CODs to existing satellite statistics. Furthermore, as seen in Sect. 2.2.5.3, total column shortwave COD is the quantity that most impacts the surface radiative balance. Equations 2.6 and 2.7 were inverted using a numerical equation solver to calculate the broadband shortwave and longwave CODs τ_{SW} and τ_{LW} from the N-ICE SWd, LWd and temperature values at the time of the IAOOS profiles. Albedo was taken as fixed and equal to 0.8 in this calculation. The measurement errors of SWd, LWd and temperature (Sect. 2.2.2.2) as well as the choice of a fixed albedo create an error on τ_{SW} and τ_{LW} which is estimated through a Monte Carlo method. This error is no more than 19% for τ_{SW} and 23% for τ_{LW} (Table 2.4).

In analysing the results, it must be taken into account that the longwave optical depth of any single cloud layer is smaller than its shortwave optical depth. The shortwave-to-longwave optical depth ratio depends on the microphysical properties of clouds (droplet phase, radius) and a precise determination would require the help of radiative transfer models. In this manner, [Garnier *et al.* 2015] calculates $\tau_{532nm}/\tau_{12\mu m} \approx 1.8$ for ice particles with an effective diameter between 5 and 60 microns. We use this value as a rule of thumb to enable comparison between τ_{LW}, τ_{SW} and the IAOOS optical depths τ_{808}.

90% of τ_{LW} values obtained in this manner fall in the $1.4 - 2.5$ range (Table 2.4). It must be noted that these τ_{LW} values do not capture the optical depth of the whole column. Indeed, because cloud emissivity ε_c tends to 1 exponentially, high τ_{LW} values are likely to be underestimated. Instead, this τ_{LW} must be seen as the part of the cloud cover whose emitted radiation reaches the surface. Inverting Eq. (2.7) yields shortwave optical depths between 1.2 and 20.2, with a median of 7.8. This range shows much higher values than that of τ_{LW}, even when accounting for the longwave-to-shortwave ratio. This is because the shortwave radiative flux is impacted by the whole cloud column, and not only the first few layers. IAOOS optical depths (τ_{808} in Table 2.4) are much lower than both τ_{LW} and τ_{SW}, with 90% of values between 0.5 and 1.9. In fact, the ratio $\tau_{808}/(1.8 \cdot \tau_{LW})$ has a median value of 0.22 (range $0.15 - 0.43$), while τ_{808}/τ_{SW} has a median value of 0.11 (range $0.03 - 0.68$). This means that first-layer clouds measured by IAOOS contribute around a quarter of the optical depth of clouds which have a longwave radiative impact on the surface, and 11% of the total cloud column.

While this value is low, it is coherent with the observation that SHEBA-measured total cloud thicknesses are up to 7 times higher than the IAOOS-measured first layer thickness (Sect. 2.2.4.2). Regardless of potential underestimations in IAOOS measurements, it strongly suggests that further cloud layers must be present at higher altitudes. Some of these, possibly cirrus clouds, would then have a shortwave but no longwave impact on the surface. Furthermore, visual inspection of the relative humidity (RH) and temperature profiles obtained through radiosonde measurements during N-ICE supports the idea that the IAOOS lidar correctly identifies the first cloud layer and probably misses higher cloud layers. Indeed, strong temperature inversion and diminution of RH are most often present at the lidar-identified cloud top. Further inversions and high RH values are often present, marking higher altitude cloud layers that are invisible to the lidar.

Chapter 3

Modulation of boundary layer stability and the surface energy budget by a local flow in central Alaska

---

Contents

3.1 Introduction

The second boundary-layer process studied in this thesis was SBIs. Long-lasting very stable conditions are a typical feature of polar winters, especially in the absence of clouds when the surface undergoes very strong radiative cooling. They are thought to contribute to Arctic amplification through the lapse-rate feedback. Another important aspect is their role in limiting atmospheric pollutant dispersion, which impacts Arctic communities. The ALPACA (Alaskan Layered Pollution And Chemical Analysis) campaign was planned to take place in Fairbanks, Alaska, from January–March 2021, with the participation of researchers from several French laboratories (among which the LATMOS). Its aim was to increase understanding of the development of wintertime pollution episodes: one part of this was the study of aerosol chemistry in cold, dark conditions while the other was the development of SBIs. Indeed, while temperature inversions are very frequent in Fairbanks [Bourne *et al.* 2010, Mayfield & Fochesatto 2013], they are also impacted by topographically channelled flows from connecting valleys [Fochesatto *et al.* 2013].

In order to prepare for ALPACA 2021, a pre-campaign took place in November–December 2019, in which I was able to participate. A 4-component radiometer and sonic anemometer were installed in an open, snow covered field while a lidar was set up in a shelter downtown. Measurements showed that the field site was under a specific wind regime which impacted the development of SBIs. The results were written as a paper which has been accepted in Boundary-Layer Meteorology. They are reproduced below.

3.2 Article

3.2.1 Introduction

Surface-based temperature inversions (SBIs) are a ubiquitous feature of the Arctic winter atmosphere, occurring as often as 70% of the time [Serreze *et al.* 1992, Bradley *et al.* 1992]. The study of these inversions is motivated in two ways. Firstly, they have important implications for air pollution in the Arctic. SBIs “trap" emissions from surface sources by imposing a shallow stratified layer close to the surface. Combined with low horizontal winds, this can lead to an accumulation of pollutants near the surface. For example, SBIs in Fairbanks, Alaska, are such that the temperature at 30 m is often 5 K higher than that at 2 m [Mayfield & Fochesatto 2013, Malingowski *et al.* 2014]. Fairbanks is therefore regularly classified as a non-attainment zone according to the PM2.5 National Ambient Air Quality Standard. Secondly, strong SBIs have been shown to confine the warming caused by climate change to the surface, while increased vertical mixing is linked to a dilution of the warming to higher altitudes [Bintanja *et al.* 2011]. This mechanism, termed “lapse-rate feedback", is a major contributor to Arctic Amplification [Pithan & Mauritsen 2014].

In the Arctic winter, the presence of snow-covered, emissive surfaces combined with the absence of incoming shortwave radiation leads to longwave radiative cooling becoming the main contributor to the surface energy budget. This effect is particularly large in anticyclonic conditions when clouds and surface winds are inhibited. In these conditions, a “very stable" regime often develops: turbulent heat fluxes are small and the lowest layer of the atmosphere cools rapidly, creating an SBI. As surface stability increases, vertical motions are suppressed. This then further reduces the turbulent heat flux. The ensuing positive feedback loop leads to a sharply increasing temperature profile, and the surface being thermally and mechanically decoupled from the overlying atmosphere [van Hooijdonk *et al.* 2015].

Alternatively, the boundary layer may operate in a “weakly stable" regime, in which the wind speed is sufficient to maintain a turbulent sensible heat flux which compensates the radiative cooling. These two regimes have been shown to be separated by a critical wind speed, termed “minimum wind speed for sustainable turbulence" [van de Wiel *et al.* 2012, van Hooijdonk *et al.* 2015]. A conceptual model of the surface-based temperature inversion under these two regimes was developed by [van de Wiel *et al.* 2017], and the existence of these two distinct regimes separated by a sharp transition was confirmed at Cabauw in the Netherlands [van Hooijdonk *et al.* 2015] and Dome C in Antarctica [Vignon *et al.* 2017].

SBIs are common and have long been studied in Fairbanks, the main population centre of Interior Alaska. By calculating monthly averages of radiosonde profiles from 1957–2008, [Bourne *et al.* 2010] found that SBIs occurred 60 – 80 % of the time in November and December, with a temperature difference across the inversion of 7.5 – 10.5 °C and an inversion depth of 500–550 meters. [Mayfield & Fochesatto 2013], on the other hand, differentiated between SBIs and elevated inversions, taking into account the frequent layering of individual radiosonde profiles. They found an SBI occurrence frequency of 64 % for the months of October–March from 2000–2009. Fairbanks is situated in the Tanana Valley and is surrounded on three sides by hills. These hills are separated by valleys, one of which (Goldstream) connects directly to the Tanana Valley on the north-west edge of Fairbanks (Fig. 3.1). This topography means that a local scale circulation, termed “shallow cold flow" (SCF), is often observed under anticyclonic synoptic conditions [Fochesatto *et al.* 2013].

While the development of strong SBIs is often driven by high pressures and clear-skies, they can also potentially be impacted by the local circulations which develop when anticyclonic conditions prevail in the region. Previous studies have explored the variability of nocturnal stability conditions caused by local flows in the mid-latitudes. [Martínez *et al.* 2010], for example, made use of an extensive dataset to link the flow in a wide basin in Northern Spain to the nocturnal cooling rate. [Mahrt *et al.* 2001], using data from CASES-99 (in Leon, Kansas), showed that strongly stable conditions develop at the beginning of the night in a shallow gully, accompanied by a very weak, shallow flow. Influences of regional scale meteorology and valley flows on SBIs have also been reported in the Alps [Rotach *et al.* 2004, Haid *et al.* 2021]. In the present paper, the impact of a local flow on SBIs and the surface energy balance at a high-latitude site in the winter is explored, with the ensuing specificity that stability is developed over the course of a few days rather than hours if the synoptic conditions remain favourable.

First, the 2019 pre-ALPACA (Alaskan Layered Pollution And Chemical Analysis) winter campaign in Fairbanks, Alaska and the resulting dataset are presented (Sect. 3.2.2). Second, a case study is presented in which a strong SBI was caused by favourable synoptic conditions at the Fairbanks International Airport, but not at the campaign measurement site some 3.5 km away. This indicates that there is local variability in the development of SBIs in Fairbanks (Sect. 3.2.3). The entire campaign data is then exploited to show that a local flow which is enhanced under clear-sky conditions exists at the measurement site, and to explore its impact on the surface-based temperature inversions and energy balance (Sect. 3.2.4). Conclusions are presented in Sect. 3.2.5.

3.2.2 Pre-ALPACA winter 2019 campaign

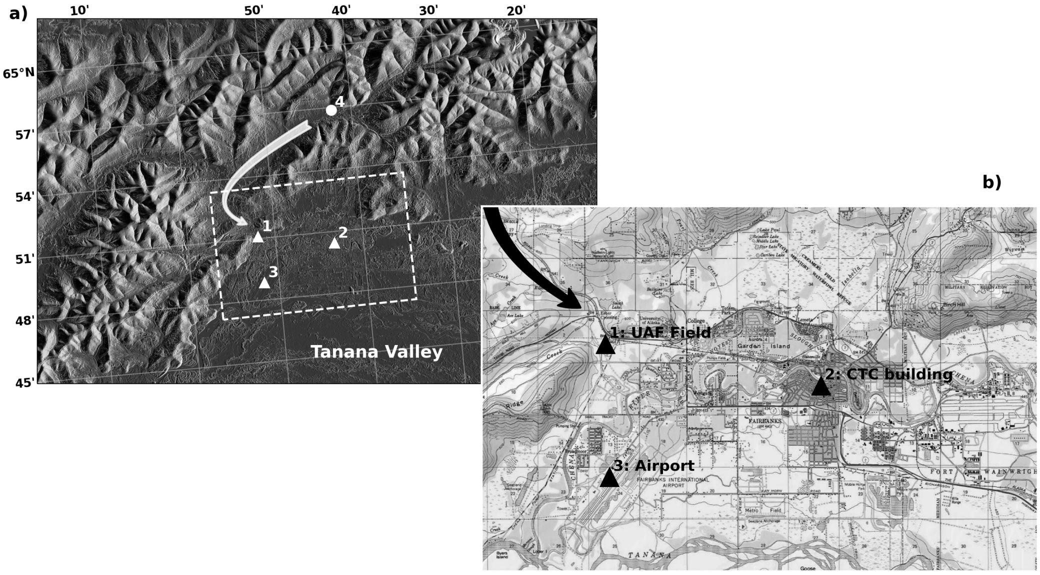

Figure 3.1: Map of the measurement sites during the pre-ALPACA 2019 campaign, within the wider topographic context of the Fairbanks basin (panel a), and zoomed to show the city layout (panel b). The triangles 1–3 mark the main measurement sites: the UAF field site, the CTC building, and the Fairbanks airport respectively. The dot marked “4" indicates the location of the Goldstream valley. The white and black arrows show the proposed direction of a local flow from the Goldstream to the Tanana valley, where Fairbanks is located. The elevation data used to generate panel a is the Alaska IFSAR 5 m DEM dataset, downloaded from the USGS National Map website: `https://apps.nationalmap.gov/downloader/`. Panel b is an USGS Topo map, taken from the TopoView website: `https://ngmdb.usgs.gov/topoview/viewer/`.

3.2.2.1 Campaign goals and theoretical framework

A pre-ALPACA winter campaign took place in November–December 2019, in Fairbanks (Alaska). It was led by researchers from six French laboratories and the University of Alaska Fairbanks (UAF) and acted as a “preliminary run" to the main ALPACA campaign, planned to take place in January–February 2022 as part of the PACES (air Pollution in the Arctic: Climate, Environment and Societies) International Global Atmospheric Chemistry (IGAC) and International Arctic Science Committee (IASC) initiative [Simpson *et al.* 2019].

The aim of the pre-ALPACA campaign was to gain some first insights into the processes influencing the formation of wintertime pollution episodes. Fairbanks regularly encounters high aerosol loadings in winter due to high local emissions and stable weather conditions. As well as investigating aerosol formation in dark, cold winter conditions, another crucial goal of the campaign was to study processes influencing the formation of strongly stable surface conditions, as they impact the dispersion of surface emissions. This paper presents an analysis of the energy fluxes and meteorological measurements from the 2019 campaign with a focus on the life cycle of surface-based temperature inversions.

First, the theoretical framework, notations and conventions used for the energy budget are introduced. The studied system consists of the air layer below the instrument height (2 m) and a snow layer of depth $d_s \approx 33 \pm 1$ cm (measurement made with a ruler). The snow is conceptually separated into two layers. The top one (1), of height h_s, is thin and is assumed to have the same temperature as the snow–air interface (i.e. the surface). It therefore stores energy by warming and cooling rapidly. The bottom one (2) is assumed to vary more slowly in temperature, and is therefore considered to be an “insulation" layer which transfers the heat conductively from the ground to the surface. This is supported by [Helgason & Pomeroy 2012], where it was shown that the first few centimetres of the snowpack follow very similar temperature evolutions to the surface, while the bottom of the snowpack varies much more slowly in temperature. This approach allows us to take into account the energy storage in the snowpack. The energy budget applied to the air layer and snow layer (1) is therefore:

$$S_a + S_s = R_n + H + G + L + \delta E. \tag{3.1}$$

The left hand side of this equation is the heat storage in the air (S_a) and first snow layers (S_s). Because of the very low heat capacity of air, around 1005 J K^{-1} kg^{-1}, S_a is negligible compare to S_s and its calculation will not be detailed. The heat storage in the first snow layer can be calculated as:

$$S_s = \rho_s C_{p,s} h_s \frac{\partial T_S}{\partial t}, \tag{3.2}$$

with $\rho_s = 290$ kg m^{-3} is the snow density, $C_{p,s} = 2$ J K^{-1} g^{-1} the specific heat of snow and T_S the temperature of the snow-air interface which is measured by the radiometer (Eq. 3.4). The snow density and specific heat capacity values are taken from [Helgason & Pomeroy 2012]. The value of h_s is chosen to be 5 ± 5 cm by visual inspection of the snow temperature measurements of [Helgason & Pomeroy 2012].

The different heat fluxes are on the right hand side of Eq. 3.1. They are all considered to be positive when the heat is transferred towards the surface, either from the atmosphere or the ground below. The first two terms, R_n and H, are the radiative and turbulent sensible heat fluxes. Their measurement during the course of the campaign is detailed in Sect. 3.2.2.2.

G is the ground heat flux, i.e. the conductive heat flux from the ground through the snow layer (2). It was estimated using the following equation:

$$G = -\frac{\lambda_s}{d_s - h_s}(T_S - T_G), \tag{3.3}$$

with λ_s the snow conductivity and T_G the ground temperature. T_G is considered to be constant = -2 ± 2 °C throughout our period of study. This is supported by the fact that soil temperature at the the Ameriflux US-Uaf site [Ueyama *et al.* 2018], only around 1.5 km away from the UAF field, varied only from -2.5 to -0.5 °C from 26 November to 14 December 2019. The snow conductivity is considered to be $\lambda_s = 0.2 \pm 0.05$ W m^{-1} K^{-1}, which was the value chosen by [Helgason & Pomeroy 2012] in quite similar conditions. The error in G was calculated by propagating the errors on λ_s, d_s, h_s and the temperatures.

L is the turbulent latent heat flux, which was not measured but was assumed to be negligible, at least over the case study (4–8 December) period. This is supported by the low specific humidity and very cold weather, which lead to low saturation specific humidity. For example, on 6 December 0000 UTC, the radiosonde at the Fairbanks airport measured a specific humidity of 4.7×10^{-4} kg kg^{-1} while the surface saturation specific humidity was 3.9×10^{-4} kg kg^{-1}.

The last term, δE, is the residual or SEB closure. It encompasses a number of terms which are usually considered to be negligible, such as advection (horizontal and vertical) and the horizontal divergence of the turbulent sensible heat flux. In Sect. 3.2.4.4, δE is calculated as the difference between the heat storage and the other fluxes. The error on δE is calculated by propagating the flux errors.

3.2.2.2 Instruments and data treatment

The instrument characteristics and the main aspects of the data treatment are outlined below. The main instruments for measuring the energy fluxes and relevant physical quantities included a sonic anemometer and a radiometer, which were installed in a flat and homogeneous field at the UAF Campus Farm. A microlidar was installed in downtown Fairbanks near the CTC (Community & Technical College) building (Fig. 2.1). They were all installed and running from 26 November to 12 December (Table 3.1). Most statistics hereafter will be derived from this complete measurement period. The period from 4 to 8 December is of particular interest because synoptic conditions were favourable to the development of a surface-based temperature inversion (Sect. 3.2.3).

Sonic anemometer The sonic anemometer measured the temperature and the three components of the wind field at 10 Hz frequency. A separate thermometer deployed on the mast at approximately 2 m height during the 4–10 December period was used to calibrate the sonic temperature.

The 10 Hz measurements are despiked [Vickers & Mahrt 1997], and then averaged over fixed 30 min intervals to obtain mean horizontal wind speed U, wind direction θ and temperature T_{2m}. The turbulent sensible heat flux is also calculated over these intervals, following a procedure which is detailed in [Fochesatto *et al.* 2013].

Quality control of the sonic anemometer measurements of H is ensured by applying the stationarity test of [Foken & Wichura 1996]. We then exclude from further analysis 30 min periods which are shown to be non-stationary. This represents 48 % of the measurement periods. The relative error on H is estimated at 30 % following [Weill *et al.* 2012].

Instrument	**Operation date**	**Location**	**Measured variables**
Campbell Scientific 107 Temp. probe	04/12/2019–10/12/2019	UAF Field	temperature @ 2 m
RMYoung 81000 3D sonic anemometer	26/11/2019–15/12/2019 (**)	UAF Field	wind speed @ 2 m
			wind direction @ 2 m
			turbulent sensible heat flux
Kipp & Zonen CNR4 net radiometer	25/11/2019–12/12/2019	UAF Field	↑ ↓ longwave radiative flux
			↑ ↓ shortwave radiative flux
CIMEL CE376 micro-lidar (MILAN)	24/11/2019–13/12/2019	CTC building	cloud base
			cloud optical depth ($\lambda =$ 532 nm)
Radiosonde (*)	Daily at 0000 & 1200 UTC	Fairbanks airport	temperature profile
			wind speed & dir. profile

Table 3.1: Summary of the different instruments installed during the pre-ALPACA 2019 winter campaign and of the associated measured variables. (*) The radiosonde data was taken from the University of Wyoming website: http://weather.uwyo.edu/upperair/sounding.html. (**) The sonic anemometer was installed on 26 November but data from 26/11 to 30/11 was excluded due to acquisition issues.

Lidar MILAN is a micro-lidar produced by Cimel Electronique (CE376) which is specialized for the study of tropospheric clouds and aerosols. It operates at two wavelengths, one in the visible spectrum (green: 532 nm) and one in the near infra-red (808 nm), and measures polarization. Here, only the profiles at the 532 nm wavelength were analyzed. Indeed, the objective was the detection of clouds, for which one wavelength is sufficient. Furthermore, the green source was more powerful and offered a greater vertical range: greater than 10 km in night-time conditions, i.e. a majority of the time in Fairbanks in December. Acquired profiles are averaged over 10 minutes to reduce noise while keeping information on cloud cover variability. The exploitable measurements were limited to altitudes above 210 m. Cloud layer base and optical depth are obtained using the procedure detailed in [Maillard *et al.* 2021].

For each profile, the optical depth of all detected cloud layers are summed to yield a total optical depth value τ. The lowest layer base altitude B is also calculated. If no layer is present, then B is indicated as missing data. Both B and τ are then averaged over the three profiles which occur during each sonic anemometer 30-minute measurement period. A 30-minute measurement period is determined to be "clear" if $\overline{B} > 8$ km or $\overline{\tau} < 0.2$. This accounts for 29% of measurement periods. On the other hand, it is deemed to be "cloudy" if $\overline{B} < 500$ m or $\overline{\tau} > 0.8$. This occurs a further 42% of the time. Indeterminate cases make up the remaining 29% of measurement periods.

Radiometer The CNR4 Net Radiometer produced by Kipp & Zonen is composed of two pyranometers–pyrgeometer pairs, one nadir looking to measure the upwelling fluxes and one zenith looking to measure the downwelling fluxes. The pyranometers measure the radiation in the 300–2800 nm spectral range, while the spectral range of the pyrgeometers is 4.5–42 μm. The total net radiative flux R_n is equal to $LW_n + SW_n$, with LW_n the net longwave flux and SW_n the net shortwave flux, and is positive when heat is transferred to the ground.

The surface temperature T_S can also be calculated from the radiometer measurements:

$$T_S = \left(\frac{LW_u - (1-\varepsilon) LW_d}{\varepsilon \sigma_{\mathrm{SB}}} \right)^{1/4}, \tag{3.4}$$

with LW_u and LW_d the upwards and downwards longwave radiative fluxes measured by the radiometer, ε the snow emissivity and $\sigma_{\mathrm{SB}} = 5.67 \times 10^{-8}$ W m^{-2} K^{-4} the Stefan–Boltzmann constant. The snow emissivity is chosen equal to 0.99 in accordance with [Weill *et al.* 2012].

Measurements were made every minute and averaged over 30 min periods in order to match the turbulent flux measurements (Sect. 3.2.2.2). The error on R_n is estimated from the 30 min period standard deviations of the individual radiative flux components, with a minimum of 5 W m^{-2}.

3.2.2.3 Other available datasets

Radiosondes are launched twice a day, at 0000 and 1200 UTC at the Fairbanks International Airport (Fig. 2.1). The wind and temperature profiles from these radiosonde launches were retrieved from the University of Wyoming website (Table 3.1). The near surface temperature gradient is calculated from the first two levels of radiosonde data. The first level is at the surface, while the second level varied in altitude from 12 to 171 m (median: 22 m, mean: 43 m) over the course of the campaign.

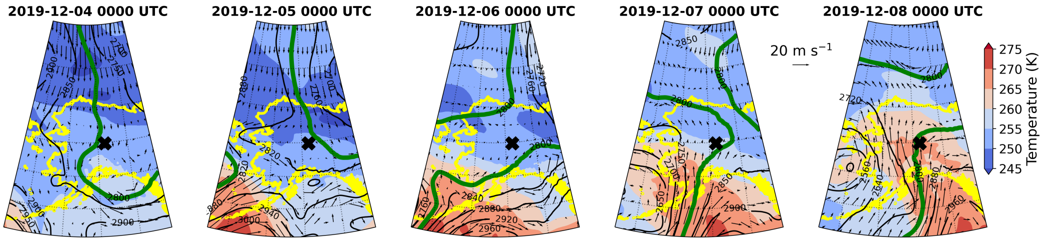

Figure 3.2: Maps of the ERA5 geopotential height (contours), winds (arrows) and temperature (colours) at 700 hPa from 4 Dec 2019 to 8 Dec 2019 at 0000 UTC. The wind and temperature scales are the same for each plot and are indicated on the right. The bold green line marks the 2800 m contour of geopotential height. The yellow line marks the Alaskan coastlines and the black cross indicates the location of Fairbanks

ERA5 is the latest reanalysis from the European Centre for Medium-Range Weather Forecast [Hersbach *et al.* 2020]. It provides hourly or four-times-daily estimates of many weather variables on a 0.25° × 0.25° grid and with 137 vertical pressure levels. Values of geopotential, temperature and winds at the 700 hPa level over Alaska are used to discuss the synoptic situation. Hourly estimates of surface level variables such as temperature and wind speeds are also provided. Timeseries of these variables at the nearest grid point to Fairbanks (64.75 °N, -147.75 °W) were extracted for comparison to the Field site measurements (Sect. 3.2.4.1).

3.2.3 Local variability in surface based inversion development: a case study

3.2.3.1 Evolution of a surface based inversion at Fairbanks airport

From 4–8 December 2019, the buildup, then breakup, of a surface-based temperature inversion at Fairbanks airport was observed. The evolution of the inversion is visible in the profiles obtained at the airport from radiosonde launches and can be divided into three phases.

- From 4 to 5 December 0000 UTC, an anticyclone was positioned over central Alaska (Fig. 3.2). High pressures and subsidence led the cloud layer to decrease in altitude from 3 km to less than 2 km (Fig. 3.3a) while the air column cooled

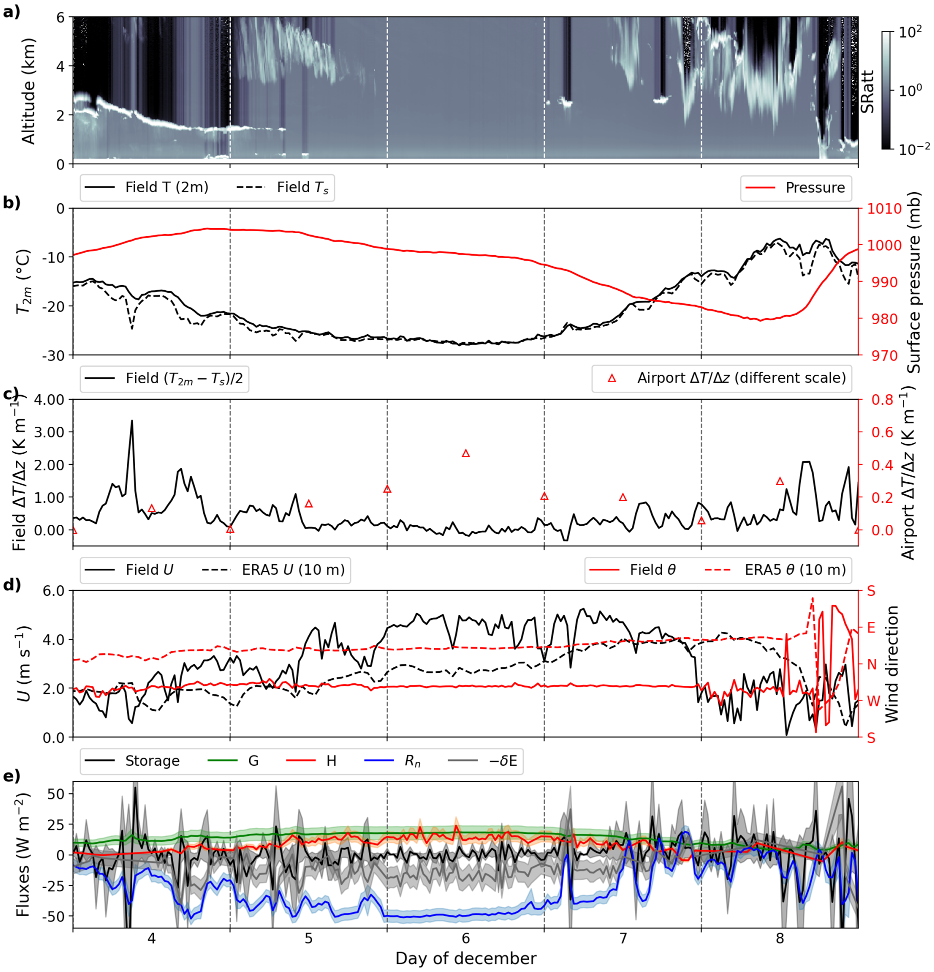

Figure 3.3: Timeseries of the measurements from 4–8 December 2019 at Fairbanks. Panel a: attenuated scattering ratio (SR_{att}) from the MILAN lidar. Panel b: 2 m temperature (continuous black) surface temperature (dashed black) and surface pressure (red) measured at the UAF Field. Panel c: near surface temperature gradient from the radiosonde measurements (right axis) and the field measurements (left axis). Note the different scales for both measurements. Panel d: continuous lines represent the wind speed U (black) and wind direction θ (red) measured by the sonic anemometer at the UAF Field. Dashed lines represent the same variables at 10 m from the ERA5 reanalysis. Panel e: measured and estimated terms of the surface energy budget (Eq. 3.1) at the Field site. Shown error bars correspond to the uncertainties which are estimated as in Sect. 3.2.2.2. For greater readability, the opposite of the residual ($-\delta E$) has been represented

as a whole (Fig. 3.4a). As is frequent in anticyclonic conditions, synoptic winds were weak and wind speeds close to the ground remained under 2 m s^{-1} (Fig. 3.4b).

- From 5–6 December 0000 UTC, clouds were absent and the surface net radiative flux was strongly negative (Fig. 3.3e). This led to the surface continuing to cool while the air above 80 m stayed at a near-constant temperature (around -20 °C), therefore creating a strong temperature gradient near the surface (Fig. 3.4c). This gradient was strongest around 1200 UTC on 6 December, when the surface temperature at the airport reached a minimum of -30 °C.

- From 7 December, a pressure dipole is installed over south Alaska and funnels warm air from the Gulf of Alaska to Interior Alaska (Fig. 3.2). Consequently, heat advection was positive over Fairbanks (from ERA5 reanalyses, not shown), wind speeds increased above 500 m altitude, and the whole column started to warm again. At the end of 7 December, clouds returned and the net radiative flux at the surface became positive again (Fig. 3.3a,e). The surface then began to warm rapidly (Fig. 3.4c). The surface inversion at Fairbanks airport was completely erased on 8 December 1200 UTC.

The observed evolution of the surface-based temperature inversion at the airport was therefore largely controlled by the synoptic conditions. Its development was triggered by anticyclonic, subsident conditions which favour strong radiative cooling at the surface, and it was destroyed by an east–west pressure dipole advecting warm air and clouds from the south.

3.2.3.2 Surface energy fluxes and temperature gradient at the Field site

The temperature gradient measured at the Field site did not follow the same evolution as the airport. Instead, $\Delta T = T_{2m} - T_S$ decreased from 4 December and remained low from 5–7 December (Fig. 3.3c). A direct comparison between the two measurements is complicated because while the Field ΔT is the difference between the air temperature at 2 m and the snow surface temperature, the radiosondes measure only the air temperature at the surface and at a second launch-dependent altitude. From 5–7 December this second altitude varied from 14 to 28 m (mean: 20 m). The airport $\Delta T/\Delta z$ therefore represents a more vertically-averaged gradient, which explains that it is smaller in magnitude than the Field $\Delta T/\Delta z$ (Fig. 3.3c). It is possible that the rather coarse radiosonde vertical resolution “hides" a neutral gradient layer in the first 2 m, similar to what is observed at the Field. However, this does not seem likely for two reasons. First, in the case of a radiatively driven SBI, such as the one occurring at the airport, the temperature gradient is typically strongest close to the ground. Second, the surface air temperature is around 3 °C colder at Fairbanks airport than at the Field. In any case, there is a markedly different trend between the small-scale Field and the more vertically-averaged Fairbanks airport temperature gradients, the former decreasing while the latter increases.

This ΔT trend at the Field site appears to be linked to the wind speed. In contrast to the airport, where the surface wind speed remained low close to the surface from 4–8 December, the Field wind speed increased from 3 December and was maximum from 5–7 December at the Field site, before collapsing on 8 December

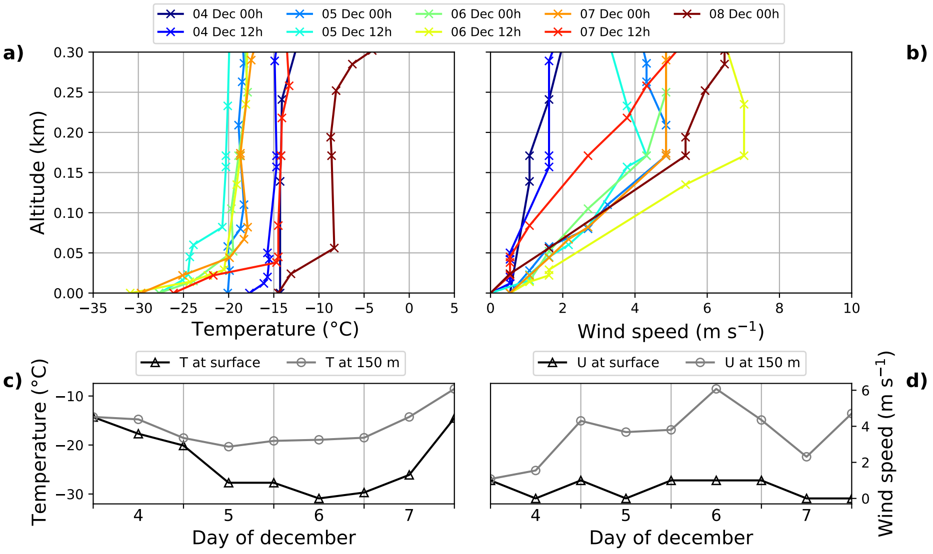

Figure 3.4: Radiosonde profiles of dry-bulb temperature (panel a) and wind speed (panel b) from the Fairbanks airport for the period from 4 December 0000 UTC to 8 December 0000 UTC. Panel c and d show the time evolution of the temperature and wind speed respectively, at the surface and at 150 m, as interpolated from the radiosonde data

(Fig. 3.3d). Physically, this is expected to have an impact on both H and ΔT, because increased wind shear leads to an increase in turbulent mixing. This in turn heightens H and tends to mechanically return the temperature profile to a neutral gradient.

Indeed, H increased and ΔT decreased in parallel to the increase in wind speed from 3 to 6 December (Fig. 3.5). The opposite evolution then took place from 7 to 8 December. Note that the fact that the turbulent sensible heat flux remained quite large on 7 December (Fig. 3.5) even though the surface ΔT was near zero implies that a temperature gradient persisting somewhere else in the air column was acting as a heat reservoir, perhaps affecting the surface through larger eddies [Mayfield & Fochesatto 2019]. If the whole column were near neutral (i.e. well mixed), the turbulent sensible heat flux would be expected to collapse.

The 4–8 December episode indicates that there are important local variations in the development of SBIs. While the airport exhibited a strong temperature gradient and low wind speeds directly linked to anticyclonic synoptic conditions, the Field site had higher wind speeds and very small ΔT. In the next section, it will be shown that these higher wind speeds were caused by a local flow which influences the SEB and consequently affects the development of surface-based temperature inversions at the Field site.

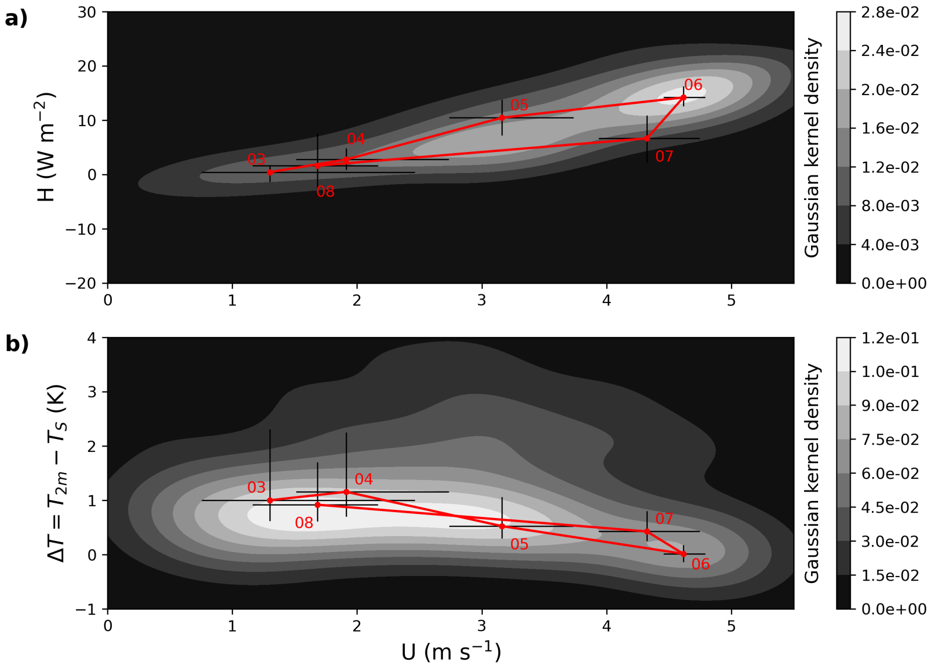

Figure 3.5: Panel a: turbulent sensible heat flux vs wind speed. The grey contours represent the Gaussian kernel density over the whole measurement period, i.e. lighter values denote greater point density. The red dots represent the median measurements for each day from 3 to 8 Dec (the date is labelled in red: the black horizontal and vertical bars represent 25th and 75th percentile). Panel b: the same, for ΔT as a function of wind speed

3.2.4 Impact of the local flow on the surface energy budget and temperature gradient

3.2.4.1 Characterisation of the local flow

The presence of a local flow with particular characteristics has already been attested at this site by [Fochesatto *et al.* 2013]. They considered that this was a flow from the Goldstream Valley to the North (Fig. 2.1a), and suggested that it could be either a drainage flow triggered by strong radiative cooling of the Goldstream valley slopes or a channelling of the larger-scale, northerly synoptic flow through the mountain valleys. They defined “shallow cold flow" (SCF) events as periods when the wind speed is greater than 1 m s^{-1}, the wind direction is north-westerly, and the winds are decoupled from the main meso-scale motion. During the pre-ALPACA campaign, a particular wind regime similar to the SCF was observed at the Field site at a height of 2 m. Its characteristics are outlined below.

Firstly, the wind direction at the Field site was largely north-westerly over the course of the campaign, with 50 % of values between 293° and 305°. This orientation indicates a flow coming from the Goldstream Valley (Fig. 2.1). This is in contrast to the ERA5 values at the nearest grid point, which are north-easterly (e.g., Fig. 3.3d). These are assumed to be representative of larger-scale flows, as ERA5 has a 0.25° resolution and is not able to capture a local circulation from the Goldstream valley. Furthermore, while the 64.75 °N, -147.75 °W model grid node is the closest to the Field site, it is further south in the Tanana valley and would likely not be impacted by a flow from the Goldstream Valley.

Secondly, this wind was enhanced under clear sky conditions. For periods identified as clear by the lidar (Sect 3.2.2.2), the median wind speed is 3.9 m s^{-1} and 90 % of wind directions are between 292 and 310°. On the other hand, for periods identified as cloudy, the median wind speed is 2.2 m s^{-1}, with a larger scatter in wind direction. The difference between wind speed distribution under clear and cloudy conditions is different at a statistically significant level: Mann-Whitney $U = 32189$, p-value $< 10^{-3}$ for sample sizes of 256 and 385 respectively [Mann & Whitney 1947b].

This wind regime is highlighted in the case study described in Sect. 3.2.4. Wind speeds at the Field site increased to more than 5 m s^{-1} under subsident, clear–sky conditions and the wind exhibited a consistent north-westerly direction. The orientation relative to the topography and the association with clear-sky periods suggests that this flow is a sort of drainage or topography-driven flow. However, we lacked the measurements necessary to establish either its origin or its spatial extent robustly. For this reason, it will be termed “Local Flow" (LF) to avoid conflating it with the SCF of [Fochesatto *et al.* 2013]. In Sect. 3.2.4.2, the impact of this LF on the surface energy balance at the Field site is explored.

3.2.4.2 Identification of two distinct modes in the surface energy budget

Previous studies have shown that the net longwave radiative flux at the surface is bimodal during the Arctic winter [Stramler *et al.* 2011, Graham *et al.* 2017]. The first mode is around -40 W m^{-2} and is associated with the absence of low level, high emissivity clouds, while the second mode is around 0 W m^{-2} and is associated with their presence. Here, individual 30 minute measurement periods are defined as “clear" or “cloudy" based on the lidar observations (Sect. 3.2.2.2). Net longwave flux measurements are distributed around -45 W m^{-2} during clear periods, and around -5 W m^{-2} during cloudy periods, in good agreement with previous high-latitude observations. Because SW_n is negligible during this period, this is also true of the net radiative flux (Fig. 3.6a). The overlap between the two modes is quite small, and the total distribution of R_n is bimodal.

The turbulent sensible heat flux depends on the wind speed (Sect. 3.2.3.2). Values of H are distributed around 0 W m^{-2} when the wind speed is less than 2 m s^{-1}. On the other hand, when the wind speed is greater than 3 m s^{-1}, H is distributed around 12 W m^{-2}. The spread is larger in this second mode, so that the overlap between the two is slightly larger than for the radiative fluxes (Fig. 3.6b). However, the two distributions are still different at a statistically significant level. The Mann-Whitney U-test [Mann & Whitney 1947b] yields a p-value $< 10^{-10}$ (the sample sizes

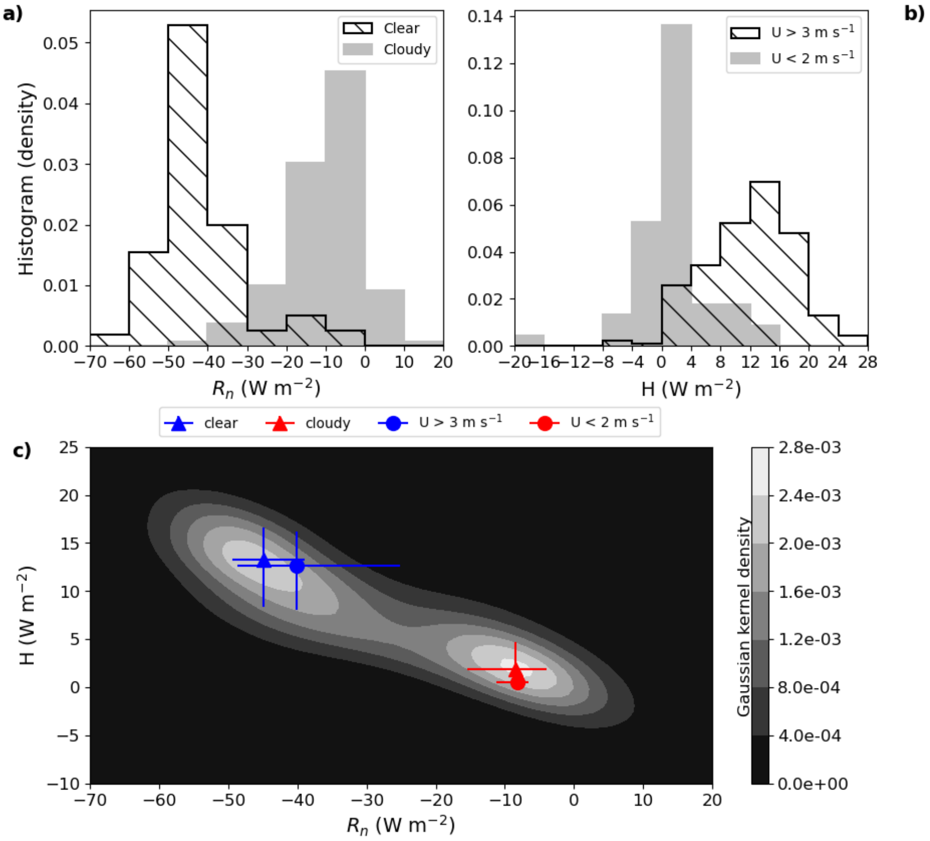

Figure 3.6: Top panels: histograms of (a) the net radiative flux (R_n) in the presence (grey) and absence of clouds (hatched black) and (b) the turbulent sensible heat flux in high (hatched black) and low (grey) wind speed conditions respectively. Panel c: the grey scale represents the calculated gaussian kernel point density in the (R_n, H) space. The symbols represent the median (R_n, H) pair for either clear (blue triangle) or cloudy (red triangle) conditions, and for wind speeds less than 2 m s^{-1} (red circles) or more than 3 m s^{-1} (blue circle). The errorbar corresponds to the 25th and 75th percentiles. These statistics were drawn from the entire campaign period

of the two distributions are 255 and 58 and the test statistic, U, is = 1039). These values are comparable in magnitude to those measured by [Fochesatto *et al.* 2013] at the same site in the absence and presence of the SCF.

These net radiative and turbulent sensible heat flux modes are linked (Fig. 3.6c). The Gaussian kernel density (grey field contours) of measurements during the pre-ALPACA campaign show that there are two modes in the (H, R_n) space. The first corresponds to $R_n \approx$ -5 W m^{-2} and $H \approx$ 0 W m^{-2} and the second corresponds to $R_n \approx$ -45 W m^{-2} and $H \approx$ 14 W m^{-2}. This reflects the observed association between clear skies and the presence of an enhanced LF (Sect. 3.2.4.1). Indeed, measurements that correspond to cloudy periods or low wind speeds are clustered in the first mode while measurements corresponding to clear instants or high wind speeds are clustered in the second mode (Fig. 3.6c). It should be noted that some measurement periods with U greater than 3 m s^{-1} also have a net radiative flux well within the cloudy mode, leading to the larger error bars associated with the blue circle (Fig. 3.6c). This is because while high wind speeds are generally associated with clear skies at the Field site, they sometimes persist throughout short periods of cloudiness - for example, on 7 December (Fig. 3.3c).

Schematically, the SEB at the Field site exhibits two preferred modes. The first, with near zero radiative and turbulent heat fluxes, is linked to cloudy skies and weak winds. The second, with very strongly negative radiative fluxes and high turbulent heat fluxes, is linked to clear skies and higher local wind speeds due to the presence of the LF. The conjunction of clear skies/low R_n and low wind speeds/low H occurs more rarely. The formation of a surface-based temperature inversion at the UAF field is therefore a balancing act. On the one hand, clear skies and high pressures create a large negative R_n, which is necessary for the surface to begin cooling. On the other, the same situation has the potential to strengthen the LF, which tends to destroy the inversion by increasing mixing due to stronger wind shear. This mechanism is explored in more detail in Sect. 3.2.4.3.

3.2.4.3 The local flow dampens the effect of strong radiative cooling

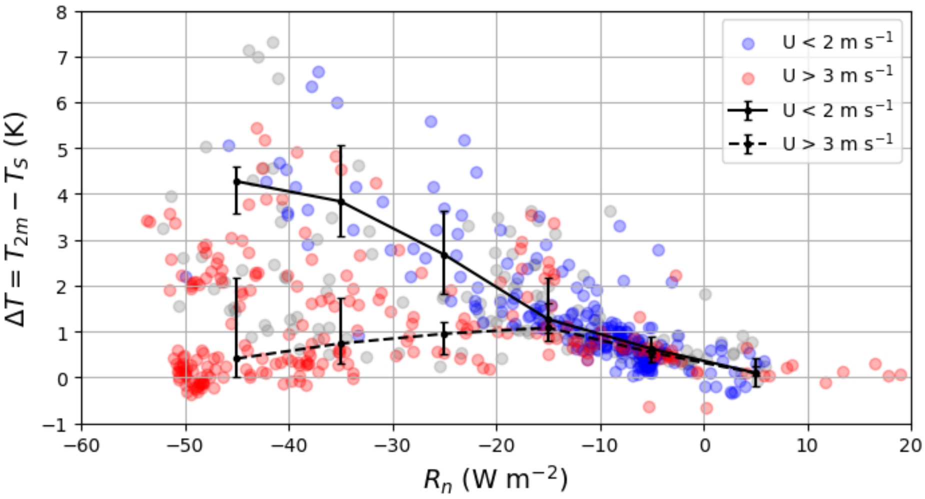

Figure 3.7: Surface temperature gradient (ΔT) as a function of the net radiative flux at the Field site. The two lines correspond to the medians for each 10 W m^{-2} bin, for wind speeds of less than 2 m s^{-1} (blue points) and more than 3 m s^{-1} (red points) respectively. Grey points correspond to U between 2 and 3 m s^{-1}. Error bars denote the 25th and 75th percentiles; these statistics were drawn from the entire campaign period

Recent studies have introduced the concept of a critical wind speed separating two distinct turbulence regimes, often termed “weakly" and “strongly" stable [Sun *et al.* 2012, Sun *et al.* 2016]. Here, the impact of the wind speed on the surface inversion response to strong radiative cooling is examined. For $R_n >$ -15 W m^{-2}, ΔT was observed to increase slowly with decreasing net radiative flux at the Field site (Fig. 3.7). The rate of increase is the same for all wind speeds, i.e. around -0.06 K W^{-1} m^2. However, for lower values of R_n, the effect of the net radiative heat flux on the surface-based temperature inversion strongly depends on the wind speed. For $U > 3$ m s^{-1}, ΔT is independent of R_n (the slope is 0.02 K W^{-1} m^2, but the decrease is non-significative in light of the error bars). This is coherent with the weakly stable regime. As the shear at these higher wind speeds generates enough turbulent sensible heat flux to make up for the radiative loss, ΔT is not sensitive to the value of R_n and remains close to zero. In other terms, the air from 0 to 2 m is well mixed. Note that the red outliers at $R_n > 10$ W m^{-2} correspond to 30 min measurement periods when short-lived clouds passed over the Field site on 7 December, leading to a temporary elevation of R_n at continued low ΔT. For U lower than 2 m s^{-1}, on the other hand, ΔT increases sharply with decreasing net radiative flux, at a rate of -0.11 K W^{-1} m^2. This is the expected evolution in the strongly stable regime. Indeed, this regime is radiatively driven: the turbulent sensible heat flux cannot compensate for the strongly negative radiative flux, and so the equilibrium ΔT will depend on the magnitude of the radiative imbalance.

The presence of the LF at the Field site therefore controls the response of the stability to strong radiative cooling conditions. Qualitatively, in clear sky conditions, the regime is strongly stable when U is under 2 m s^{-1} and weakly stable when U is over 3 m s^{-1}, with a critical wind speed in the 2–3 m s^{-1} interval. This represents a new finding in the Arctic context. At Dome C in the Antarctic, [Vignon *et al.* 2017] found a critical 10 m wind speed threshold between 5–7 m s^{-1}. Below, this value will be compared to theoretical predictions.

It has been shown that the critical wind speed depends on the surface radiative flux [van de Wiel *et al.* 2012]. This is because the shear necessary to create the sensible heat flux compensating a very large radiative deficit will be higher than if it is close to 0 W m^{-2}. To be more precise, the turbulent sensible heat flux must not compensate R_n, but its difference with G. [van Hooijdonk *et al.* 2015] derive the following expression for the critical wind speed:

$$U_{\min} = \left(\frac{27\alpha}{4}\right)^{1/3} \left\{ \frac{g}{\theta_0 \kappa^2} \frac{(|R_n| - |G|)}{\rho_a C_{p,a}} z \left[\ln\left(z/z_0\right)\right]^2 \right\}^{1/3}, \tag{3.5}$$

with α the stability parameter, $g = 9.81$ m s^{-2} the gravity acceleration, θ_0 the air potential temperature, $\kappa = 0.4$ the von Kármán constant, G the ground flux, and $z = 2$ m the altitude above the surface. The roughness length z_0 chosen here was 10^{-4} m, which is typical of relatively flat, snow-covered surfaces [Weill *et al.* 2012, Helgason & Pomeroy 2012]. Here, we consider values of $\theta_0 = 250$ K and $\alpha = 4$, inline with [van de Wiel *et al.* 2012].

Equation 3.5 shows that $U_{\min}$ increases monotonously with the heat demand at the surface, i.e. $|R_n| - |G|$. $U_{\min}$ is between 2 and 3 m s^{-1} for values of the heat demand at the surface between 8 and 25 W m^{-2}, which is the case for 46 % of the measurements where $R_n >$ -15 W m^{-2}. If the heat demand is between 25 and 40 W m^{-2}, then $U_{\min}$ is between 3 and 3.5 m s^{-1}. This corresponds to a further 43 % of measurements where the net radiative flux is less than -15 W m^{-2}. In total, 89 % of measurements with $R_n <$ -15 W m^{-2} would have a theoretical critical wind speed greater than 2 m s^{-1} according to Eq. 3.5.

These theoretical values of the critical wind speed are coherent with the observed behaviour illustrated in Fig. 3.7. For net radiative fluxes at the surface lower than -15 W m^{-2}, the theoretical critical wind speed is overwhelmingly over 2 m s^{-1}. This explains that wind speeds lower than 2 m s^{-1} at the Field site correspond to a strongly stable regime, where the near surface inversion increases sharply with decreasing net radiative flux at the surface. However, a significant fraction of the measurement periods have a theoretical critical wind speed greater than 3 m s^{-1}. Qualitatively, this fits with the large spread of values for $R_n <$ -30 W m^{-2} and $U >$ 3 m s^{-1} (red points) in Fig. 3.7. The criterion “U > 3 m s^{-1}" is not sufficient to guarantee that the wind speed is above the critical threshold, thus leading to the observed large number of outliers overlapping with blue points at $R_n <$ -30 W m^{-2}.

The use of Eq. 3.5 as a comparison to our data raises two issues. Firstly, it is obtained by supposing that Monin–Obukhov hypothesis holds true, and that the wind profile is logarithmic. These conditions might not to hold when the LF is occurring at the Field site, if it is a drainage flow with a wind maximum very close to the ground. Secondly, Eq. 3.5 implicitly supposes that there is no significant residual in the SEB. The magnitude of the residual and its potential link to advection is explored in Sect. 3.2.4.4.

3.2.4.4 Surface energy budget closure

Over the course of the campaign, the residual was found to have a median value of 13 W m^{-2}, with 90 % of values falling between -4 and 29 W m^{-2} (note that for reasons of readability, $-\delta E$ is represented on Fig. 3.3e). The residual is therefore largely positive, indicating a missing heat transfer from the atmosphere to the ground which is particularly large (median 19 W m^{-2}) during clear periods. In contrast, the median residual was only around 2 W m^{-2} for cloudy periods. This is because the ground and turbulent sensible heat fluxes cannot make up for the very strongly negative R_n of clear periods. In the following discussion the lack of closure in the case study period is examined in more detail. Figure 3.3e shows that the residual is almost as large as the ground and turbulent heat fluxes from 5 to 7 December (around 18 W m^{-2}), although the error bars are large.

This is not an unusual observation in an Arctic context. Similar values of the residual (18 W m^{-2}) were also obtained in comparable conditions (Arctic night) by [Helgason & Pomeroy 2012]. The dataset in their study was more complete as regards latent heat fluxes and ground heat fluxes and the residual was found to be outside of random measurement errors. Reviewing possible sources of systematic measurement errors, the authors concluded that non-turbulent exchanges of sensible heat between air and snow could be of importance given the strong correlation between the temperatures of near-surface air and snow. However, such an exchange of heat would not impact the energy balance of the system as defined in Sect. 3.2.2.1, since the top 5 cm of snow are already supposed to be in thermodynamic equilibrium with the air. Increasing h_s to 10 or even 20 cm has negligible impact on the residual during the case study, as the surface temperature changed little during this time. Another possibility evoked by [Helgason & Pomeroy 2012] is that a strong temperature gradient in the lowest meters would cause a turbulent sensible heat flux divergence between the surface and the measurement height, so that the measured H would not be representative of its surface value. This seems unlikely here as ΔT is close to 0 K over this period when the residual is highest.

Other possible sources of systematic error on the SEB include the presence of eddies with timescales larger than the 30 min period used for calculation of the turbulent sensible heat flux [Malhi *et al.* 2005, Mauder *et al.* 2020]. Indeed, the detrending method outlined in Sect. 3.2.2.1 acts as a high-pass filter with a cutoff at 30 min. Neglecting lower-frequency transport of sensible heat would lead to an underestimation of H, and therefore a lack of heat at the surface such as is observed here. However, visual inspection of the cospectra of vertical wind and temperature does not support this conclusion, with exchanges of heat appearing to be minimal at timescales greater than 30 minutes (not shown). The footprint of the eddy covariance measurement is another possible issue. [Fochesatto *et al.* 2013] compared measurements of H at the Field site obtained by a sonic anemometer and a large-aperture scintillometer (LAS) and found that the sonic anemometer captured around 75% of the flux measured by the LAS. Since the LAS measurement is an integral over an approximately 500 m line, this suggests that the representativeness of the sonic anemometer footprint might be an issue. However, correcting the ALPACA 2019 measurements to account for this effect only reduces the residual by around 5 W m^{-2}.

Lastly, we consider the possibility that the residual is due to advection, either vertical or horizontal. Previous studies have shown that vertical advection may cause important heat fluxes even for vertical wind speeds below the instrumental measurement capablities (a few cm s^{-1}) when the vertical temperature gradient is large [Nakamura & Mahrt 2006, Leuning *et al.* 2012], which is not the case during the case study. Therefore it is unlikely that vertical advection could explain the 18 W m^{-2} residual during this period. On the other hand, large residuals occurred in clear-sky conditions during the entire campaign, and clear sky conditions coincided with heightened horizontal wind speeds ($U > 3$ m s^{-1}).

The horizontal temperature gradient needed to explain the entire residual is calculated, following [Leuning *et al.* 2012]:

$$\frac{\partial T}{\partial x} = \frac{\delta E}{h_a \rho_a C_{p,a} U/2}, \tag{3.6}$$

with $h_a = 2$ m the altitude of the instruments, and U the horizontal wind speed.

[Leuning *et al.* 2012] use $U/2$ to approximate the mean wind speed in the layer between the surface and h_a. Using $U = 5$ m s^{-1} and $\delta E = 18$ W m^{-2}, Eq. 3.6 yields a horizontal temperature gradient of 3 K km^{-1}. This is unrealistically large. However, for the LF where the wind speed maximum might be close to the ground and the roughness length is small, the mean wind speed between 0 and h_a may be closer to U than $U/2$. In that case, the necessary horizontal temperature gradient to close the SEB would be only 1.5 K km^{-1}.

As there unfortunately were no along-flow wind and temperature measurements during the campaign, the true value of advection cannot be estimated.

3.2.5 Conclusions and perspectives

This paper analyzed observations from the pre-ALPACA 2019 winter campaign, which took place from 23 November to 12 December 2019 in Fairbanks, Alaska, and investigates the impact of a local flow on the surface energy balance and surface-based temperature inversion development.

First, a case study highlighting the studied phenomenon was introduced. In the days leading up to 5 December 2019, high synoptic caused subsidence in the upper levels of the troposphere, leading to the disappearance of clouds through adiabatic compression and largely negative (less than -50 W m^{-2}) net radiative fluxes in Fairbanks. A strong surface-based temperature inversion was observed to develop at the airport over this period, while surface level wind speeds remained low (under 2 m s^{-1}). At the Field measurement site, in contrast, the wind speed was seen to increase on 5 December to values greater than 5 m s^{-1}. The turbulent sensible heat flux increased in parallel, while the near surface temperature gradient ($\Delta T = T_{2m} - T_S$) decreased. On 6 December, the temperature gradient reached its maximum at the airport and its minimum at the Field site, suggesting that different processes are operating at the two measurement sites.

The whole campaign dataset was then analyzed. It was shown that a particular wind regime, termed Local Flow (LF), occurred at the Field measurement site. The LF was characterised by a consistent north–westerly wind direction, corresponding to the output of the Goldstream Valley. It was greatly enhanced under clear sky conditions: wind speeds were significantly higher at the Field site in the absence of clouds than in their presence.

The association of clear skies and increased wind speeds was significant because wind speed is an important factor in determining the stability regime. When the wind speed was less than 2 m s^{-1}, the surface ΔT increased strongly with decreasing net radiative flux, leading to a radiatively controlled strongly stable regime for R_n less than -30 W m^{-2}. On the other hand, when wind speeds were greater than 3 m s^{-1}, turbulence could be sustained even for very strongly negative net radiative fluxes (weakly stable regime). The resulting mechanical mixing meant that the near surface temperature gradient remained close to zero. Due to the LF, this was the most frequent scenario under clear skies at the Field site.

The surface energy budget at the Field site thus exhibited two preferred modes over the course of the campaign. The first mode was associated with low winds and the presence of clouds. The net radiative flux was around -5 W m^{-2} while the turbulent sensible heat flux was around 0 W m^{-2}, and the SEB residual was small. The second mode was characterized by elevated wind speeds and clear skies. The net radiative flux was approximately -45 W m^{-2} and the turbulent sensible heat flux around 13 W m^{-2}. In this second mode, the residual of the SEB was positive beyond the scope of random measurement errors, indicating a missing positive heat flux at the surface. For the 5–7 December episode, we estimate that a horizontal temperature gradient of 1.5 – 3 K km^{-1} would account for the residual through horizontal heat advection by the LF.

In summary, the results presented here have shown that small-scale flows can penetrate stable cold air pools in the Arctic, such as the Tanana Valley, and locally modify the SEB and stability regime. This is potentially important for studies of local air pollution at high-latitudes since pollution episodes occur during cold, stable conditions. However, open questions remain concerning the dynamic characteristics of this flow and the representativeness of the Field measurement site. Temperature profiles up to 50 m would help to characterize the surface inversion development and the turbulent mixing scales. A tighter network of instruments, both at the Field and in the wider Fairbanks area, would make it possible to assess the origin and horizontal dimensions of the LF once it penetrates the Tanana Valley as well as to estimate heat advection.

Chapter 4

Dependence of the clear-sky temperature inversion on wind speed: a modelling study

---

Contents

4.1 Introduction

The analysis of the pre-ALPACA measurements had shown that local flows can generate sufficient turbulence levels to inhibit the development of strongly stable conditions, even under strong radiative cooling (Chapter 3). The results appeared in line with predictions from MWST. First attempts at modelling the 4–8 December 2019 "case study" periods with WRF showed that while the model did not capture the specific local flow that had been observed, it did reproduce some wind speed variability linked to the topography. This then raised the question of how this would impact the modelled surface layer temperature inversion, and whether the WRF surface layer schemes reproduced the behaviour of small analytical models such as [van de Wiel *et al.* 2017]. As most of the Interior Alaska region is covered in forest, it became necessary to take into account the effects of the vegetation canopy - as is done in some of the WRF surface layer schemes. To that end, a 2-layer analogue of the model of [van de Wiel *et al.* 2017] was created. The model behaviour was then compared to measurements at a forest site. The results of this analysis are detailed in the following sections.

4.2 Context and objective

SBIs are extremely frequent in the cold, dark conditions of the Arctic winter [Serreze *et al.* 1992, Bradley *et al.* 1992]. The usual pattern is that cloudy conditions are associated to a near-neutral surface layer, while clear skies are associated to strong SBIs [Malingowski *et al.* 2014]. However, modelling temperature inversions remains a challenge and an area of ongoing study [Steeneveld *et al.* 2006, Sterk *et al.* 2013, Holtslag *et al.* 2013, Baas *et al.* 2017].

One of the main difficulties is with modelling the turbulent heat fluxes. Typical Monin–Obukhov stability theory (MOST) assumes constant fluxes in the surface layer and so-called z-less scaling [Monin & Obukhov 1954, Wyngaard & Coté 1972] and its limits of applicability have been discussed. This has led to the recognition of different turbulent regimes. The first, called the weakly regime, is fully consistent with Monin–Obukhov stability theory. In this regime, the turbulent heat fluxes increase with increasing temperature gradient (because more heat is available to be transported). The inertial range in the turbulence spectra is well defined, and exhibits a Kolmogorov slope of -5/3 [Kaimal & Finnigan 1994]. The other is the strongly stable regime, where turbulent sensible heat fluxes instead decrease with increasing temperature gradient, because the effect of strong stability lead to a turbulence decay. In this regime, Kolmogorov turbulence disappears; turbulence becomes intermittent, and driven by processes at larger time scales such as the Coriolis force [Grachev *et al.* 2008] or gravity waves [Sorbjan & Czerwinska 2013]. However, it does not disappear entirely so that the flow never becomes laminar [Grachev *et al.* 2013].

There is general agreement on the nature of these two turbulence regimes (although sometimes, a third "transitional" regime is considered). However, the separation between the two is debated: traditionally, the Richardson number or Monin–Obukhov parameters are used. [Grachev *et al.* 2013], for example, suggested that a gradient or flux Richardson number of 0.2 was a lower threshold for the strongly stable state, while [Mahrt *et al.* 2014] found that $\zeta = 0.06$ separated the two states. More recent works have focused on the impact of wind speeds, or wind shear, on determining the regime [Sun *et al.* 2012, van de Wiel *et al.* 2007, van de Wiel *et al.* 2012], in a framework called minimum wind speed for sustainable turbulence. For example, [van Hooijdonk *et al.* 2015], building on the work of [van de Wiel *et al.* 2012], used external forcings to the surface layer (such as a constant wind speed, replacing the synoptic pressure gradient, and downwards radiative fluxes) to determine a new parameter called the shear capacity. This parameter has been found to better predict the stability regime than the traditional local parameters such as ζ or R_f. In this new framework, the stability regime is not a feature solely of the turbulence, but of the surface layer as a whole.

Determining the stability regime and the turbulent heat fluxes is, however, only one part of determining the SBI strength. This depends on the surface temperature, which is in turn determined by the SEB. Analysis of measurements in the Antarctic has shown that plotting ΔT (the temperature difference between the surface and 10 m) versus the wind speed at 10 m under clear-sky winter conditions reveals two distinct regimes, separated by a transition: one at low wind speeds and high ΔT, and the other at high wind speeds and low ΔT [Vignon *et al.* 2017]. This characteristic shape was termed 'S' shape (although the 'S' is technically backwards), because of the transition exhibited some non-monotonous behaviour. The transition between the two regimes was found to agree well with predictions from MWST. Drawing on these studies, a small analytical model was developed by [van de Wiel *et al.* 2017] and shown to reproduce the 'S' shape.

The minimum wind speed for sustainable turbulence therefore offers a promising framework for the analysis and modelling of SBIs. For the moment, however, these analyses have been restricted to the extreme conditions of Antarctica, where the surface is vegetation-free snow and ice. The Arctic and sub-Arctic also experience regular inversions with strong implications on pollution dispersion. However, a large part of this region is covered by forest, which is known to impact the turbulent heat fluxes [Batchvarova *et al.* 2001]. For example, unstable stratification may remain within the canopy layer even when overlying air layer is very stable [Jacobs *et al.* 1992], and gradients directly above the canopy may be modified by the roughness sublayer [Mölder *et al.* 1999, Babić *et al.* 2016]. Forest canopies also act as grey bodies, both emitting and absorbing longwave fluxes. In seeking to extend the use of MWST, it is therefore important to consider the impact of trees. Another important question concerns the coherence of meso-scale models with MWST. [Vignon *et al.* 2018], for example, showed that the meso-scale model LMDZ reproduced an 'S' shape transition of surface temperature gradient with wind speed, with the shape of the transition depending on the stability function used. No studies have yet shown whether this is the case for WRF, which is one of the most commonly used meso-scale models.

In this chapter, the impact of wind speed on the temperature gradient in clear-sky, winter conditions over a forest surface will be investigated. The behaviour of the WRF surface layer and land-surface model in reproducing the very and weakly stable regimes and the transition between the two in a continental, high-latitude context will be explored and potential improvements will be evaluated. First, simple analytical 1 and 2-layer models of the surface layer will be introduced, and they will be contrasted with commonly used WRF surface layer modules (Sect. 4.3). Then, the aims and methodology will be explored (Sect. 4.4). Lastly, the results will be discussed (Sect. 4.5).

4.3 Theoretical basis

4.3.1 1-layer model for the surface layer

In order to determine the surface temperature T_s, the SEB must be solved. Here, a cold, dry boundary layer is assumed and the latent heat fluxes are therefore neglected. Furthermore, for simplicity, it is assumed that the shortwave radiation is also negligible; this is reasonable considering the low incoming solar radiation and high surface albedo. This leaves $\mathrm{LW_{net}}$, G and H to be calculated. In the following, the equations and notations draw on [van de Wiel *et al.* 2017]. A schematic of the system is shown in Fig. 4.1.

$$\begin{aligned}\mathrm{LW_{net}} &= \mathrm{LW_d} - \mathrm{LW_u} \\ &= \mathrm{LW_d} - \varepsilon_s \sigma T_s^4 \\ &\approx \mathrm{LW_d} - \varepsilon_s \sigma T_a^4 + 4\varepsilon_s \sigma T_a^3 (T_a - T_s) \\ &\approx -Q_i + 4\varepsilon_s \sigma T_s^3 (T_a - T_s) \\ \text{where } Q_i &= -\mathrm{LW_d} + \varepsilon_s \sigma T_a^4\end{aligned} \tag{4.1}$$

with $\varepsilon_s = 0.99$ the surface emissivity, $\sigma = 5.67 \times 10^{-8}$ W m^{-2} K^{-4} the Stefan–Boltzmann constant, and T_a the air temperature at height z_a. Q_i is termed the isothermal net radiation: indeed, it corresponds to the net longwave flux if $T_s = T_a$ [Holtslag & Bruin 1988]. The second term in the expression of $\mathrm{LW_{net}}$ therefore represents the change in the net radiation due to the deviation from the isothermal profile.

$$\mathrm{H} = \rho C_p C_D U_a (T_a - T_s) \tag{4.2}$$

with $\rho \approx 1.4$ kg m^{-3} the air density, $C_p = 1005$ J K^{-1} kg^{-1} the heat capacity of air, and U_a the wind speed at altitude z_a. C_D is the turbulent diffusion coefficient, which depends on the stability: its expression will be detailed below.

$$\begin{aligned}\mathrm{G} &= -\frac{\lambda_s}{d_s}(T_s - T_g) \\ &= \frac{\lambda_s}{d_s}(T_a - T_s) - \frac{\lambda_s}{d_s}(T_a - T_g)\end{aligned} \tag{4.3}$$

with λ_s the snow conductivity, d_s the snow depth and T_g the ground temperature. The notation Λ_s for $\frac{\lambda_s}{d_s}$ will be used in the following for greater readability.

Combining these three equations into the SEB leads to the following expression for $\Delta T = T_a - T_s$:

$$\Delta T = \frac{Q_i + \Lambda_s (T_a - T_g)}{4\varepsilon_s \sigma T_a^3 + \Lambda_s + \rho C_p C_D U_a} \tag{4.4}$$

where the notation $\lambda_c = 4\varepsilon_s \sigma T_a^3 + \Lambda_s$, named coupling parameter in [van de Wiel *et al.* 2017], is introduced for simplicity. This is the equation form found in [van de Wiel *et al.* 2017], except that it is assumed that $T_a \approx T_g$ so that the second term on the numerator disappears. The difficulty in solving this equation

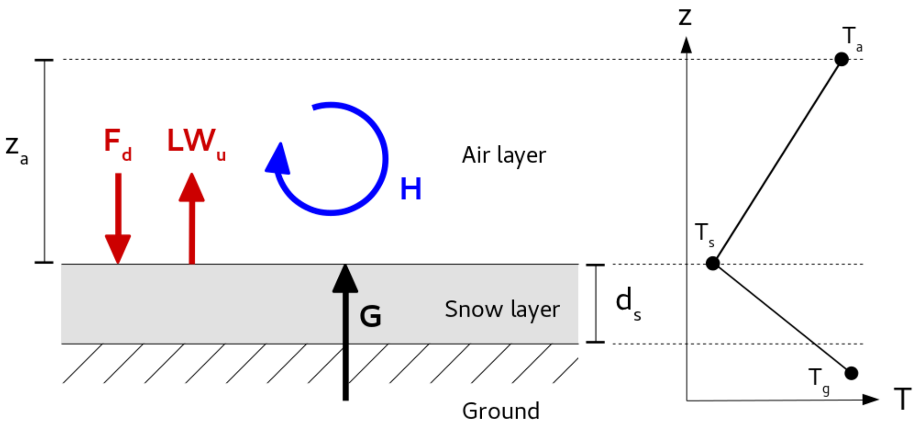

Figure 4.1: Schematic of the one layer model described in section 4.3.1.

to obtain ΔT is that C_D is typically assumed to depend on the stability. Using the integral formulation of the Monin–Obukhov theory:

$$C_D = \frac{\kappa^2}{(\log(\frac{z_a}{z_0}) - \psi(\zeta) + \psi(\frac{z_0}{L}))^2} \tag{4.5}$$

with $\kappa = 0.4$ the van Kármán constant, ψ the integral stability function, and z_0 the roughness length (here supposed to be the same for momentum and heat). Alternatively, C_D can be expressed as a function of the bulk Richardson number R_b:

$$C_D = \frac{\kappa^2}{\log(\frac{z_a}{z_0})^2} \cdot f(R_b) \tag{4.6}$$

These two formulations are equivalent for the right expressions of f and ψ [England & McNider 1995]. f is equal to 1 in near-neutral stability, and then decreases to 0 with increasing R_b. ψ is equal to 0 when $\zeta \approx 0$, and it increases with increasing ζ. Many different expressions of both f and ψ are found in the literature [Businger *et al.* 1971, Holtslag & Bruin 1988, England & McNider 1995, van de Wiel *et al.* 2017]. Usually, these are classified as "short-tail" (i.e., with a very sharp increase/decrease so that C_D quickly drops to 0 at increasing stability) or "long-tail" (i.e., the the transition is smoother so that some turbulent sensible heat flux is maintained for longer).

Because the stability parameters ζ and R_b both depend on the wind speed and near surface temperature gradient, this means that Eq. 4.4 is not as straightforwardly linear as it appears. Two limit cases emerge:

$$\begin{aligned} C_D &\xrightarrow[\zeta, R_b \to +\infty]{} 0 \implies \Delta T \xrightarrow[\zeta, R_b \to +\infty]{} \frac{Q_i + \Lambda_s(T_a - T_g)}{\lambda_c} \\ C_D &\xrightarrow[\zeta, R_b \to 0]{} \frac{\kappa^2}{\log(\frac{z}{z_0})^2} \implies \Delta T \xrightarrow[\zeta, R_b \to 0]{} \frac{Q_i + \Lambda_s(T_a - T_g)}{\lambda_c + \rho C_p \frac{\kappa^2}{\log(\frac{z_a}{z_0})^2} U_a} \end{aligned} \tag{4.7}$$

The first case corresponds to the "very stable" regime of MWST, and the second case to the "weakly stable" regime. Because R_b is inversely proportional to U_a^2, the very stable regime is reached for low values of U_a and the weakly stable for large values of U_a. A transition between the two then occurs at a so-called critical wind speed [van de Wiel *et al.* 2017]. This leads to the characteristic (backwards) 'S' shape in the relation between ΔT and U_a, as shown in Fig. 4.2a. Although the link between ζ and U_a is less evident, the same reasoning holds for the ζ formulation. Note that if the coupling between the ground and the atmosphere is not taken into account, i.e. $\lambda_c = 0$, ΔT does not have a finite limit in the very stable regime. This is analogous to the model in [van de Wiel *et al.* 2012], where the "energy demand at the surface" is considered to be constant instead of varying with temperature. Below a certain wind speed threshold, termed minimum wind speed for sustainable turbulence, no equilibrium ΔT was then reached.

Although the transition between weakly and strongly stable regimes is an aspect of all simulations shown in Fig. 4.2a, its exact shape varies depending on the values of the isothermal net radiation, roughness length, and stability function. Firstly, ΔT is larger at $Q_i = 60$ W m^{-2} than $Q_i = 50$ W m^{-2}; this is especially marked in the very stable regime. Indeed, more radiative cooling leads to a stronger SBI. This can also easily be deduced from Eq. 4.4. Secondly, decreasing z_0 leads to a later and less abrupt transition between weakly and strongly stable regimes. Lastly, changing the stability function from "short-tail" to "long-tail" also leads to a more gradual transition, but without increasing the transition wind speed.

4.3.2 2-layer model for the surface layer

In the presence of trees or other tall vegetation, it can be helpful to consider a 2-layer model. In its simplest form, this is composed of the surface, a "canopy" layer where the air is in thermodynamic equilibrium with the vegetation, and an overlying air layer (Fig. 4.3). The effect of the canopy on the longwave radiative and turbulent fluxes can then be taken into account.

Assuming for simplicity that $\varepsilon_s \approx 1$, the surface energy balance is:

$$\begin{aligned} &\mathrm{LW}_{d,bc} - \mathrm{LW}_{u,bc} + G + H_c = 0 \\ \implies &(1-\varepsilon_c)\mathrm{LW}_d + \varepsilon_c \sigma T_c^4 - \sigma T_s^4 - \Lambda_s(T_s - T_g) - \rho C_p C_{D,c} U_c (T_s - T_c) = 0 \end{aligned} \tag{4.8}$$

where $\mathrm{LW}_{d,bc}$ and $\mathrm{LW}_{u,bc}$ are the downwards and upwards fluxes below the canopy level, ε_c is the canopy emissivity, T_c the canopy temperature, U_c the canopy wind speed and $C_{D,c}$ the turbulent diffusion coefficient for the surface to canopy sensible heat exchange. Using the same linearisation procedure as in 4.3.1, this then transforms to:

$$\begin{aligned} -(1-\varepsilon_c)Q_i - \frac{\lambda_s}{d_s}(T_a - T_g) &+ \Delta T_1 \left[\rho C_p C_{D,c} U_c + 4\sigma T_a^3 + \Lambda_s\right] \\ &+ \Delta T_2 \left[(1-\varepsilon_c) 4\sigma T_a^3 + \Lambda_s\right] \\ &= 0 \end{aligned} \tag{4.9}$$

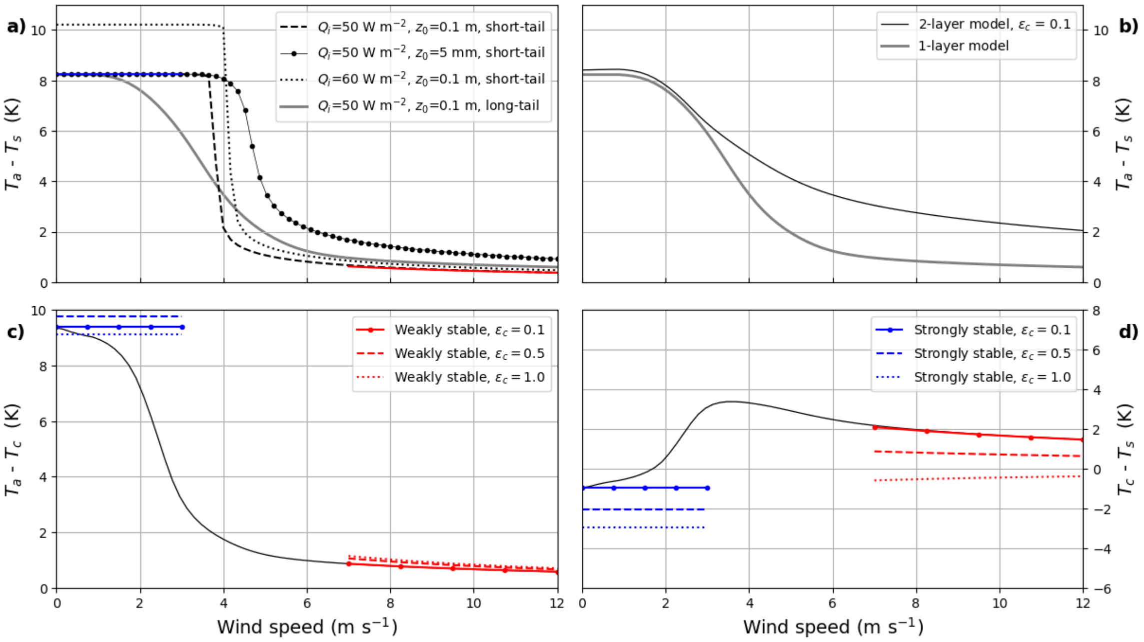

Figure 4.2: Panel a: ΔT vs U_a according to Eq. 4.4 at an altitude $z = 14$ m. The impact of different parameters and stability functions (short-tail or long-tail) is shown. The blue and red lines represent the very stable and weakly stable regimes respectively (Eq. 4.7), for $Q_i = 50$ W m^{-2} and $z_0 = 5$ mm. Panel b: comparison of the 1- and 2-layer models. Panel c: ΔT_2 as a function U_a; red and blue lines correspond to the weakly and strongly stable regimes respectively, as outlined in Eq. 4.15. The different line styles correspond to different values of the canopy emissivity. The thin black line is a representation of the transition between the two regimes for $\varepsilon_c = 0.5$, which has been calculated using the MYJ algorithm with the Ameriflux stability function (Sects. 4.3.3 and 4.4.1). All curves have been calculated using $Q_i = 50$ W m^{-2}, T_a = -10 °C, T_g = -2 °C and $\Lambda_s = 1$ W m^{-2} K^{-1}. Panel d: same, for ΔT_1.

where $\Delta T_1 = T_c - T_s$ is the surface to canopy temperature gradient and $\Delta T_2 = T_a - T_c$ is temperature difference between the canopy and the overlying air.

The energy balance applied to the canopy layer yields:

$$\begin{aligned} &\mathrm{LW}_d - \mathrm{LW}_u - (\mathrm{LW}_{d,bc} - \mathrm{LW}_{u,bc}) + H_a - H_c = 0 \\ \Longrightarrow\ &\varepsilon_c \mathrm{LW}_d + \varepsilon_c \sigma T_s^4 - 2\varepsilon_c \sigma T_c^4 - \rho C_p C_{D,a} U_a (T_c - T_a) \\ &- \rho C_p C_{D,c} U_c (T_c - T_s) = 0 \end{aligned} \tag{4.10}$$

with $C_{D,a}$ the turbulent diffusion coefficient for the canopy to air sensible heat

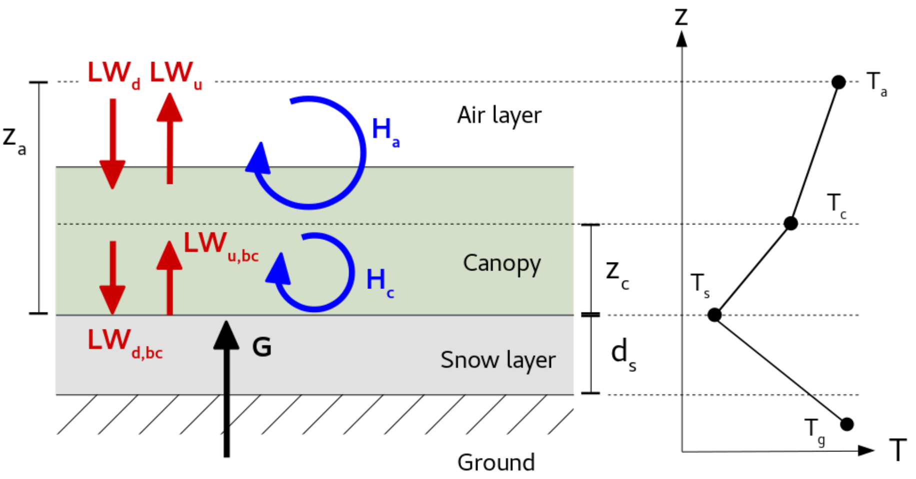

Figure 4.3: Schematic of the two layer model described in section 4.3.2.

exchange. Similarly, this transforms to:

$$\begin{aligned} -\varepsilon_c Q_i - \Delta T_1 \left[\rho C_p C_{D,c} U_c + 4\varepsilon_c \sigma T_a^3\right] \\ + \Delta T_2 \left[\rho C_p C_{D,a} U_a + 4\varepsilon_c \sigma T_a^3\right] \\ = 0 \end{aligned} \tag{4.11}$$

Summing Eqs. 4.9 and 4.11 yields the following, instructive equation:

$$\begin{aligned} -Q_i - \Lambda_s (T_a - T_g) + \Delta T_1 \left[(1-\varepsilon_c) 4\sigma T_a^3 + \Lambda_s\right] \\ + \Delta T_2 \left[4\sigma T_a^3 + \Lambda_s + \rho C_p C_{D,a} U_a\right] \\ = 0 \end{aligned} \tag{4.12}$$

which is very similar to Eq. 4.4, except that the energy source term $(Q_i + \Lambda_s(T_a - T_g))$ has an additional term, which is proportional to ΔT_1. Since ΔT_1 is expected to be less sensitive to the forcing wind speed U_a than ΔT_2, this suggests that ΔT_2 will conserve the same 'S' shape transition between a strongly stable and a weakly stable state as in the one layer model.

As with the one layer model, insight into the behaviour of ΔT_1 and ΔT_2 can be gained by studying the asymptotic cases: the weakly and strongly stable states. The analytical expressions are more complicated, and here only the case where $\varepsilon_c = 1$ (corresponding to an opaque canopy) will be considered. In this situation, and if turbulence is completely collapsed (i.e. $C_{D,a} = C_{D,c} = 0$), Eqs. 4.9 and 4.12 lead to the following values for the temperature gradients:

$$\begin{aligned} \Delta T_2 &= \frac{Q_i \left[1 + 1/(4\sigma T_a^3)\right] + \Lambda_s (T_a - T_g)}{4\sigma T_a^3 + 2\Lambda_s} \\ \Delta T_1 &= \frac{-Q_i/(4\sigma T_a^3) + \Lambda_s (T_a - T_g)}{4\sigma T_a^3 + 2\Lambda_s} \end{aligned} \tag{4.13}$$

and therefore,

$$\Delta T_1 + \Delta T_2 = \frac{Q_i + 2\Lambda_s(T_a - T_g)}{4\sigma T_a^3 + 2\Lambda_s} \tag{4.14}$$

The total temperature gradient (between air and surface) is therefore similar to the one layer case, but with an "equivalent snow conductivity" twice the real value. It can also be noted that while ΔT_2 is always positive, ΔT_1 is negative unless $T_g < T_a - \frac{Q_i}{\Lambda_s 4\sigma T_a^3}$, which is very unlikely to occur with the values typical of high-latitude winter. In short, the very stable case is characterised by a temperature decrease from surface to canopy, and an increase from canopy to the overlying air. This is contradictory with the idea that $C_{D,c}$ collapses to 0, because in the presence of a negative temperature gradient buoyancy effects may generate turbulence without significant mechanical shear. Indeed, solving Eqs. 4.9 and 4.12 numerically for $U_c = U_a = 0.001$ m s^{-1} (using appropriate schemes for calculating the turbulent diffusion coefficients) shows that $C_{D,c}U_c$ maintains a value of ≈ 0.0017 m s^{-1}. Therefore, while the surface layer as a whole may be considered strongly stable (because $T_a - T_s$ is very large), the situation in the individual layers may be different. This is in agreement with [Batchvarova *et al.* 2001], which found that the canopy layer may remain unstable even when the air aloft is very stably stratified.

Numerically, the weakly and strongly stable regimes can therefore be estimated using the following values of the turbulent diffusion coefficients:

$$\begin{aligned} C_{D,a} &= \begin{cases} 0. & \text{(strongly stable)} \\ \frac{\kappa^2}{\ln((z_a - d)/z_0)^2} & \text{(weakly stable)} \end{cases} \\ C_{D,c} &= \begin{cases} 0.0017/U_c & \text{(strongly stable)} \\ \frac{\kappa^2}{\ln(z_c/z_{0g})^2} & \text{(weakly stable)} \end{cases} \end{aligned} \tag{4.15}$$

where d is the displacement height due to the presence of the canopy, z_0 is the "above canopy" roughness length and z_{0g} is the roughness length of the ground, as seen "below the canopy". There are other ways to estimate the below canopy turbulent diffusion coefficient for weakly stable cases, for example by assuming an exponential wind profile in the canopy as in [Mahat *et al.* 2013]. However, this is the simplest expression and will serve for illustrative purposes. For the time being also, U_c may be very roughly estimated to be proportional to U_a: for example, $U_c = 0.25 \cdot U_a$.

The result of this estimation is shown in Fig. 4.2 for three values of ε_c. As had been hypothesized above, ΔT_2 exhibits the same 'S' shape as in the one layer model. On the other hand, ΔT_1 is larger in the weakly stable regime than in the strongly stable regime (where it is negative, in coherence with the above discussion), and its shape is more dependant on values of the canopy emissivity. For $\varepsilon_c = 1$, appears to tend to zero at large values of U_a while keeping negative values. On the other hand, for $\varepsilon_c = 0.5$ and 0, it turns positive and then decreases with increasing wind speeds, therefore reaching a maximum somewhere between 2 and 6 m s^{-1} (see illustrative black curve).

4.3.3 WRF specificities

The relevant part of the WRF model are the surface layer module, which calculates the turbulent exchange coefficient (C_D), and the land-surface model, which then uses the turbulent exchange coefficient to determine the surface temperature. Although many different schemes are available for each module, we have chosen to focus on only two in order to gain a deeper understanding of their working and to improve them.

The simplest land surface model scheme is Noah-LSM [Chen & Dudhia 2001, Ek *et al.* 2003]. When there is a snow cover, Noah-LSM functions exactly as Eq. 4.4. The snowpack is considered as a single layer, while the soil is subdivided into four layers for which the heat diffusion equation is solved, yielding the topmost soil layer temperature T_g. Here, we used Noah-LSM in conjunction with the Mellor-Yamada-Janjic surface layer scheme. This is known to perform well in stable conditions, and has the advantage of being relatively simple. In short, C_D is calculated as in Eq. 4.5, with the difference that the roughness length for momentum (z_{0m}) and heat (z_{0h}) are differentiated. z_{0m} is fixed according to the land-use type and vegetation while z_{0h} depends on the stability (through the Richardson number):

$$\begin{aligned} C_D &= \frac{\kappa^2}{(\log(\frac{z}{z_{0m}}) - \psi(\zeta) + \psi(\frac{z_{0m}}{L})) \cdot (\log(\frac{z}{z_{0h}}) - \psi(\zeta) + \psi(\frac{z_{0h}}{L}))} \\ z_{0h} &= z_{0m} e^{-\kappa \cdot 0.1 \cdot (1 + \frac{R_b}{R_c}^2) \sqrt{u^* z_{0m}/\nu_a}} \end{aligned} \tag{4.16}$$

with $\nu_a = 1.47 \times 10^{-5}$ m^2 s^{-1} the air kinematic viscosity and R_c a critical Richardson number, here equal to 0.505. ψ has the following expression in stable conditions (i.e. $\zeta \geq 0$):

$$\psi(\zeta) = 0.7 \cdot \zeta + 0.75 \cdot \zeta \cdot (6 - 0.35\zeta) \cdot e^{-0.35\zeta} \tag{4.17}$$

This is similar, but not equal to, the Holtslag integral stability function [Holtslag & Bruin 1988] up to values of $\zeta \approx 1$. Indeed, a specificity of the MYJ scheme is that ζ has a set maximum value of 1. This means that C_D never goes to 0, some turbulent sensible heat flux is always maintained and therefore the very stable regime, is not independent of U_a. This is visible on Fig. 4.4: for $U_a < 3$ m s^{-1}, ΔT decreases steadily with wind speed. For low values of the momentum roughness length the distinction between very and weakly stable regimes even completely disappears, with ΔT instead decreasing almost linearly as a function of U_a.

Solving this form of the equation for C_D, requires that Monin-Obukhov length be known, which in turn requires knowledge of both u^* and H and thus C_D. The solving procedure is therefore iterative.

Recently, Noah-LSM was updated to "enhance the conceptual realism" by introducing, among others, a vegetation energy balance, a layered snowpack, and soil moisture – groundwater interaction. This updated version is called Noah-MP [Niu *et al.* 2011], and it includes its own surface layer scheme. Two options are

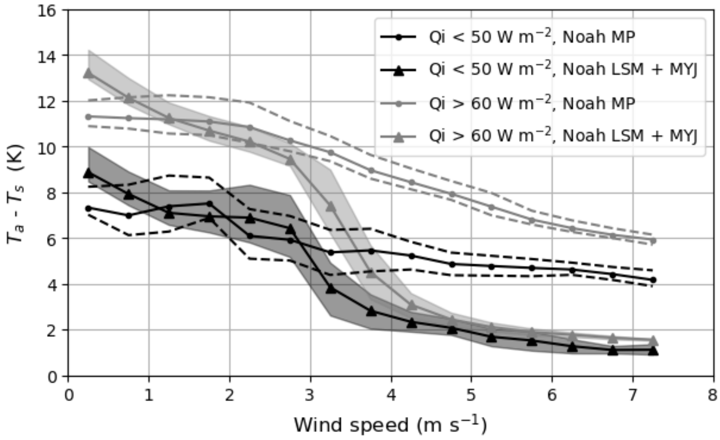

Figure 4.4: ΔT vs wind speed averaged over all points with a land-use index of 1 or 5 (indicating trees, with z_{0m} between 0.1 and 0.3 m) of a WRF 1 km resolution run (Sect. 4.4.3). The black (grey) lines indicate that the averaging was done for points with values of $Q_i > 60$ (< 50) W m^{-2}. Dot markers correspond to a run with the Noah-MP scheme while triangle markers correspond to a run with the Noah-LSM scheme. Dashed lines and filled areas represent the 25th to 75th percentiles.

provided; here, we will use only the "original Noah" surface layer, which is identical to MYJ except that it uses the Businger-Dyer stability function. Each grid node is divided into a vegetated and a non-vegetated fraction. The non-vegetated fraction surface temperature is calculated similarly to Noah-LSM, except that the snowpack is divided into up to three different layers and the ground heat flux is calculated through the topmost snow layer only. The vegetated fraction calculation is a more complex version of a 2-layer model, where the vegetation temperature is considered to be different from the air temperature in the canopy. The vegetation acts as a grey body with emissivity $\varepsilon_v = 1 - e^{-LAI}$ and exchanges sensible heat with the canopy air. The canopy air is transparent to longwave radiation, simply exchanging sensible heat with the surface, the overlying air and the vegetation. In short, the radiative and sensible heat budgets of the canopy layer in Sect. 4.3.2 are separated. In practice, however, the temperature difference between the vegetation and the canopy air did not exceed 0.5 K during our runs, so that a simple 2-layer model provides a good approximation for the behaviour of Noah-MP. Here, we will therefore not detail the calculation of the tree – canopy air sensible heat exchange.

The turbulent diffusion coefficient for the canopy to overlying air sensible heat exchange, $C_{D,a}$, is calculated using the "original Noah" scheme with a roughness length and displacement height which depend on the land use category; the displacement height is calculated as $d = 0.65 \cdot h_{can}$, where h_{can} is the canopy top height. $C_{D,c}$ is calculated by assuming an exponential wind profile, similar to what

	Evergreen Needleleaf Forest	**Mixed Forest**	**Wooded Tundra**	**Mixed Tundra**	**Ameriflux PRR site**
VAI (m^2 m^{-2})	4.4	2.4	1.2	0.7	0.73
h_{can} (m)	20	16	4	2	3
z_{0m} (m)	1.09	0.8	0.3	0.2	0.4
d (m)	13	10.4	2.6	1.3	0.9
f_{veg}	0.7 (table) 0.9 (LAI)	0.8 (table) 0.7 (LAI)	0.6 (table) 0.45 (LAI)	0.6 (table) 0.3 (LAI)	$\mathrm{f}_{veg}\varepsilon_c \approx$ 0.15
ε_v	0.99	0.91	0.7	0.5	

Table 4.1: Noah-MP surface characteristics for four different land use types: Evergreen Needleleaf Forest, Mixed Forest, Wooded Tundra and Mixed Tundra. The characteristics include the Vegetation Area Index (VAI), canopy height (h_{can}), momentum roughness length (z_{0m}), displacement height d, vegetation fraction (f_{veg}) and vegetation emissivity (ε_v). The last column shows the surface characteristics at the Ameriflux Poker Flats Research Range in Interior Alaska, which will be presented in Sect. 4.4.1.

is described in [Mahat *et al.* 2013]:

$$\begin{aligned} K_h &= \frac{\kappa^2 \cdot U_c \cdot (h_{can} - d)}{\log((z_a - d)/z_{0mg})} \\ C_{D,c}U_c &= \frac{K_h \cdot n}{h_{can} \cdot e^n \left(\exp\left[-nz_c/h_{can}\right] - \exp\left[-n(d + z_{0m})/h_{can}\right]\right)} \end{aligned} \tag{4.18}$$

where n is the exponential decay coefficient, which depends on the LAI, canopy top height, and stability.

The total grid box surface temperature is then calculated from the two values obtained for the vegetated and non-vegetated parts ($T_{s,v}$ and $T_{s,nv}$):

$$T_s = \mathrm{f}_{veg}T_{s,v} + (1 - \mathrm{f}_{veg})T_{s,nv} \tag{4.19}$$

where f_{veg} is the vegetation fraction in each model grid box. There are multiple calculation options for this parameter in Noah-MP. It can either be taken from the vegetation parameter table, which is also used by Noah-LSM, or it can be determined from the leaf area index using the following formula:

$$\mathrm{f}_{veg} = 1 - e^{-0.52LAI} \tag{4.20}$$

LAI itself can either be taken from the Noah-MP parameter table or determined "dynamically" by a carbon budget subroutine. Typical values of LAI and f_{veg} for different land-use categories are shown in Table 4.1.

It should be noted that the vegetation emissivity used in Noah-MP is not equivalent to the canopy emissivity in the simple 2-layer model described in Sect. 4.3.2. In effect, Noah-MP supposes that the vegetated fraction has an emissivity of ε_v and the non-vegetated fraction has an emissivity of 0: the average canopy emissivity (such as is used by the model in Sect. 4.3.2) is therefore $\varepsilon_c = \mathrm{f}_{veg}\varepsilon_v$.

4.4 Methodology

In this section, the methodology is presented. First, the Ameriflux Poker Flats Research Range (PRR) site and dataset are introduced (Sect. 4.4.1). These long-term measurements are then analysed from a statistical point of view to gain a better understanding of the behaviour of the temperature inversion as a response to varying wind speed in clear-sky, no-sunlight winter conditions at a forested site. Secondly, the studied models are presented (Sect. 4.4.2). These include the Noah-LSM and Noah-MP land surface models which have been extracted from the larger WRF framework and recoded in Python, and two modified versions. The original models and modified versions can then be evaluated "offline" in comparison to the PRR site measurements. Thirdly, the proposed modifications are coded in WRF and their impact on the output is studied on a relevant case study: the 4–8 December 2019 clear-sky episode in Fairbanks, Alaska (Sect. 4.4.3).

4.4.1 Measurements at the Ameriflux Poker Flats Research Range

Figure 4.5: Left: photo of the 17 m high measurement tower at the Poker Flats Research Range Ameriflux site. Right: photo of the PRR site as seen from the measurement tower. Credit: Lisa Johnson.

The Ameriflux PRR site is located in the Poker Flats Research Range (65°07'24.4" N, 147°29'15.2" W), around 30 km away from Fairbanks (Interior Alaska). It has been operating since 2010, when it was established as part of the JAMSTEC-IARC Collaboration Study (JICS) [Sugiura *et al.* 2011] and its data is made available online on the Ameriflux website [Kobayashi *et al.* 2019] (`https://ameriflux.lbl.gov/sites/siteinfo/US-Prr`). Its 17 m measurement tower is implanted in a black spruce forest with sparsely distributed and short trees (Fig. 4.5). The tree density, as measured in 2010, was 3967 trees ha^{-1} and the average tree height was 2.44 m: the tallest tree was 6.4 m but 75% of trees were shorter than 3 m [Nakai *et al.* 2013]. The leaf area index (LAI) was 0.73 [Nakai *et al.* 2013]. Both of these values are much smaller than those found in Noah-MP for evergreen forests (Table 4.1).

Variable	**Instrument**	**Measurement altitude (m)**
Wind speed (m s^{-1})	010C (MetOne, USA)	1.5, 3, 4.5, 6, 7.5, 9, 13, 16
Temperature (K)	HMP155 (Vaisala, Finland)	1.5, 3, 4.5, 6, 9, 11, 13, 16
Turbulent sens. heat flux (W m^{-2})	WindMaster Pro (Gill, UK)	1.9, 11
Friction velocity (m s^{-1})	WindMaster Pro (Gill, UK)	1.9, 11
Radiative fluxes (W m^{-2})	CNR4 (Kipp & Zonen, Netherlands)	1.3, 16
Snow depth (m)	SR50A (Campbell Sci., USA)	0
Soil temperature (K)	107 (Campbell Sci., USA)	-0.05, -0.1

Table 4.2: Meteorological variables measured at the Ameriflux PRR site, including instruments and measurement heights [Nakai *et al.* 2013]. Note that wind speed is also measured at 11 m, with the sonic anemometer. [Nakai *et al.* 2013] indicates that temperature was also measured at 7.5 m, but these measurements do not appear to be available on the Ameriflux website.

The Ameriflux PRR measurements which will be used here are summarised in Table 4.2. These include wind speeds and temperatures at 8 different heights (from 1.5 to 16 m), as well as turbulent and radiative fluxes. The surface temperature was calculated from the radiative flux measurements at 1.3 m, assuming a snow surface emissivity of 0.99. As this study focuses on the clear-sky surface layer in wintertime conditions, the data was curated accordingly. Only time points in the months of November – March with snow depth greater than 10 cm were kept. No measurements of the cloud cover are available at the PRR site, so clear-sky instants were defined as those with net longwave radiation less than -30 W m^{-2}. Indeed, as is typical in high-latitude site, the R_n distribution at the PRR site was bimodal; the low R_n mode was considered to correspond to the absence of clouds and the high R_n mode to their presence. Measurements with $R_n >$ -30 W m^{-2} were therefore discarded. As the PRR site is located slightly below the Arctic circle, there is still some solar radiation at the surface in the winter time. In order to simplify the analysis, only time points with downwelling shortwave radiation less than 30 W m^{-2} were kept; as the snow albedo is very high, this corresponds to a net shortwave flux less than 5 W m^{-2}. Lastly, measurements with latent heat flux greater than 5 W m^{-2} in absolute value were discarded.

The average emissivity of the canopy layer $\varepsilon_c = \mathrm{f}_{veg}\varepsilon_v$ can be calculated from above and below canopy radiation measurements:

$$\mathrm{LW}_{d,bc} - \mathrm{LW}_u = (1 - \mathrm{f}_{veg}\varepsilon_v)\,[\mathrm{LW}_d - \mathrm{LW}_{u,bc}] \tag{4.21}$$

As shown in Fig. 4.6c, this gives a best estimation of $\varepsilon_c \approx 0.15$. This is coherent with the Noah-MP calculation of f_{veg} and ε_v as a function of LAI. Indeed, measured LAI at the PRR site is 0.73, yielding $\mathrm{f}_{veg} \approx 0.3$ and $\varepsilon_v \approx 0.5$.

The value of z_{0m} can also be calculated from the sonic anemometer data. Indeed,

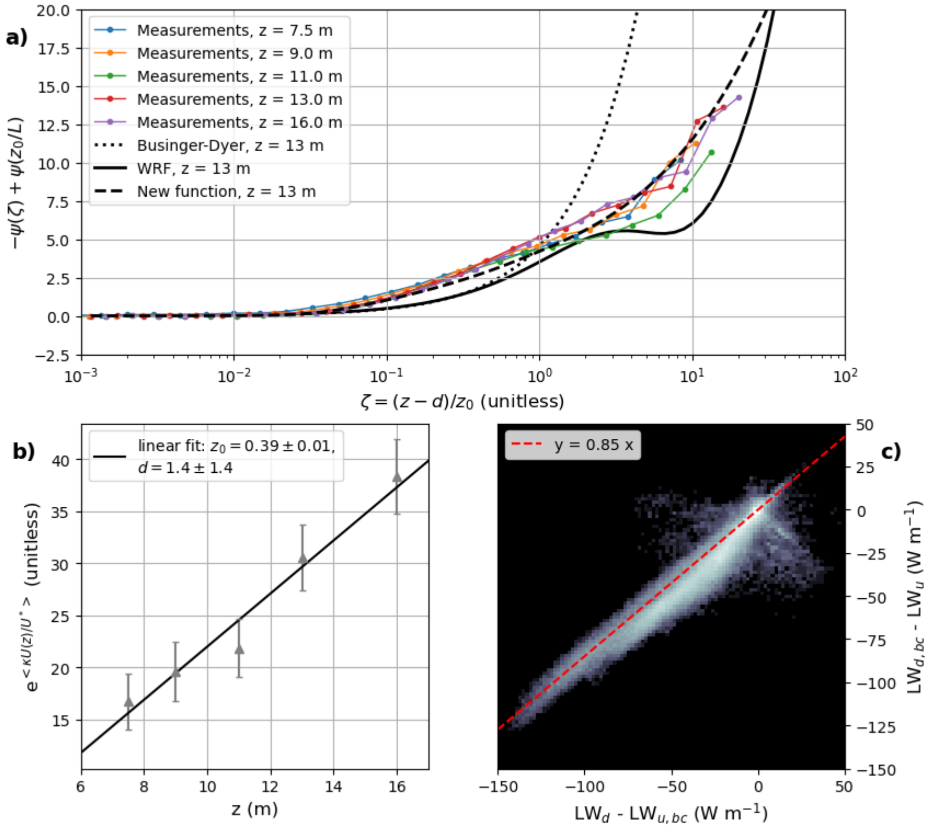

Figure 4.6: Panel a: momentum integral stability function as a function of ζ determined from the PRR site measurement (coloured lines) and calculated using the Businger-Dyer and WRF formulations (black lines). The dashed line corresponds to the new determined function for ψ (Eq. 4.22). Panel b: determination of the PRR site above-canopy momentum roughness length and displacement height. Panel c: 2D histogram of $\mathrm{LW}_{d,bc} - \mathrm{LW}_u$ vs $\mathrm{LW}_d - \mathrm{LW}_{u,bc}$. The red line corresponds to $y = 0.85x$, yielding a canopy emissivity of 0.15.

at weak stability ($\zeta \ll 1$), the wind profile is approximately logarithmic:

$$U_a \approx \frac{u^*}{\kappa} \log\left(\frac{z-d}{z_{0m}}\right)$$

Therefore, d and z_{0m} can be determined through a linear regression of $e^{\kappa U_a/u^*}$ against z when the data is restricted to values of $\zeta < 10^{-2}$. Here, z_{0m} was found to be 0.39 m with $d = 1.4 \pm 1.4$ m (Fig. 4.6b), which makes sense for a forest environment with short trees. The integral stability function ψ can also be determined from the data (assuming, as is often done, that it is the same for momentum and heat). In order to do this,

$$\Psi = -\psi(\zeta) + \psi(\frac{z_{0m}}{L}) = \frac{U_a}{u^*}\kappa - \log\left(\frac{z-d}{z_{0m}}\right)$$

is plotted as a function of ζ (Fig. 4.6a). Because z_{0m}/L is negligible compared to ζ, Ψ is approximately equal to $\psi(\zeta)$ at the first order. Here, we found that measured ψ is more gradual (i.e., more long-tailed) than the Businger-Dyer [Businger *et al.* 1971] or WRF (Eq. 4.17) functions. In fact, when plotted on a log-log scale, it became apparent that Ψ was proportional to $\sqrt{\zeta}$ at low values of ζ, and proportional to ζ^2 at high values of ζ. This differs from the often used z-less scaling, which implies that ψ must be proportional to ζ at least up to $\zeta \approx 0.1$ [Monin & Obukhov 1954, Grachev *et al.* 2013]; this is the case for the WRF and Businger-Dyer functions. Measurement error may explain some of the difference at $\zeta < 0.1$ as Ψ is very small in these conditions.

For our purposes, we determined an analytical expression of ψ to best fit to the Ψ measurements and left aside the question of the z-less scaling. The following expression for ψ was therefore considered:

$$\begin{aligned} \psi(\zeta) &= -a \cdot \zeta^{r(\zeta)} \\ r(\zeta) &= -0.75 \cdot \arctan(b \cdot \zeta - c)\frac{2}{\pi} + 1.25 \end{aligned} \tag{4.22}$$

This was chosen because $\arctan(x)$ tends to $\pm\frac{\pi}{2}$ when x tends to $\pm\infty$, with a smooth transition around $x = 0$. $r(\zeta)$ will therefore tend to 0.5 at low values of ζ and 2 at high values of ζ, similar to observations. The b and c coefficients must be chosen so that the timing and speed of the transition between the $\sqrt{\zeta}$ and ζ^2 asymptotes matches the observations. Values of $a = 5$, $b = 20$ and $c = 0.1$ were found to give a good fit to the observations (Fig. 4.6a). This expression of ψ was termed the PRR stability function.

The Ameriflux PRR site characteristics are summarized in Table 4.1. Although the location of the PRR site is given to be Evergreen Needleleaf Forest by the MODIS land-use categories as well as by the Ameriflux website, its canopy height and turbulent and radiative characteristics are actually most similar to a Wooded or Mixed Tundra.

4.4.2 Offline model evaluation

Two 1-layer and two 2-layer models are compared (Table 4.3). The 1-layer models include the original MYJ–Noah-LSM (oMYJ) combination, presented in Sect. 4.3.3, and a modified MYJ–Noah-LSM (mMYJ). The 2-layer models include the original Noah-MP (oMP) (with original Noah surface layer) and a modified version of Noah-MP (mMP). The oMYJ and oMP models were extracted from the WRF framework and recoded in Python in a minimal form, i.e. only the parts relating to the surface temperature calculation were kept. In particular, all latent heat flux calculations were ignored; the snow conductivity was assumed to be constant, equal to 0.3 W m^{-1} K^{-1}; and snow depth and ground temperature were used as input variables rather than being calculated. The recoding was checked to be correct by comparing the calculated turbulent diffusion coefficients to the output of actual WRF runs for different wind speeds.

Short name	Model	Type	Parameters	Turbulent diffusion coefficient	Comments
oMYJ	Recoded MYJ + Noah-LSM	1-layer	$d = 0$ m	WRF stability function	Max ζ set to 1
mMYJ	Modified MYJ + Noah-LSM	1-layer	$d = 1.4$ m	PRR stability function	Max ζ set to 100
oMP	Recoded Noah-MP (Original Noah surface layer)	2-layer	$d = 1.4$ m $z_{0mg} = 0.002$ m LAI = 0.73	Businger-Dyer stability function (top layer); Eq. 4.18 formulation (bottom layer)	Max ζ set to 1 – different vegetation and canopy air temp.
mMP	Modified Noah-MP	2-layer	idem.	PRR stability function (top layer); idem (bottom layer)	Max ζ set to 100 – $z_{0h} = 0.01 \cdot z_{0m}$ – $K = 0.0005$ (see text) – same vegetation and canopy air temp.

Table 4.3: Summary of the four surface models evaluated in this study. For all four models, z_{0m} was set to 0.39 m and λ_s to 0.3 W m^{-1} K^{-1}.

The guiding principle for the modifications to both original models was to improve the modelled dependency of the temperature inversion on the wind speed ('S' shape). This included removing the imposed maximum on ζ, so that a truly stable regime is allowed to develop. The stability function was also modified to better fit to its measured value (Sect. 4.4.1): this makes the transition more gradual, and avoids the non-monotonicity associated to the WRF stability function at $\zeta > 1$. Furthermore, a displacement height is added in the mMYJ model.

Modifications implemented in mMP included forcing the vegetation and canopy air temperature to be equal, so that the energy balance for the vegetated part is as described in 4.3.2. The canopy to ground turbulent diffusion coefficient was also calculated as in the MYJ surface layer instead of using Eq. 4.18. Lastly, a constant coefficient $K = 5 \times 10^{-4}$ m s^{-1} was added to $C_{D,a}U_a$. This effectively imposes a lower limit on the turbulent diffusion coefficient in a gradual way, without having to force a minimum which would create a discontinuity. At wind speeds greater than 3 m s^{-1}, this constant coefficient is negligible compared to the calculated value of $C_{D,a}U_c$. It should be noted that in effect, the original Noah-MP also imposes such a limit through indirect methods (for example, by imposing a minimum value of 1 m s^{-1} for U_a or a maximum value of 1 for ζ), so that the smallest value of $C_{D,a}U_c$ over the 20-day run described in Sect. 4.4.3 was 2.4×10^{-3} m s^{-1}. The reasons for imposing a lower limit on the turbulence are explored further in Sect. 4.5.1. Input parameters to all four models are set to correspond to the characteristics of the PRR site as determined in Sect. 4.4.1. For oMP and modified Noah-MP (mMP), f_{veg} was determined from the leaf area index using Eq. 4.20.

The five input variables to the Python models are the measured air temperature at 16 m, wind speed at 16 m, downwards longwave flux above the canopy, snow depth, and ground temperature. The output is the surface temperature (and canopy temperature for the 2-layer models). Running the models over the entirety of the curated PRR dataset yielded 5412 modelled values of surface temperature, which were then compared to the corresponding 5412 measured values of T_s. The results are analysed in Sect. 4.5.2.

4.4.3 WRF modelling: the 4–8 December 2019 case study

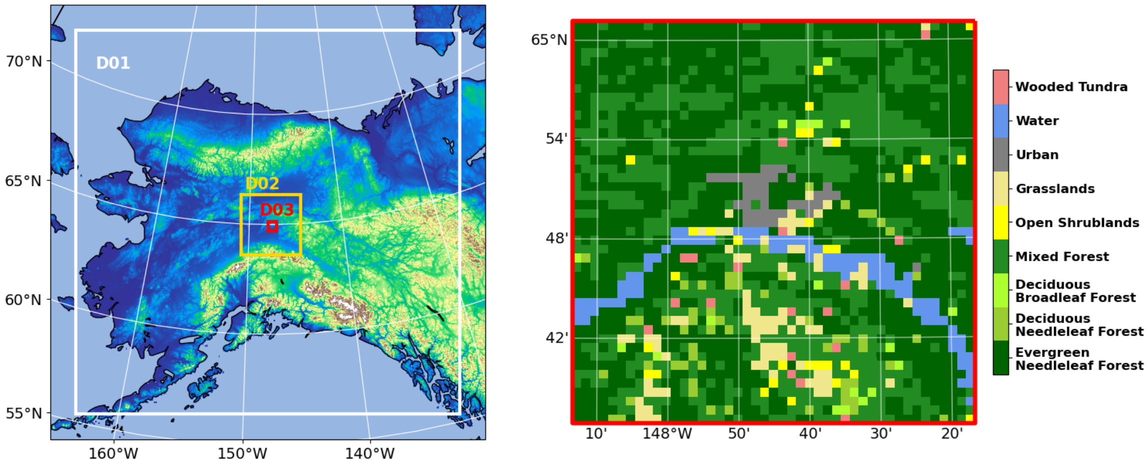

Figure 4.7: Left: representation of the nested domains in the studied WRF run. The first domain (D01) resolution is 15 km, second domain (D02) is 3 km, and third domain (D03) is 1 km. Right: MODIS land use category in D03. The city of Fairbanks is situated in the grey area (which indicates an urban land surface).

Module	Option
SW & LW radiation	RRTMG (Rapid Radiative Transfer Model) [Iacono *et al.* 2008]
Cumulus	Kain-Fritsch [Kain 2004] (only D01)
Boundary-layer	Mellor-Yamada-Janjic [Janjić 1994]
Microphysics	2-moment Morrison [Morrison *et al.* 2009]

Table 4.4: Summary of the different options used for the WRF runs.

The impact of the different WRF surface layer parametrisations on the model output are studied using a case study approach. From 4 to 8 December 2019, high pressures over central Alaska led to the disappearance of clouds, and the development of a strong SBI in the Fairbanks basin which lasted several days. This episode is described in detail in Chapter 3; because Fairbanks is surrounded almost entirely by forest, this is an instructive episode for testing the four models described above in real conditions.

WRF is set up with three nested domains (D01, D02 and D03). The boundary conditions for the largest domain (D01) are taken from ERA5, which is the latest reanalysis from the European Centre for Medium-Range Weather Forecast [Hersbach *et al.* 2020]. Its spatial resolution is 0.25°×0.25° and data is available every 6h. This domain is nudged to the ERA5 reanalysis above the boundary-layer to ensure that it does not diverge away from them during the first 7 days (i.e.,most of the "spin up" period). D01 then provides the boundary conditions for D02, and D02 provides the boundary conditions for D03; no feedback from the smaller to the larger domains is allowed. D01 has a 15 km resolution and spans the majority of Alaska, except for the Aleutian Islands. D02 and D01 have a 3 and 1 km resolution respectively. The model is run with 50 vertical levels in order to have a sufficient number of grid points in the boundary layer. The geometric height of the levels varies, but the lowest level is usually 13 to 15 m above the surface. The runs start on 23 November and end on 10 December, which allows for ten days of "spin up" before the period of interest.

The options used for the main WRF modules are summarized in Table 4.4. The MYJ scheme is chosen for the boundary-layer [Janjić 1994]. This is a 1.5–order local closure model: the turbulent kinetic energy (TKE) is a prognostic variable which is used to determine the turbulent diffusion coefficient at each height. It is often used for modelling stable boundary layers [Mölders & Kramm 2010, Sterk *et al.* 2015]. Indeed, it generates less turbulent mixing than non-local boundary-layer models such as the Yonsei University (YSU) scheme [Hong *et al.* 2006], which may cause it to have cold biases in more convective situations [Hu *et al.* 2010]. The MYJ surface layer, described above, is made to be used in conjunction with this boundary-layer scheme. Note that no cumulus scheme is used for the two smaller domains.

The evolution of the temperature difference between the lowest model level and the surface can then compared for the four simulations over the 4–8 December 2019 episode. The land use category at 1 km resolution is predominantly Mixed and Evergreen Needleleaf Forest (Fig. 4.7), so that model performance over forested areas can be contrasted. The results are shown in Sect. 4.5.3.

4.5 Results

4.5.1 Link between temperature gradients and wind speed at the Ameriflux PRR site

The average temperature profile (in difference from the temperature at 16 m) is shown in Fig. 4.8a. The impact of wind speed on the surface layer temperature profile is clear. For $U_a < 2$ m s^{-1}, the temperature decreases rapidly all the way

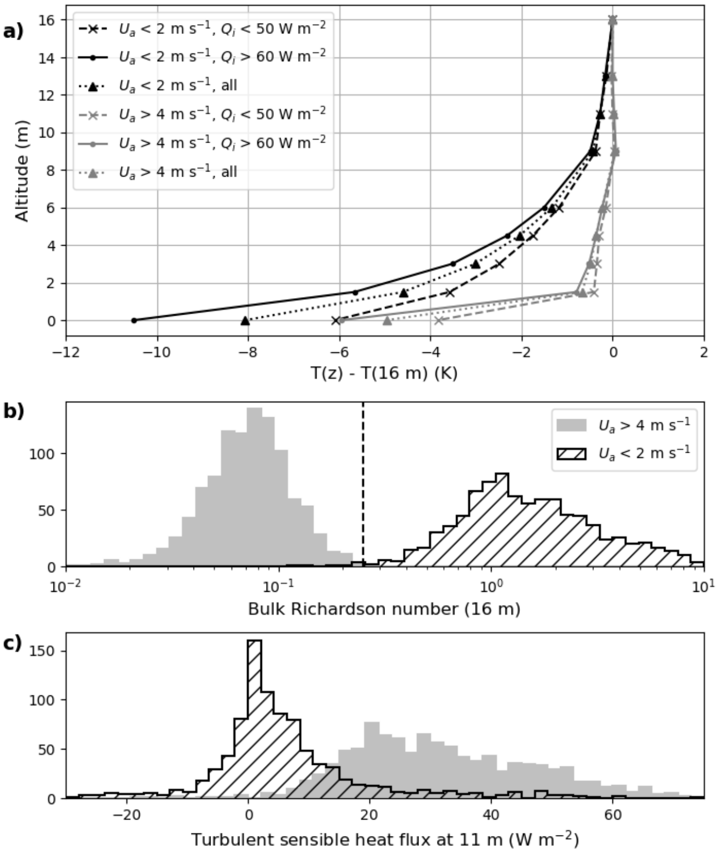

Figure 4.8: Panel a: average temperature difference from 16 m for wind speeds at 16 m smaller than 2 m s^{-1} (black lines) and higher than 4 m s^{-1} (grey lines). Continuous lines correspond to $Q_i > 60$ W m^{-2} and dashed lines to $Q_i < 50$ W m^{-2}. Panel b: histogram of R_b values calculated at 16 m, for wind speeds greater than 4 m s^{-1} (filled grey) or smaller than 2 m s^{-1} (hashed black). Panel c: histogram of turbulent sensible heat flux measured at 11 m (identical colours).

down to the surface and the bulk Richardson number is overwhelmingly greater than 0.25 (Fig. 4.8b), which is the traditionally cited limit value beyond which turbulence collapses. However, while the turbulent sensible heat flux has a low mean value of 4 W m^{-2}, its distribution remains quite spread out, with 5th and 95th percentiles of -12 and 30 W m^{-2} respectively (Fig. 4.8c). This indicates that there is some remaining turbulence.

For $U_a > 4$ m s^{-1}, the temperature gradient is very weak (approximately 0.5 °C) down to 1.5 m, with a strong temperature gradient remaining in the last meters. The top to bottom temperature difference is nevertheless smaller than for $U_a < 2$ m s^{-1}, leading to R_b values that are smaller than 0.25. Accordingly, the turbulent sensible heat flux is much larger than for the lower wind speeds: its mean is 32 W m^{-2}, with 90% of values between 11 and 60 W m^{-2}. The fact that both R_b and

H have clearly distinct distributions for wind speeds greater than 4 and lower than 2 m s^{-1} suggests that a threshold wind speed for sustainable turbulence probably occurs in this range. It should further be noted that while only the bulk Richardson number at 16 m is calculated here, the distributions are similar at other altitudes higher than 6 m. The impact of the radiative input (Q_i) is also clear in Fig. 4.8a. The average profiles corresponding to values of $Q_i > 60$ W m^{-2} exhibit a larger temperature gradient than those corresponding to values lower than 50 W m^{-2}, especially at low wind speeds. This is coherent with Sect. 4.3: greater radiative cooling leads to a larger SBI.

The relationship between the average air to surface temperature difference and wind speed is shown in Fig. 4.9c. $\Delta T = T_a - T_s$ decreases with U_a, reaching a minimum for $U_a > 5$ m s^{-1}, and there is a clear distinction between the averages corresponding to Q_i lower than 50 and greater than 60 W m^{-2} respectively. ΔT can further be broken down into $\Delta T_1 = T_{1.5m} - T_s$ (Fig. 4.9b) and $\Delta T_2 = T_a - T_{1.5m}$ (Fig. 4.9a). ΔT_2 exhibits a very clear 'S' shape, collapsing to less than 1 K at wind speeds higher than 4 m s^{-1}. ΔT_1, on the other hand, is maximum around 3 m s^{-1} for both ranges of Q_i. These behaviours are reminiscent of the two-layer model (Sect. 4.3.2): the main difference here is that ΔT_1 remains positive instead of decreasing to negative values at low wind speeds.

Examination of the temperature profiles and gradients in relation to wind speed at the PRR site therefore suggests that a 2-layer model may be able to reproduce the temperature gradients, with the temperature at 1.5 m being a proxy for the canopy temperature. The observations are compared in more detail to the models in Sect. 4.5.2.

4.5.2 Offline model behaviour compared to the PRR site measurements

The output of the 1-layer models (oMYJ and mMYJ) are shown in blue in Fig. 4.9c). Both tend to similar values as the observations for low wind speeds, although oMYJ does not reach a constant regime because ζ is limited to values of 1. Because this limit is removed in mMYJ, it better reproduces two regimes separated by a transition; this transition is however more gradual because the PRR stability function was used. Both models, however, predict too small values of ΔT at high wind speeds compared to the observations.

The 2-layer models, on the other hand, both show a much more gradual decrease of ΔT with U_a. Indeed, the decrease is so gradual in the output of oMP that it is not possible to discern two distinct regimes - even though the stability function used is Businger-Dyer, which is very short-tailed (see Fig. 4.2a, black lines compared to the grey line which corresponds to the the PRR stability function). One reason for this is that many limits are placed to maintain turbulence: u^* cannot become larger than 0.07 m s^{-1}, ζ must remain smaller than 1, and when the wind speed is used for calculating the turbulent diffusion coefficient it takes a minimum value of 1 m s^{-1} (this is only the case within the surface layer modules, so that WRF

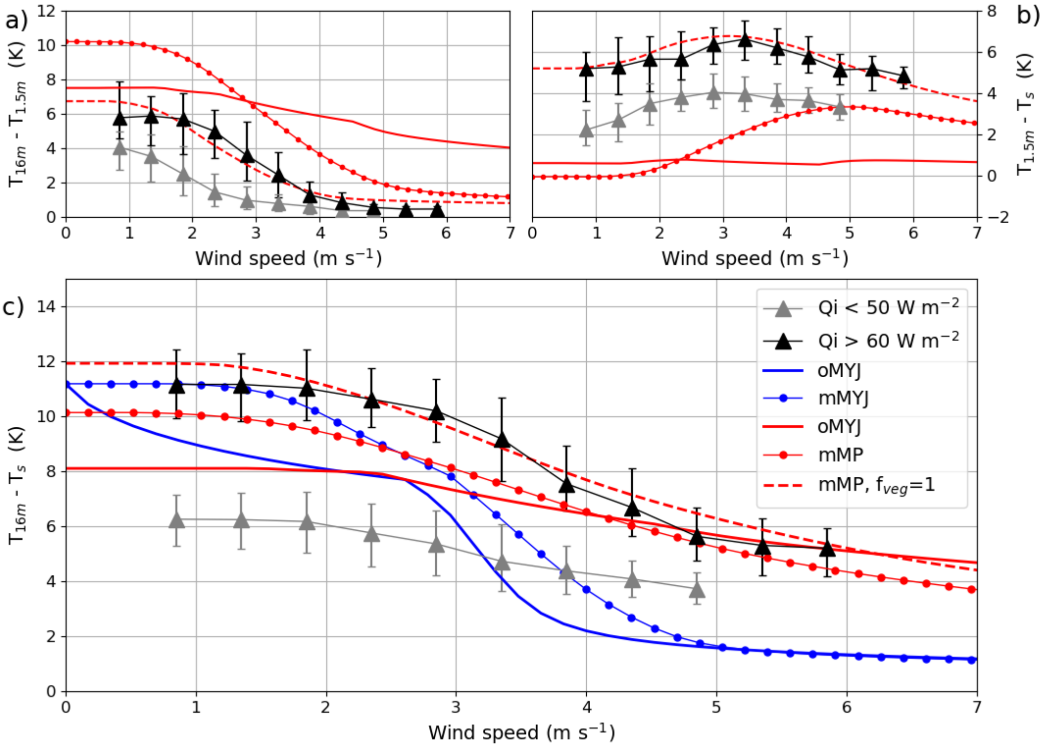

Figure 4.9: Panel a: average temperature difference between z_a = 16 m and 1.5 m as a function of wind speed at 16 m. Black and grey lines indicate averaged measurements for Q_i > 60 W m^{-2} and Q_i < 50 W m^{-2} respectively. Panel b: same, but for average temperature difference between 1.5 m and the surface. Panel c: same, but for the temperature difference between 16 m and the surface. The blue continuous and dotted lines correspond to the output of the oMYJ and mMYJ models respectively, for input values $Q_i = 65$ W m^{-2}, $T_a = 263.15$ K, $T_g = 271.15$ K and $\Lambda_s = 1$ W m^{-2} K^{-1}. The red continuous and dotted lines correspond to the output of the oMP and mMP models respectively, with the same input values of Q_i, T_a, T_g and Λ_s: ΔT_2 is plotted on panel a, ΔT_1 on panel b, and ΔT on panel c. The red dashed line corresponds to the same simulation as the dotted red line, except that f$_{veg}$ = 1.

still outputs wind speeds values less than 1 m s^{-1}). Although it is true that some turbulence is always maintained, as shown by the measurements at the PRR site (Fig. 4.8), the result is that Noah-MP model outputs too low ΔT values at very low wind speeds. oMP also does not reproduce the individual behaviour of ΔT_1 and ΔT_2: its calculated ΔT_2 does not have an 'S' shape as a function of wind speed and ΔT_1 exhibits no maximum.

The behaviour of mMP is more satisfactory. ΔT_2 shows a clear transition between a low-wind speed, high gradient state and a high-wind speed state where the gradient is close to 0. ΔT_1 has a maximum between 3 and 5 m s^{-1} (depending on the value of f_{veg}). ΔT, finally, is close to observation both in the high and low wind speed limits. Two things must be noted here. First, that values of ΔT_1 remain positive at low wind speeds because, as noted in Sect. 4.4.2, a constant K equal to 5×10^{-4} m s^{-1} has been added to $C_{D,a}U_a$. Similar to the limits imposed in oMP, this serves to maintain a certain level of turbulence and avoid the collapse of the turbulent sensible heat flux. Without this, ΔT_1 would decrease much more strongly as described in Sect. 4.3.2. Adding a constant, as opposed to imposing a maximum value, is a more gradual method which does not distort the shape of the transition. The constant value is chosen to best represent the observations, and should be discussed in regards to other datasets.

Secondly, two versions of mMP are shown in Fig. 4.9. The first corresponds to $f_{veg} = 0.3$ and $\varepsilon_v = 0.5$, which are the values which would be calculated by WRF from a LAI of 0.73 according to Eq. 4.20. The second corresponds to $f_{veg} = 1$ and $\varepsilon_v = 0.15$. The results are substantially different, especially as concerns the canopy temperature (and therefore ΔT_1 and ΔT_2). Indeed, as outlined in Sect. 4.3.2, the canopy tends to become colder than the surface for higher values of ε_v, and this is the case for the simulation with $f_{veg} = 0.3$. Furthermore, the transition wind speed (for ΔT_2) and wind speed at maximum ΔT_2 is shifted to lower values for the simulation with $f_{veg} = 1$.
These two sets of values both correspond to $\varepsilon_c = 0.15$, and therefore to the same radiative flux balance. However, the difference in outcome suggests that due to the turbulent fluxes, separating a bare from a vegetated fraction is not equivalent to considering only one layer, but with lower emissivity. The simulation with $f_{veg} = 1$ seems to perform better. One possible explanation is linked to the size of the eddies transporting heat. If they are of similar size to the typical distance between the trees, the turbulent transport of heat would not necessarily behave differently over a "bare" fraction than over a "vegetated" fraction. Instead, all turbulent transport would occur in an averaged manner. Indeed, the turbulent characteristics calculated in Sect. 4.4.1 are likely representative of this average, depending on the instrument footprint. At the PRR site, average tree distance is approximately 2.2 m assuming that the trees are homogeneously distributed (which seems reasonable from site photos, Fig. 4.5).

It is, however, not clear whether this is a robust feature of 2-layer model. Indeed, oMP does not appear to perform better when f_{veg} is set to 1 and ε_c to 0.15: its calculated values of ΔT decrease more rapidly with wind speed, and therefore remain smaller than the measured temperature difference over the whole wind speed range (not shown). In the following, the values of $f_{veg} = 0.3$ and $\varepsilon_v = 0.5$ are used for both 2-layer models.

The models are then run over all the PRR measurement points. Compared to the above analysis, this makes it possible to evaluate their behaviour for a wide variety of input values. Overall, all models capture some of the variability in ΔT, probably due to the influence of the downwards radiative fluxes. It is clear however that the 1-layer models always underestimate ΔT when the measured ΔT is lowest, which corresponds to conditions of high wind speeds (Fig. 4.10). oMYJ also underestimates

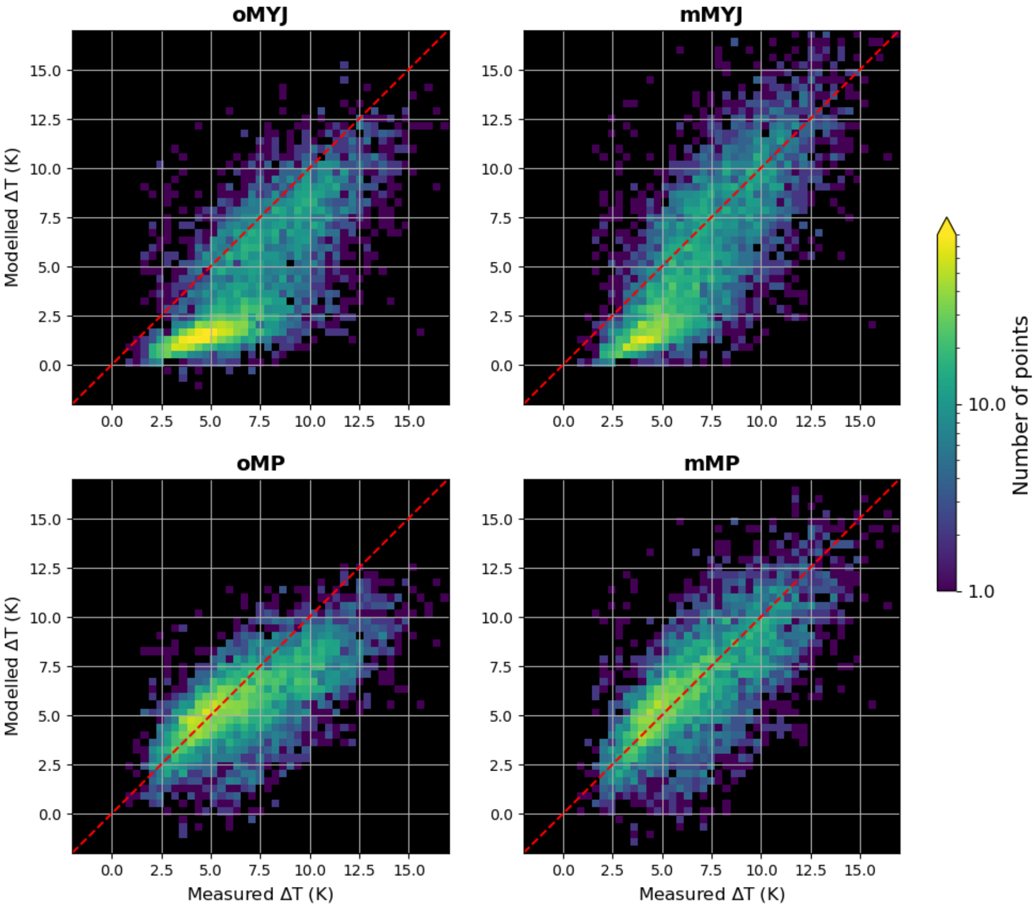

Figure 4.10: 2D histograms of the modelled vs measured $T_{16m} - T_s$ for the four models. Top row: 1-layer models (left: oMYJ and right: mMYJ). Bottom row: 2-layer models (left: oMP and right: mMP). The colour represents the number of points, in a log-normal scale and the red dashed line corresponds to the 1:1 line.

when the measured ΔT is very high, but this effect has been corrected in mMYJ by allowing a stronger decrease in turbulence. The root mean square error (RMSE) of mMYJ is therefore approximately 2.8 K as opposed to 3.4 K for the original MYJ–Noah-LSM.

The 2-layer models both perform better than the 1-layer models, supporting the idea that they are more adapted for use in a forest environment. The original Noah-MP model cannot reproduce strong values of ΔT because of excessive forced turbulence; mMP fares better in that regard. Its RMSE is slightly better (2.2 instead of 2.3 K). Note that running mMP with $\mathrm{f}_{veg} = 1$ and $\varepsilon_v = 0.15$ leads to an RMSE of 2.1 K.

4.5.3 WRF case study results

All of the three studied WRF setups correctly reproduced the synoptic conditions described in Sect. 3. Cloud fraction was zero above the smallest domain from 5

December 0000 UTC to 7 December 0100 UTC, with very similar timing between the simulations. This corresponds to the lidar observations: the low cloud cover disappeared before 5 December 1200 UTC, and the higher clouds a few hours later. Accordingly, WRF calculated Q_i was greater than 60 W m^{-2} from 4 to 7 December, with greater variability at the beginning and end of this period and very low variability on the 6th, a day which was entirely clear. The three WRF runs therefore also correctly predicted a global increase in the near-surface temperature gradient from 4 to 5 December, and a decrease from 7 to 8 December (Fig. 4.11). The lowest wind speeds overall were obtained on 4 and 5 December, after which they gradually increased. Putting aside the Field site which had a specific dynamic, this is similar to what was observed by the radiosondes at the Fairbanks airport (Fig. 3.4b). Interestingly, the three simulations exhibit the same four "nodes" of low wind speeds in the Fairbanks basin: these are most visible on 6 and 7 December (Fig. 4.11). These nodes are likely linked to the topography, with two of them close to the location of the Field site. Observations suggest that this should on the contrary be an area of heightened wind speeds compared to the centre of Fairbanks.

The influence of the wind speed on the temperature inversion is particularly obvious for the oMYJ and mMYJ simulations. From 5 to 7 December, the downwards radiative flux similar over the whole of the domain; nevertheless, the strength of the inversion is very contrasted over the domain. As 5 December had the low wind speeds over most of the domain, it also has the most area covered by strong inversions. On other days, around half of the whole domain area still appears to have temperature differences less than 4 K. On 7 December for example, the minimum ΔT in the mMYJ run is around 0 K while the maximum is around 15 K. The variations in ΔT are then spatially closely linked to the variations in wind speed, with the four "nodes" of low wind speed also being the locations of the highest temperature gradients. The main difference between the original MYJ–Noah-LSM and modified MYJ–Noah-LSM runs appear to be that the areas of low wind speeds have larger ΔT in the mMYJ run, which is coherent with the analysis of Sect. 4.5.2. Interestingly, the changes made to the surface layer appear to have had a feedback effect on the wind speed, which is larger in the mMYJ run: this is particularly visible on 6 and 7 December (Fig. 4.11).

The oMP run is qualitatively different. There is much less spatial variability in ΔT: overall, values range from 6 to 12 K from 5 to 7 December. In particular, there are no areas where the inversion is totally collapsed on these days, contrarily to the MYJ–Noah-LSM runs. This is coherent with results obtained from the recoded Noah-MP model (Sect. 4.5.2).

Overall, the surface layer and land surface model choice has a strong impact on the strength of the modelled temperature inversions and especially its stability. On 6 and 7 December, all three simulations had co-existing clear-skies (and therefore strong radiative cooling) and likely topographically driven wind speed variability. This means that the modelled dependence of the temperature gradient on the wind speed is the major factor determining the accuracy of the SBI representation, which has implications for studies of pollution using WRF.

4.6 Conclusions and discussions

A simple 2-layer analytical model of the stable surface layer was developed and contrasted with the existing 1-layer models of [van de Wiel *et al.* 2017]. The 2-layer model predicted a more gradual dependency of ΔT on the wind speed than the 1-layer models with equivalent roughness lengths and stability function. The top layer exhibited the 'S' shape dependence of the temperature gradient on the wind speed which is typical of 1-layer models. The bottom layer, on the other hand, had a maximum temperature gradient at the transition wind speed. However, results depended strongly on the value of the first layer emissivity. Insights gained from the theoretical models were applied to the study two surface layer/land surface model modules in WRF: Noah-MP and the Noah-LSM–MYJ combination. It was found that these models tend to set very restrictive boundaries on the turbulent diffusion coefficients and stability parameters, so that strong temperature gradients cannot be reached.

A combined approach was then used to study the performance of different surface layer models in more detail. First, an extensive set of measurements from the Poker Flats Research Range was analysed. It was found that under clear-sky, snow-covered, night-time conditions, the temperature gradient depended strongly on both the downwards longwave flux and the wind speed. When the wind speed at 16 m was smaller than 2 m s^{-1}, the temperature profile showed a very strong inversion down to the surface and the Richardson number was larger than 0.25, the traditional "cutoff" value for turbulence. Nevertheless, some turbulent sensible heat flux remained. On the other hand, when the wind speed was larger than 4 m s^{-1}, the temperature profile was roughly constant down to 1.5 m, below which a strong temperature gradient remained. The Richardson number was then below 0.25, corresponding to the traditional "weakly stable" regime. Furthermore, the dependence of the individual layer temperature inversion on wind speed were qualitatively similar to the theoretical 2-layer model.

Four different surface layer/ land-surface models were then coded into Python: the Noah-LSM–MYJ combination, Noah-MP, and modified versions of the two. These were compared to the observations first qualitatively, and then by inputting measured values of temperature and wind speed at different altitudes in the surface layer and comparing the outputted value of ΔT to the measurements. It was found that the 2-layer models both gave better results than the 1-layer models, which tended to predict too low temperature gradients at high wind speeds. On the other hand, the original Noah-MP predicted too low temperature gradients at low wind speeds. All in all, the modified Noah-MP gave the best results, especially for the individual layer temperature gradients.

Three of these four different models (original and modified Noah-LSM–MYJ, and Noah-MP) were then run in the larger WRF framework over a case study period and the results were compared. It was found that the Noah-LSM models tended to predict very large spatial variability of the temperature gradient, due to modelled variations of the wind speed. They did not therefore reproduce a global "cold pool" over the Tanana river basin. The Noah-MP model had weaker inversions, but they were more spread out spatially.

Open questions remain concerning the impact of local parameters on the simulations. Although the PRR site is classified as "Evergreen Needleleaf Forest", it trees are very short and spaced out, and its emissivity and roughness length low for a forest site. These parameters were shown to impact the behaviour of the lowest layer temperature gradient. Indeed, at high emissivities, the canopy layer is theoretically predicted to become colder than the surface. Furthermore, the value of the turbulent diffusion parameter for the surface to canopy air heat exchanges is taken from Monin–Obukhov similarity theory which assumes a log wind profile. Other parametrisations, such as the log-exp profile of [Mahat *et al.* 2013] which is implemented in Noah-MP, could conceivably yield better results in a denser forest. It would therefore be necessary to test the behaviour of the model compared to a denser forest site with higher trees.

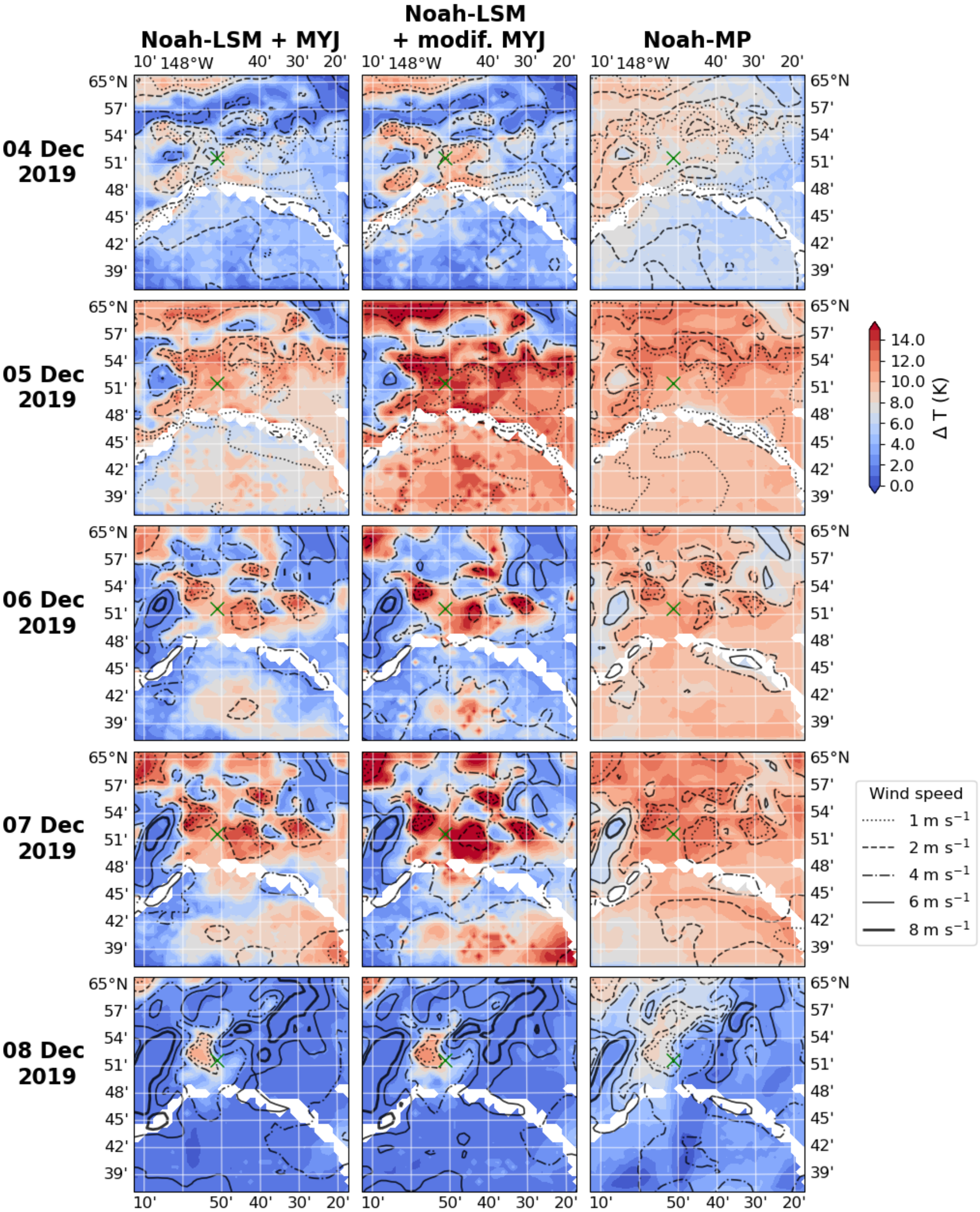

Figure 4.11: Temperature difference between the first model level and the surface (colour) and wind speed at the first model level (black lines) in the smallest domain for three different simulations (oMYJ, mMYJ and oMP) between 4 and 8 December 2019. All plots are taken at 0000 UTC. White pixels correspond to the Tanana River. The green cross indicates the location of the Field site.

Chapter 5

Conclusion

Contents

5.1 Results summary

In this thesis, boundary-layer processes and their impact on the SEB in the Arctic were studied, with a focus on two main characteristics of the Arctic boundary-layer: low-level clouds and surface based temperature inversions. Clouds in the Arctic are known to be very frequent, especially in the summer over the Arctic Ocean. They impact radiation received at the surface, with the net cloud radiative forcing depending on surface albedo, cloud water content and optical depth, and solar zenith angle. This surface impact is of climate importance, as the presence of clouds over open water is associated to increased surface warming in autumn [Kay & Gettelman 2009]; on the other hand, summer clouds control the sea-ice albedo feedback by slowing ice melt in the summer [Choi *et al.* 2020]. Understanding these effects requires solid data on cloud characteristics and their seasonal variation. However, cloud measurements are currently lacking over the sea-ice due to logistical constraints.

The first part of this thesis was therefore devoted to the analysis of a novel dataset of clouds properties derived from the IAOOS measurement campaign. 1777 profiles were collected from 2013 to 2019 by lidars mounted on ice-locked, drifting buoys. Despite technical difficulties like the icing over of the lidar window and receiver saturation due to the very low cloud cover, these profiles were exploited to detect low-cloud presence. It was found that clouds occurred more than 85% of the time from May to October, while the lowest clouds frequencies were in April, November and December (there were no exploitable profiles from January–March due to severe icing of the lidars). In most cases, the lidar signal was quickly absorbed so that only the characteristics of first cloud layers could be determined. This first cloud layer was both geometrically and optically thicker in October than in the summer, possibly linked to moisture intrusions caused by cyclonic activity from the Atlantic, and its base was found to be under 120 m in nearly all observations. The impact of clouds on the surface was then analyzed, using radiative flux data from the April–June period of the N-ICE 2015 campaign, during which

IAOOS buoys were deployed close to the main ice camp. The April–June distribution of measured LW_{net} during N-ICE 2015 was bimodal. The first LW_{net} mode, which accounted for around 20% of measurements, was centered around -72 W m^{-2}. Time-wise, these measurements were associated with cloudless IAOOS lidar profiles. The second mode (around 80% of cases) was centred around -11 W m^{-2} and linked to cloudy lidar profiles. The April–June CF_{LW} was therefore estimated to be 60 W m^{-2} on average. The winter LW_{net} distribution was already known to be bimodal [Stramler *et al.* 2011, Graham *et al.* 2017], with the difference between the "radiatively clear" and "opaquely cloudy" modes being around 40 W m^{-2}. The longwave radiative warming exerted by Arctic clouds is therefore larger in the summer than in the winter, likely due to higher cloud temperatures and greater liquid water content. The cloud shortwave radiative forcing was observed to depend strongly on SZ and cloud optical depth. When the sun was highest in the sky ($SZ \approx 60°$), CF_{SW} ranged from -20 W m^{-2} to -60 W m^{-2}. During N-ICE, the total cloud radiative forcing was therefore always positive, although sometimes weakly so. In order to estimate the total cloud radiative forcing beyond the end of the N-ICE measurement period, simple parametrisations of the cloud longwave and shortwave forcings were developed. Using these parametrisations and a simplified evolution of the summer albedo, it was estimated that optically thin clouds continue to warm the surface from June to September, while optically thick clouds have a cooling effect from mid June to mid August. Indeed, in the summer, no statistically significant temperature difference was found between 2 m temperatures measured by the IAOOS buoys in the presence and absence of clouds. This reinforced the idea that clouds do not uniformly cool the surface in the summer. These results highlighted that it is vital to take COD into account when estimating the possible climate impacts of clouds, and contributed to answer the thesis' first major question.

The second part of the thesis focused on the development of SBIs and their link to the surface energy balance. SBIs are known to develop preferentially in clear-sky winter conditions when the strong radiative deficit causes the surface to cool rapidly, leading to dampened turbulence and very stable conditions [Malingowski *et al.* 2014]. Nevertheless, recent theoretical and experimental studies have shown that the surface layer may remain weakly stable if the wind speed is above a certain threshold, known as minimum wind speed for sustainable turbulence [van de Wiel *et al.* 2017, Vignon *et al.* 2017]. This is significant because even in anticyclonic conditions, elevated wind speed may be maintained in the boundary-layer in the presence of topographically driven local flows [Fochesatto *et al.* 2013].

These questions were investigated during the pre-ALPACA campaign, which took place from 23 November to 12 December 2019 in Fairbanks, Alaska. A 4-component radiometer, sonic anemometer, and temperature sensor were deployed on a small mast in an open, snow-covered field while a lidar was placed in a downtown shelter. Radiosonde data was also available at the nearby Fairbanks airport. The 4–8 December period emerged as an instructive case study. The beginning of this period was marked by anticyclonic conditions over Interior Alaska: clouds disappeared due to adiabatic compression over Fairbanks, leading to net radiative fluxes of less than

-50 W m^{-2}. A strong SBI then developed at the Fairbanks airport on 6 December, associated to weak surface winds (less than 2 m s^{-1}). At the field measurement site, however, the near surface temperature gradient decreased over the same period and became negligible while wind speeds increased to over 5 m s^{-1}. This suggested that different processes were impacting the temperature gradient at the airport and Field sites. The entire campaign period was then analyzed from a statistical perspective. It became evident that the wind increase on 5 December was part of a larger pattern of elevated wind speed in clear-sky conditions at the Field site. Furthermore, the wind direction was north-westerly, indicating a flow from the Goldstream Valley. These elements suggested that a particular wind regime (possibly a drainage flow) occurred at the Field site, similar to the observations of [Fochesatto *et al.* 2013]. This wind regime led to the SEB having two preferred states. The first, associated to the presence of clouds and low wind speeds, was marked by net radiative and turbulent sensible heat fluxes close to 0 W m^{-2}. The second, associated to the absence of clouds and heightened wind speeds, was characterised by net radiative fluxes around - 45 W m^{-2} and turbulent sensible heat fluxes around 13 W m^{-2}: the case study period corresponded to this pattern. Furthermore, it was shown that wind speed determined the response of the near surface temperature gradient ΔT to $\mathrm{LW_{net}}$. When winds were below 2 m s^{-1}, ΔT increased strongly with decreasing $\mathrm{LW_{net}}$. On the other hand, when winds were above 3 m s^{-1}, ΔT was largely insensitive to $\mathrm{LW_{net}}$ because a non-negligible turbulent sensible heat flux could be maintained even at large radiative deficit. An MWST between 2–3 m s^{-1} was found to be in line with theoretical predictions based on [van Hooijdonk *et al.* 2015]. None of the two preferred states of the SEB were therefore linked to strong ΔT: the first because of low levels of radiative cooling, and the second because wind shear maintained significant mixing. As a result, long-lasting stable conditions were not established at the Field site.

These results showed that in the presence of complex topography in a sub-Arctic zone, local flows can lead to important spatial variations in SBIs under clear-sky conditions. This addressed the thesis' second major question, but subsequently led us to wonder whether meso-scale models correctly represent the dependence of the near-surface temperature gradient on wind speed. Because much of the sub-Arctic in general - and of the Fairbanks area in particular - is covered in forest, attention was paid to the impact of forest canopies on SBIs. First, two often used surface layer schemes/land surface model were isolated from the main framework of the WRF model. The first (oMYJ) was the combination of the Mellor-Yamada-Janjic (MYJ) surface layer and Noah-LSM. It was found to work in a similar fashion to the 1-layer analytical model of [van de Wiel *et al.* 2017], except that limits were placed on the stability parameter ζ so that excessive turbulence remained at low wind speeds and the very stable regime was eroded. The second isolated model (oMP) was the more recent Noah-MP scheme, which works both as a surface layer and land surface model. This is in effect a 2-layer model, with the canopy being explicitly taken into account. For comparison, a 2-layer analytical model was developed in the spirit of [van de Wiel *et al.* 2017]. This was composed of an air layer, a canopy layer, and the surface, implicitly assuming thermodynamic equilibrium between trees and canopy air. This model predicted an 'S' shape dependence of the temperature gradient on the wind speed for the air layer. The canopy layer temperature gradient, on the other hand, did not show this 'S' shape. For low values of the canopy emissivity, the temperature gradient reached a positive maximum value at intermediate wind speeds, before decreasing slowly. This was coherent with long-term observations at the Poker Flats Research Range (PRR), an Ameriflux measurement site 30 km away from Fairbanks, which showed that a strong temperature gradient maintained itself in the canopy even at high wind speeds. In comparison to this simplified scheme, oMP also was also found to place significant limits on the turbulent collapse at low wind speeds. Modified versions of oMYJ and oMP (mMYJ and mMP) were developed which placed less constraints on the turbulence. The four schemes were then evaluated compared to the Ameriflux PRR measurements. It was found that the 1-layer models underestimated the near surface temperature gradient in the weakly stable regime. The 2-layer models performed better on this point. Furthermore, the original models had difficulty in reproducing very strong values of ΔT. All in all, oMP performed best compared to the measurements. This showed the importance of both taking into account the canopy layer, and not placing restrictive limits on the turbulence, for modelling the SBI in forested areas.

5.2 Thesis perspectives

The impact of clouds and local circulations on the surface energy balance was highlighted in this thesis. Other factors impacting the SEB and SBI include surface characteristics, such as the presence of a forest canopy and the snow cover. This poses several questions and opens perspectives for future work.

In the Arctic Ocean, the lidar dataset obtained during IAOOS campaign was exploited to gain insight on the macro-physical characteristics of Arctic clouds. In parallel, work has been done to obtain the downwards radiative fluxes from the lidar-measured background radiation. So far, this method has been validated using the lidar data from the IAOOS buoys which were launched during N-ICE 2015 [Loyer *et al.* 2021]. Applying it to the rest of the IAOOS database will yield a multi-year dataset of the radiative fluxes in the high Arctic and open perspectives for extending the analysis of Chapter 2. Beyond IAOOS, the TARA Ocean Foundation is proposing an ambitious project for an International Polar Station, in the framework of which ships bearing measurement stations will be deployed from 2024 to 2045. This aims to fulfill the need for long-term monitoring of processes coupling the atmosphere, ocean and biology in the Arctic Ocean. The LATMOS contribution to this project, building on the experience of IAOOS, will be to install a radar and lidar in these floating stations, making it possible to measure cloud occurrence, microphysical and optical characteristics.

In the continental Arctic, this thesis raised questions concerning local flows, and in particular the one observed at the Field site during the pre-ALPACA campaign.

The only data available to describe this flow during the pre-ALPACA campaign came from one sonic anemometer at the Field site. This means that the spatial extent of this flow remains uncertain. First, its vertical extent, turbulent structure, and interaction with the temperature profile are unknown. Measurements of the turbulent sensible heat flux showed that it did not collapse when the near surface temperature gradient was nearly zero. This suggests that the column was not entirely well mixed; instead, some temperature inversion likely remained higher up and was being mixed down by larger eddies. Temperature profilers and wind lidars were present during the ALPACA campaign which took place from January to March 2022 and first observations suggest that they captured the local flow. Their data should shed some light on this question. Secondly, the origin of the flow and its horizontal dimensions once it enters the Tanana valley are also unclear. It was hypothesized to come from the Goldstream valley due to its location; however, upstream measurements are needed to verify this theory. These were also available during the ALPACA 2022 campaign and their analysis could constitute a follow-up study. More measurements might also shed light on whether this flow impacts the stability over downtown Fairbanks, which would have an impact on pollution dispersion. However, modelling could also be a useful tool for this. Presently, it does not appear that WRF is able to capture this flow, even at 1 km resolution. This suggests that a higher resolution of the topography is needed, which would in turn require running large-eddy simulations.

Other perspectives arise from the modelling of SBIs and turbulence in the presence of forest canopies. The analytical 2-layer model which was developed points to a strong impact of the canopy emissivity on the below-canopy temperature gradient. For very emissive canopies, the below-canopy layer is predicted to remain unstable even if the overlying air is very stably stratified. The Ameriflux PRR site was characterised by low canopy emissivity: it would therefore be interesting to compare the model behaviour to measurements in a dense forest with taller trees. It is furthermore unclear if the bulk Monin-Obukhov scheme used to represent the below-canopy turbulent fluxes would be appropriate in a denser forest, as opposed to a scheme such as [Mahat *et al.* 2013]. Lastly, the role of the vegetation fraction in the flux calculation should be discussed further. At the Ameriflux PRR site, the model performed better when there was no conceptual separation of a vegetated and non-vegetated fraction. This was theorised to be linked to the presence of eddies larger than the typical distance between the trees. This issue should be studied further. Once these points have been cleared, it would possible to re-code the mMP model, which was found to perform best, into the larger WRF framework.

The impact of clouds, wind and the forest canopy on the surface energy balance in the Arctic will further be investigated by the IMPECCABLE (IMPact on the Energy budget of mixed-phase Clouds and Canopy in the Arctic Boundary-LayEr) project, funded by Sorbonne Université - Émergence. As part of this project, a measurement campaign will take place at a forested site in Sodankylä, Finland from October 2022 to May 2023. Cloud macro- and microphysical characteristics will be determined using a radar-lidar synergy, and will be compared to radiometric measurements of the surface radiative fluxes in order to derive more precise parametrisations of these fluxes for meso-scale models. A radiometer- and sonic anemometer- equipped measurement mast will make it possible to investigate the energy balance of the canopy layer, and link it to the temperature gradients above and below the canopy. This will provide a very complete dataset characterising the boundary-layer and surface energy balance in the winter, and an important extension to the work begun in this thesis.

Bibliography

[Arrhenius 1896] S. Arrhenius. *On the influence of carbonic acid in the air upon the temperature of the ground.* Philos. Mag. J. Sci, vol. 5, pages 237–276, 1896. (Cited on pages 2 and 15.)

[Baas *et al.* 2017] P. Baas, B. J. H. van de Wiel, S. J. A. van der Linden and F. C. Bosveld. *From Near-Neutral to Strongly Stratified: Adequately Modelling the Clear-Sky Nocturnal Boundary Layer at Cabauw.* Boundary-Layer Meteorology, vol. 166, no. 2, pages 217–238, oct 2017. (Cited on page 96.)

[Baas *et al.* 2019] Peter Baas, Bas J. H. van de Wiel, Erik van Meijgaard, Etienne Vignon, Christophe Genthon, Steven J. A. van der Linden and Stephan R. de Roode. *Transitions in the wintertime near-surface temperature inversion at Dome C, Antarctica.* Quarterly Journal of the Royal Meteorological Society, vol. 145, no. 720, pages 930–946, 2019. (Cited on page 36.)

[Babić *et al.* 2016] Karmen Babić, Mathias W. Rotach and Zvjezdana B. Klaić. *Evaluation of local similarity theory in the wintertime nocturnal boundary layer over heterogeneous surface.* Agricultural and Forest Meteorology, vol. 228-229, pages 164–179, November 2016. (Cited on page 97.)

[Batchvarova *et al.* 2001] Ekaterine Batchvarova, Svan-Erik Gryning and Charlotte Bay Hasager. *Regional Fluxes Of Momentum And Sensible Heat Over A Sub-Arctic Landscape During Late Winter.* Boundary-Layer Meteorology, vol. 99, no. 3, pages 489–507, June 2001. (Cited on pages 33, 37, 97 and 103.)

[Beesley & Moritz 1999] J. A. Beesley and R. E. Moritz. *Toward an Explanation of the Annual Cycle of Cloudiness over the Arctic Ocean.* Journal of Climate, vol. 12, no. 2, pages 395–415, February 1999. (Cited on page 20.)

[Bintanja *et al.* 2011] R. Bintanja, E. C. van der Linden and W. Hazeleger. *Boundary layer stability and Arctic climate change: a feedback study using EC-Earth.* Climate Dynamics, vol. 39, no. 11, pages 2659–2673, dec 2011. (Cited on pages 2, 16 and 74.)

[Blanchard *et al.* 2014] Yann Blanchard, Jacques Pelon, Edwin W. Eloranta, Kenneth P. Moran, Julien Delanoë and Geneviève Sèze. *A Synergistic Analysis of Cloud Cover and Vertical Distribution from A-Train and Ground-Based Sensors over the High Arctic Station Eureka from 2006 to 2010.* Journal of Applied Meteorology and Climatology, vol. 53, no. 11, pages 2553–2570, 11 2014. (Cited on pages 3, 20 and 50.)

[Bourne *et al.* 2010] S.M. Bourne, U.S. Bhatt, J. Zhang and R. Thoman. *Surface-based temperature inversions in Alaska from a climate perspective.* Atmospheric Research, vol. 95, no. 2, pages 353–366, 2010. Special Section: Little Alaska Weather Symposium 2008. (Cited on pages 73 and 75.)

[Bradley *et al.* 1992] R. S. Bradley, F. T. Keimig and H. F. Diaz. *Climatology of surface based inversions in the North American Arctic.* Journal of Geophysical Research, pages 15699–15712, 1992. (Cited on pages 3, 23, 74 and 96.)

[Bucholtz 1995] A. Bucholtz. *Rayleigh-scattering calculations for the terrestrial atmosphere.* Optical Society of America, vol. 34, pages 2765–2773, 1995. (Cited on page 47.)

[Busch *et al.* 1982] N. Busch, U. Ebel, H. Kraus and E. Schaller. *The structure of the subpolar inversion-capped ABL.* Archives for meteorology, geophysics, and bioclimatology, Series A, vol. 31, no. 1, pages 1–18, March 1982. (Cited on page 23.)

[Businger *et al.* 1971] J. A. Businger, J. C. Wyngaard, Y. Izumi and E. F. Bradley. *Flux-Profile Relationships in the Atmospheric Surface Layer.* Journal of the Atmospheric Sciences, vol. 28, no. 2, pages 181–189, mar 1971. (Cited on pages 24, 32, 33, 99 and 110.)

[Cesana *et al.* 2012] G. Cesana, J. E. Kay, H. Chepfer, J. M. English and G. de Boer. *Ubiquitous low-level liquid-containing Arctic clouds: new observations and climate model constraints from CALIPSO-GOCCP.* Geophysical Research Letters, vol. 39, page L20804, 2012. (Cited on pages 58 and 60.)

[Chan & Comiso 2013] Mark Aaron Chan and Josefino C. Comiso. *Arctic Cloud Characteristics as Derived from MODIS, CALIPSO, and CloudSat.* Journal of Climate, vol. 26, no. 10, pages 3285–3306, 2013. (Cited on pages 3, 20, 41 and 49.)

[Chen & Dudhia 2001] Fei Chen and Jimy Dudhia. *Coupling an Advanced Land Surface–Hydrology Model with the Penn State–NCAR MM5 Modeling System. Part I: Model Implementation and Sensitivity.* Monthly Weather Review, vol. 129, no. 4, pages 569–585, April 2001. (Cited on page 104.)

[Cheng-Ying *et al.* 2011] Dai Cheng-Ying, Gao Zhi-Qiu, Wang Qing and Cheng Gang. *Analysis of Atmospheric Boundary Layer Height Characteristics over the Arctic Ocean Using the Aircraft and GPS Soundings.* Atmospheric and Oceanic Science Letters, vol. 4, no. 2, pages 124–130, jan 2011. (Cited on page 18.)

[Choi *et al.* 2020] Yong-Sang Choi, Jiwon Hwang, Jung Ok, Doo-Sun R. Park, Hui Su, Jonathan H. Jiang, Lei Huang and Ty Limpasuvan. *Effect of Arctic clouds on the ice-albedo feedback in midsummer.* International Journal of Climatology, vol. 40, no. 10, pages 4707–4714, 2020. (Cited on pages 2, 16, 35 and 123.)

[Cohen *et al.* 2017] Lana Cohen, Stephen R. Hudson, Von P. Walden, Robert M. Graham and Mats A. Granskog. *Meteorological conditions in a thinner Arctic sea ice regime from winter to summer during the Norwegian Young Sea Ice expedition (N-ICE2015).* Journal of Geophysical Research: Atmospheres, vol. 122, no. 14, pages 7235–7259, jul 2017. (Cited on pages 43 and 44.)

[Copernicus Climate Change Service (C3S)] Copernicus Climate Change Service (C3S). *ERA5: Fifth generation of ECMWF atmospheric reanalyses of the global climate.* (Cited on page 45.)

[Curry *et al.* 1988] J. A. Curry, E. E. Ebert and G. F. Herman. *Mean and turbulent structure of the summertime Arctic cloudy boundary layer.* Quarterly Journal of the Royal Meteorological Society, vol. 114, pages 715–746, 1988. (Cited on pages 40 and 52.)

[Curry *et al.* 1996] J. A. Curry, W. B. Rossow, D. Randall and J. L. Schramm. *Overview of Arctic cloud and radiation characteristics.* Journal of Climate, pages 1731–1763, 1996. (Cited on pages 19, 22, 40, 49, 52 and 56.)

[de Boer *et al.* 2009] Gijs de Boer, Edwin W. Eloranta and Matthew D. Shupe. *Arctic Mixed-Phase Stratiform Cloud Properties from Multiple Years of Surface-Based Measurements at Two High-Latitude Locations.* Journal of Atmospheric Science, vol. 66, no. 9, pages 2874–2887, 09 2009. (Cited on pages 3, 22 and 54.)

[Di Biagio *et al.* 2018] C. Di Biagio, J. Pelon, G. Ancellet, A. Bazureau and V. Mariage. *Sources, load, vertical distribution, and fate of wintertime aerosols north of Svalbard from combined V4 CALIOP data, ground-based IAOOS lidar observations and trajectory analysis.* Journal of Geophysical Research: Atmospheres, vol. 123, no. 2, pages 1363–1383, jan 2018. (Cited on pages 35, 40, 42, 43 and 48.)

[Di Biagio *et al.* 2021] C. Di Biagio, J. Pelon, Y. Blanchard, L. Loyer, S. R. Hudson, V. P. Walden, J. C. Raut, S. Kato, V. Mariage and M. A. Granskog. *Toward a Better Surface Radiation Budget Analysis Over Sea Ice in the High Arctic Ocean: A Comparative Study Between Satellite, Reanalysis, and local-scale Observations.* Journal of Geophysical Research: Atmospheres, vol. 126, no. 4, page e2020JD032555, 2021. (Cited on pages 35 and 40.)

[Ding *et al.* 2017] Qinghua Ding, Axel Schweiger, Michelle L'Heureux, David S. Battisti, Stephen Po-Chedley, Nathaniel C. Johnson, Eduardo Blanchard-Wrigglesworth, Kirstin Harnos, Qin Zhang, Ryan Eastman and Eric J. Steig. *Influence of high-latitude atmospheric circulation changes on summertime Arctic sea ice.* Nature Climate Change, vol. 7, no. 4, pages 289–295, mar 2017. (Cited on page 58.)

[Dong & Mace 2003] Xiquan Dong and Gerald G. Mace. *Arctic Stratus Cloud Properties and Radiative Forcing Derived from Ground-Based Data Collected at Barrow, Alaska.* Journal of Climate, vol. 16, no. 3, pages 445–461, 02 2003. (Cited on pages 19 and 54.)

[Dong *et al.* 2010] Xiquan Dong, Baike Xi, Kathryn Crosby, Charles N. Long, Robert S. Stone and Matthew D. Shupe. *A 10 year climatology of Arctic cloud fraction and radiative forcing at Barrow, Alaska.* Journal of Geophysical Research: Atmospheres, vol. 115, no. D17, 2010. (Cited on pages 3, 19, 30 and 31.)

[Dyer 1974] A. J. Dyer. *A review of flux-profile relationships.* Boundary-Layer Meteorology, vol. 7, no. 3, pages 363–372, November 1974. (Cited on page 32.)

[Ek *et al.* 2003] M. B. Ek, K. E. Mitchell, Y. Lin, E. Rogers, P. Grunmann, V. Koren, G. Gayno and J. D. Tarpley. *Implementation of Noah land surface model advances in the National Centers for Environmental Prediction operational mesoscale Eta model.* Journal of Geophysical Research: Atmospheres, vol. 108, no. D22, nov 2003. (Cited on page 104.)

[Engelmann *et al.* 2021] Ronny Engelmann, Albert Ansmann, Kevin Ohneiser, Hannes Griesche, Martin Radenz, Julian Hofer, Dietrich Althausen, Sandro Dahlke, Marion Maturilli, Igor Veselovskii, Cristofer Jimenez, Robert Wiesen, Holger Baars, Johannes Bühl, Henriette Gebauer, Moritz Haarig, Patric Seifert, Ulla Wandinger and Andreas Macke. *Wildfire smoke, Arctic haze, and aerosol effects on mixed-phase and cirrus clouds over the North Pole region during MOSAiC: an introduction.* Atmospheric Chemistry and Physics, vol. 21, no. 17, pages 13397–13423, September 2021. (Cited on page 19.)

[England & McNider 1995] David E. England and Richard T. McNider. *Stability functions based upon shear functions.* Boundary-Layer Meteorology, vol. 74, no. 1, pages 113–130, April 1995. (Cited on pages 33 and 99.)

[Exc 2018] *SPCM-AQRH datasheet*, 2018. (Cited on page 46.)

[Fisher 1922] R. A. Fisher. *On the Interpretation of Chi 2 from Contingency Tables, and the Calculation of P.* Journal of the Royal Statistical Society, vol. 85, no. 1, page 87, jan 1922. (Cited on page 53.)

[Fitzpatrick *et al.* 2003] M. F. Fitzpatrick, R. E. Brandt and S. G. Warren. *Transmission of solar radiation by clouds over snow and ice surfaces: a parameterization in terms of optical depth, solar zenith angle, and surface albedo.* Journal of Climate, vol. 17, pages 266–275, 2003. (Cited on pages 31 and 64.)

[Fochesatto *et al.* 2013] Gilberto J. Fochesatto, John A. Mayfield, Derek P. Starkenburg, Matthew A. Gruber and James Conner. *Occurrence of shallow cold* *flows in the winter atmospheric boundary layer of interior of Alaska.* Meteorology and Atmospheric Physics, vol. 127, no. 4, pages 369–382, oct 2013. (Cited on pages 36, 73, 75, 78, 85, 86, 87, 91, 124 and 125.)

[Foken & Wichura 1996] Th. Foken and B. Wichura. *Tools for quality assessment of surface-based flux measurements.* Agricultural and Forest Meteorology, vol. 78, no. 1-2, pages 83–105, jan 1996. (Cited on page 78.)

[Galperin *et al.* 2007] Boris Galperin, Semion Sukoriansky and Philip S. Anderson. *On the critical Richardson number in stably stratified turbulence.* Atmospheric Science Letters, vol. 8, no. 3, pages 65–69, 2007. (Cited on page 25.)

[Garnier *et al.* 2015] A. Garnier, J. Pelon, M. A. Vaughan, D. M. Winker, C. R. Trepte and P. Dubuisson. *Lidar multiple scattering factors inferred from CALIPSO lidar and IIR retrievals of semi-transparent cirrus cloud optical depths over oceans.* Atmospheric Mesaurement Techniques, vol. 8, pages 2759–2774, 2015. (Cited on pages 54 and 71.)

[Grachev *et al.* 2005] Andrey A. Grachev, Christopher W. Fairall, P. Ola G. Persson, Edgar L. Andreas and Peter S. Guest. *Stable Boundary-Layer Scaling Regimes: The Sheba Data.* Boundary-Layer Meteorology, vol. 116, no. 2, pages 201–235, August 2005. (Cited on pages 3, 24, 26 and 32.)

[Grachev *et al.* 2008] Andrey A. Grachev, Edgar L. Andreas, Christopher W. Fairall, Peter S. Guest and P. Ola G. Persson. *Turbulent measurements in the stable atmospheric boundary layer during SHEBA: ten years after.* Acta Geophysica, vol. 56, no. 1, pages 142–166, March 2008. (Cited on page 96.)

[Grachev *et al.* 2013] Andrey A. Grachev, Edgar L. Andreas, Christopher W. Fairall, Peter S. Guest and P. Ola G. Persson. *The Critical Richardson Number and Limits of Applicability of Local Similarity Theory in the Stable Boundary Layer.* Boundary-Layer Meteorology, vol. 147, no. 1, pages 51–82, April 2013. (Cited on pages 4, 25, 96 and 110.)

[Graham *et al.* 2017] R. M. Graham, A. Rinke, L. Cohen, S. R. Hudson, V. P. Walden, M. A. Granskog, W. Dorn, M. Kayser and M. Maturilli. *A comparison of the two Arctic atmospheric winter states observed during N-ICE2015 and SHEBA.* Journal of Geophysical Research: Atmospheres, vol. 122, no. 11, pages 5716–5737, jun 2017. (Cited on pages 4, 30, 44, 60, 61, 86 and 124.)

[Graham *et al.* 2019] Robert M Graham, Lana Cohen, Nicole Ritzhaupt, Benjamin Segger, Rune G Graversen, Annette Rinke, Von P Walden, Mats A Granskog and Stephen R Hudson. *Evaluation of six atmospheric reanalyses over Arctic sea ice from winter to early summer.* Journal of Climate, vol. 32, no. 14, pages 4121–4143, 2019. (Cited on page 61.)

[Graversen & Wang 2009] R. G. Graversen and M. Wang. *Polar amplification in a coupled climate model with locked albedo.* Climate Dynamics, vol. 33, pages 629–643, 2009. (Cited on page 15.)

[Graversen *et al.* 2008] Rune G. Graversen, Thorsten Mauritsen, Michael Tjernström, Erland Källén and Gunilla Svensson. *Vertical structure of recent Arctic warming.* Nature, vol. 451, no. 7174, pages 53–56, January 2008. (Cited on page 15.)

[Hahn *et al.* 1995] C. J. Hahn, S. G. Warren and J. London. *The effect of moonlight on observation of cloud cover at night, and application to cloud climatology.* Journal of Climate, vol. 8, pages 1429–1446, 1995. (Cited on pages 2, 19, 21 and 50.)

[Haid *et al.* 2021] Maren Haid, Alexander Gohm, Lukas Umek, Helen C. Ward and Mathias W. Rotach. *Cold-Air Pool Processes in the Inn Valley During Föhn: A Comparison of Four Cases During the PIANO Campaign.* Boundary-Layer Meteorology, October 2021. (Cited on page 75.)

[Hegyi & Taylor 2017] Bradley M. Hegyi and Patrick C. Taylor. *The regional influence of the Arctic Oscillation and Arctic Dipole on the wintertime Arctic surface radiation budget and sea ice growth.* Geophysical Research Letters, vol. 44, no. 9, pages 4341–4350, 2017. (Cited on page 15.)

[Helgason & Pomeroy 2012] Warren Helgason and John Pomeroy. *Problems Closing the Energy Balance over a Homogeneous Snow Cover during Midwinter.* Journal of Hydrometeorology, vol. 13, no. 2, pages 557–572, apr 2012. (Cited on pages 34, 77, 78, 89, 90 and 91.)

[Hersbach *et al.* 2020] Hans Hersbach, Bill Bell, Paul Berrisford, Shoji Hirahara, András Horányi, Joaquín Muñoz-Sabater, Julien Nicolas, Carole Peubey, Raluca Radu, Dinand Schepers, Adrian Simmons, Cornel Soci, Saleh Abdalla, Xavier Abellan, Gianpaolo Balsamo, Peter Bechtold, Gionata Biavati, Jean Bidlot, Massimo Bonavita, Giovanna Chiara, Per Dahlgren, Dick Dee, Michail Diamantakis, Rossana Dragani, Johannes Flemming, Richard Forbes, Manuel Fuentes, Alan Geer, Leo Haimberger, Sean Healy, Robin J. Hogan, Elías Hólm, Marta Janisková, Sarah Keeley, Patrick Laloyaux, Philippe Lopez, Cristina Lupu, Gabor Radnoti, Patricia Rosnay, Iryna Rozum, Freja Vamborg, Sebastien Villaume and Jean-Noël Thépaut. *The ERA5 global reanalysis.* Quarterly Journal of the Royal Meteorological Society, vol. 146, no. 730, pages 1999–2049, 6 2020. (Cited on pages 45, 81 and 113.)

[Holtslag & Bruin 1988] A. a. M. Holtslag and H. A. R. De Bruin. *Applied Modeling of the Nighttime Surface Energy Balance over Land.* Journal of Applied Meteorology and Climatology, vol. 27, no. 6, pages 689–704, June 1988. (Cited on pages 98, 99 and 104.)

[Holtslag *et al.* 2013] A. a. M. Holtslag, G. Svensson, P. Baas, S. Basu, B. Beare, A. C. M. Beljaars, F. C. Bosveld, J. Cuxart, J. Lindvall, G. J. Steeneveld, M. Tjernström and B. J. H. Van De Wiel. *Stable Atmospheric Boundary Layers and Diurnal Cycles: Challenges for Weather and Climate Models.* Bulletin of the American Meteorological Society, vol. 94, no. 11, pages 1691–1706, November 2013. (Cited on pages 36, 37 and 96.)

[Hong *et al.* 2006] Song-You Hong, Yign Noh and Jimy Dudhia. *A New Vertical Diffusion Package with an Explicit Treatment of Entrainment Processes.* Monthly Weather Review, vol. 134, no. 9, pages 2318–2341, sep 2006. (Cited on page 113.)

[Hu *et al.* 2010] Xiao-Ming Hu, John W. Nielsen-Gammon and Fuqing Zhang. *Evaluation of Three Planetary Boundary Layer Schemes in the WRF Model.* Journal of Applied Meteorology and Climatology, vol. 49, no. 9, pages 1831–1844, sep 2010. (Cited on page 113.)

[Hudson *et al.* 2016] Stephen R. Hudson, Lana Cohen and Von P. Walden. *N-ICE2015 surface broadband radiation data*, 2016. (Cited on pages 44, 60 and 63.)

[Iacono *et al.* 2008] Michael J. Iacono, Jennifer S. Delamere, Eli J. Mlawer, Mark W. Shephard, Shepard A. Clough and William D. Collins. *Radiative forcing by long-lived greenhouse gases: Calculations with the AER radiative transfer models.* Journal of Geophysical Research: Atmospheres, vol. 113, no. D13, 2008. (Cited on page 112.)

[Intrieri *et al.* 002a] J. M. Intrieri, C. W. Fairall, M. D. Shupe, P. O. G. Persson, E. L. Andreas, P. S. Guest and R. E. Moritz. *An annual cycle of Arctic surface cloud forcing at SHEBA.* Journal of Geophysical Research, vol. 107, page 8039, 2002a. (Cited on pages 4 and 41.)

[Intrieri *et al.* 002b] J. M. Intrieri, M. D. Shupe, T. Uttal and B. J. McCarty. *An annual cycle of Arctic cloud characteristics observed by radar and lidar at SHEBA.* Journal of Geophysical Research, vol. 107, page 8030, 2002b. (Cited on pages 3, 19, 50, 52 and 53.)

[Jacobs *et al.* 1992] A. F. G. Jacobs, J. H. van Boxel and R. H. Shaw. *The dependence of canopy layer turbulence on within-canopy thermal stratification.* Agricultural and Forest Meteorology, vol. 58, no. 3, pages 247–256, April 1992. (Cited on page 97.)

[Janjić 1994] Zaviša I. Janjić. *The Step-Mountain Eta Coordinate Model: Further Developments of the Convection, Viscous Sublayer, and Turbulence Closure Schemes.* Monthly Weather Review, vol. 122, no. 5, pages 927–945, May 1994. (Cited on pages 112 and 113.)

[Kahl 1990] Jonathan D. Kahl. *Characteristics of the low-level temperature inversion along the Alaskan Arctic coast.* International Journal of Climatology, vol. 10, no. 5, pages 537–548, 1990. (Cited on page 23.)

[Kaimal & Finnigan 1994] J.C. Kaimal and J. J. Finnigan. Atmospheric boundary layer flows: Their structure and measurement. Oxford University Press, 1994. (Cited on page 96.)

[Kain 2004] John S. Kain. *The Kain–Fritsch Convective Parameterization: An Update.* Journal of Applied Meteorology and Climatology, vol. 43, no. 1, pages 170–181, January 2004. (Cited on page 112.)

[Kambezidis *et al.* 2017] H. D. Kambezidis, B. E. Psiloglou, D. Karagiannis, U. C. Dumka and D. G. Kaskaoutis. *Meteorological Radiation Model (MRM v6.1): Improvements in diffuse radiation estimates and a new approach for implementation of cloud products.* Renewable Sustainable Energy Rev, vol. 74, pages 616–637, 2017. (Cited on page 64.)

[Kay & Gettelman 2009] J. E. Kay and A. Gettelman. *Cloud influence on and response to seasonal Arctic ice loss.* Journal of Geophysical Research, vol. 114, page D18204, 2009. (Cited on pages 2, 15, 16, 20, 35, 40 and 123.)

[Kay *et al.* 2016] J. E. Kay, T. L'Ecuyer, H. Chepfer, N. Loeb, A. Morrison and G. Cesana. *Recent advances in arctic cloud and climate research.* Current Climate Change Reports, vol. 2, pages 159–169, 2016. (Cited on pages 35 and 41.)

[Kobayashi *et al.* 2019] Hideki Kobayashi, Hiroki Ikawa and Rikie Suzuki. *AmeriFlux BASE US-Prr Poker Flat Research Range Black Spruce Forest (Ver. 3-5)*, 2019. (Cited on page 107.)

[Koenig *et al.* 2016] Zoé Koenig, Christine Provost, Nicolas Villacieros-Robineau, Nathalie Sennéchael and Amelie Meyer. *Winter ocean-ice interactions under thin sea ice observed by IAOOS platforms during N-ICE2015: Salty surface mixed layer and active basal melt.* Journal of Geophysical Research: Oceans, vol. 121, no. 10, pages 7898–7916, 2016. (Cited on pages 35, 40 and 43.)

[Kwok *et al.* 2013] R. Kwok, G. Spreen and S. Pang. *Arctic sea ice circulation and drift speed: Decadal trends and ocean currents.* Journal of Geophysical Research: Oceans, vol. 118, no. 5, pages 2408–2425, 2013. (Cited on page 15.)

[L2] (Cited on page 42.)

[Langer *et al.* 2011] M. Langer, S. Westermann, S. Muster, K. Piel and J. Boike. *The surface energy balance of a polygonal tundra site in northern Siberia – Part 2: Winter.* The Cryosphere, vol. 5, no. 2, pages 509–524, jun 2011. (Cited on pages 33 and 34.)

[Leuning *et al.* 2012] Ray Leuning, Eva van Gorsel, William J. Massman and Peter R. Isaac. *Reflections on the surface energy imbalance problem.* Agricultural and Forest Meteorology, vol. 156, pages 65–74, apr 2012. (Cited on pages 28, 91 and 92.)

[Liu *et al.* 2012] Y. Liu, J. R. Key, S. A. Ackermann, G.G. Mace and Q. Zhang. *Arctic cloud macrophysical characteristics from CloudSat and CALIPSO.* Remote Sensing of Environment, vol. 124, pages 159–173, 2012. (Cited on pages 20, 21, 51 and 52.)

[Louis 1979] Jean-François Louis. *A parametric model of vertical eddy fluxes in the atmosphere.* Boundary-Layer Meteorology, vol. 17, no. 2, pages 187–202, September 1979. (Cited on page 32.)

[Loyer *et al.* 2021] Lilian Loyer, Jean-Christophe Raut, Claudia Di Biagio, Julia Maillard, Vincent Mariage and Jacques Pelon. *Radiative fluxes in the High Arctic region derived from ground-based lidar measurements onboard drifting buoys.* Atmospheric Measurement Techniques Discussions, pages 1–29, November 2021. (Cited on pages 31 and 126.)

[Mahat *et al.* 2013] Vinod Mahat, David G. Tarboton and Noah P. Molotch. *Testing above- and below-canopy representations of turbulent fluxes in an energy balance snowmelt model.* Water Resources Research, vol. 49, no. 2, pages 1107–1122, 2013. (Cited on pages 103, 106, 121 and 127.)

[Mahrt *et al.* 2001] L. Mahrt, Dean Vickers, Reina Nakamura, M. R. Soler, Jielun Sun, Sean Burns and D.H. Lenschow. *Shallow Drainage Flows.* Boundary-Layer Meteorology, vol. 101, no. 2, pages 243–260, nov 2001. (Cited on page 75.)

[Mahrt *et al.* 2014] L. Mahrt, Jielun Sun and David Stauffer. *Dependence of Turbulent Velocities on Wind Speed and Stratification.* Boundary-Layer Meteorology, vol. 155, no. 1, pages 55–71, dec 2014. (Cited on page 96.)

[Mahrt 1998] L. Mahrt. *Nocturnal Boundary-Layer Regimes.* Boundary-Layer Meteorology, vol. 88, no. 2, pages 255–278, August 1998. (Cited on pages 3, 4 and 24.)

[Maillard *et al.* 2021] J. Maillard, F. Ravetta, J.-C. Raut, V. Mariage and J. Pelon. *Characterisation and surface radiative impact of Arctic low clouds from the IAOOS field experiment.* Atmospheric Chemistry and Physics, vol. 21, no. 5, pages 4079–4101, 2021. (Cited on pages 7, 40 and 80.)

[Malhi *et al.* 2005] Yadvinder Malhi, Keith McNaughton and Celso Von Randow. *A.* In Xuhui Lee, William Massman and Beverly Law, editors, Handbook of Micrometeorology: A Guide for Surface Flux Measurement and Analysis, pages 101–118. Springer Netherlands, Dordrecht, 2005. (Cited on pages 33 and 91.)

[Malhi 1995] Yadvinder S. Malhi. *The significance of the dual solutions for heat fluxes measured by the temperature fluctuation method in stable conditions.* Boundary-Layer Meteorology, vol. 74, no. 4, pages 389–396, June 1995. (Cited on pages 4 and 24.)

[Malingowski *et al.* 2014] J. Malingowski, D. Atkinson, J. Fochesatto, J. Cherry and E. Stevens. *An observational study of radiation temperature inversions in Fairbanks, Alaska.* Polar Sci, vol. 8, pages 24–39, 2014. (Cited on pages 23, 36, 74, 96 and 124.)

[Mann & Whitney 1947a] H. B. Mann and D. R. Whitney. *On a Test of Whether one of Two Random Variables is Stochastically Larger than the Other.* Annals of Mathematical Statistics, vol. 18, no. 1, pages 50–60, 03 1947. (Cited on page 54.)

[Mann & Whitney 1947b] H. B. Mann and D. R. Whitney. *On a Test of Whether one of Two Random Variables is Stochastically Larger than the Other.* The Annals of Mathematical Statistics, vol. 18, no. 1, pages 50–60, 1947. (Cited on page 86.)

[Mariage *et al.* 2017] Vincent Mariage, Jacques Pelon, Frédéric Blouzon, Stéphane Victori, Nicolas Geyskens, Nadir Amarouche, Christine Drezen, Antoine Guillot, Michel Calzas, Magali Garracio, Nicolas Wegmuller, Nathalie Sennéchael and Christine Provost. *IAOOS microlidar-on-buoy development and first atmospheric observations obtained during 2014 and 2015 arctic drifts.* Opt Express, vol. 25, no. 4, pages A73–A84, Feb 2017. (Cited on pages 42 and 48.)

[Mariage 2015] V. Mariage. *Développement et mise en oeuvre de LiDAR embarqués sur bouées dérivantes pour l'étude des propriétés des aérosols et des nuages en Arctique et des forçages radiatifs induits.* phdthesis, Université Pierre et Marie Curie - Paris VI, 2015. (Cited on pages 6, 35, 42, 45, 46 and 67.)

[Martínez *et al.* 2010] D. Martínez, M. A. Jiménez, J. Cuxart and L. Mahrt. *Heterogeneous Nocturnal Cooling in a Large Basin Under Very Stable Conditions.* Boundary-Layer Meteorology, vol. 137, no. 1, pages 97–113, jul 2010. (Cited on pages 23 and 75.)

[Mauder *et al.* 2020] Matthias Mauder, Thomas Foken and Joan Cuxart. *Surface-Energy-Balance Closure over Land: A Review.* Boundary-Layer Meteorology, vol. 177, no. 2-3, pages 395–426, may 2020. (Cited on pages 28 and 91.)

[Mayfield & Fochesatto 2013] John A. Mayfield and Gilberto J. Fochesatto. *The Layered Structure of the Winter Atmospheric Boundary Layer in the Interior of Alaska.* Journal of Applied Meteorology and Climatology, vol. 52, no. 4, pages 953–973, apr 2013. (Cited on pages 73, 74 and 75.)

[Mayfield & Fochesatto 2019] John A. Mayfield and Gilberto J. Fochesatto. *The Turbulence Regime of the Atmospheric Surface Layer in the Presence of Shallow Cold Drainage Flows: Application of Laser Scintillometry.* In Régis Barillé, editor, Turbulence and Related Phenomena, chapter 5. IntechOpen, Rijeka, 2019. (Cited on page 84.)

[Mioche & Jourdan 2018] Guillaume Mioche and Olivier Jourdan. *Chapter 6 - Spaceborne Remote Sensing and Airborne In Situ Observations of Arctic Mixed-Phase Clouds.* pages 121–150. Elsevier, January 2018. (Cited on page 20.)

[Mioche *et al.* 2015] G. Mioche, O. Jourdan, M. Ceccaldi and J. Delanoë. *Variability of mixed-phase clouds in the Arctic with a focus on the Svalbard region: a study based on spaceborne active remote sensing.* Atmospheric Chemistry and Physics, vol. 15, no. 5, pages 2445–2461, mar 2015. (Cited on pages 3 and 22.)

[Monin & Obukhov 1954] A Monin and A Obukhov. *Basic laws of turbulent mixing in the surface layer of the atmosphere.* Trudy Geofiz Inst Acad Nauk SSSR, vol. 24, no. 151, pages 163–187, 1954. (Cited on pages 96 and 110.)

[Moritz *et al.* 2002] Richard E. Moritz, Cecilia M. Bitz and Eric J. Steig. *Dynamics of Recent Climate Change in the Arctic.* Science, vol. 297, no. 5586, pages 1497–1502, August 2002. (Cited on page 15.)

[Morrison *et al.* 2009] H. Morrison, G. Thompson and V. Tatarskii. *Impact of Cloud Microphysics on the Development of Trailing Stratiform Precipitation in a Simulated Squall Line: Comparison of One- and Two-Moment Schemes.* Monthly Weather Review, vol. 137, no. 3, pages 991–1007, March 2009. (Cited on page 112.)

[Morrison *et al.* 2011] H. Morrison, G. de Boer, G. Feingold, J. Harrington, M. D. Shupe and K. Sulia. *Resilience of persistant Arctic mixed-phase clouds.* Nature Geoscience, vol. 5, pages 11–17, 2011. (Cited on page 40.)

[Morrison *et al.* 2018] A. L. Morrison, J. E. Kay, H. Chepfer, R. Guzman and V. Yettella. *Isolating the Liquid Cloud Response to Recent Arctic Sea Ice Variability Using Spaceborne Lidar Observations.* Journal of Geophysical Research: Atmospheres, vol. 123, no. 1, pages 473–490, 2018. (Cited on page 20.)

[Mölder *et al.* 1999] Meelis Mölder, Achim Grelle, Anders Lindroth and Sven Halldin. *Flux-profile relationships over a boreal forest — roughness sublayer corrections.* Agricultural and Forest Meteorology, vol. 98-99, pages 645–658, December 1999. (Cited on page 97.)

[Mölders & Kramm 2010] Nicole Mölders and Gerhard Kramm. *A case study on wintertime inversions in Interior Alaska with WRF.* Atmospheric Research, vol. 95, no. 2-3, pages 314–332, feb 2010. (Cited on page 113.)

[Nakai *et al.* 2013] Taro Nakai, Yongwon Kim, Robert C. Busey, Rikie Suzuki, Shin Nagai, Hideki Kobayashi, Hotaek Park, Konosuke Sugiura and Akihiko Ito. *Characteristics of evapotranspiration from a permafrost black spruce forest in interior Alaska.* Polar Science, vol. 7, no. 2, pages 136–148, June 2013. (Cited on pages 107 and 108.)

[Nakamura & Mahrt 2006] Reina Nakamura and L. Mahrt. *Vertically integrated sensible-heat budgets for stable nocturnal boundary layers.* Quarterly Journal of the Royal Meteorological Society, vol. 132, no. 615, pages 383–403, jan 2006. (Cited on page 91.)

[Niemelä *et al.* 2001a] Sami Niemelä, Petri Räisänen and Hannu Savijärvi. *Comparison of surface radiative flux parameterizations: Part I: Longwave radiation.* Atmospheric Research, vol. 58, no. 1, pages 1 – 18, 2001. (Cited on page 63.)

[Niemelä *et al.* 2001b] Sami Niemelä, Petri Räisänen and Hannu Savijärvi. *Comparison of surface radiative flux parameterizations: Part II: Shortwave radiation.* Atmospheric Research, vol. 58, no. 2, pages 141–154, jul 2001. (Cited on page 64.)

[Niu *et al.* 2011] Guo-Yue Niu, Zong-Liang Yang, Kenneth E. Mitchell, Fei Chen, Michael B. Ek, Michael Barlage, Anil Kumar, Kevin Manning, Dev Niyogi, Enrique Rosero, Mukul Tewari and Youlong Xia. *The community Noah land surface model with multiparameterization options (Noah-MP): 1. Model description and evaluation with local-scale measurements.* Journal of Geophysical Research: Atmospheres, vol. 116, no. D12, 2011. (Cited on page 104.)

[Nomokonova *et al.* 2019] Tatiana Nomokonova, Kerstin Ebell, Ulrich Löhnert, Marion Maturilli, Christoph Ritter and Ewan O'Connor. *Statistics on clouds and their relation to thermodynamic conditions at Ny-Alesund using ground-based sensor synergy.* Atmospheric Chemistry and Physics, vol. 19, no. 6, pages 4105–4126, apr 2019. (Cited on page 41.)

[O'Connor *et al.* 2004] E. J. O'Connor, A. J. Illingworth and R. J. Hogan. *A technique for autocalibration of cloud lidar.* Journal of Atmospheric and Oceanic Technology, vol. 21, pages 777–786, 2004. (Cited on page 54.)

[Overland & Wang 2005] James E. Overland and Muyin Wang. *The third Arctic climate pattern: 1930s and early 2000s.* Geophysical Research Letters, vol. 32, no. 23, 2005. (Cited on pages 14 and 15.)

[Overland *et al.* 2012] James E. Overland, Jennifer A. Francis, Edward Hanna and Muyin Wang. *The recent shift in early summer Arctic atmospheric circulation.* Geophysical Research Letters, vol. 39, no. 19, 2012. (Cited on page 15.)

[Overland *et al.* 2018] J. Overland, E. Dunlea, J. E. Box, R. Corell, M. Forsius, V. Kattsov, M. Olsen, J. Pawlak, L.-O. Reiersen and M. Wang. *The urgency of Arctic change.* Polar Science, pages 1–8, 2018. (Cited on pages 1 and 15.)

[Palo *et al.* 2017] Timo Palo, Timo Vihma, Jaak Jaagus and Erko Jakobson. *Observations of temperature inversions over central Arctic sea ice in summer.* Quarterly Journal of the Royal Meteorological Society, vol. 143, no. 708, pages 2741–2754, 2017. (Cited on page 23.)

[Perovich 2002] D. K. Perovich. *Seasonal evolution of the albedo of multiyear Arctic sea ice.* Journal of Geophysical Research, vol. 107, no. C10, 2002. (Cited on pages 28 and 66.)

[Pietroni *et al.* 2011] Ilaria Pietroni, Stefania Argentini, Igor Petenko and Roberto Sozzi. *Measurements and Parametrizations of the Atmospheric Boundary-Layer Height at Dome C, Antarctica.* Boundary-Layer Meteorology, vol. 143, no. 1, pages 189–206, dec 2011. (Cited on page 18.)

[Pithan & Mauritsen 2013] Felix Pithan and Thorsten Mauritsen. *Comments on "Current GCMs' Unrealistic Negative Feedback in the Arctic".* Journal of Climate, vol. 26, no. 19, pages 7783–7788, October 2013. (Cited on page 16.)

[Pithan & Mauritsen 2014] F. Pithan and T. Mauritsen. *Arctic amplification dominated by temperature feedbacks in contemporary climate models.* Nature Geoscience, vol. 7, pages 181–184, 2014. (Cited on pages 2, 16, 40, 60 and 74.)

[Platt 1973] C. M. R. Platt. *Lidar and radiometric observations of cirrus clouds.* Journal of Atmospheric Science, vol. 30, pages 1192–1204, 1973. (Cited on pages 30 and 48.)

[Pomeroy & Brun 2001] J Pomeroy and E Brun. *Physical properties of snow.* In H. G. Jones, editor, Snow ecology, chapter 2, pages 45–126. Cambridge University Press, 2001. (Cited on pages 32 and 34.)

[Quadrelli & Wallace 2004] Roberta Quadrelli and John M. Wallace. *A Simplified Linear Framework for Interpreting Patterns of Northern Hemisphere Wintertime Climate Variability.* Journal of Climate, vol. 17, no. 19, pages 3728–3744, October 2004. (Cited on page 15.)

[Raddatz *et al.* 2015] R. L. Raddatz, T. N. Papakyriakou, B. G. Else, M. G. Asplin, L. M. Candlish, R. J. Galley and D. G. Barber. *Downwelling longwave radiation and atmospheric winter states in the western maritime Arctic.* International Journal of Climatology, vol. 35, no. 9, pages 2339–2351, 2015. (Cited on page 30.)

[Refaat *et al.* 2008] T. F. Refaat, S. Ismail, M. N. Abedin, S. M. Spuler, S. D. Mayor and U. N. Singh. *Lidar backscatter signal recovery from phototransistor systematic effect by deconvolution.* Applied Optics, vol. 47, pages 5281–5295, 2008. (Cited on page 46.)

[Reno *et al.* 2012] M. J. Reno, C. W. Hansen and J. Stein. *Global horizontal irradiance clear sky models: implementation and analysis.* Technical report, Sandia National Laboratories, 2012. (Cited on page 64.)

[Richardson 1972] W. H. Richardson. *Bayesian-Based Iterative Method of Image Restoration.* Journal of the Optical Society of America, vol. 62, pages 55–59, 1972. (Cited on page 46.)

[Rigor *et al.* 2002] Ignatius G. Rigor, John M. Wallace and Roger L. Colony. *Response of Sea Ice to the Arctic Oscillation.* Journal of Climate, vol. 15, no. 18, pages 2648–2663, September 2002. (Cited on page 15.)

[Rohr *et al.* 1988] J. J. Rohr, E. C. Itsweire, K. N. Helland and C. W. Van Atta. *Growth and decay of turbulence in a stably stratified shear flow.* Journal of Fluid Mechanics, vol. 195, pages 77–111, October 1988. (Cited on page 24.)

[Rotach *et al.* 2004] Mathias W. Rotach, Pierluigi Calanca, Giovanni Graziani, Joachim Gurtz, D. G. Steyn, Roland Vogt, Marco Andretta, Andreas Christen, Stanislaw Cieslik, Richard Connolly, Stephan F. J. De Wekker, Stefano Galmarini, Evgeny N. Kadygrov, Vladislav Kadygrov, Evgeny Miller, Bruno Neininger, Magdalena Rucker, Eva Van Gorsel, Heidi Weber, Alexandra Weiss and Massimiliano Zappa. *Turbulence Structure and Exchange Processes in an Alpine Valley: The Riviera Project.* Bulletin of the American Meteorological Society, vol. 85, no. 9, pages 1367–1386, September 2004. (Cited on page 75.)

[Sandu *et al.* 2013] Irina Sandu, Anton Beljaars, Peter Bechtold, Thorsten Mauritsen and Gianpaolo Balsamo. *Why is it so difficult to represent stably stratified conditions in numerical weather prediction (NWP) models?* Journal of Advances in Modeling Earth Systems, vol. 5, no. 2, pages 117–133, 2013. (Cited on page 36.)

[Schmetz *et al.* 1986] P. Schmetz, J. Schmetz and E. Raschke. *Evaluation of daytime downward longwave radiation at the surface from satellite and grid point data.* Theoretical and Applied Climatology, vol. 37, pages 136–149, 1986. (Cited on page 63.)

[Sengupta *et al.* 2003] M. Sengupta, E. E. Clothiaux, T. P. Ackermann, S. Kato and Q. Min. *Importance of accurate liquid water path for estimation of solar radiation in warm boundary layer clouds: an observational study.* Journal of Climate, vol. 16, pages 2997–3009, 2003. (Cited on page 22.)

[Serreze & Barry 2011] M. C. Serreze and R. G. Barry. *Processes and impacts of Arctic amplification: a research synthesis.* Global Planet Change, vol. 77, pages 85–96, 2011. (Cited on pages 1 and 15.)

[Serreze *et al.* 1992] M. C. Serreze, J. D. Kahl and R. C. Schnell. *Low-level temperature inversions of the Eurasian Arctic and comparisons with Soviet drifting* *station data*. Journal of Climate, pages 615–629, 1992. (Cited on pages 3, 22, 23, 74 and 96.)

[Shupe & Intrieri 2003] M. D. Shupe and J. M. Intrieri. *Cloud radiative forcing of the Arctic surface: the influence of cloud properties, surface albedo, and solar zenith angle*. Journal of Climate, vol. 17, pages 616–628, 2003. (Cited on pages 22, 29, 30, 31 and 63.)

[Shupe *et al.* 2006] M. D. Shupe, S. Y. Matrosov and T. Uttal. *Arctic mixed-phase cloud properties derived from surface-based sensors at SHEBA*. Journal of Atmospheric Science, vol. 63, pages 697–709, 2006. (Cited on pages 20, 40, 41 and 67.)

[Shupe *et al.* 2007] M. Shupe, J. Intrieri and T. Uttal. *ETL Radar-Lidar 10-min Cloud Physical Properties. Version 1.0.*, 2007. (Cited on pages 53 and 54.)

[Shupe *et al.* 2011] Matthew D. Shupe, Von P. Walden, Edwin Eloranta, Taneil Uttal, James R. Campbell, Sandra M. Starkweather and Masataka Shiobara. *Clouds at Arctic Atmospheric Observatories. Part I: Occurrence and Macrophysical Properties*. Journal of Applied Meteorology and Climatology, vol. 50, no. 3, pages 626–644, mar 2011. (Cited on page 41.)

[Simpson *et al.* 2019] William Simpson, Kathy Law, Julia Schmale, Kerri Pratt, Stephen Arnold and Jingqiu Mao. *Alaskan Layered Pollution And Chemical Analysis (ALPACA) White Paper*. Technical report, University of Alaska Fairbanks, 2019. (Cited on page 76.)

[Sorbjan & Czerwinska 2013] Zbigniew Sorbjan and Agnieszka Czerwinska. *Statistics of Turbulence in the Stable Boundary Layer Affected by Gravity Waves*. Boundary-Layer Meteorology, vol. 148, no. 1, pages 73–91, July 2013. (Cited on page 96.)

[Sotiropoulou *et al.* 2016] Georgia Sotiropoulou, Michael Tjernström, Joseph Sedlar, Peggy Achtert, Barbara J. Brooks, Ian M. Brooks, P. Ola G. Persson, John Prytherch, Dominic J. Salisbury, Matthew D. Shupe, Paul E. Johnston and Dan Wolfe. *Atmospheric conditions during the Arctic Clouds in Summer Experiment (ACSE): Contrasting open water and sea ice surfaces during melt and freeze-up seasons*. Journal of Climate, vol. 29, no. 24, pages 8721–8744, nov 2016. (Cited on page 41.)

[Steeneveld *et al.* 2006] G. J. Steeneveld, B. J. H. Van De Wiel and A. A. M. Holtslag. *Modelling the Arctic Stable Boundary Layer and its Coupling to the Surface*. Boundary-Layer Meteorology, vol. 118, no. 2, pages 357–378, feb 2006. (Cited on page 96.)

[Sterk *et al.* 2013] H. a. M. Sterk, G. J. Steeneveld and A. a. M. Holtslag. *The role of snow-surface coupling, radiation, and turbulent mixing in modeling a* *stable boundary layer over Arctic sea ice.* Journal of Geophysical Research: Atmospheres, vol. 118, no. 3, pages 1199–1217, 2013. (Cited on page 96.)

[Sterk *et al.* 2015] H. a. M. Sterk, G. J. Steeneveld, T. Vihma, P. S. Anderson, F. C. Bosveld and A. a. M. Holtslag. *Clear-sky stable boundary layers with low winds over snow-covered surfaces. Part 1: WRF model evaluation.* Quarterly Journal of the Royal Meteorological Society, vol. 141, no. 691, pages 2165–2184, 2015. (Cited on pages 36, 37 and 113.)

[Stramler *et al.* 2011] K. Stramler, A. D. Del Genio and W. B. Rossow. *Synoptically driven Arctic winter states.* Journal of Climate, vol. 24, pages 1747–1762, 2011. (Cited on pages 4, 30, 41, 58, 86 and 124.)

[Stull 1988] Roland B. Stull, editor. An introduction to boundary layer meteorology. Springer Netherlands, 1988. (Cited on pages 2, 17 and 26.)

[Sugiura *et al.* 2011] Konosuke Sugiura, Rikie Suzuki, Taro Nakai, Bob Busey, Larry Hinzman, Hotaek Park, Yongwon Kim, Shin Nagai, Kazuyuki Saito, Jessica Cherry, Akihiko Ito, Tetsuo Ohata and John Walsh. *Supersite as a common platform for multi-observations in Alaska for a collaborative framework between JAMSTEC and IARC.* JAMSTEC Report of Research and Development, vol. 12, pages 61–69, 2011. (Cited on page 107.)

[Sun *et al.* 2012] Jielun Sun, Larry Mahrt, Robert M. Banta and Yelena L. Pichugina. *Turbulence Regimes and Turbulence Intermittency in the Stable Boundary Layer during CASES-99.* Journal of Atmospheric Science, vol. 69, no. 1, pages 338–351, jan 2012. (Cited on pages 89 and 96.)

[Sun *et al.* 2016] Jielun Sun, Donald H. Lenschow, Margaret A. LeMone and Larry Mahrt. *The Role of Large-Coherent-Eddy Transport in the Atmospheric Surface Layer Based on CASES-99 Observations.* Boundary-Layer Meteorology, vol. 160, no. 1, pages 83–111, feb 2016. (Cited on page 89.)

[Tastula & Vihma 2011] Esa-Matti Tastula and Timo Vihma. *WRF Model Experiments on the Antarctic Atmosphere in Winter.* Monthly Weather Review, vol. 139, no. 4, pages 1279–1291, April 2011. (Cited on page 36.)

[Taylor *et al.* 2015] Patrick C. Taylor, Seiji Kato, Kuan-Man Xu and Ming Cai. *Covariance between Arctic sea ice and clouds within atmospheric state regimes at the satellite footprint level.* Journal of Geophysical Research: Atmospheres, vol. 120, no. 24, pages 12656–12678, 2015. (Cited on page 20.)

[Thompson & Wallace 1998] David W. J. Thompson and John M. Wallace. *The Arctic oscillation signature in the wintertime geopotential height and temperature fields.* Geophysical Research Letters, vol. 25, no. 9, pages 1297–1300, 1998. (Cited on page 14.)

[Tjernström *et al.* 2008] Michael Tjernström, Joseph Sedlar and Matthew D. Shupe. *How Well Do Regional Climate Models Reproduce Radiation and Clouds in the Arctic? An Evaluation of ARCMIP Simulations.* Journal of Applied Meteorology and Climatology, vol. 47, no. 9, pages 2405–2422, 2008. (Cited on page 40.)

[Tjernström *et al.* 2012] M Tjernström, Cathryn E Birch, Ian M Brooks, Matthew D Shupe, P Ola G Persson, Joseph Sedlar, Thorsten Mauritsen, Caroline Leck, Jussi Paatero, Malagorzata Szczodrak*et al. Meteorological conditions in the central Arctic summer during the Arctic Summer Cloud Ocean Study (ASCOS).* Atmos Chem Phys, vol. 12, no. 15, pages 6863–6889, 2012. (Cited on pages 19, 33 and 53.)

[Tjernström *et al.* 2014] Michael Tjernström, Caroline Leck, Cathryn E Birch, Jan W Bottenheim, Barbara J Brooks, Ian M Brooks, Leif Bäcklin, Rachel Chang, Gerrit de Leeuw, Luca Di Liberto*et al. The Arctic Summer Cloud Ocean Study (ASCOS): overview and experimental design.* Atmospheric Chemistry and Physics, 2014. (Cited on page 41.)

[Tjernström 2005] Michael Tjernström. *The Summer Arctic Boundary Layer during the Arctic Ocean Experiment 2001 (AOE-2001).* Boundary-Layer Meteorology, vol. 117, no. 1, pages 5–36, oct 2005. (Cited on page 18.)

[Turner 2005] D. D. Turner. *Arctic mixed-phase cloud properties from AERI Lidar observations: algorithm and results from SHEBA.* Journal of Applied Meteorology, vol. 44, pages 427–444, 2005. (Cited on pages 22 and 56.)

[Ueyama *et al.* 2018] Masahito Ueyama, Hiroki Iwata and Yoshinobu Harazono. *AmeriFlux AmeriFlux US-Uaf University of Alaska, Fairbanks, Ver. 9-5, Ameriflux AMP (Dataset)*, 2018. (Cited on page 77.)

[Uttal *et al.* 2016] Taneil Uttal, Sandra Starkweather, James R. Drummond, Timo Vihma, Alexander P. Makshtas, Lisa S. Darby, John F. Burkhart, Christopher J. Cox, Lauren N. Schmeisser, Thomas Haiden, Marion Maturilli, Matthew D. Shupe, Gijs De Boer, Auromeet Saha, Andrey A. Grachev, Sara M. Crepinsek, Lori Bruhwiler, Barry Goodison, Bruce McArthur, Von P. Walden, Edward J. Dlugokencky, P. Ola G. Persson, Glen Lesins, Tuomas Laurila, John A. Ogren, Robert Stone, Charles N. Long, Sangeeta Sharma, Andreas Massling, David D. Turner, Diane M. Stanitski, Eija Asmi, Mika Aurela, Henrik Skov, Konstantinos Eleftheriadis, Aki Virkkula, Andrew Platt, Eirik J. Førland, Yoshihiro Iijima, Ingeborg E. Nielsen, Michael H. Bergin, Lauren Candlish, Nikita S. Zimov, Sergey A. Zimov, Norman T. O'Neill, Pierre F. Fogal, Rigel Kivi, Elena A. Konopleva-Akish, Johannes Verlinde, Vasily Y. Kustov, Brian Vasel, Viktor M. Ivakhov, Yrjö Viisanen and Janet M. Intrieri. *International Arctic Systems for Observing the Atmosphere: An International Polar Year Legacy Consortium.* Bulletin of the

American Meteorological Society, vol. 97, no. 6, pages 1033–1056, 07 2016. (Cited on page 41.)

[van de Wiel *et al.* 2007] B. J. H. van de Wiel, A. F. Moene, G. J. Steeneveld, O. K. Hartogensis and A. A. M. Holtslag. *Predicting the Collapse of Turbulence in Stably Stratified Boundary Layers.* Flow, Turbulence and Combustion, vol. 79, no. 3, pages 251–274, October 2007. (Cited on page 96.)

[van de Wiel *et al.* 2012] B. J. H. van de Wiel, A. F. Moene, H. J. J. Jonker, P. Baas, S. Basu, J. M. M. Donda, J. Sun and A. A. M. Holtslag. *The Minimum Wind Speed for Sustainable Turbulence in the Nocturnal Boundary Layer.* Journal of Atmospheric Science, vol. 69, no. 11, pages 3116–3127, nov 2012. (Cited on pages 25, 32, 36, 74, 89, 96 and 100.)

[van de Wiel *et al.* 2017] Bas J. H. van de Wiel, Etienne Vignon, Peter Baas, Ivo G. S. van Hooijdonk, Steven J. A. van der Linden, J. Antoon van Hooft, Fred C. Bosveld, Stefan R. de Roode, Arnold F. Moene and Christophe Genthon. *Regime Transitions in Near-Surface Temperature Inversions: A Conceptual Model.* Journal of the Atmospheric Sciences, vol. 74, no. 4, pages 1057–1073, mar 2017. (Cited on pages 9, 25, 32, 37, 74, 96, 97, 98, 99, 100, 120, 124 and 125.)

[van Hooijdonk *et al.* 2015] Ivo G. S. van Hooijdonk, Judith M. M. Donda, Herman J. H. Clercx, Fred C. Bosveld and Bas J. H. van de Wiel. *Shear Capacity as Prognostic for Nocturnal Boundary Layer Regimes.* Journal of Atmospheric Science, vol. 72, no. 4, pages 1518–1532, mar 2015. (Cited on pages 25, 26, 32, 36, 74, 75, 89, 96 and 125.)

[Van Ulden & Wieringa 1996] A. P. Van Ulden and J. Wieringa. Atmospheric Boundary Layer Research at Cabauw. Springer Netherlands, Dordrecht, 1996. (Cited on page 24.)

[Vavrus 2004] Steve Vavrus. *The Impact of Cloud Feedbacks on Arctic Climate under Greenhouse Forcing.* Journal of Climate, vol. 17, no. 3, pages 603–615, February 2004. (Cited on page 16.)

[Vickers & Mahrt 1997] Dean Vickers and L. Mahrt. *Quality Control and Flux Sampling Problems for Tower and Aircraft Data.* Journal of Atmospheric and Oceanic Technology, vol. 14, no. 3, pages 512–526, June 1997. (Cited on page 78.)

[Vignon *et al.* 2017] Etienne Vignon, Bas J. H. van de Wiel, Ivo G. S. van Hooijdonk, Christophe Genthon, Steven J. A. van der Linden, J. Antoon van Hooft, Peter Baas, William Maurel, Olivier Traullé and Giampietro Casasanta. *Stable boundary-layer regimes at Dome C, Antarctica: observation and analysis.* Quarterly Journal of the Royal Meteorological Society, vol. 143, no. 704, pages 1241–1253, mar 2017. (Cited on pages 26, 75, 89, 97 and 124.)

[Vignon *et al.* 2018] Etienne Vignon, Frédéric Hourdin, Christophe Genthon, Bas J. H. Van de Wiel, Hubert Gallée, Jean-Baptiste Madeleine and Julien Beaumet. *Modeling the Dynamics of the Atmospheric Boundary Layer Over the Antarctic Plateau With a General Circulation Model.* Journal of Advances in Modeling Earth Systems, vol. 10, no. 1, pages 98–125, jan 2018. (Cited on page 97.)

[Walden *et al.* 2016] V. P. Walden, S. R. Hudson and L. Cohen. *Norwegian Young Sea Ice Experiment (N-ICE) Field Campaign Report*, mar 2016. (Cited on pages 35, 41 and 43.)

[Walden *et al.* 2017] Von P. Walden, Stephen R. Hudson, Lana Cohen, Sarah Y. Murphy and Mats A. Granskog. *Atmospheric components of the surface energy budget over young sea ice: Results from the N-ICE2015 campaign.* Journal of Geophysical Research: Atmospheres, vol. 122, no. 16, pages 8427–8446, aug 2017. (Cited on pages 28, 33, 43, 44 and 61.)

[Wang & Key 2004] X. Wang and J. R. Key. *Arctic surface, cloud and radiation properties based on the AVHHR Polar Pathfinder dataset. Part I: spatial and temporal characteristics.* Journal of Climate, vol. 18, pages 2558–2574, 2004. (Cited on pages 3, 21, 22, 30, 31, 41, 49, 51 and 56.)

[Warren 1982] Stephen G. Warren. *Optical properties of snow.* Reviews of Geophysics, vol. 20, no. 1, pages 67–89, 1982. (Cited on page 28.)

[Weatherly *et al.* 1998] John W. Weatherly, Bruce P. Briegleb, William G. Large and James A. Maslanik. *Sea Ice and Polar Climate in the NCAR CSM*.* Journal of Climate, vol. 11, no. 6, pages 1472–1486, jun 1998. (Cited on pages 65 and 66.)

[Webb 1970] E. K. Webb. *Profile relationships: The log-linear range, and extension to strong stability.* Quarterly Journal of the Royal Meteorological Society, vol. 96, no. 407, pages 67–90, 1970. (Cited on page 24.)

[Weill *et al.* 2012] Alain Weill, Laurence Eymard, Frédéric Vivier, Ania Matulka, Rodrigue Loisil, Nadir Amarouche, Jean Michel Panel, Antonio Lourenço, Angelo Viola, Vito Vitale, Stefania Argentini and Heike Kupfer. *First Observations of Energy Budget and Bulk Fluxes at Ny Ålesund (Svalbard) during a 2010 Transition Period as Analyzed with the BEAR Station.* ISRN Meteorology, vol. 2012, page 675820, 2012. (Cited on pages 78, 80 and 89.)

[Wendisch *et al.* 2019] Manfred Wendisch, Andreas Macke, André Ehrlich, Christof Lüpkes, Mario Mech, Dmitry Chechin, Klaus Dethloff, Carola Barrientos Velasco, Heiko Bozem, Marlen Brückner, Hans-Christian Clemen, Susanne Crewell, Tobias Donth, Regis Dupuy, Kerstin Ebell, Ulrike Egerer, Ronny Engelmann, Christa Engler, Oliver Eppers, Martin Gehrmann, Xianda Gong, Matthias Gottschalk, Christophe Gourbeyre, Hannes Griesche, Jörg Hartmann, Markus Hartmann, Bernd Heinold, Andreas Herber, Hartmut Herrmann, Georg Heygster, Peter Hoor, Soheila Jafariserajehlou, Evelyn Jäkel, Emma Järvinen, Olivier Jourdan, Udo Kästner, Simonas Kecorius, Erlend M. Knudsen, Franziska Köllner, Jan Kretzschmar, Luca Lelli, Delphine Leroy, Marion Maturilli, Linlu Mei, Stephan Mertes, Guillaume Mioche, Roland Neuber, Marcel Nicolaus, Tatiana Nomokonova, Justus Notholt, Mathias Palm, Manuela van Pinxteren, Johannes Quaas, Philipp Richter, Elena Ruiz-Donoso, Michael Schäfer, Katja Schmieder, Martin Schnaiter, Johannes Schneider, Alfons Schwarzenböck, Patric Seifert, Matthew D. Shupe, Holger Siebert, Gunnar Spreen, Johannes Stapf, Frank Stratmann, Teresa Vogl, André Welti, Heike Wex, Alfred Wiedensohler, Marco Zanatta and Sebastian Zeppenfeld. *The Arctic Cloud Puzzle: Using ACLOUD/PASCAL Multiplatform Observations to Unravel the Role of Clouds and Aerosol Particles in Arctic Amplification.* Bulletin of the American Meteorological Society, vol. 100, no. 5, pages 841–871, may 2019. (Cited on page 41.)

[Westermann *et al.* 2009] S. Westermann, J. Lüers, M. Langer, K. Piel and J. Boike. *The annual surface energy budget of a high-arctic permafrost site on Svalbard, Norway.* The Cryosphere, vol. 3, no. 2, pages 245–263, dec 2009. (Cited on pages 33 and 34.)

[Winker & Vaughan 1994] D. M. Winker and M. A. Vaughan. *Vertical distribution of clouds over Hampton, Virginia observed by lidar under the ECLIPS and FIRE ETO programs.* Atmospheric Research, vol. 34, pages 117–133, 1994. (Cited on page 47.)

[Winker *et al.* 2009] David M. Winker, Mark A. Vaughan, Ali Omar, Yongxiang Hu, Kathleen A. Powell, Zhaoyan Liu, William H. Hunt and Stuart A. Young. *Overview of the CALIPSO mission and CALIOP data processing algorithms.* Journal of Atmospheric and Oceanic Technology, vol. 26, no. 11, pages 2310–2323, nov 2009. (Cited on pages 41, 47 and 48.)

[Winton 2006] M. Winton. *Amplified Arctic climate change: What does surface albedo feedback have to do with it?* Geophysical Research Letters, vol. 33, page L03701, 2006. (Cited on pages 2, 15 and 40.)

[Woods *et al.* 2013] C. Woods, R. Caballero and G. Svensson. *Large-scale circulation associated with moisture intrusions into the Arctic during the winter.* Geophysical Research Letters, vol. 40, pages 4717–4721, 2013. (Cited on pages 15, 20, 58 and 60.)

[Wu *et al.* 2006] Bingyi Wu, Jia Wang and John E. Walsh. *Dipole Anomaly in the Winter Arctic Atmosphere and Its Association with Sea Ice Motion.* Journal of Climate, vol. 19, no. 2, pages 210–225, January 2006. (Cited on page 15.)

[Wyngaard & Coté 1972] J. C. Wyngaard and O. R. Coté. *Cospectral similarity in the atmospheric surface layer.* Quarterly Journal of the Royal Meteorological Society, vol. 98, no. 417, pages 590–603, 1972. (Cited on page 96.)

[Zhang *et al.* 2011] Yehui Zhang, Dian J. Seidel, Jean-Christophe Golaz, Clara Deser and Robert A. Tomas. *Climatological Characteristics of Arctic and Antarctic Surface-Based Inversions.* Journal of Climate, vol. 24, no. 19, pages 5167–5186, oct 2011. (Cited on pages 3 and 23.)

[Zygmuntowska *et al.* 2012] M. Zygmuntowska, T. Mauritsen, J. Quaas and L. Kaleschke. *Arctic clouds and surface radiation - a critical comparison of satellite retrievals and the ERA-Interim reanalysis.* Atmospheric Chemistry and Phys, vol. 12, pages 6667–6677, 2012. (Cited on pages 3, 20, 40, 41, 49 and 51.)

Boundary-layer processes impacting the surface energy balance in the Arctic

Abstract: The Arctic is warming at two to three times as fast as the rest of the Earth, and it is therefore a crucial area of study for atmospheric scientists. However, the logistical difficulty of leading measure campaigns at high latitudes means that some key boundary-layer processes are still poorly understood. This thesis aimed to gain insight on two characteristics of the Arctic boundary-layer (clouds and surface based temperature inversions) and to determine their impact on the surface energy balance through a combination of novel measurements and modelling.

First, a novel statistic of cloud frequency and characteristics over the Arctic sea-ice was derived from a set of 1777 lidar profiles obtained during the 5-year Ice, Atmosphere, Ocean Observation Systems (IAOOS) campaign. Clouds were found to occur more than 85% of the time from May to October and single cloud layers were optically and geometrically thickest in October, possibly linked to moisture intrusions in autumn. Total cloud radiative forcing over a typical summer cycle was estimated to be negative for optically thin clouds, but positive for optically thick clouds.

Second, the impact of wind speeds on the development of surface based temperature inversions (SBI) in the continental Arctic was investigated. The analysis of measurements from the pre-ALPACA winter 2019 campaign that took place in Fairbanks, Alaska, showed that a local, likely topographically driven flow developed under anticyclonic conditions. This flow inhibited the development of strong SBIs by sustaining significant turbulence even under very strong radiative cooling. A transitional wind speed between weakly and strongly stable regimes was evidenced; this was coherent with the predictions of Minimum Wind speed for Sustainable Turbulence (MWST) theory.

The modelling of clear-sky surface layer temperature inversions and their dependence on wind speed was then studied, with a focus on forest areas. A 2-layer analytical model of the vegetated surface layer was developed. This model exhibited a slower decrease of the SBI strength with wind speed compared to a 1-layer model, which was shown to be coherent with observations at an Ameriflux site close to Fairbanks. These models were then compared to two WRF (Weather Research and Forecasting) surface layer schemes, which were found to place excessive limits on the turbulence, preventing the development of large temperature gradients.

The Arctic boundary-layer has become an active field of research in recent years. In this context, modelling advances and numerous planned campaigns open many perspectives for furthering the work presented in this thesis.

Keywords: Arctic, boundary-layer, clouds, temperature inversions

Résumé : L'Arctique se réchauffe deux à trois fois plus vite que le reste de la Terre, et c'est donc une zone d'étude cruciale des sciences de l'atmosphère. Cependant, la difficulté logistique de mener des campagnes de mesure à hautes latitudes fait que certains processus clés de la couche limite sont encore mal compris. Cette thèse a pour but d'étudier deux caractéristiques de la couche limite de l'Arctique (les nuages et les inversions de température en surface) et de déterminer leur impact sur le bilan d'énergie de surface en combinant observations et modélisation.

Tout d'abord, une nouvelle statistique des caractéristiques nuageuses au-dessus de la banquise a été dérivée d'un ensemble de 1777 profils lidar obtenus au cours de la campagne Ice, Atmosphere, Ocean Observation Systems (IAOOS). Lors de cette campagne, les nuages étaient présents plus de 85% du temps de mai à octobre et l'épaisseur (optique et géométrique) des couches de nuages individuelles était maximale en octobre. Le forçage radiatif total des nuages en été a été était négatif pour les nuages optiquement minces, mais positif pour les nuages optiquement épais.

Deuxièmement, l'impact des vitesses de vent sur le développement des inversions de température en surface en Arctique continental a été étudié. L'analyse des mesures de la campagne pré-ALPACA, qui a eu lieu à Fairbanks, Alaska, en hiver 2019, a montré qu'une circulation locale se renforce en conditions anticycloniques. Cet écoulement inhibe le développement de fortes inversions de température en alimentant la turbulence, même lorsque le refroidissement radiatif est très fort. La vitesse de vent à laquelle il y a transition entre des conditions peu et très stables a également pu être estimée. Celle-ci est cohérente avec les prédictions de la théorie de la vitesse minimale du vent (MWST).

La modélisation des inversions de température en conditions de ciel clair en lien avec la vitesse du vent a ensuite été étudiée, plus particulièrement en zones de couvert forestier. Un modèle analytique à deux couches de la couche de surface végétalisée a été développé. Ce modèle prévoit une diminution plus lente du gradient de température en fonction de la vitesse du vent par rapport à un modèle à une seul couche, et il est cohérent avec les observations menées à un site du réseau Ameriflux près de Fairbanks. En revanche, deux schémas de couche de surface du WRF (Weather Research and Forecasting) se sont avérés imposer des limites excessives à la turbulence, empêchant le développement de gradients de température importants.

La couche limite de l'Arctique est devenue un domaine de recherche actif ces dernières années. Dans ce contexte, les progrès de la modélisation et les nombreuses campagnes prévues ouvrent de nombreuses perspectives pour approfondir le travail présenté dans cette thèse.

Mots clés : Arctique, couche limite, nuages, inversions de température